

University of Warwick institutional repository: <http://go.warwick.ac.uk/wrap>

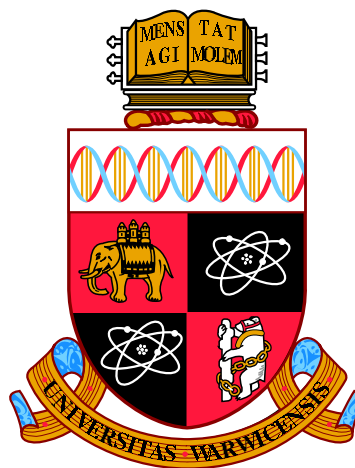
A Thesis Submitted for the Degree of PhD at the University of Warwick

<http://go.warwick.ac.uk/wrap/66689>

This thesis is made available online and is protected by original copyright.

Please scroll down to view the document itself.

Please refer to the repository record for this item for information to help you to cite it. Our policy information is available from the repository home page.



**Development of Solid State NMR on Disordered
Systems, from Bioactive glasses to Mullites**

by

Scott Paul King

Thesis

Submitted to the University of Warwick

for the degree of

Doctor of Philosophy

Department of Physics

June 2014

THE UNIVERSITY OF
WARWICK

Contents

List of Tables	v
List of Figures	vii
Acknowledgments	x
Declarations	xi
Abstract	xii
Abbreviations	xiii
Chapter 1 Introduction	1
1.1 History of NMR	1
1.2 NMR of Bioactive Phosphate Glasses: Motivation	7
1.3 NMR of Mullite Structures: Motivation	9
Chapter 2 NMR Theory	12
2.1 Zeeman Interaction	12
2.2 Density Operator	16
2.2.1 Evolution of the Density Operator	17
2.3 Hamiltonians and Interactions	18
2.3.1 External Interactions	19
2.4 Internal Interactions	22
2.4.1 Frame Rotations and Tensors	22
2.4.2 Magic Angle Spinning (MAS)	25
2.4.3 Chemical Shielding	28
2.4.4 Dipolar Interaction	30

2.4.5	<i>J</i> Coupling	34
2.4.6	Quadrupole Interaction	36
Chapter 3 Experimental Details		47
3.1	The NMR Signal	47
3.2	Two Dimensional NMR	49
3.3	Phase Cycling	51
3.4	Pulsed Experiments	53
3.4.1	Product Operators	53
3.4.2	Spin Echo	56
3.4.3	INADEQUATE and refocused INADEQUATE	59
3.4.4	Z-filters	63
3.4.5	REINE	64
3.4.6	<i>J</i> -HMQC	66
3.4.7	MQMAS	69
3.5	Signal to Noise	73
3.6	Relaxation	74
3.7	Simulation Details	74
3.7.1	DMFit	75
3.7.2	Quadfit	75
Chapter 4 Aluminium Doped Phosphate Bioactive Glasses		78
4.1	Introduction	78
4.2	Experimental Details	80
4.3	Results	82
4.3.1	²⁷ Al MAS NMR	82
4.3.2	²³ Na MAS NMR	84
4.3.3	³¹ P 1D MAS NMR	85
4.3.4	2D ³¹ P REINE MAS NMR	86
4.4	Discussion	91
4.5	Summary and Conclusion	95

Chapter 5	Gallium Doped Phosphate Bioactive Glasses	96
5.1	Introduction	96
5.2	Experimental Details	99
5.3	Results	102
5.3.1	1D ^{31}P Single Pulse MAS NMR	102
5.3.2	2D ^{31}P REINE MAS NMR	106
5.3.3	^{23}Na Single Pulse MAS NMR	111
5.3.4	^{71}Ga Single Pulse MAS NMR	113
5.3.5	$\{^{31}\text{P}\}$ - ^{71}Ga J -HMQC	116
5.3.6	^{17}O Spin Echo MAS NMR and 3QMAS	118
5.4	Discussion and Conclusions	122
Chapter 6	A Multinuclear NMR Study of the Tri-cluster and Defect Sites in Mullite and Boron Doped Mullite Systems	126
6.1	Introduction	126
6.2	Experimental Details	131
6.3	Results	134
6.3.1	^{27}Al MAS NMR	134
6.3.2	^{11}B MAS NMR	139
6.3.3	^{29}Si MAS NMR	141
6.3.4	^{29}Si refocused INADEQUATE	145
6.3.5	$\{^{29}\text{Si}\}$ - ^{27}Al J -HMQC	147
6.4	Discussion and Conclusion	150
Chapter 7	Summary	153
7.1	Phosphate Bioactive Glasses	153
7.2	Mullites	155
Appendix A	Appendix	173
A.1	Reduced Wigner rotation matrix elements $d_{kl}^j(\beta)$	173
A.2	Coefficients for the Second Order Quadrupole Interaction along with MQMAS ratio	174

A.3	^{23}Na MAS NMR parameters from simulation of Al doped bioactive glasses single pulse NMR spectra.	174
A.4	Simulation parameters from ^{31}P MAS NMR data of Al phosphate glasses.	175
A.5	Fitting Results from Time-Domain spin echo fits of ^{31}P REINE curves for $Q^1 - Q^1$ and $Q^1 - Q^2$ peaks of Al phosphate glasses	176
A.6	Fitting Results from Time-Domain spin echo fits of ^{31}P REINE curves for $Q^2 - Q^2$ peaks of Al phosphate glasses	177
A.7	Fitting Results from Time-Domain spin echo fits of ^{31}P REINE curves for $Q^1 - Q^2$ and $Q^2 - Q^2$ peaks of Ga phosphate glasses	178

List of Tables

3.1	Phase cycling table for simple pulse sequence.	53
4.1	Compositions of glasses under investigation, with varying Al and Na content.	81
4.2	^{27}Al MAS-NMR parameters from simulation of Al doped bioactive glasses single pulse NMR spectra.	84
5.1	Compositions of glasses under investigation, with varying Ga and Na content.	99
5.2	Fitting parameters from ^{31}P NMR of Ga glass samples.	104
5.3	^{23}Na MAS NMR parameters from simulation of Ga doped bio-active glasses single pulse NMR spectra.	111
5.4	^{71}Ga MAS NMR parameters from simulation of Ga doped bio-active glasses single pulse NMR spectra.	115
5.5	^{17}O NMR parameters from simulation of slices from 3QMAS NMR spectra.	121
6.1	Compositions of mullite samples under investigation.	132
6.2	^{27}Al MAS NMR parameters from simulation of mullite single pulse NMR spectra.	136
6.3	^{11}B MAS NMR parameters obtained from simulating single pulse mullite NMR data.	141
6.4	Simulation parameters from ^{29}Si MAS NMR of mullite samples.	143
A.1	Coefficients for the Second Order Quadrupole Interaction for spin $3/2$ and $5/2$ nuclei.	174

A.2	^{23}Na MAS NMR parameters from simulation of Al doped bioactive glasses single pulse NMR spectra.	174
A.3	Fitting parameters from ^{31}P NMR of Al glass samples.	175
A.4	Fitting Results from Time-Domain spin echo fits of ^{31}P REINE curves for $Q^1 - Q^1$ and $Q^1 - Q^2$ peaks for aluminium phosphate glass.	176
A.5	Fitting Results from Time-Domain spin echo fits of ^{31}P REINE curves for $Q^2 - Q^2$ peaks for aluminium phosphate glass.	177
A.6	Fitting Results from Time-Domain spin echo fits of ^{31}P REINE curves for $Q^1 - Q^1$ and $Q^1 - Q^2$ peaks for gallium phosphate glass.	178

List of Figures

2.1	Zeeman effect	13
2.2	Euler angles	24
2.3	Frame rotations	26
2.4	Chemical shift anisotropy (CSA) powder patterns	31
2.5	Orientation of the internuclear vector and Pake Doublet	32
2.6	Energy level diagram for isolated spin $I = \frac{1}{2}$ nucleus and for a pair of coupled spin $I = \frac{1}{2}$ nuclei, in the presence of a magnetic field	36
2.7	Energy level diagram for a spin $\frac{3}{2}$ nucleus.	41
2.8	Typical second order quadrupole broadened lineshapes under MAS.	45
3.1	Absorptive and dispersive lineshapes	48
3.2	Simple pulse sequence	51
3.3	Spin echo pulse sequence	56
3.4	INADEQUATE, refocused INADEQUATE and REINE pulse sequence.	60
3.5	J -HMQC pulse sequence	67
3.6	MQMAS pulse sequence	70
3.7	Split t_1 MQMAS pulse sequence	71
3.8	Change in Quadfit lineshape upon change in the C_Q width	76
4.1	^{27}Al single pulse MAS-NMR spectra and simulated fits for each Al glass composition.	83
4.2	^{23}Na single pulse MAS-NMR spectra and simulated fits for each Al glass composition.	85
4.3	^{31}P single pulse MAS-NMR spectra for each Al glass composition.	86
4.4	^{31}P REINE spectra at $\tau_j = 0.8$ ms for each Al glass composition	88

4.5	Time-domain spin echo curves obtained from the summed intensity for the Q^1 - Q^1 and Q^1 - Q^2 ^{31}P REINE peaks for each Al glass composition.	90
4.6	^{31}P Q^1 - Q^2 REINE peak pixel by pixel fitting for Al glasses	92
4.7	Time domain spin echo curves obtained from the summed intensity of the ^{31}P Q^2 - Q^2 REINE peaks for Al glasses	94
5.1	^{31}P single pulse MAS NMR spectra and simulated fits for the three Ga glass series.	103
5.2	^{31}P REINE spectra at $\tau_j = 0.8$ ms for each Ga glass composition.	107
5.3	Time-domain spin echo curves obtained from the summed intensity for the Q^1 - Q^2 and Q^2 - Q^2 ^{31}P REINE peaks for each Ga glass composition.	108
5.4	^{31}P Q^1 - Q^2 REINE peak pixel by pixel fitting for Ga glass compositions	109
5.5	^{23}Na single pulse NMR spectra and simulated fits for Ga glasses	112
5.6	^{71}Ga single pulse MAS-NMR along with simulated fits for Ga glasses	114
5.7	$\{^{31}\text{P}\}$ - ^{71}Ga J -HMQC of P45Ga15 glass	117
5.8	^{17}O Spin Echo NMR of P50Gax ^{17}O labelled samples	118
5.9	^{17}O 3QMAS NMR of P50Gax ^{17}O labelled samples	119
5.10	Slices of NBO resonance from ^{17}O 3QMAS of P50Gax glasses.	120
6.1	Diagram of the mullite structure.	127
6.2	Diagram of the B doped mullite structure.	130
6.3	Multifield single pulse ^{27}Al MAS NMR spectra along with simulated fits of 3:2 mullite samples.	135
6.4	Multifield single pulse ^{27}Al MAS NMR spectra along with simulated fits of sillimanite	137
6.5	Multifield 3QMAS ^{27}Al spectra of 3:2 mullite samples.	138
6.6	Multifield ^{27}Al MAS NMR spectra of 2:1 mullite.	140
6.7	^{11}B single pulse MAS NMR and 3QMAS spectra of B doped mullites.	140
6.8	^{29}Si single pulse MAS NMR spectra along with simulated fits of 3:2 mullites.	142
6.9	Comparison of ^{29}Si single pulse MAS NMR spectra of 2:1 mullite and 3:2 mullite.	145
6.10	1D ^{29}Si refocused INADEQUATE of 3:2 undoped and 6 % B doped mullite.	147

6.11	$\{^{29}\text{Si}\}$ - ^{27}Al J -HMQC of 3:2 undoped and 6 % B doped mullites. 148
------	--	-------------

Acknowledgments

Firstly, I would like to thank my supervisor Dr John Hanna, for his guidance and support throughout every aspect of this PhD project. I would also like to thank my second supervisor Professor Steven Brown for his input, particularly early on in my research whilst getting to grips with 2D NMR and the REINE pulse sequence. I'm extremely grateful to the Engineering and Physical Sciences Research Council (EPSRC) for helping to fund my project, without which this research wouldn't have been possible. I am indebted to the great support of everyone in the Solid State NMR group at the University of Warwick, in particular Dr Andy Howes and Dr Tom Kemp for assisting with any technical issues arising in the lab, Dr Dinu Iuga for his guidance whilst using the 850 MHz facility, and Dr Greg Rees for his assistance in teaching me NMR in the early stages of my project.

The many collaborators I have had the pleasure to work with throughout my time in NMR, from a vast range of institutions, enabled me to obtain experience in a wide range of research areas, which I acknowledge helped me to develop as an NMR spectroscopist. I would like to thank Dr Hanna Lühns and Professor Reinhard Fischer (University of Bremen) for providing me with high quality mullite samples and for their knowledge on the mullite systems, always happy to answer any questions I may have relating to their complex structure. In addition, everyone involved in the collaborations involving the glass materials; from providing samples, helping with labelling, and informative discussions, including Dr Richard Martin (Aston University), Professor Jonathan Knowles (UCL), Dr Jodie Smith and Dr Dave Pickup (University of Kent). Dr. Paul Guerry is acknowledged for providing the MATLAB fitting routines used in the analysis of the REINE data.

Lastly and most importantly the completion of this project would not have come about if it were not for the encouragement of my friends and family, especially my parents, sister and grandparents, for their love and support throughout.

Declarations

I hereby declare that this thesis **Development of Solid State NMR on Disordered Systems, from Bioactive glasses to Mullites** is an original work and has not been submitted for a degree or diploma or other qualification at any other University.

Results from other authors are referenced in the usual manner throughout the text. All collaborative results are indicated in the text along with the nature and extent of my individual contribution, a brief summary is given here:

In Chapter 4 the samples were synthesised by Dr Jodie Smith and Dr Dave Pickup at the University of Kent. The ^{27}Al measurements presented in Chapter 4 have been carried out by myself and feature in the publication “Structural study of Al_2O_3 - Na_2O - CaO - P_2O_5 bioactive glasses as a function of aluminium content”. J.M. Smith, S. P. King, E. R. Barney, J. V. Hanna, R. J. Newport, and D. M. Pickup. *The Journal of Chemical Physics*, 2013, 138, 034501. The MATLAB package used for analysis of the REINE data was kindly provided by Paul Guerry, which itself had previously been modified from Paul Hodgkinsons fitting routines.

The gallium phosphate glass series in Chapter 5 was synthesised by Professor Jonathan Knowles’ group at UCL, with the exception of the ^{17}O labelled samples which were provided by Dr Richard Martin at Aston University. ^{17}O labelled CaO used for the synthesis of the labelled samples was kindly provided by Franck Fayon (Universite d’Orleans).

All mullite samples from Chapter 6 were synthesised by Dr Hanna Lührs and Professor Reinhard X. Fischer at the University of Bremen. Dr Hanna Lührs also assisted in providing the diagrams of the mullite structure. The single crystal 2:1 mullite sample was provided by Professor Hartmut Schneider (University of Bremen). The ^{11}B MAS results shown in Chapter 6, obtained by myself, have been previously featured in the publication “Neutron diffraction and ^{11}B solid state NMR studies of the crystal structure of B-doped mullite”. H. Lührs, S. P. King, J. V. Hanna, H. Schneider, and R. X. Fischer. *Zeitschrift für Kristallographie*, 2013, 228, 457-466.

Abstract

Phosphate glasses for potential applications as bioactive materials have been studied using Solid state Nuclear Magnetic Resonance (NMR), owing to the fact that their bioactivity is strongly correlated to their atomic structure. A multinuclear NMR approach has been conducted on numerous series of phosphate bioactive glasses including ^{31}P , ^{23}Na , along with ^{27}Al MAS NMR on a series of Al doped glasses, and the less widely studied ^{71}Ga and ^{17}O MAS NMR on multiple series of Ga doped glasses. In addition, the first implementation of the recently developed ^{31}P refocused INADEQUATE Spin-Echo (REINE) experiment on a coherent series of glasses has been shown, providing greater insight into the distribution of J couplings throughout the phosphate network.

Upon incorporation of Al into the phosphate network, ^{27}Al MAS NMR has shown a subsequent change from initially octahedral to tetrahedral Al coordination. In addition, an increase in shielding and decrease in the quadrupolar parameter C_Q of the Na ions from ^{23}Na MAS NMR, along with a decrease in the ^{31}P J coupling indicated from the REINE data, evidences the role of Al within the glass network cross linking phosphate chains, resulting in a strengthened more condensed network.

In the Ga doped glass series the ^{71}Ga MAS NMR data shows a similar trend for the Ga coordination as found in the Al series, with the ^{23}Na MAS NMR also indicating comparable results. The ^{31}P REINE results however, do not provide observable trends, thus indicating that the Ga is having a slight different influence in the glass network to that of the Al cation. ^{17}O 3QMAS results show the presence of both non bridging and bridging oxygens as expected in these systems.

Mullite materials are of interest to material scientists owing to their favourable properties, making them ideal for ‘advanced ceramic’ applications. However, the structure of mullite is complex owing to the disorder, arising from the vacancies present in the aluminosilicate network. A comprehensive multinuclear solid state MAS NMR investigation has been carried out on the structure of both undoped 3:2 mullite, and B doped 3:2 mullite materials. ^{27}Al single pulse MAS NMR has enabled the identification of the octahedral and tetrahedral sites present, along with the ^{27}Al 3QMAS experiment providing conclusive evidence of the Al tri-cluster sites in the structure. 100 % ^{29}Si labelled samples have enabled the acquisition of quantitative and high resolution ^{29}Si MAS NMR data, along with ^{29}Si refocused INADEQUATE and $\{^{29}\text{Si}\}$ - ^{27}Al J -HMQC correlation experiments, providing detailed information on the connectivities in the aluminosilicate network. Both the ^{27}Al and ^{29}Si MAS NMR data have enabled determination of the nature of the tri-cluster site. ^{11}B MAS NMR on B doped 3:2 mullite materials have shown B to occupy a BO_3 coordination within the mullite structure according to a substitution with Si, cross linking the octahedral Al chains.

Abbreviations

3Q	Triple Quantum
ADP	Ammonium Dihydrogen Phosphate
AIT*	Aluminium site within a tri-cluster
BO	Bridging Oxygens
COSY	Correlation Spectroscopy
CP	Cross Polarisation
CRAMPS	Combined Rotation and Multiple-Pulse Sequence
CSA	Chemical Shift Anisotropy
CT	Central Transition
CW	Continuous Wave
DAS	Dynamic Angle Spinning
DFT	Density Functional Theory
DLS	Distance Least Squares
DNP	Dynamic Nuclear Polarisation
DOR	Double Angle Rotation
DQ	Double Quantum
EFG	Electric Field Gradient
EPR	Electron Paramagnetic Resonance
FDA	Food and Drug Administration (US)
FID	Free Induction Decay
FTIR	Fourier Transform Infrared Spectroscopy
HMQC	Hetronuclear Multiple Quantum Correlation Experiment
Hz	Hertz
INADEQUATE	Incredible Natural Abundance Double Quantum Transfer Experiment
INEPT	Insensitive Nuclei Enhanced by Polarisation Transfer Experiment
IUPAC	International Union of Pure and Applied Chemistry

LAB	Lab Reference Frame
MAS	Magic Angle Spinning
MQMAS	Multiple Quantum Magic Angle Spinning Experiment
MRI	Magnetic Resonance Imaging
NBO	Non Bridging Oxygens
NMR	Nuclear Magnetic Resonance
PAS	Principle Axis Rotation Frame
REINE	Refocused INADEQUATE Spin-Echo
rf	Radiofrequency
S/N	Signal to Noise Ratio
SQ	Single Quantum
TMS	Tetramethylsilane
TO	Terminal Oxygens
TPPI	Time-Proportional Phase Incrementation
TQ	Triple Quantum
XRD	X-Ray Diffraction
YAG	Yttrium Aluminium Garnet
ZQ	Zero Quantum

Chapter 1

Introduction

1.1 History of NMR

Before the 20th century the subject of nuclear physics had not really been established, with the discovery by Rutherford in 1907 of the model of the atom consisting of a dense positive nucleus surrounded by the negative electron, and later in 1932 the nucleus by James Chadwick, both laying down the groundwork for the field.[1, 2] It was only a short time after this discovery of the neutron in 1938, that the resonance effect of nuclear matter was observed by Isidor Isaac Rabi. Rabi's experiment consisted of a molecular beam of LiCl that was deflected by an inhomogeneous magnetic field and subsequently refocused by a second field. Resonance was observed when upon variation of the field a drop in intensity due to a failure in the refocusing occurred.[3] Rabi was awarded the Nobel prize in physics for his work in 1944 "*for his resonance method for recording the magnetic properties of atomic nuclei.*"

In fact the first attempt to measure an NMR signal was actually a few years earlier in 1936 by Gorter and Broer, endeavouring to observe signals in LiCl and KF powders. However no signal was measured, with the unsuccessful results published later. The reason behind this failed attempt is unclear, although it is usually attributed to long relaxation times and the poor signal to noise of the primitive apparatus used.[4]

It would have to wait until after the Second World War before the next major step in the story of NMR would take place, when two research groups switched to observing Nuclear Magnetic Resonance on condensed matter, rather than by molecular beams, despite the previous failure of Gorter in this area. Edward Purcell working at

MIT carried out the first ‘solid state’ NMR experiment, detecting NMR absorption of protons in a tank of paraffin, upon changing the applied magnetic field. Meanwhile, Felix Bloch at Stanford carried out the first ‘liquid state’ NMR, using a transmitter receiver set up in the presence of a magnetic field, to obtain nuclear induction in water. Both Bloch and Purcell were credited with the discovery of what we think of as modern day NMR, with both of their results published early in 1946, for which they were subsequently awarded the Nobel Prize in 1952 “*for their development of new methods for nuclear magnetic precision measurements and discoveries in connection therewith.*” [5–7] It is an interesting point that the two different methods implemented by the two groups for detecting resonances actually represent the two methods for explaining the NMR phenomenon, with the absorption from Purcell’s method best described by quantum mechanics, and Bloch’s method of induction described by the classical description of electromagnetic induction.

Early work in the field of NMR was predominantly carried out by Physicists, in the hope of using the nuclear resonance frequency of a nuclear species to measure its magnetic moment, as it was a non destructive way to obtain these precision measurements. This work was based on the early assumption that the resonance frequency of a particular nuclear species depended only upon the strength of the applied field. However, this was all about to change during the 1950s with the surprise discovery by Proctor and Yu that the ^{14}N resonance frequency observed depended strongly on the chemical compound under observation.[8] This effect had also been observed by Dickinson who noted “*for ^{19}F the value of the applied magnetic field H_0 for nuclear magnetic resonance at a fixed frequency depends on the chemical compound containing the fluorine nucleus.*” [9] A year earlier Walter Knight had observed a similar phenomenon in a series of metals, however this was due to delocalised conducting electrons in the vicinity of the metal nucleus, what we now know as the ‘Knight Shift’ in metals.[10] A full theory of the chemical shift was presented in 1950 by Ramsey.[11] The discovery of the chemical shift, resulting in different resonance frequencies for a particular nuclear species due to differences in the chemical structure, ultimately led to the technique being taken up by chemists to become the vital tool for structural characterisation it is today.

Around the same time George E. Pake led further ground breaking research

looking at a single crystal of gypsum ($\text{CaSO}_4 \cdot 2\text{H}_2\text{O}$), containing two protons which represent the only significantly magnetic species when looking at its ^1H resonance.[12] The observed pair of doublets, indicated that each proton could see the two states of its coupled neighbour, both up and down. Pake then expanded this to powdered solids to identify the ‘Pake doublet’, arising from the different orientations of different crystals within a powder. Using NMR to observe H atoms became a useful tool to exploit, due to the difficulty in observing these small nuclei by other techniques, such as XRD, due to scattering effects from heavier atoms. In addition, the ability to probe and measure intermolecular distances due to the $1/r^3$ dependence of the dipolar interaction was also noted by Pake. The commonly held view of the turning point towards ‘high resolution’ NMR actually came from the work of Dharmatti and Packard in 1951.[13] Due to improvements in magnet inhomogeneity, they managed to observe a spectrum of ethanol showing three distinct lines with ratios 1:2:3 for the first time, providing direct evidence for the $\text{CH}_3\text{CH}_2\text{OH}$ formula.

Early NMR experimental approaches had taken advantage of the readily available rf apparatus left over from the war. However, a need for more user-friendly apparatus was essential as chemists were becoming more interested in exploiting the technique during the 1950s. Commercial spectrometers became available in the early 50s, developed by Varian associates after their application for a patent as early as 1946 (the same year as the discovery by Bloch and Purcell) although it wasn’t granted until 1951. The first operating spectrometers operated at a proton larmor frequency of 30 MHz (0.7 T), and although manufactured commercially these initial designs were not user friendly. Early experiments consisted of sweeping the magnetic field, acquiring signal over a large frequency range using Continuous Wave excitation (CW). However, the inefficiency of this method resulted in only one frequency step recorded at any one time, thus in addition to gathering signal, baseline noise was also acquired if the exact position of the resonance was unknown, leading to an inefficient use of time. An alternative method was to use rf pulses, which was the method exploited by Erwin Hahn in 1949 to measure spin-lattice relaxation times, and Henry Torrey measuring nutation resonance, providing the first applications of rf pulses in NMR.[14, 15]. Bloch had in fact proposed the pulsed method in his paper in 1946, with little effort in the intermediate years to progress this alternate method into the mainstream.

Poor sensitivity from low Boltzmann factors of NMR states at room temperature was a key challenge that was successfully tackled in 1963 by Klein and Barton.[16] They determined that by accumulating many relatively rapid scans of the full spectrum, so that the signals add coherently whereas the noise adds randomly, signal to noise may be enhanced by one to two orders of magnitude without sacrifice of bandwidth. This was then followed in 1966 by Ernst and Anderson by the Fourier transform method, where short pulses of high power rf radiation were applied with the response of the system observed and Fourier transformed to obtain a frequency domain spectrum.[17] This again improved sensitivity and made data acquisition a much faster process. Although at this stage computing power to carry out the Fourier transformations meant that obtaining a fully processed spectrum could take a matter of days.

Magnet design was an early problem to overcome, with permanent and electromagnets both being used by different research groups, however they were limited by their strength. The first superconducting magnet for NMR studies was implemented in 1964, which meant much higher fields were accessible, although the economy of these early systems was poor with short liquid helium hold times, leading to refills being required twice a week. [18]

With the discovery of the chemical shift and later the J coupling the dominance of solution NMR became widespread, with narrow resonances obtained emanating from the molecular tumbling in solution removing any anisotropies.[19, 20] A significant breakthrough in solid state NMR came with the observation that interactions causing broadening of resonances had an angular dependence that could be removed upon successful rotation of the sample at a well defined angle. Magic angle spinning (MAS) was invented by two groups simultaneously; E. Raymond Andrew in the UK, and by I.J. Lowe in the US.[21–23] However, its commercial viability wasn't appreciated until much later on due to the difficulty in the experimental design of a stable MAS method, with solution NMR remaining the more accessible and widely researched area.

With the advent of pulsed Fourier transform NMR, developments could be made in utilising rf pulses to exploit 'spin dynamics'. The most fundamental of which was made by accident, when Hahn was experimenting with high power rf pulses of short duration. He found that at times when no pulse was applied '*the weird signal appeared*'. (as discussed in Hahn, Erwin L.: Pulsed NMR-A Personal History [24]), which was

found to be reproducible, he had discovered the spin echo.[25]. This was later modified into the conventional $90^\circ\text{-}\tau/2\text{-}180^\circ\text{-}\tau/2$ spin echo by Carr and Purcell, which went on to become the basic building block for a wide range of future NMR pulse sequences.[26]

The desire to manipulate spins was generally twofold; to enhance signal due to the poor sensitivity of NMR, or to exploit or remove a particular NMR interaction. Cross polarisation (CP) exploited the first of these, transferring polarisation from the more abundant spin to the less abundant spin, whereas heteronuclear decoupling achieved the second by suppressing broadening due to undesired interactions.[27, 28] Pines and his co-workers combined the two techniques to obtain a ^{13}C chemical shift spectrum of a solid using this dilute nuclei.[29] The idea to combine the approach of CP with heteronuclear decoupling whilst also under magic angle spinning of Stejskal and Schaefer successfully achieved removal of broadening due to anisotropic interactions, with the larger homogeneous dipolar broadening removed by decoupling due to it being too large to be successfully averaged away by achievable MAS rates at the time, and with the smaller chemical shift anisotropy (CSA) removed by MAS.[30]

The idea for 2D NMR spectroscopy was first proposed by Jean Jeener at the Ampere International Summer School II, (Basko Polje, 1971), but the basic theory and first experiments were published by Richard R. Ernst's group.[31] This seminal paper laid the groundwork for many 2D experiments to come, including the 2D heteronuclear correlation,[32, 33] the 2D INEPT (Insensitive Nuclei Enhanced by Polarisation Transfer),[34] the combined rotation at the magic angle and multiple pulse (CRAMPS) technique,[35] and the homonuclear INADEQUATE, [36] contributing to the wealth of information achievable from manipulating spins via NMR.

Arguably one of the most significant discoveries in the field of magnetic resonance, or at least the one most recognisable to the general public, would be in its use to form images, particularly of human organs for medical diagnostics. The first Magnetic Resonance Imaging (MRI) images were collected in 1974 by Peter Mansfield in the UK and Paul C. Lauterbur in the USA, where they used magnetic field gradients for the spatial localisation of NMR signals.[37, 38] This achievement granted them the joint award of the Nobel Prize in Physiology or Medicine in 2003, after the technique had already progressed into a huge field of research in its own right.

Another branch out field from nuclear magnetic resonance was that of Dynamic

Nuclear Polarisation (DNP), with the aim of enhancing weak signals obtained in NMR. DNP was first proposed by Overhauser in 1953 as a means of enhancing nuclear polarisation via transferring polarisation from the electrons of paramagnetic impurities by microwave irradiation close to the electron resonance frequency, enhancing the signal obtained.[39] Early studies showed its effect in enhancing signals in metals, then subsequently liquids.[40, 41] Since the early 90s however, with improvements of microwave sources, DNP has undergone a new ‘renaissance’, with papers by Griffin and co-workers showing high field MAS-DNP using a gyrotron source.[42, 43] This was followed by the invention of the dissolution DNP method, where a factor of 10,000 enhancement for liquid signals was achieved. Whereby in this method the sample is polarised at low temperature by microwave irradiation, the sample is then dissolved in a hot solvent and quickly put into the NMR tube in the magnetic field where detection occurs.[44]

During the early days of NMR, quadrupole nuclei were difficult to study, owing to them experiencing large broadening from the quadrupole interaction at the low magnetic fields available at the time. However, research to combat these effects was not neglected, with line narrowing methods developed, with initial studies using conventional MAS, leading to the more technically advanced methods of DOR and DAS to remove the residual second order quadrupole effects.[45–50] However the real turning point for studies of quadrupole nuclei came in 1995 with the ground breaking pulse sequence by Frydman and Harwood, the multiple-quantum magic-angle spinning (MQ-MAS), successfully tackling the problem of broadening from the 2nd order quadrupole interaction which isn’t removed by conventional MAS.[51] The MQMAS experiment is still a routinely used tool for solid state NMR spectroscopists, with its implementation widely shown throughout this thesis.

In recent years solid state NMR has become even more widely used, by Chemists, Physicists, Engineers and Material Scientists, due to advances in experimental approaches, but mainly following great improvements in engineering and the hardware available. MAS rates of just over 100 kHz are now achievable, in addition to high magnetic fields commercially available of up to 1 GHz, facilitating in improving signal to noise and reducing unwanted broadening. This has led to the use of solid state NMR in the observation of a wide range of systems from inorganic materials, to peptides and proteins,[52, 53] continuously resulting in new cutting edge discoveries.

1.2 NMR of Bioactive Phosphate Glasses: Motivation

An area of particular interest for solid state NMR spectroscopists has been in the study of disordered materials, due to the specificity granted by the NMR technique. Other methods of structural characterisation, such as X-ray diffraction, rely upon long range periodicity, restricting their use on disordered materials which lack this long range order. Glass is such a material, with great technological importance, possessing order only on the more local nuclear scale with no long range periodicity.

Early solid state NMR studies on glasses first appeared in the 1950s,[54] although due to the broad nature of the NMR resonances arising from the vast array of nuclear sites found within its disordered structure, solid state NMR on glass systems did not really catch on until the use of magic angle spinning could be used in pulsed Fourier transform NMR studies, to achieve suitable line narrowing.[55–58] A lot of early MAS studies focused on silicate based glasses, permitting determination of the silicon coordinations present within the network. Phosphate based glasses however, were not neglected, with early work by Brow,[59, 60] and comprehensive reviews of early NMR phosphate glass results given by Eckert and Kirpatrick and Brow,[61, 62] proving NMR to be a big contributor in the field, due to the vast array of structural information obtained along with its non destructive nature, whilst requiring little sample preparation. Despite the disordered nature of these structures, from amassing the vast array of data from the numerous studies, simple structural models have been created, with the publications by Hoppe in 1996, and Brow at the turn of the 21st century, showing the significant progress in the understanding of these disordered phosphate materials.[63, 64]

The driving force behind understanding the structure of glassy materials originates in the desire for knowledge that will help in their development for their numerous applications. One area of significant interest is in the use of glass as biomaterials, for instance as artificial implants. The developments that initiated this field of research were carried out by Larry Hench, who carrying out work funded by the US army, had the desire to design a material that would help prevent unnecessary amputation of wounded soldiers limbs, due to rejection of bioinert implants routinely used at the time.[66] The original premise of Hench’s research was to design a material that would successfully

form a Hydroxyapatite layer *in vivo* that would not get rejected by the body, due to a major proportion of bone being composed of Hydroxyapatite. Thus Bioglass[®] was developed, a glass comprising of Ca and phosphate, within a Na₂O -SiO₂ matrix.[65] The first implementation of Bioglass[®] clinically was in 1985 to solve hearing loss, by replacing bones within the inner ear with a Bioglass[®] substitute. A review of the motivation behind the discovery of Bioglass[®] and its history through the past 40 years is given in full by Hench in “The Story of Bioglass[®]”. [66]

Technological advances in silicate based Bioglasses[®] have not been the only area of successful research in the field of biomaterials, with Ca phosphate based bioceramics used in dentistry and medicine for over 20 years.[67] Attention has also been focused on developing phosphate based bioactive glasses, similar to the original Bioglass[®]. The advantage of a glass material is that a wide variety of dopant cations can be incorporated to the structure, with the purpose of fulfilling a specific role. In comparison to the silicate based bioactive glasses, which have break down times within the body on the order of years,[68] phosphate bioactive glasses have much faster dissolution rates which could allow them to perform different functions. For instance, phosphate bioactive glasses have been developed as novel delivery devices providing controlled release of ions such as antibacterial Ag or Cu.[69, 70] In addition, various developments for phosphate glasses for hard tissue engineering as biodegradable scaffolds that are eventually replaced by natural tissue has been proposed, with a comprehensive review of the area given by Abou Neel and Pickup. [71]

The key characteristics of phosphate bioactive glasses is both the bioactivity and the dissolution rates, as control of both can allow specific functions to be achieved, with numerous studies focused on measuring both of these factors for particular glass compositions.[72–77] Both bioactivity and dissolution rates are strongly correlated to the atomic structure of the glass network, thus a detailed understanding of the structure, permits the greatest control of the glasses properties. In recent years, many NMR studies on phosphate bioactive glasses have been undertaken, with the technique shown to provide detailed valuable structural information.[71, 78, 79]

The work in this thesis involves using multinuclear solid state MAS NMR techniques, to look in detail at the structure of numerous series of phosphate glasses, for potential bioactive applications. Recent developments in the field of solid state MAS

NMR will be used, including the implementation of the ^{31}P REINE pulse sequence on a series of glasses for the first time, providing valuable information on the disorder in the phosphate network. ^{17}O and ^{71}Ga NMR will also be presented, which previously have proved difficult to study using solid state MAS NMR, due to their quadrupole nature and their low natural abundance (in particular ^{17}O , which is only 0.037 %). The intention is to provide a much deeper insight into the structure of these disordered systems, with the ultimate aim of helping to further stimulate their use as potential biomaterials.

1.3 NMR of Mullite Structures: Motivation

Understanding and studying the structure of ceramic materials is important not only owing to their occurrence in nature, but also due to their widespread production and use for over thousands of years for wide ranging applications. The aluminosilicate ceramic mullite is no exception to this, taking its name from the Isle of Mull in Scotland where it was initially discovered, in regions where hot lava comes into contact with Al_2O_3 rich sedimentary rocks.[80] Despite its rare presence in nature, mullite is a common phase in many conventional man made ceramics including clay products, pottery, porcelains, sanitary ceramics, refractories and in structural clay products like building bricks, pipes and tiles. Thus, mullite has arguably had a large influence indirectly on the development of civilisation throughout the history of mankind. Recently mullite has gained significant interest for use in ‘advanced ceramics’ due to its very appealing properties, including high thermal stability, low thermal expansion, low thermal conductivity, high creep resistance, corrosion stability, and its hard wearing nature.[81] The fact that the starting materials required for mullite formation are abundant in large quantities on earth, and the ability of mullite to form a solid solution in a large $\text{Al}_2\text{O}_3/\text{SiO}_2$ range, giving it the ability to incorporate a wide range of foreign cations, coupled with the fact that the structural principles of mullites can be extended to a wide ‘family range’ of related phases with different compositions, all add to its appeal for engineers and materials scientists alike.

The name mullite was first proposed in the work by Bowen and Greig in 1924, who found that stable aluminosilicate in the Al_2O_3 - SiO_2 system has 3:2 ($3\text{Al}_2\text{O}_3\cdot 2\text{SiO}_2$)

instead of the 1:1 ($\text{Al}_2\text{O}_3\text{SiO}_2$) composition as was commonly thought prior to this.[82] The general formula for the structure of mullite is $\text{Al}_2[\text{Al}_{2+2x}\text{Si}_{2-2x}]\text{O}_{10-x}$ with x typically varying from $x = 0.2$ to 0.9 . Many studies on the crystallographic structure of mullite have since been published, with the general consensus being that its structure is very similar to that of the crystalline aluminosilicate sillimanite (Al_2SiO_5).[80, 83, 84] Like sillimanite, mullite consists of chains of Al octahedra running down the crystallographic c -axis, with these chains cross linked by tetrahedral double chains of $(\text{Al},\text{Si})\text{O}_4$ tetrahedra. In mullite however, some of the O bridging the tetrahedra are vacant (thus making it distinct from sillimanite), resulting in the formation of proposed tri-cluster sites (T_3O). This leads to a slight disorder in the structure due to this vacancy, making the creation of an absolute model of the mullite structure incomplete, due to the complexity of the vast array of possible crystallographic sites present.

As already mentioned, one of the favourable properties of mullites lies in its ability to incorporate a wide range of different cations, whilst still retaining the mullite type structure and thus its favourable properties. Al borates are a related class of material that like mullites possess stability to very high temperatures and pressures. The $\text{Al}_{18}\text{B}_4\text{O}_{33}$ phase ($9\text{Al}_2\text{O}_3 \cdot 2\text{B}_2\text{O}_3$) has gained specific interest, used as both a refractory lining due to its low thermal expansion and its corrosion resistance against B rich glasses, and for the reinforcement of metal matrices.[85, 86] There are many phases within the Al_2O_3 - B_2O_3 series which are structurally related to mullite, and therefore a combination of the two systems promises a great potential to design high-performance materials. A solid solution between mullite and $\text{Al}_{18}\text{B}_4\text{O}_{33}$ was proposed in the 1950's with the term 'B mullite' or 'boron-mullite' introduced by Werding and Schreyer.[87, 88] Recent work has however shown that there is no complete solid solution between mullites and Al borates.[86, 89, 90] Although, significant changes of lattice parameters b and c occurs with B doping, in contrast no significant changes are observed for lattice parameter a , which is linearly correlated with the Al/Si ratio in mullite.[86, 89, 90]

Solid state MAS NMR studies on mullite systems have long been carried out. Turner *et al.* showed the first ^{27}Al MAS NMR data on mullite materials, distinguishing between the octahedral and tetrahedral resonances, along with attributing a site in the intermediate regime to possibly be a tri-cluster species.[91] ^{29}Si MAS NMR was first shown by Merwin *et al.*, along with further ^{27}Al MAS NMR data, again with assignment

of the tri-cluster species.[92] Further ^{29}Si assignments have been carried out in many studies since, most notably by Ban and Okada, Jaymes *et al.*, and Schmucker *et al.*.[93–96] However the most conclusive evidence of the tri-cluster species has been presented by Bodart *et al.* from ^{27}Al 3QMAS measurements on a 2:1 mullite system.[97] The suitability of using solid state MAS NMR to probe the mullite structure emanates from mullite crystallography not being straightforward, due to the vacancies resulting in an apparent disorder. Therefore, NMR remains a key tool in its structural characterisation, due to its nuclear specificity, probing the nuclear sites directly.

Since the previous studies surrounding both mullites and B doped mullites, developments in solid state NMR techniques have greatly improved. This means that structural questions that still remain unanswered regarding the mullite structure, can now be addressed using these more advanced techniques. For instance, the desire for clear unambiguous confirmation of the presence of the tri-cluster resonance using ^{27}Al MAS NMR in the 3:2 mullite system can be achieved by exploiting the 2D method of MQMAS, as done by Bodart *et al.* on a 2:1 mullite system. This enables the separation of resonances in a second dimension, typically broadened by the second order quadrupole interaction precluding their observation from 1D MAS NMR.[97] Further information will also be obtained upon using 2D NMR correlation methods, which have become more widespread in solid state NMR since the late 1990's, in order to provide a more complete picture of the network connectivities within this complicated structure. Focus will be on both the ‘conventional’ aluminosilicate 3:2 mullite, in addition to a series of B doped 3:2 mullites providing further advancement in this field of materials of great industrial importance.

Chapter 2

NMR Theory

The theory in this section is based upon a number of sources, mainly the texts: ‘*Introduction to Solid State NMR Spectroscopy*’ M.J. Duer.[98] ‘*Spin Dynamics*’ M.H. Levitt.[99] ‘*NMR: the Toolkit*’ P.J Hore, J A. Jones, and S. Wimperis.[100] ‘*Multinuclear Solid State NMR of Inorganic Materials*’ K.J.D. MacKenzie, and M.E. Smith.[101] ‘*Solid-state NMR : basic principles & practice*’ D.C. Apperley, R.K. Harris, and P. Hodgkinson. [102]

2.1 Zeeman Interaction

All subatomic particles have a series of fundamental properties such as mass and charge, however a further intrinsic property determined from Quantum Mechanics is that of spin angular momentum. This is defined by the spin angular momentum quantum number, I , which can take positive integer or half integer values, and for atomic nuclei takes a specific value for each individual isotope, dependent on the constituent nucleons. Further to this, the spin angular momentum is quantized in units of \hbar into $2I+1$ possible energy levels, represented by the azimuthal quantum number m , $m = +I, +I-1, \dots, -I$.

In the absence of a magnetic field all of these energy levels are degenerate. However, in the presence of an external magnetic field this degeneracy is lifted causing the spin states to split, resulting in a separation of energy levels. This is due to the interaction between B_0 and the magnetic moment and is commonly known as the Zeeman Effect, as shown in Figure 2.1.

The classical expression for the Zeeman interaction is

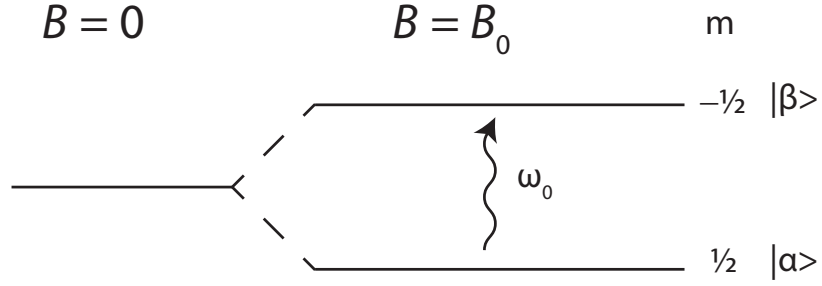


Figure 2.1: Diagram showing the Zeeman effect for a $I = \frac{1}{2}$. In the absence of a magnetic field the energy levels are degenerate. Whereas application of a magnetic field, B_0 , lifts the degeneracy resulting in two energy levels α and β , $m = \frac{1}{2}$ and $-\frac{1}{2}$, respectively, with an energy difference in frequency units of ω_0 between them.

$$E = -\boldsymbol{\mu} \cdot \mathbf{B}_0 \quad (2.1)$$

where $\boldsymbol{\mu}$ is the magnetic moment represented by:

$$\boldsymbol{\mu} = \gamma \mathbf{I}, \quad (2.2)$$

and γ is the gyromagnetic ratio specific for each individual nuclei. However, in NMR we want to express this in terms of Quantum Mechanical operators, so the Zeeman energy Hamiltonian in a static field is represented by:

$$\hat{\mathcal{H}}_Z = -\boldsymbol{\mu} \cdot \mathbf{B}_0. \quad (2.3)$$

By convention when the angular momentum is aligned in the z-direction then, $\mathbf{I} = (0, 0, I_z)$, as is the external field, $\mathbf{B}_0 = (0, 0, B_0)$, and using Equation 2.2 the Hamiltonian can be written as:

$$\hat{\mathcal{H}}_Z = -\gamma \hat{I}_z B_0 \quad (2.4)$$

or

$$\hat{\mathcal{H}}_Z = \omega_0 \hat{I}_z. \quad (2.5)$$

Note that above the factor of \hbar has been omitted, with energies representing multiples of \hbar , in angular frequency units. ω_0 is the Larmor frequency given by:

$$\omega_0 = -\gamma B_0. \quad (2.6)$$

Therefore, the Larmor frequency is dependent upon the external magnetic field applied, and due to the gyromagnetic ratio being specific for each type of nucleus, it has a different strength depending on the nucleus in question.

A quantum mechanical description is necessary for the most accurate description of an NMR experiment. The state of a quantum mechanical system can be described by a quantum mechanical wavefunction $|\psi\rangle$ which represents the physical properties of the system. An operator can be defined that corresponds to an observable quantity, for example energy or angular momentum, that acts upon the wavefunction. Upon repeating an experiment many times the average value we obtain is represented by the expectation value:

$$\langle \hat{A} \rangle = \langle \psi | \hat{A} | \psi \rangle. \quad (2.7)$$

Application of the relevant angular momentum operator $\hat{I}_x, \hat{I}_y, \hat{I}_z, \hat{I}^2$, which represent the x, y, z components of the nuclear spin and magnitude of the nuclear spin squared respectively, can lead to observables relating to the nuclear spin. This set of operators obey the commutation relations:

$$[\hat{I}^2, \hat{I}_z] = 0 \quad (2.8)$$

$$[\hat{I}_x, \hat{I}_y] = i\hat{I}_z \quad (2.9)$$

and any cyclic permutation of the subscripts, and are linked by the relation:

$$\hat{I}^2 = \hat{I}_x^2 + \hat{I}_y^2 + \hat{I}_z^2. \quad (2.10)$$

These commutation relations show that as only one component of the spin angular momentum commutes with the total spin angular momentum, only one component is observable at a particular time, by convention \hat{I}_z . In addition the individual components don't commute with each other.

From Equation 2.5 it can be seen that the eigenfunctions of $\hat{\mathcal{H}}$ are the same as

\hat{I}_z written as $|I, m\rangle$, or:

$$\hat{I}_z |I, m\rangle = m |I, m\rangle. \quad (2.11)$$

For a spin $I = \frac{1}{2}$ nucleus, which is the simplest case relevant for NMR, $m = +\frac{1}{2}$ and $-\frac{1}{2}$, represented as $\alpha = \frac{1}{2}$ and $\beta = -\frac{1}{2}$, spin up and spin down, respectively. Therefore, the eigenvalues become:

$$\hat{I}_z |\alpha\rangle = +\frac{1}{2} |\alpha\rangle \quad \hat{I}_z |\beta\rangle = -\frac{1}{2} |\beta\rangle \quad (2.12)$$

and from Equation 2.5:

$$\hat{\mathcal{H}} |\alpha\rangle = +\frac{1}{2}\omega_0 |\alpha\rangle \quad \hat{\mathcal{H}} |\beta\rangle = -\frac{1}{2}\omega_0 |\beta\rangle. \quad (2.13)$$

Thus the difference between the Zeeman states is ω_0 , as stated in Equation 2.5. From Equation 2.12 we can use the eigenvalues to construct a matrix representation of the \hat{I}_z operator:

$$\hat{I}_z = \begin{pmatrix} \frac{1}{2} & 0 \\ 0 & -\frac{1}{2} \end{pmatrix}. \quad (2.14)$$

The complete wavefunction is a superposition of the α and β basis sets:

$$|\psi\rangle = c_\alpha |\alpha\rangle + c_\beta |\beta\rangle \quad (2.15)$$

where c_α and c_β represent the contribution of each state. The expectation value of the \hat{I}_z operator using Equation 2.7 is given by:

$$\langle \hat{I}_z \rangle = \frac{1}{2}(c_\alpha c_\alpha^* - c_\beta c_\beta^*), \quad (2.16)$$

showing that the longitudinal component is directly related to the probability of the system been found in either of these spin states.

In contrast, operators with x and y angular momentum don't have $|\alpha\rangle$ and $|\beta\rangle$ as eigenstates. Instead they inter convert $|\alpha\rangle$ and $|\beta\rangle$:

$$\begin{aligned}\hat{I}_x |\alpha\rangle &= \frac{1}{2} |\beta\rangle & \hat{I}_x |\beta\rangle &= \frac{1}{2} |\alpha\rangle \\ \hat{I}_y |\alpha\rangle &= \frac{1}{2} i |\beta\rangle & \hat{I}_y |\beta\rangle &= \frac{1}{2} i |\alpha\rangle.\end{aligned}\tag{2.17}$$

In matrix form these \hat{I}_x and \hat{I}_y operators are:

$$\hat{I}_x = \begin{pmatrix} 0 & \frac{1}{2} \\ \frac{1}{2} & 0 \end{pmatrix} \quad \hat{I}_y = \begin{pmatrix} 0 & -\frac{1}{2}i \\ \frac{1}{2}i & 0 \end{pmatrix}\tag{2.18}$$

with expectation values given by:

$$\langle \hat{I}_x \rangle = \frac{1}{2} (c_\alpha c_\beta^* + c_\beta c_\alpha^*)\tag{2.19}$$

$$\langle \hat{I}_y \rangle = \frac{1}{2} i (c_\alpha c_\beta^* - c_\beta c_\alpha^*)\tag{2.20}$$

2.2 Density Operator

The methods outlined in the previous section are adequate for describing simple systems, however for systems consisting of many spins, or for $I > \frac{1}{2}$, a linear treatment can become complicated involving many terms. The density operator method is a much more convenient approach utilising matrices. The density operator can be defined as:

$$\hat{\rho} = \overline{|\psi\rangle \langle \psi|}\tag{2.21}$$

where the overbar represents an ensemble average of the spin system. The density matrix is:

$$\rho_{rs} = \langle r | \hat{\rho} | s \rangle = c_r c_s^*.\tag{2.22}$$

For a single spin this density matrix becomes:

$$\rho = \begin{pmatrix} c_\alpha c_\alpha^* & c_\alpha c_\beta^* \\ c_\beta c_\alpha^* & c_\beta c_\beta^* \end{pmatrix}\tag{2.23}$$

therefore, we now have a matrix ρ , that relates to the sample, and one that relates the measurement of a particular operator, \hat{A} . A product of the two yields:

$$\rho\hat{A} = \begin{pmatrix} c_\alpha c_\alpha^* & c_\alpha c_\beta^* \\ c_\beta c_\alpha^* & c_\beta c_\beta^* \end{pmatrix} \begin{pmatrix} A_{\alpha\alpha} & A_{\alpha\beta} \\ A_{\beta\alpha} & A_{\beta\beta} \end{pmatrix} \quad (2.24)$$

$$= \begin{pmatrix} c_\alpha c_\alpha^* A_{\alpha\alpha} + c_\alpha c_\beta^* A_{\beta\alpha} & c_\alpha c_\alpha^* A_{\alpha\beta} + c_\alpha c_\beta^* A_{\beta\beta} \\ c_\beta c_\alpha^* A_{\alpha\alpha} + c_\beta c_\beta^* A_{\beta\alpha} & c_\beta c_\alpha^* A_{\alpha\beta} + c_\beta c_\beta^* A_{\beta\beta} \end{pmatrix} \quad (2.25)$$

and upon inspection of Equation 2.24 above it can be seen that the expectation value of this operator in terms of this density operator is:

$$\langle \hat{A} \rangle = Tr[\rho A]. \quad (2.26)$$

The above equation shows that independent of the number of spins within the system, any macroscopic observation of the system can be represented by the two operators representing the measured observable and the entire spin ensemble.

If we compare Equation 2.23 to the expressions for the expectation values of \hat{I}_z , Equation 2.16, it can be seen that \hat{I}_z is represented by like terms, therefore the diagonal elements of Equation 2.23 represent populations of basis functions. Whereas the expectation values for \hat{I}_x and \hat{I}_y , Equations 2.19 and 2.20, show that the off diagonal elements represent a mixture of states, known as coherences.

2.2.1 Evolution of the Density Operator

A NMR experiment consists of periods of free precession and rf pulses changing over time, which can be described by the time dependent Schrödinger equation:

$$\frac{d}{dt} |\psi\rangle = -i\hat{\mathcal{H}} |\psi\rangle. \quad (2.27)$$

We can use this to determine how the density operator changes over time:

$$\frac{d\rho}{dt} = -i[\hat{\mathcal{H}}, \rho] \quad (2.28)$$

this is known as the Liouville von-Neumann equation and has the solution:[100]

$$\begin{aligned}\hat{\rho}(t) &= e^{-i\hat{\mathcal{H}}t}\hat{\rho}(0)e^{+i\hat{\mathcal{H}}t} \\ &= \hat{U}(t)\hat{\rho}(0)\hat{U}(t)^{-1}.\end{aligned}\tag{2.29}$$

This is an important result as it states that if we know the density operator at a starting point ($t = 0$), and if we know the Hamiltonians, then we can calculate the density operator at any later time, t . Here $\hat{U}(t)$ is known as the propagator, which if $\hat{\mathcal{H}}$ is constant, can be expressed as:

$$\hat{U}(t) = e^{-i\hat{\mathcal{H}}t}.\tag{2.30}$$

If $\hat{\mathcal{H}}$ is not constant then the propagator can be separated into a series of Hamiltonians each acting consecutively for a time period, *e.g.*,

$$\hat{U}(t) = e^{-i\hat{\mathcal{H}}_1 t_1} e^{-i\hat{\mathcal{H}}_2 t_2} e^{-i\hat{\mathcal{H}}_3 t_3} \dots e^{-i\hat{\mathcal{H}}_n t_n}.\tag{2.31}$$

2.3 Hamiltonians and Interactions

The Hamiltonian that describes the NMR system can be represented by a linear combination of different interaction Hamiltonians that each play a part on the observed NMR signal:

$$\hat{\mathcal{H}}_{Total} = \hat{\mathcal{H}}_{rf} + \hat{\mathcal{H}}_Z + \hat{\mathcal{H}}_{cs} + \hat{\mathcal{H}}_J + \hat{\mathcal{H}}_D + \hat{\mathcal{H}}_Q + \dots\tag{2.32}$$

the above Hamiltonians can be classified into either external or internal Hamiltonians. The external interactions include: $\hat{\mathcal{H}}_Z$ which describes the Hamiltonian for the Zeeman interaction, as discussed in Section 2.1, and $\hat{\mathcal{H}}_{rf}$ the perturbing interaction of the oscillating rf magnetic field that creates spin coherences. The other interactions are known as the internal interactions, which reveal the chemical information due to the response from the external magnetic fields, these are discussed in later sections.

The Hamiltonian to describe an operator \tilde{A} in Cartesian coordinates can be expressed as:

$$\hat{\mathcal{H}}_A = \hat{I} \cdot \tilde{A} \cdot \hat{S} = \begin{pmatrix} \hat{I}_x & \hat{I}_y & \hat{I}_z \end{pmatrix} \begin{pmatrix} A_{xx} & A_{xy} & A_{xz} \\ A_{yx} & A_{yy} & A_{yz} \\ A_{zx} & A_{zy} & A_{zz} \end{pmatrix} \begin{pmatrix} \hat{S}_x \\ \hat{S}_y \\ \hat{S}_z \end{pmatrix} \quad (2.33)$$

where \hat{I} is the spin operator, \tilde{A} a second rank tensor describing the interaction, and \hat{S} either the external field or a further spin operator.

2.3.1 External Interactions

To observe an NMR signal we require transverse magnetisation, which is a so-called coherence state. This can be achieved by perturbing the spins from equilibrium by application of a magnetic field, that is much weaker than the external magnetic field ($B_1 \ll B_0$). The oscillation frequency of this B_1 field is comparable to the Larmor frequency of the nuclei under observation, *i.e.* $\omega_{rf} \approx \omega_0$, in order to ensure resonance is achieved,

$$\hat{B}_1 = 2B_1(\cos[\omega_{rf}t + \phi])\hat{\underline{i}} \quad (2.34)$$

$$= B_1(e^{+i\omega_{rf}t} + e^{-i\omega_{rf}t})\hat{\underline{i}}, \quad \text{if } \phi = 0 \quad (2.35)$$

where $\hat{\underline{i}}$ is the unit vector along the axis in question, and ϕ is the initial phase of the pulse. Therefore, the B_1 field is made up of two counter rotating fields, with frequencies $+\omega_{rf}$ and $-\omega_{rf}$, however we can safely neglect one of these, $-\omega_{rf}$ by convention, owing to only one being near the Larmor frequency. If we consider the Hamiltonian for an arbitrary rf field this can be simplified to:

$$\hat{\mathcal{H}}_{rf} = -\gamma B_1[\hat{I}_x \cos(\omega_{rf}t + \phi) + \hat{I}_y \sin(\omega_{rf}t + \phi)]. \quad (2.36)$$

To simplify Equation 2.36, we can transform to a rotating frame, rotating at ω_{rf} about the z axis, making this Hamiltonian time independent:

$$\hat{\mathcal{H}}_{rf}^{rot} = \omega_1[\hat{I}_x \cos\phi + \hat{I}_y \sin\phi] \quad (2.37)$$

here ω_1 is the strength of the rf field applied, the so called nutation frequency, defined by:

$$\omega_1 = -\gamma B_1. \quad (2.38)$$

Equation 2.37 shows that the initial phase, ϕ , defines the orientation of the pulse applied in the xy plane, for instance if we apply $\phi = 0$:

$$\hat{\mathcal{H}}_{rf}^{rot} = \omega_1 \hat{I}_x, \quad (2.39)$$

therefore the pulse appears as a static magnetic field applied along the x -axis. Using the solution to the Liouville-von Neumann Equation we can observe what happens under this pulse:

$$\hat{\rho}(t) = e^{-i\omega_1 t \hat{I}_x} \hat{\rho}(0) e^{+i\omega_1 t \hat{I}_x}. \quad (2.40)$$

At equilibrium the spins are in the \hat{I}_z state, therefore:

$$\hat{\rho}(0) = \hat{I}_z \quad (2.41)$$

$\hat{\rho}(t)$ can then be expressed as: [100]

$$\rho(t) = \begin{pmatrix} \frac{1}{2} \cos \omega_1 t & \frac{i}{2} \sin \omega_1 t \\ -\frac{i}{2} \sin \omega_1 t & -\frac{1}{2} \cos \omega_1 t \end{pmatrix} \quad (2.42)$$

where, in addition to populations, the rf pulse has created coherences, the off diagonal elements. The expectation values of the \hat{I}_z , \hat{I}_x and \hat{I}_y operators can then be determined using Equation 2.26:

$$\langle \hat{I}_x \rangle = Tr[\rho \hat{I}_x] = 0 \quad (2.43)$$

$$\langle \hat{I}_y \rangle = Tr[\rho \hat{I}_y] = -\frac{1}{2} \sin \omega_1 t \quad (2.44)$$

$$\langle \hat{I}_z \rangle = Tr[\rho \hat{I}_z] = \frac{1}{2} \cos \omega_1 t \quad (2.45)$$

This shows that upon application of a pulse along the x -axis, the expectation values of \hat{I}_z and \hat{I}_y oscillate at the nutation frequency. Population inversion is achieved when

$\omega_1 t = \pi$, whereas to create a pure coherence state $\omega_1 t = \frac{\pi}{2}$. Here $\omega_1 t$ is commonly known as the flip angle in NMR, this will be covered in more detail in the Section 3.4.1.

Similarly to the $\hat{\mathcal{H}}_{rf}$ Hamiltonian, the Zeeman Hamiltonian can also be expressed in the rotating frame. Recall Equation 2.5, which if we transfer to the rotating frame becomes:

$$\hat{\mathcal{H}}_z^{rot} = (\omega_0 - \omega_{rf})\hat{I}_z = \Omega\hat{I}_z \quad (2.46)$$

where Ω is known as the resonance offset. This results in more manageable values of the frequency observed, as it corresponds to mixing down the signal with a reference frequency, therefore detecting kHz frequencies rather than the MHz of the Larmor frequency.

A similar approach as shown previously for the application of the rf x -pulse, can now be applied to use the Liouville von-Neumann equation to observe the state of the transverse magnetisation under a resonance offset:

$$\hat{\rho}(t) = e^{-i\Omega t\hat{I}_z}\hat{\rho}(0)e^{+i\Omega t\hat{I}_z}. \quad (2.47)$$

In this case

$$\rho(0) = \hat{I}_x \quad (2.48)$$

therefore the density operator at time t is expressed as:

$$\hat{\rho}(t) = \begin{pmatrix} 0 & \frac{1}{2}e^{-i\Omega t} \\ \frac{1}{2}e^{i\Omega t} & 0 \end{pmatrix}. \quad (2.49)$$

Measurement of this transverse signal can be detected by acting on this density operator

with the complex conjugate of the lowering operator $(\hat{I}_-)^* = \hat{I}_+$:

$$s(t) = \text{Tr}[\hat{\rho}(t)\hat{I}_+] \quad (2.50)$$

$$= \text{Tr} \left[\begin{pmatrix} 0 & \frac{1}{2}e^{-i\Omega t} \\ \frac{1}{2}e^{i\Omega t} & 0 \end{pmatrix} \begin{pmatrix} 0 & 1 \\ 0 & 0 \end{pmatrix} \right] \quad (2.51)$$

$$= \text{Tr} \begin{pmatrix} 0 & 0 \\ 0 & \frac{1}{2}e^{i\Omega t} \end{pmatrix} \quad (2.52)$$

$$= \frac{1}{2}e^{i\Omega t} \quad (2.53)$$

$$= \frac{1}{2}(\cos(\Omega t) + i\sin(\Omega t)). \quad (2.54)$$

This allows the detection of the signal, consisting of two signals $\frac{\pi}{2}$ out of phase, thus giving a sense of precession of the signal, as the oscillating magnetic fields induces a current in the NMR coil, as will be discussed in Section 3. The above equations show that the single quantum coherences that are generated by the rf pulse during the NMR experiment, result in the NMR signal obtained. Although higher order coherences are possible for coupled systems, we cannot directly observe them in an NMR experiment, however some techniques exploit these higher coherence orders, as will be discussed later.

2.4 Internal Interactions

2.4.1 Frame Rotations and Tensors

In addition to the external interactions that we can control in the NMR experiment, such as the magnetic fields, internal interactions from the local environment of the nuclear spins also play a part in the behaviour of the spin system. The fact that the external interactions are usually much larger than the effects of the internal interactions arising from the local molecular environment of the spins themselves, is what makes NMR an interesting technique. In the NMR experiment we actually have the spin system coupled to the external system. Upon making small changes to the external system, via application of an rf pulse, we can obtain information on the molecular environment, due to the perturbations observed via these internal interactions. The

total Hamiltonian can be expressed as:

$$\hat{\mathcal{H}}_T = \hat{\mathcal{H}}_0 + \hat{\mathcal{H}}_1 \quad (2.55)$$

where $\hat{\mathcal{H}}_0$ is the Zeeman Hamiltonian and $\hat{\mathcal{H}}_1$ is a first order perturbation to the Zeeman Hamiltonian, composed of the rf pulse and the internal interactions. A first order perturbation approach is sufficient to describe most interactions, as usually they are much smaller than the effect of the dominant Zeeman interaction. However, for the case of large quadrupole interactions a second order treatment may be required, as will be discussed later.

The internal interactions in NMR can be described by second rank tensors owing to their 3D orientation dependence. The most convenient way to represent these tensors is in the Principal Axis System (PAS) of the interaction, where the tensor is diagonalised, with only diagonal elements of the tensor being non zero. However the PAS frame for each interaction will be different, and as the dominant interaction in the NMR experiment is usually the Zeeman interaction, it is necessary to rotate the tensors describing the internal interactions from their PAS frame into the lab frame where the NMR measurement is taken.

To carry out these rotations it is easier to express the internal interaction Hamiltonians in spherical tensor form, by converting from the usual Cartesian representation:

$$\hat{\mathcal{H}} = \sum_{j=0}^2 \sum_{m=-j}^{+j} (-1)^m A_{j,m} \hat{T}_{j,-m}, \quad (2.56)$$

where A_{jm} is the spatial component of the tensor representing the magnitude of the interactions, and \hat{T}_{j-m} the spin component representing the quantum mechanical operators. It is important to note that under rotations only the spatial term is affected.

In the PAS frame, as only the diagonal terms are non zero, not all terms in Equation 2.56 will be retained. Equation 2.56 becomes:

$$\hat{\mathcal{H}}^P = A_{00}^P \hat{T}_{00} + A_{20}^P \hat{T}_{20} + A_{22}^P \hat{T}_{2-2} + A_{2-2}^P \hat{T}_{22}. \quad (2.57)$$

When rotating between different frames of reference Euler angles are used, corresponding to three angles α, β and γ , as given by the rotation operator:

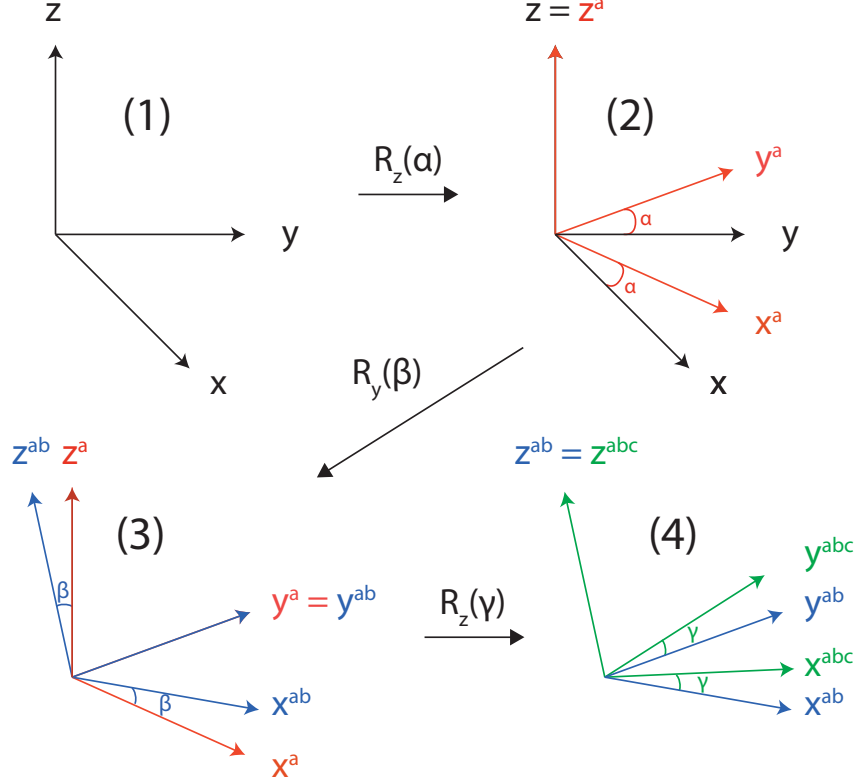


Figure 2.2: The convention upon using Euler angles to rotate between frames of reference. From frame (1) a rotation by α about the z -axis, results in the frame (2). Secondly a rotation about the new y -axis through β gives frame (3). Then a final rotation through γ about the final z -axis, results in frame (4). The convention used is that of passive rotations.

$$\hat{R}(\alpha, \beta, \gamma) = \hat{R}_z(\alpha) \hat{R}_y(\beta) \hat{R}_z(\gamma) \quad (2.58)$$

Figure 2.2 shows how these rotations are applied. Initially a rotation by α about the z -axis, followed by a rotation about the new y -axis through β , then a final rotation through γ about the final z -axis. It is important to note that different conventions of these rotations exist, but the convention used in this thesis, is that of passive rotations.[98]

An operator \hat{R} acting on a spherical tensor can be described by:

$$\hat{R}(A_{jm}) = \sum_{m'=-j}^{m'=+j} D_{m'm}^j(\alpha, \beta, \gamma) A'_{jm'} \quad (2.59)$$

where $D_{m'm}^j(\alpha, \beta, \gamma)$ is a rotation matrix, the Wigner D-matrix. Therefore, upon rotation the spherical tensor is converted into a sum of spherical tensors with the same

rank j , but different order m . The Wigner D-matrix is defined in terms of the Euler angles as [103, 104]:

$$D_{m'm}^j(\alpha\beta\gamma) = e^{-im'\alpha} d_{m'm}^j(\beta) e^{-im\gamma} \quad (2.60)$$

where $d_{m'm}^j$ are the reduced Wigner matrices which can be found in reference tables, see Appendix A.1 [100].

Thus, for the specific case of the NMR experiment, in transforming frames from the PAS to the lab frame (L), we have:

$$A_{jm'}^L = \sum_m A_{jm}^P D_{mm'}^j(\alpha_{PL}, \beta_{PL}, \gamma_{PL}) \quad (2.61)$$

so with any spherical tensor in the PAS frame of a particular interaction we can now transform to the more general lab frame.

It is important to note that due to the interactions being considered as first order perturbations, only spin terms that commute with the Zeeman interaction, \hat{I}_z , are retained:

$$[\hat{I}_z, \hat{T}_{jm}] = m\hat{T}_{jm}. \quad (2.62)$$

The above equation only commutes when $m = 0$, meaning that in the lab frame only A_{j0}^L terms are retained. This is known as the secular approximation, and only holds when first order perturbations to the Zeeman interaction are considered. Therefore:

$$\hat{\mathcal{H}}^L = A_{00}^L \hat{T}_{00} + A_{20}^L \hat{T}_{20} \quad (2.63)$$

where A_{00}^L corresponds to the isotropic component of the particular interaction, and A_{20}^L the anisotropic component.

2.4.2 Magic Angle Spinning (MAS)

In solution state NMR rapid molecular tumbling results in all different orientations of the molecule being experienced over a short time scale, thus averaging away the anisotropic components of the internal interactions. This leads to very narrow lines corresponding to only the isotropic part of the interactions. However, in solid state

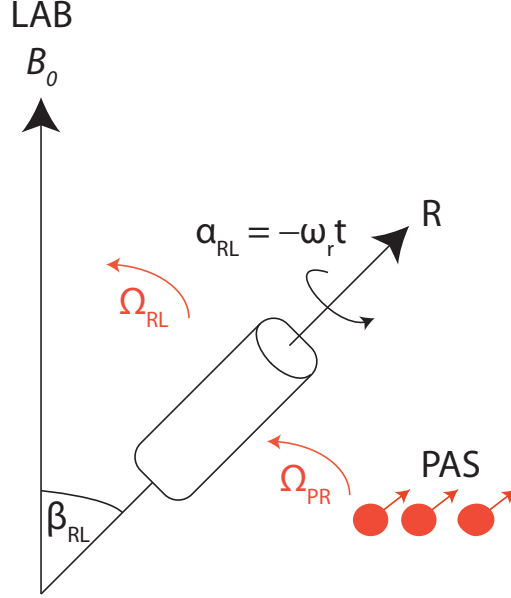


Figure 2.3: Diagram showing the orientation of the MAS rotor with respect to the external B_0 field. Euler angles are shown for the transformations between the PAS to the rotor frame, and then a further rotation to the lab frame.

NMR due to the rigidity of solids, this molecular tumbling does not occur, thus resulting in the anisotropic component still being present. This will lead to broadening of the lineshapes observed, especially in the case of powdered solids where a range of orientations will be present, resulting in the overlap of many different anisotropic resonances. Therefore, in solid state NMR a commonly employed technique is that of Magic Angle Spinning (MAS), whereby the sample is orientated at a fixed angle to the external magnetic field and rotated about this axis, with the aim of removing this anisotropic component of the interactions.

A further transformation is now required from the PAS frame to the so called rotor frame, the rotor being the small container the sample is put into and subsequently rotated in, and finally a further transformation to the lab frame where the NMR measurement is taken. There are now two sets of Euler angles we need to consider:

$$\Omega_{RL} = (\alpha_{RL}, \beta_{RL}, \gamma_{RL}) \quad (2.64)$$

$$\Omega_{PR} = (\alpha_{PR}, \beta_{PR}, \gamma_{PR}). \quad (2.65)$$

Figure 2.3 shows the transformations that are required and the corresponding Euler angles applicable for the rotation from the rotor to the lab frame. Of the three angles

of Ω_{RL} , the user has control of γ_{RL} , enabling it to be set to zero. β_{RL} is the angle of the rotor with respect to the magnetic field, and α_{RL} the rotor position, that is time dependent, t , and also depends upon the frequency of rotation, ω_r .

For the two rotations, Equation 2.61 can be written as:

$$A_{20}^L = A_{20}^P \sum_{m=-2}^2 D_{m0}^2(\Omega_{RL}) D_{0m}^2(\Omega_{PR}) \quad (2.66)$$

only the A_{20}^L term is important as previously mentioned, Equation 2.63. The Wigner D-matrix for the transformation from the rotor to the lab frame is given by:

$$D_{m0}^2(\Omega_{RL}) = e^{im\omega_r t} d_{0m}^2(\beta_{RL}). \quad (2.67)$$

Upon rotating the sample using Magic Angle Spinning, if we average over one complete rotor period, $t_r = \frac{2\pi}{\omega_r}$ then:

$$\int_0^{\frac{2\pi}{\omega_r}} e^{im\omega_r t} dt = 0 \quad \text{if } m \neq 0 \quad (2.68)$$

$$= 1 \quad \text{if } m = 0 \quad (2.69)$$

so when $m = 0$, the time dependent component equates to unity after one rotation period. For all other values of m the time dependent part becomes zero after one rotor period. Equation 2.66 becomes:

$$\langle A_{20}^L \rangle_{t_r} = A_{20}^P D_{00}^2(\Omega_{PR}) d_{00}^2(\beta_{RL}), \quad (2.70)$$

where the reduced Wigner Matrix has the form:

$$d_{00}^2(\beta_{RL}) = \frac{1}{2}(3\cos^2\beta_{RL} - 1), \quad (2.71)$$

known as the $P_2(\cos\theta)$ Legendre polynomial. It can be seen that upon setting β_{RL} to an angle of 54.74° this $(3\cos^2\beta_{RL} - 1)$ term goes to zero upon averaging over one rotor period. This angle is aptly known as the Magic Angle, and Equation 2.66 subsequently becomes zero with the anisotropy removed. MAS will average second rank tensors to zero after one rotor period, and with most of the significant interactions in solid state

NMR being described by second rank tensors, this makes MAS a powerful tool.

However, if the spectra are not acquired at an integer of a complete rotor period, as is often the case, ($m \neq 0$), the other terms of Equation 2.66 must be considered. Thus calculating the remaining Wigner rotation matrices under MAS the spatial term becomes:

$$A_{20}^L = A_{20}^P \left[\frac{1}{2} \sin^2 \beta_{PR} \cos(2\gamma_{PR} - 2\omega_r t) - \frac{1}{\sqrt{2}} \sin 2\beta_{PR} \cos(\gamma_{PR} - \omega_r t) \right] \quad (2.72)$$

these terms oscillating at ω_r and $2\omega_r$ are what give rise to what is known as ‘spinning sidebands’. Upon rotation of the sample at the magic angle the powder lineshape splits up into a series of resonances separated in Hz, by the MAS frequency ω_r . As ω_r is increased the intensity of these spinning sidebands decrease, ultimately disappearing when the spinning frequency is much greater than the size of the anisotropy. This leads to one resonance observed at the isotropic chemical shift.

2.4.3 Chemical Shielding

Arguably the most important internal interaction in NMR is that of chemical shielding, as it gives direct evidence on the local chemical environment. In the presence of a strong magnetic field, in the case of the NMR experiment that of B_0 , the magnetic field experienced by the nuclear site can differ from the applied field. This is because of the fact that currents in the electron orbitals surrounding the nucleus induce a different magnetic field experienced at the nuclear site, *i.e.* so called shielding or de-shielding the nucleus. Due to the 3D nature of this electron density, the chemical shielding is described by a second rank tensor, $\tilde{\sigma}$. The Hamiltonian describing the chemical shielding for a spin I is given by:

$$\hat{\mathcal{H}}_{cs} = \gamma \hat{I} \cdot \tilde{\sigma} \cdot B_0. \quad (2.73)$$

As previously stated all interactions can be defined within their principal axis system (PAS), which for the shielding tensor is:

$$\sigma^P = \begin{pmatrix} \sigma_{XX} & 0 & 0 \\ 0 & \sigma_{YY} & 0 \\ 0 & 0 & \sigma_{ZZ} \end{pmatrix} \quad (2.74)$$

where capital subscripts denote the PAS frame. Upon rotation from the PAS frame of the shielding interaction into the lab frame the tensor becomes:

$$\sigma^L = \begin{pmatrix} \sigma_{xx} & \sigma_{xy} & \sigma_{xz} \\ \sigma_{yx} & \sigma_{yy} & \sigma_{yz} \\ \sigma_{zx} & \sigma_{zy} & \sigma_{zz} \end{pmatrix}. \quad (2.75)$$

This can then be combined with the expression for the external magnetic field. The field at the nucleus including both contribution from the shielding and the external field is then:

$$\hat{B} = (1 - \sigma).B_0 = \begin{pmatrix} 1 - \sigma_{xx} & -\sigma_{xy} & -\sigma_{xz} \\ -\sigma_{yx} & 1 - \sigma_{yy} & -\sigma_{yz} \\ -\sigma_{zx} & -\sigma_{zy} & 1 - \sigma_{zz} \end{pmatrix} \begin{pmatrix} 0 \\ 0 \\ B_0 \end{pmatrix} = \begin{pmatrix} -\sigma_{xz}B_0 \\ -\sigma_{yz}B_0 \\ (1 - \sigma_{zz})B_0 \end{pmatrix}. \quad (2.76)$$

In the above both contributions due to $-\sigma_{xz}$ and $-\sigma_{yz}$ can be neglected as they represent second order contributions. This then gives the total Hamiltonian for the chemical shielding interaction as:

$$\hat{\mathcal{H}}_{cs} = \gamma \hat{I}_z \cdot \sigma_{zz} \cdot B_0. \quad (2.77)$$

An expression for σ_{zz} is then required to accurately describe this Hamiltonian:[101]

$$\sigma_{zz}(\theta, \phi) = \sigma_{iso} + \frac{1}{2}\Delta[(3\cos^2\theta - 1) - \eta(\sin^2\theta\cos 2\phi)] \quad (2.78)$$

where the angles θ and ϕ represent polar angles that arise from the rotation from the PAS to the lab frame. The three terms σ_{iso} , Δ , and η characterise the local symmetry around the nucleus and are expressed as

$$\sigma_{iso} = \frac{1}{3}(\sigma_{XX}^P + \sigma_{YY}^P + \sigma_{ZZ}^P) \quad (2.79)$$

$$\Delta = \sigma_{ZZ}^P - \sigma_{iso} \quad (2.80)$$

$$\eta = \frac{\sigma_{YY}^P - \sigma_{XX}^P}{\Delta} \quad (2.81)$$

σ_{iso} is the isotropic value, corresponding to the average of the diagonal elements, as the name suggests being isotropic means it is invariant under rotations. Δ and η are the anisotropy and the asymmetry, respectively, and give information on the local symmetry around the nuclear site. It is common practice for these three terms to be quoted as a measure of the shielding interaction, rather than the three principal components.

In solid state NMR the sample under observation is usually in powder form, thus all possible orientations of crystallites, hence θ and ϕ , are represented resulting in different chemical shielding values. A powder pattern subsequently forms, spanning a range of frequencies. The distinctive lineshape of this pattern depends heavily upon the symmetry of the tensor, as shown in Figure 2.4.

As shown in Section 2.4.2 MAS can be used to remove anisotropic broadening due to first order interactions, after two successive frame rotations. This is commonly applied to remove the effect of CSA in the solid state, thus leaving a resonance with the only chemical shielding effect being from the isotropic value. The isotropic shielding is normalised with respect to a reference Larmor frequency for the observed nucleus by:

$$\delta_{iso} = \frac{\nu_{sample} - \nu_{ref}}{\nu_{ref}} \times 10^6 = \frac{\sigma_{ref} - \sigma_{sample}}{1 - \sigma_{ref}} \quad (2.82)$$

to obtain the isotropic chemical shift δ_{iso} , which is quoted in parts per million (ppm), and is usually what experimentalists measure. Due to the normalisation with respect to a known reference frequency, chemical shifts are independent of B_0 , thus enabling a method of comparison for spectroscopists at a wide range of field strengths.

2.4.4 Dipolar Interaction

Nuclear spins have an associated magnetic moment, as represented in Equation 2.2, which, when in close proximity with one another, will interact through space. This interaction, known as the dipolar coupling, is important in NMR. If we consider the

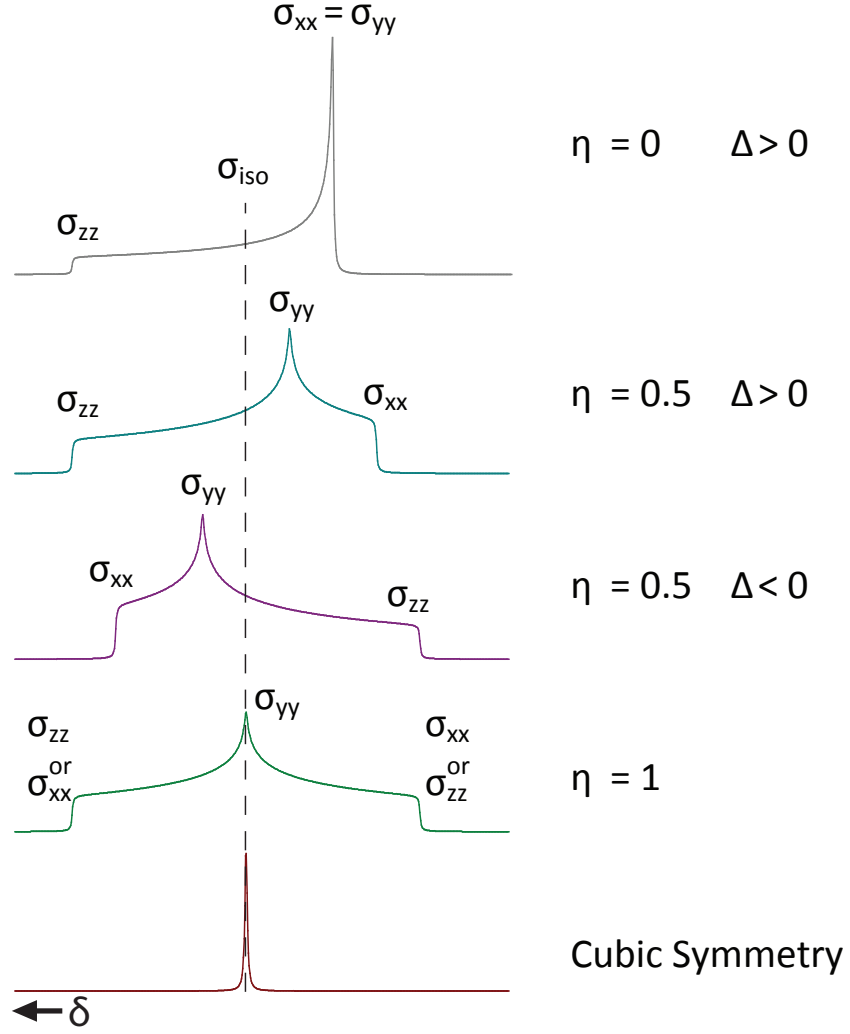


Figure 2.4: Chemical shift anisotropy (CSA) powder patterns, made up of randomly orientated crystallites. Lineshapes observed due to different values of η and Δ . Bottom spectrum for the case of cubic symmetry is what is observed under MAS whereby the anisotropy is removed, using rotor-synchronised acquisition.

classical energy of the interaction between two magnetic dipoles we obtain:

$$\mathcal{H}_D = -\frac{\mu_0}{4\pi} \frac{\hbar\gamma_I\gamma_S}{r^3} (\hat{I} \cdot \hat{S} - \frac{3(\hat{I} \cdot \hat{r})(\hat{S} \cdot \hat{r})}{r^2}) \quad (2.83)$$

where \hat{I} and \hat{S} represent the two coupled spins, and r the distance between them. We can define a dipolar coupling constant as:

$$d_{IS} = -\frac{\mu_0}{4\pi} \frac{\hbar\gamma_I\gamma_S}{r^3}, \quad (2.84)$$

the strength of the interaction therefore depends on the inverse cubed separation of the nuclei and the product of the gyromagnetic ratios (γ). Therefore, the interaction can

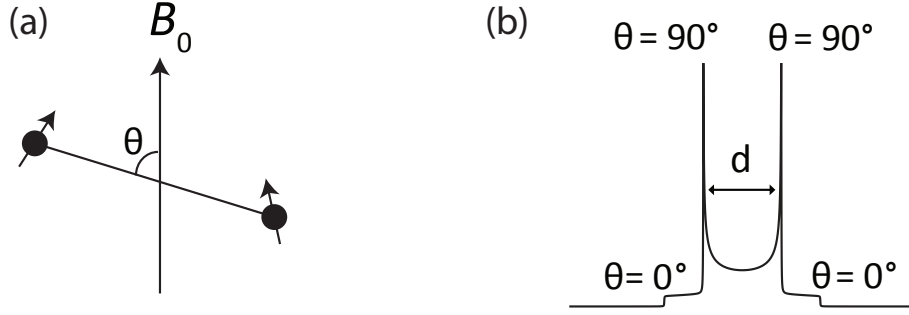


Figure 2.5: (a) Diagram showing the orientation of the internuclear vector (θ), between two dipolar coupled spins. (b) Powdered static lineshape for dipolar coupled heteronuclear spin pair showing the “Pake Doublet”. The “horns” represent $\theta = 90^\circ$, where the internuclear vector is perpendicular to B_0 . The humps at the end of the tail represent $\theta = 0^\circ$, where the internuclear vector is parallel to B_0 .

be a good measure of internuclear distances. The Hamiltonian represented in Cartesian tensors is given by:

$$\hat{\mathcal{H}}_D = -2\hat{I} \cdot \tilde{D} \cdot \hat{S} \quad (2.85)$$

in angular frequency units. Here \hat{D} is the dipolar coupling tensor which describes how the magnetic field at one spin is affected by the other spin, upon variation of the I-S internuclear vector in the applied field, see Figure 2.5. However, it is more useful to represent the dipolar coupling Hamiltonian in spherical tensor form. In its principal axis system it is given by:

$$\hat{\mathcal{H}}_D^P = A_{20}^P \hat{T}_{20} \quad (2.86)$$

only the A_{20}^P remains due to the fact that the dipolar interaction is traceless $A_{xx} + A_{yy} + A_{zz} = 0$, and axially symmetric $A_{xx} = A_{yy}$. This has the consequence that the dipolar interaction contains no isotropic terms, only having anisotropic contributions. In solution molecular tumbling averages away this anisotropic interaction resulting in no dipolar broadening, although relaxation effects are still experienced. Due to the lack of motion in the solid state the anisotropic term remains, with the spatial term given by:

$$A_{20}^P = \sqrt{6}d_{IS}. \quad (2.87)$$

As shown previously, a transformation is then required of the spatial term in the PAS frame of the interaction, into the lab frame where the NMR measurement is observed:

$$A_{20}^L = A_{20}^P D_{00}^2 = \sqrt{6} d_{IS} \frac{1}{2} (3 \cos^2 \theta - 1) \quad (2.88)$$

where the angle θ is the angle between the internuclear vector and B_0 . The spin spherical tensor term is given by:

$$\hat{T}_{20} = \frac{1}{\sqrt{6}} (3 \hat{I}_z \hat{S}_z - \hat{\mathbf{I}} \cdot \hat{\mathbf{S}}). \quad (2.89)$$

Therefore combining Equation 2.88 and 2.89 the dipolar Hamiltonian becomes:

$$\hat{\mathcal{H}}_D = d_{IS} \frac{1}{2} (3 \cos^2 \theta - 1) (3 \hat{I}_z \hat{S}_z - \hat{\mathbf{I}} \cdot \hat{\mathbf{S}}). \quad (2.90)$$

The term $\hat{\mathbf{I}} \cdot \hat{\mathbf{S}}$ can be written as $\hat{I}_x \hat{S}_x + \hat{I}_y \hat{S}_y + \hat{I}_z \hat{S}_z$, leading Equation 2.90 to be written as:

$$\hat{\mathcal{H}}_D = d_{IS} \frac{1}{2} (3 \cos^2 \theta - 1) (2 \hat{I}_z \hat{S}_z - (\hat{I}_x \hat{S}_x + \hat{I}_y \hat{S}_y)). \quad (2.91)$$

For the case of two coupled spin $\frac{1}{2}$ nuclei the spin angular momentum operators can be expressed as:

$$2 \hat{I}_z \hat{S}_z = \begin{pmatrix} \frac{1}{2} & 0 & 0 & 0 \\ 0 & -\frac{1}{2} & 0 & 0 \\ 0 & 0 & -\frac{1}{2} & 0 \\ 0 & 0 & 0 & \frac{1}{2} \end{pmatrix}, \quad (\hat{I}_x \hat{S}_x + \hat{I}_y \hat{S}_y) = \begin{pmatrix} 0 & 0 & 0 & 0 \\ 0 & 0 & \frac{1}{2} & 0 \\ 0 & \frac{1}{2} & 0 & 0 \\ 0 & 0 & 0 & 0 \end{pmatrix} \quad (2.92)$$

substituting these operators into Equation 2.90:

$$\hat{\mathcal{H}}_D = d_{IS} \frac{1}{2} (3 \cos^2 \theta - 1) \begin{pmatrix} \frac{1}{2} & 0 & 0 & 0 \\ 0 & -\frac{1}{2} & -\frac{1}{2} & 0 \\ 0 & -\frac{1}{2} & -\frac{1}{2} & 0 \\ 0 & 0 & 0 & \frac{1}{2} \end{pmatrix}. \quad (2.93)$$

The nuclear spins involved in the dipolar interaction can be of one of two cases, either of the same nuclear species, so called homonuclear dipolar coupling, or of a completely

different nuclear species, heteronuclear dipolar coupling. For the heteronuclear case the off diagonal terms in the matrix in Equation 2.93 are zero, and hence the $\hat{I}_x\hat{S}_x + \hat{I}_y\hat{S}_y$ terms. Therefore, the spin states are only the Zeeman energy states and the result is a first order energy shift to the Zeeman interaction. Whereas for the homonuclear spin case the off diagonal terms are now relevant, representing a mixing of spin states. This causes an additional complication, as the eigenstates now consist of a linear combination of the $\alpha\beta$ and $\beta\alpha$ degenerate Zeeman levels. For a many spin system this leads to a range of transition frequencies, thus resulting in an overall Gaussian broadening to the lineshape observed.[98]

For the heteronuclear coupling due to the lack of mixing of the energy levels, there are two possible transitions for each spin, each containing a $(3\cos^2\theta - 1)$ dependence, thus giving rise to a typical powder pattern, the so called Pake Doublet.[12] The doublet nature comes from the fact that one transition has the opposite sign to the other, resulting in two lines, mirror images of each other, superimposed on one another. This is shown in Figure 2.5, where the “horns” of the lineshape represent $\theta = 90^\circ$ and the outer limits $\theta = 0^\circ$, with the distance between the splitting of the two “horns” and the total width being related to the dipolar coupling constant.[12]

In practice the spin system is likely to consist of a combination of both of these interactions at once, due to many different spins coupled together at once resulting in an overall broadening of the lineshape observed. In Section 2.4.2 it was shown how the spatial part of an interaction Hamiltonian is averaged to zero when rotated, orientated at the magic angle. This is true for the heteronuclear dipolar interaction, enabling lineshapes free from the broadening to be obtained. However, the homonuclear dipolar coupling requires very fast MAS frequencies in order to remove the line broadening associated with it, due to the mixing of the Zeeman energy states. The homonuclear interaction however, will not play a big part in the NMR results observed in this thesis.

2.4.5 J Coupling

In addition to the through space dipolar a further coupling can arise in the form of the indirect through bond coupling, also known as the J coupling. The J interaction arises when the spin of one nucleus polarises a nearby electron spin, the spin polarisation is then transferred to other bonded electrons, which ultimately transfer the polarisation

to a second nucleus. The Hamiltonian of the J coupling is:

$$\hat{\mathcal{H}}_J = \hat{I} \cdot \tilde{J} \cdot \hat{S} \quad (2.94)$$

where \tilde{J} is the J coupling tensor, which is represented in Hz owing to the fact that the interaction is independent of the external field B_0 . The J coupling unlike the dipolar interaction is not traceless, therefore in solution NMR the interaction is not removed via molecular tumbling. Anisotropic terms of the J coupling do exist in the solid state, although their small size usually means that they are neglected. The interaction is almost always described by the isotropic term represented by:[105]

$$J = \frac{1}{3}(J_{xx} + J_{yy} + J_{zz}). \quad (2.95)$$

The interaction leads to splitting of resonances in the NMR spectrum, separated by J , with the splitting therefore remaining invariant between B_0 fields. In the solid state due to the fact that it is usually the smallest interaction, splitting due to the J coupling is rarely seen in most spectra, with large linewidths masking the small J splitting. Notable exceptions to this do occur however, with splittings observed in some crystalline samples when sufficient decoupling and MAS is utilised.

The splitting arising from the J coupling depends upon the nuclear spin I of the nuclei involved, and due to the through bond nature of the interaction it is most significant in covalent materials. If two nuclei, \hat{I} and \hat{S} , are coupled together, both with spin I , then the spectra of \hat{I} will be split into $2I + 1$ lines, with the splitting equal to J . The splitting can be visualised if we consider an isolated spin $I = \frac{1}{2}$, in the presence of a magnetic field, Zeeman splitting leads to two spin states α and β , with a transition between them resulting in the observation of one NMR resonance. However, for the case of two coupled spin $I = \frac{1}{2}$ nuclei, there are now four possible energy levels, $\alpha\alpha$, $\alpha\beta$, $\beta\alpha$, $\beta\beta$, therefore four allowed transitions are possible, hence two doublets, one for each spin. This is shown in more detail in Figure 2.6.

Even though the interaction is often masked in the solid state, particularly in disordered type materials, where a wide range of different sites are present, numerous experimental methods have been developed to exploit the J coupling. Pulse sequences such as the spin echo, the INADEQUATE and the J -HMQC all rely on the J coupling

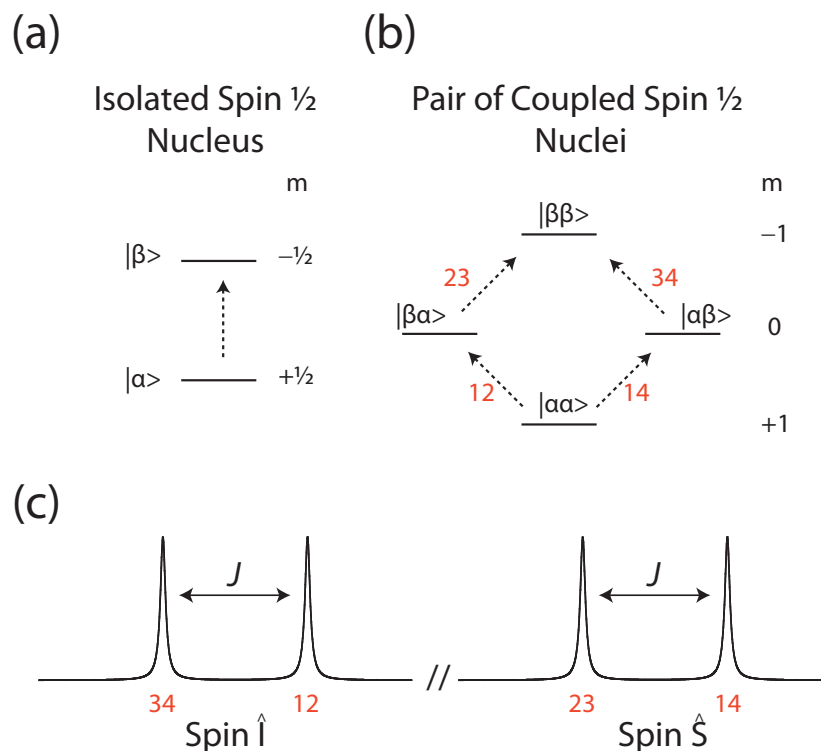


Figure 2.6: (a) Energy level diagram for an isolated spin $I = \frac{1}{2}$ nucleus in the presence of a magnetic field, showing the α and β energy levels and the allowed transition. (b) Energy level diagram for a pair of coupled spin $I = \frac{1}{2}$ nuclei in the presence of a magnetic field, showing the four possible energy levels. Allowed transitions are indicated. (c) The observed spectra for a pair of coupled spin $I = \frac{1}{2}$ nuclei in the presence of a magnetic field showing the two doublets obtained, the transitions are indicated in red corresponding to the energy level change as in (b). The splitting of the doublets is equal to the J coupling.

between nuclei, enabling information on couplings to be extracted that aren't resolvable from conventional single pulse NMR. This is covered in more detail in Section 3.

2.4.6 Quadrupole Interaction

Over 70 % of the NMR active elements in the periodic table have spin $I > \frac{1}{2}$, an important point as they can be subject to a further coupling; the quadrupole interaction. These nuclei, with $I > \frac{1}{2}$, have a non-spherical charge distribution, giving rise to a quadrupole moment. The interaction of the quadrupole moment of a nucleus with the electric field gradient (EFG) that is present across the nucleus, is the origin of this quadrupole effect. The quadrupole interaction is generally the largest and most dominant interaction of each of the internal interactions present in solid state NMR, sometimes on the order of several MHz in strength. This has important effects as it

can be much bigger than the rf nutation frequency, thus resulting in distortions of line-shapes, and can also mean in some cases the secular (high field) approximation is no longer valid.

From Slichter the energy of a charge distribution, in an electrostatic potential can be given by: [101, 106]

$$E = \int \rho(\mathbf{r}) \cdot V(\mathbf{r}) d\tau \quad (2.96)$$

where ρ is the charge density. By expanding as a Taylor series the potential in the volume surrounding the nucleus can be given as:

$$V(\mathbf{r}) = V(0) + \sum_i x_i \left. \frac{\partial V}{\partial x_i} \right|_{r=0} + \frac{1}{2!} \sum_{i,j} x_i x_j \left. \frac{\partial^2 V}{\partial^2 x_i \partial^2 x_j} \right|_{r=0} + \dots \quad (2.97)$$

where i and j represent x , y or z . The partial derivatives can be expressed as:

$$V_i = \frac{\partial V}{\partial x_i} \quad \text{and} \quad V_{ij} = \frac{\partial^2 V}{\partial^2 x_i \partial^2 x_j} \quad (2.98)$$

substituting this expression for the potential in Equation 2.97 and Equation 2.98 into Equation 2.96 we obtain:

$$E = V(0) \int \rho(\mathbf{r}) d\tau + \sum_i V_i \int x_i \rho(\mathbf{r}) d\tau + \frac{1}{2!} \sum_{i,j} V_{ij} \int x_i x_j \rho(\mathbf{r}) d\tau + \dots \quad (2.99)$$

where the energy now consists of a series of terms. The first term corresponds to the electrostatic energy which is the same in all orientations as it is a point charge. The second term, the electric dipole moment equals zero for the nuclear charge distribution, otherwise a net resultant force would act to remove this electric dipole. The third term represents the electric quadrupole moment, the origin of the quadrupole interaction. This term gives an orientational dependence of the interaction, due to the variation of charge distribution, from changes in symmetry of the site.

The electric field gradient V_{ij} is described by a second rank tensor which, like the dipolar interaction, is traceless in its PAS, $V_{xx} + V_{yy} + V_{zz} = 0$. By convention the principal values follow the condition $|V_{zz}| \geq |V_{yy}| \geq |V_{xx}|$, where the largest component V_{zz} is given by:

$$V_{zz} = eq \quad (2.100)$$

and is known as the anisotropy of the electric field gradient, and

$$\eta = \frac{V_{xx} - V_{yy}}{V_{zz}} \quad (2.101)$$

the quadrupole asymmetry parameter, which takes values $0 \leq \eta \leq 1$.

The Hamiltonian for the quadrupole interaction, for a spin I , is given by:[98, 107]

$$\hat{\mathcal{H}}_Q = \frac{eQ}{2I(2I-1)\hbar} \hat{I} \cdot \tilde{V} \cdot \hat{I} \quad (2.102)$$

from Slichter in an arbitrary x, y, z reference frame is to be given by:[106, 108]

$$\hat{\mathcal{H}}_Q = \frac{eQ}{6I(2I-1)\hbar} \sum_{i,j=x,y,z} V_{ij} \left(\frac{3}{2} (\hat{I}_i \hat{I}_j + \hat{I}_j \hat{I}_i) - \delta_{ij} I(I+1) \right) \quad (2.103)$$

where δ_{ij} is the Kronecker delta giving values:

$$\delta_{ij} = \begin{cases} 0 & \text{if } i \neq j \\ 1 & \text{if } i = j. \end{cases} \quad (2.104)$$

As with the other interactions in the PAS only the diagonal components of the V_{ij} tensor are non zero, thus the quadrupole Hamiltonian can be written in its PAS as:

$$\hat{\mathcal{H}}_Q = \frac{e^2 q Q}{4I(2I-1)\hbar} (3\hat{I}_z^2 - I(I+1) + \eta(\hat{I}_x^2 - \hat{I}_y^2)) \quad (2.105)$$

where the definitions of the anisotropy and asymmetry have been used, Equations 2.100 and 2.101 respectively. Equation 2.105 neatly shows that for the case of spin $I = \frac{1}{2}$ then $\hat{\mathcal{H}}_Q = 0$ and there is no quadrupole effect as expected. A further parameter C_Q , can be defined, known as the quadrupole coupling constant expressed in units of Hz as:

$$C_Q = \frac{e^2 q Q}{h}. \quad (2.106)$$

As shown in Section 2.4.1 when we want to apply transformations between frames spherical tensor notation is much more convenient. Due to the quadrupole interaction being described by a second rank tensor Equation 2.56 can be written for the quadrupole

interaction as:[109]

$$\hat{\mathcal{H}}_Q = \frac{eQ}{2I(2I-1)\hbar} \sum_{m=-2}^2 (-1)^m V_{2m} \hat{T}_{2-m} \quad (2.107)$$

where V_{2m} is the spatial component for the quadrupole interaction. If the summation is carried out this can be expressed as:

$$\hat{\mathcal{H}}_Q = \frac{eQ}{2I(2I-1)\hbar} (V_{20} \hat{T}_{20} - V_{21} \hat{T}_{2-1} - V_{2-1} \hat{T}_{21} + V_{22} \hat{T}_{2-2} + V_{2-2} \hat{T}_{22}). \quad (2.108)$$

The values of both V_{jm} and \hat{T}_{2-m} are given for an arbitrary reference frame, by the relations between the spherical and Cartesian tensor components as:[109]

$$V_{20} = 3\sqrt{\frac{1}{6}} V_{zz} \quad (2.109)$$

$$V_{21} = -V_{xz} - iV_{yz} \quad (2.110)$$

$$V_{2-1} = V_{xz} - iV_{yz} \quad (2.111)$$

$$V_{22} = \frac{1}{2}(V_{xx} - V_{yy}) + iV_{xy} \quad (2.112)$$

$$V_{2-2} = \frac{1}{2}(V_{xx} - V_{yy}) - iV_{xy} \quad (2.113)$$

$$\hat{T}_{20} = \frac{1}{6}\sqrt{6}[3\hat{I}_z^2 - I(I+1)] \quad (2.114)$$

$$\hat{T}_{21} = -\frac{1}{2}(\hat{I}_z \hat{I}_+ + \hat{I}_+ \hat{I}_z) \quad (2.115)$$

$$\hat{T}_{2-1} = \frac{1}{2}(\hat{I}_z \hat{I}_- + \hat{I}_- \hat{I}_z) \quad (2.116)$$

$$\hat{T}_{22} = \frac{1}{2}\hat{I}_+ \hat{I}_+ \quad (2.117)$$

$$\hat{T}_{2-2} = \frac{1}{2}\hat{I}_- \hat{I}_- \quad (2.118)$$

where the raising and lowering operators are used, as defined by $\hat{I}_+ = \hat{I}_x + i\hat{I}_y$ and $\hat{I}_- = \hat{I}_x - i\hat{I}_y$. In an arbitrary frame the quadrupole Hamiltonian becomes:

$$\begin{aligned} \hat{\mathcal{H}}_Q = \frac{eQ}{4I(2I-1)\hbar} & \left(\frac{1}{3}\sqrt{6}(3\hat{I}_z^2 - I(I+1))V_{20} - (\hat{I}_z \hat{I}_- + \hat{I}_- \hat{I}_z)V_{21} \right. \\ & \left. - (\hat{I}_z \hat{I}_+ + \hat{I}_+ \hat{I}_z)V_{2-1} + \hat{I}_+ \hat{I}_+ V_{22} + \hat{I}_+ \hat{I}_+ V_{2-2} \right). \end{aligned} \quad (2.119)$$

In the PAS frame it can be seen that:

$$\begin{aligned} V_{20} &= \sqrt{\frac{3}{2}}eq, \quad V_{21} = V_{2-1} = 0 \\ V_{22} &= V_{2-2} = \frac{1}{2}eq\eta \end{aligned} \quad (2.120)$$

In a NMR experiment even though the quadrupole interaction is usually very large, on the order of MHz, the Zeeman interaction is still usually the dominant interaction. This means that the quadrupole interaction can still be considered as a perturbation to the Zeeman states, represented by a sum of terms with decreasing significance. In some cases when the quadrupole interaction is small enough only a first order correction is needed, however commonly a second order perturbation treatment is required. Only the terms that commute with the Zeeman interaction (\hat{I}_z) are considered. The quadrupole Hamiltonian for this perturbation is given by: [102]

$$\hat{\mathcal{H}}_Q = \hat{\mathcal{H}}_Q^{(1)} + \hat{\mathcal{H}}_Q^{(2)}. \quad (2.121)$$

From [109] the Hamiltonian for the first order and second order terms are:

$$\hat{\mathcal{H}}_Q^{(1)} = \frac{eQ}{4I(2I-1)\hbar} \frac{\sqrt{6}}{3} (3\hat{I}_z^2 - I(I+1))V_{20} \quad (2.122)$$

and

$$\begin{aligned} \hat{\mathcal{H}}_Q^{(2)} &= -\frac{1}{\omega_0} \left[\frac{eQ}{4I(2I-1)\hbar} \right]^2 (2V_{2-1}V_{21}\hat{I}_z[4I(I+1) - 8\hat{I}_z^2 - 1] \\ &\quad + 2V_{2-2}V_{22}\hat{I}_z[2I(I+1) - 2\hat{I}_z^2 - 1]). \end{aligned} \quad (2.123)$$

It is important to know how these quadrupole Hamiltonians will affect the appearance of the NMR lineshape observed. An immediate and obvious point to note is that there is a dependence of the second order contribution with $\frac{1}{\omega_0}$, therefore upon increase of the external magnetic field B_0 the second order quadrupole contribution is reduced. This is not the case to first order as there is no dependence of ω_0 in Equation 2.122. If we consider the case of a spin (I) in the presence of a strong magnetic field, the Zeeman

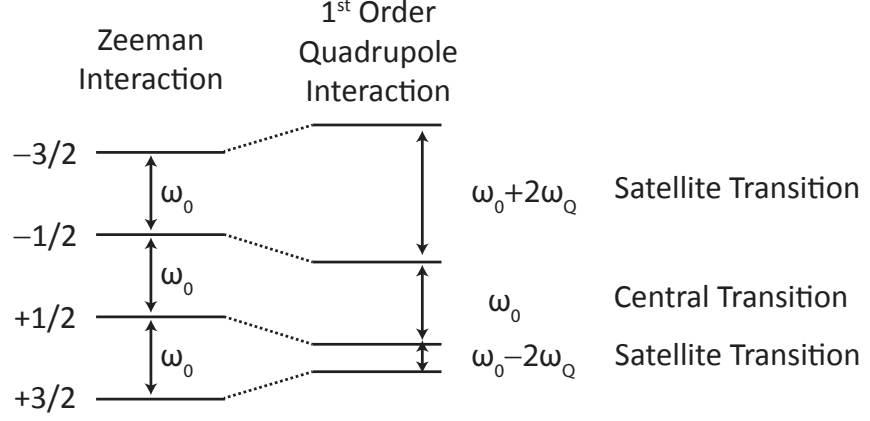


Figure 2.7: Energy level diagram for a spin $\frac{3}{2}$ nucleus, showing the splitting due to the Zeeman interaction, and the first order quadrupole interaction. It can be seen that the central transition splitting remains equal to ω_0 even under the first order quadrupole interaction.

interaction removes degeneracy to give $2I + 1$ energy levels:

$$E = \langle m | \hat{\mathcal{H}}_z | m \rangle = -m\omega_0. \quad (2.124)$$

The splitting between these energy levels is given by:

$$\omega_{m-1,m}^{(z)} = \langle m-1 | \hat{\mathcal{H}}_z | m-1 \rangle - \langle m | \hat{\mathcal{H}}_z | m \rangle = \omega_0 \quad (2.125)$$

as shown in Section 2.1. If a similar consideration is taken for the quadrupole interaction, to first order:

$$E_Q^{(1)} = \langle m | \hat{\mathcal{H}}_Q^{(1)} | m \rangle = \frac{eQ}{4I(2I-1)\hbar} \frac{\sqrt{6}}{3} (3m^2 - I(I+1)) V_{20} \quad (2.126)$$

and the resulting first order shift to the line is:

$$\begin{aligned} \omega_{m-1,m}^{(1)} &= \langle m-1 | \hat{\mathcal{H}}_Q^{(1)} | m-1 \rangle - \langle m | \hat{\mathcal{H}}_Q^{(1)} | m \rangle \\ &= \frac{3eQ}{4I(2I-1)\hbar} \frac{\sqrt{6}}{3} (1-2m) V_{20}. \end{aligned} \quad (2.127)$$

If the central transition $(-\frac{1}{2}, \frac{1}{2})$ is considered, the right hand side of Equation 2.127 goes to zero, showing that there is no effect to first order of the quadrupole interaction on the central transition, *i.e.*, the resonance still appears at ω_0 , this is shown in Figure 2.7 for the case of a $I = \frac{3}{2}$ nucleus. The other lines, which are affected to first order,

are known as the satellite transitions. For the second order contribution:

$$E_Q^{(2)} = \langle m | \hat{\mathcal{H}}_Q^{(2)} | m \rangle = -\frac{1}{\omega_0} \left[\frac{eQ}{4I(2I-1)\hbar} \right]^2 (V_{2-1}V_{21}m[4I(I+1) - 8m^2 - 1] + V_{2-2}V_{22}m[2I(I+1) - 2m^2 - 1]) \quad (2.128)$$

and the quadrupole shift to second order is:

$$\omega_{m-1,m}^{(2)} = -\frac{2}{\omega_0} \left[\frac{eQ}{4I(2I-1)\hbar} \right]^2 (V_{2-1}V_{21}(24m(m-1) - 4I(I+1) + 9) + \frac{1}{2}V_{2-2}V_{22}(12m(m-1) - 4I(I+1) + 6)). \quad (2.129)$$

unlike to first order, this second order shift clearly has an effect on the central transition. Therefore, for a transition $(m-1, m)$ the total effect to the line observed considering both the Zeeman and quadrupole effect is:

$$\omega_{m-1,m} = \omega_0 + \omega_{m-1,m}^{(1)} + \omega_{m-1,m}^{(2)}. \quad (2.130)$$

As previously shown for the other interactions, it is important to describe the quadrupole interaction in a frame where the NMR experiment is being measured, requiring rotations from its PAS to the lab frame. Using Equation 2.66:

$$\begin{aligned} V_{20}^L &= V_{20}^P D_{00}^2 + V_{22}^P D_{20}^2 + V_{2-2}^P D_{-20}^2 \\ &= V_{20}^P d_{00}^2(\beta) + V_{22}^P d_{20}^2(\beta)e^{-i2\alpha} + V_{2-2}^P d_{-20}^2(\beta)e^{i2\alpha} \end{aligned} \quad (2.131)$$

using $V_{22}^P = V_{2-2}^P$ and $d_{20}^2(\beta) = d_{-20}^2(\beta)$:

$$\begin{aligned} V_{20}^L &= V_{20}^P d_{00}^2(\beta) + V_{22}^P d_{20}^2(\beta)(e^{-i2\alpha} + e^{i2\alpha}) \\ &= V_{20}^P d_{00}^2(\beta) + V_{22}^P d_{20}^2(\beta)\cos 2\alpha \end{aligned} \quad (2.132)$$

inserting the values for the reduced Wigner matrices and Equation 2.120:

$$V_{20}^L = \sqrt{\frac{3}{2}}eq\left(\frac{1}{2}(3\cos^2\beta - 1) + \frac{1}{2}\eta\sin^2\beta\cos 2\alpha\right) \quad (2.133)$$

substituting into the first order quadrupole Hamiltonian:

$$\hat{\mathcal{H}}_Q^{(1)} = \frac{1}{3}\omega_Q(3\hat{I}_z^2 - I(I+1)) \quad (2.134)$$

where:

$$\omega_Q = \frac{3e^2Qq}{4I(2I-1)\hbar} \left(\frac{1}{2}(3\cos^2\beta - 1) + \frac{1}{2}\eta\sin^2\beta\cos 2\alpha \right) \quad (2.135)$$

the pre-factor of ω_Q can be expressed in terms of C_Q as shown earlier in Equation 2.106. In some texts χ_Q is used, which is related to C_Q by; $\chi_Q = 2\pi C_Q$, where χ_Q is in units of rads^{-1} and C_Q in units of Hz. This gives:

$$\omega_Q = \frac{3C_Q 2\pi}{4I(2I-1)\hbar} \left(\frac{1}{2}(3\cos^2\beta - 1) + \frac{1}{2}\eta\sin^2\beta\cos 2\alpha \right). \quad (2.136)$$

The quadrupole shift of energy levels to first order can be expressed in terms of the quadrupole frequency, ω_Q as:

$$\omega_{m-1,m}^{(1)} = (1-2m)\omega_Q \quad (2.137)$$

once again indicating the central transition is not shifted to first order. To obtain the second order shift in the lab frame of reference values of $V_{21}V_{2-1}$ and $V_{22}V_{2-2}$ in the lab frame are required, from [109]:

$$\begin{aligned} 2V_{21}^L V_{2-1}^L = & -\frac{3}{2}e^2q^2 \left[\left(-\frac{1}{3}\eta^2\cos^2 2\alpha + 2\eta\cos 2\alpha - 3 \right) \cos^4 \beta \right. \\ & + \left(\frac{2}{3}\eta^2\cos^2 2\alpha - 2\eta\cos 2\alpha - \frac{1}{3}\eta^2 + 3 \right) \cos^2 \beta \\ & \left. + \frac{1}{3}\eta^2(1 - \cos^2 2\alpha) \right] \end{aligned} \quad (2.138)$$

$$\begin{aligned} 2V_{22}^L V_{2-2}^L = & \frac{3}{2}e^2q^2 \left[\left(\frac{1}{24}\eta^2\cos^2 2\alpha - \frac{1}{4}\eta\cos 2\alpha + \frac{3}{8} \right) \cos^4 \beta \right. \\ & + \left(-\frac{1}{12}\eta^2\cos^2 2\alpha + \frac{1}{6}\eta^2 - \frac{3}{4} \right) \cos^2 \beta \\ & \left. + \frac{1}{24}\eta^2\cos^2 2\alpha + \frac{1}{4}\eta\cos 2\alpha + \frac{3}{8} \right]. \end{aligned} \quad (2.139)$$

The second order shift to the central transition from [109] is:

$$\begin{aligned}\omega_{-1/2,1/2}^{(2)Static} = & -\frac{1}{6\omega_0} \left[\frac{3C_Q 2\pi}{2I(2I-1)} \right]^2 \left[I(I+1) - \frac{3}{4} \right] \\ & \times [A(\alpha, \eta) \cos^4 \beta + B(\alpha, \eta) \cos^2 \beta + C(\alpha, \eta)]\end{aligned}\quad (2.140)$$

where:

$$\begin{aligned}A(\alpha, \eta) &= -\frac{27}{8} + \frac{9}{4} \eta \cos 2\alpha - \frac{3}{8} (\eta \cos 2\alpha)^2 \\ B(\alpha, \eta) &= \frac{30}{8} - \frac{1}{2} \eta^2 - 2\eta \cos 2\alpha + \frac{3}{4} (\eta \cos 2\alpha)^2 \\ C(\alpha, \eta) &= -\frac{3}{8} + \frac{1}{3} \eta^2 - \frac{1}{4} \eta \cos 2\alpha - \frac{3}{8} (\eta \cos 2\alpha)^2.\end{aligned}\quad (2.141)$$

If the simplest case of axial symmetry, $\eta = 0$ is considered then Equation 2.140 becomes:

$$\begin{aligned}\omega_{-1/2,1/2}^{(2)Static} = & -\frac{1}{16\omega_0} \left[\frac{3C_Q 2\pi}{2I(2I-1)} \right]^2 \left[I(I+1) - \frac{3}{4} \right] \\ & \times (1 - \cos^2 \beta)(9\cos^2 \beta - 1)\end{aligned}\quad (2.142)$$

the above analysis is for the case of a single crystal. For a powder spectrum, as commonly looked at in solid state NMR, all orientations of V are present with respect to B_0 , so β can take on any value from 0 to π .

Quadrupolar Interaction Under MAS

The descriptions for the quadrupole interaction shown in the previous section only accounts for the case of a static sample within the presence of a magnetic field. However, the NMR experiment is usually carried out using MAS, as previously discussed in Section 2.4.2. A further rotation is therefore required from the rotor frame. The first order quadrupole shift under MAS, looking at Equation 2.127 and using Equations 2.70 and 2.71 is:

$$\omega_{m-1,m}^{(1)MAS} = \frac{1}{2} (1 - 2m) \omega_Q (3\cos^2 \theta - 1). \quad (2.143)$$

The familiar $3\cos^2 \theta - 1$ term is again present here for the first order quadrupole interaction that is also present for the dipolar coupling and the chemical shielding. Like

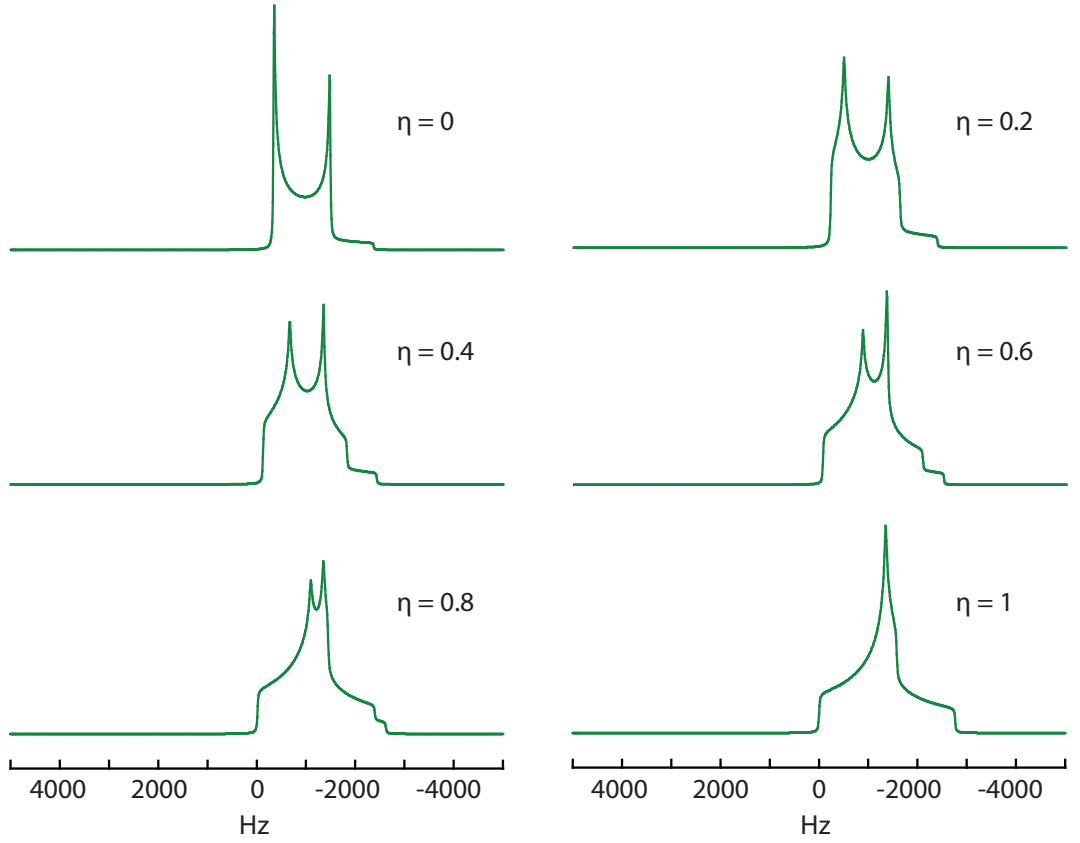


Figure 2.8: Simulations of lineshapes for quadrupole broadened spin $I = 3/2$ nucleus under MAS, displaying only the second order central transition. Variation in the line-shapes are due to changes in η , with the other parameters being $C_Q = 2$ MHz at 9.4 T. Diagram is based on Figure in [108]

these other anisotropic interactions the effect of MAS causes the first order quadrupole interaction to be averaged to zero, thus resulting in the $2I$ lines being reduced to a single line at ω_0 .

The effect of the second order quadrupole interaction shift under MAS is given in [109] as:

$$\begin{aligned}
 \omega_{m-1,m}^{(2)MAS} = & -\frac{3}{32\omega_0} \left[\frac{C_Q 2\pi}{I(2I-1)} \right]^2 \left(1 + \frac{1}{3}\eta^2 \right) \\
 & \times [2I(I+1) - 14m(m-1) - 5] \\
 & + \frac{3}{128\omega_0} \left[\frac{C_Q 2\pi}{I(2I-1)} \right]^2 \\
 & \times [6I(I+1) - 34m(m-1) - 13] \\
 & \times g(\alpha, \beta, \eta),
 \end{aligned} \tag{2.144}$$

where

$$\begin{aligned}
g(\alpha, \beta, \eta) = & \frac{1}{2}(1 + 6\cos^2\beta - 7\cos^4\beta) \\
& + \frac{1}{3}\eta(1 - 8\cos^2\beta + 7\cos^4\beta)\cos 2\alpha \\
& + \frac{1}{18}\eta^2[-7(1 - \cos^2\beta)^2 \\
& \times \cos^2 2\alpha + 8 - 4\cos^2\beta].
\end{aligned} \tag{2.145}$$

Due to there being no $3\cos^2\theta - 1$ dependence for this effect MAS does not sufficiently average away the second order quadrupole contribution, with an anisotropic powder lineshape observed even under rapid spinning, typical lineshapes are shown in Figure 2.8.

Chapter 3

Experimental Details

In the previous chapter the theory behind the phenomenon of nuclear magnetic resonance has been presented, outlining how the different nuclear interactions affect the spins under investigation. Building on from this theory, the techniques required to conduct solid state NMR experiment will now be covered, showing how NMR can be used as a tool to gain valuable structural information. The theory presented in this chapter is collected from the following sources; [98–100], in addition to other publications explicitly referred to in the text.

3.1 The NMR Signal

As shown in Section 2.3.1 the signal for a one dimensional NMR experiment is given by Equation 2.50. This can be more formally written as:

$$s(t) = \frac{1}{2}(\cos(\Omega t) + i\sin(\Omega t))e^{(-t/T_2)} \quad (3.1)$$

where the extra damping term $e^{(-t/T_2)}$ is included to indicate decay due to relaxation, as covered in the Section 3.6. The resonance offset, as previously mentioned, is used to compare the signal observed with a known reference frequency, both on the order of MHz; by displaying the difference between the two, a smaller and hence more easily processed signal will be obtained. From Equation 3.1 the NMR signal is detected as two signals 90° out of phase with one another, known as Quadrature detection. This is crucial as detection along one axis alone would mean it wouldn't be possible to determine the sign of precession of the magnetisation, i.e. to determine if the resonance

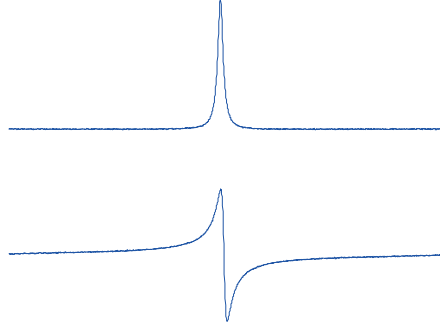


Figure 3.1: Figure showing example of absorptive (top) and dispersive (bottom) line-shapes ($A(\Delta\omega)$) and ($D(\Delta\omega)$). The absorptive lineshape is the desired lineshape corresponding to a narrow Lorentzian centred at $(+\Omega)$.

offset is positive or negative. Using Quadrature detection successfully ensures sign discrimination can be obtained.

Equation 3.1 represents the NMR signal in the time domain, which is how the data is collected in the form of the free induction decay (FID). However, to make this more useful for a spectroscopist a mathematical function the Fourier transform is carried out, to transform this time domain data into the frequency domain that is easier to visualise. The Fourier transform is given by:

$$s(\omega) = \int_{-\infty}^{\infty} s(t)e^{-i\omega t} dt \quad (3.2)$$

this results in the signal:

$$s(\omega) = A(\Delta\omega) - iD(\Delta\omega) \quad (3.3)$$

where:

$$A(\Delta\omega) = \frac{1/T_2}{(1/T_2)^2 + (\omega - \Omega)^2} \quad \text{and} \quad D(\Delta\omega) = \frac{(\omega - \Omega)}{(1/T_2)^2 + (\omega - \Omega)^2}. \quad (3.4)$$

These are known as the absorptive and dispersive parts of a Lorentzian lineshape, see Figure 3.1. Only the absorption line is usually presented, due to it being narrower and centred upon the frequency of interest Ω . However, in reality the signal is most likely not going to be purely absorptive in the real part of the spectrum and dispersive in the imaginary part, as implied in Equation 3.3, due to phase imperfections in the magnetisation collected. Therefore, “phasing” the spectrum is generally required

by the spectroscopist, involving taking linear combinations of the real and imaginary components, to achieve the desired absorptive lineshape.

3.2 Two Dimensional NMR

Commonly, more information is required than can usually be provided with a simple 1D NMR experiment alone, therefore a second varying time period can be included, which under a further Fourier transformation leads to a two dimensional frequency domain spectrum. The duration of this second time period, denoted by t_1 (Note this isn't the same as T_1 relaxation see Section 3.6) is incremented during the course of a series of FIDs being obtained, leading to a modulation of the NMR signal dependent upon this t_1 value. During the t_1 period the signal can be modulated in two different ways, phase or amplitude modulated. Phase modulation leads to undesirable phase twist lineshapes obtained in the 2D spectra unless a full echo is acquired, therefore the experiments used in this thesis will solely consist of amplitude modulation.

In a standard 2D amplitude modulated experiment the signal is given by:

$$\begin{aligned} s(t_1, t_2) &= (e^{-i\Omega t_1} + e^{+i\Omega t_1})e^{-t_1/T_2^{(1)}}e^{+i\Omega t_2}e^{-t_2/T_2^{(2)}} \\ &= 2\cos(\Omega t_1)e^{-t_1/T_2^{(1)}}e^{+i\Omega t_2}e^{-t_2/T_2^{(2)}}. \end{aligned} \quad (3.5)$$

If a Fourier transformation is applied in the F_2 dimension first, as shown for a simple 1D experiment, this becomes:

$$s(t_1, \omega_2) = 2\cos(\Omega t_1)e^{-t_1/T_2^{(1)}}(A_2^+ - iD_2^+), \quad (3.6)$$

where the terms A_n^\pm and D_n^\pm correspond to absorptive and dispersive lineshapes respectively centred at the frequency $\pm\Omega$ in the F_n dimension. The next step is to consider both the real and imaginary parts of Equation 3.6 individually and carry out the further Fourier transformation in F_1 separately, known as a hypercomplex Fourier transform. Firstly, for the real parts:

$$\begin{aligned} s(\omega_1, \omega_2)^{Re} &= [(A_1^- - iD_1^-) + (A_1^+ - iD_1^+)]A_2^+ \\ &= (A_1^- + A_1^+)A_2^+ - i(D_1^- + D_1^+)A_2^+ \end{aligned} \quad (3.7)$$

and the imaginary part:

$$\begin{aligned}
s(\omega_1, \omega_2)^{Im} &= [(A_1^+ - iD_1^+) + (A_1^- - iD_1^-)]D_2^+ \\
&= (A_1^+ + A_1^-)D_2^+ - i(D_1^+ + D_1^-)D_2^+.
\end{aligned} \tag{3.8}$$

From Equations 3.7 and 3.8 it is clear that four possible lineshape can exist corresponding to: pure absorption in F_1 and F_2 , pure dispersion in F_1 and F_2 , and both combinations of dispersive and absorptive in each dimension. Thus, using amplitude modulation alone does not result in sign discrimination due to the mixture of positive and negative amplitude and dispersive terms, so determining if the signal obtained is larger or smaller than the rf frequency is not possible. To restore sign discrimination there are two possible methods that are commonly implemented, States [110] or TPPI [111]. All of the experiments in this thesis use the States method, which involves recording two FIDs 90° out of phase with each other so that both a cosine and sine modulation is obtained with respect to t_1 :

$$\begin{aligned}
s_{sin}(t_1, t_2) &= 2\sin(\Omega t_1)e^{-t_1/T_2^{(1)}}e^{+i\Omega t_2}e^{-t_2/T_2^{(2)}} \\
s_{cos}(t_1, t_2) &= 2\cos(\Omega t_1)e^{-t_1/T_2^{(1)}}e^{+i\Omega t_2}e^{-t_2/T_2^{(2)}}.
\end{aligned} \tag{3.9}$$

Applying a Fourier transform with respect to F_2 :

$$\begin{aligned}
s_{sin}(t_1, \omega_2) &= 2\sin(\Omega t_1)e^{-t_1/T_2^{(1)}}(A_2^+ - iD_2^+) \\
s_{cos}(t_1, \omega_2) &= 2\cos(\Omega t_1)e^{-t_1/T_2^{(1)}}(A_2^+ - iD_2^+).
\end{aligned} \tag{3.10}$$

Discarding the imaginary components these equations become:

$$\begin{aligned}
s_{sin}(t_1, \omega_2)^{Re} &= 2\sin(\Omega t_1)e^{-t_1/T_2^{(1)}}A_2^+ \\
s_{cos}(t_1, \omega_2)^{Re} &= 2\cos(\Omega t_1)e^{-t_1/T_2^{(1)}}A_2^+.
\end{aligned} \tag{3.11}$$

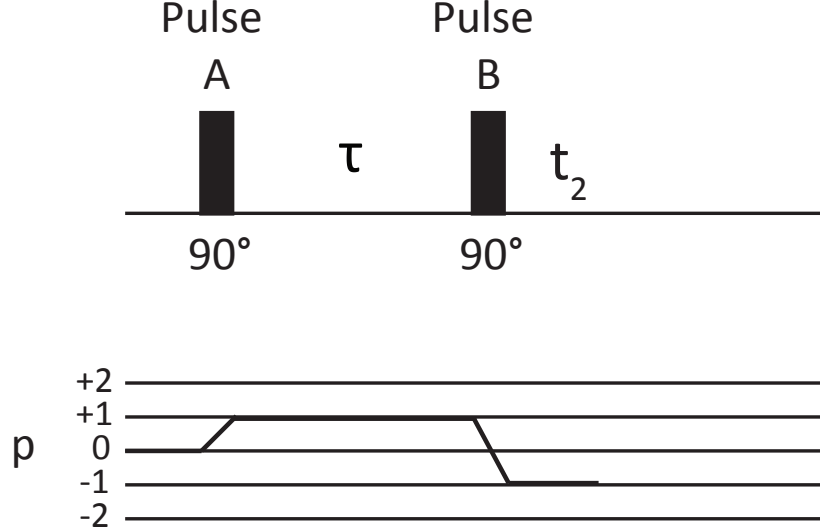


Figure 3.2: Top: Two pulse sequence diagram (COSY) showing two 90° pulses separated by delay τ . Bottom: Coherence transfer pathway showing desired coherences upon application of rf pulses. Unwanted coherences are suppressed by phase cycling.

Then carrying out the second Fourier transform, now in the F_1 dimension:

$$\begin{aligned}
 s_{\sin}(\omega_1, \omega_2)^{Re} &= i[(A_1^- - iD_1^-) - (A_1^+ - iD_1^+)]A_2^+ \\
 &= (D_1^- - D_1^+)A_2^+ + i(A_1^- - A_1^+)A_2^+ \\
 s_{\cos}(\omega_1, \omega_2)^{Re} &= [(A_1^- - iD_1^-) + (A_1^+ - iD_1^+)]A_2^+ \\
 &= (A_1^- + A_1^+)A_2^+ - i(D_1^- + D_1^+)A_2^+
 \end{aligned} \tag{3.12}$$

Upon inspection of Equation 3.12 if we take the imaginary part of the *sin* originating term and the real part of the *cos* originating term, upon taking the difference between the two:

$$Re[s_{\cos}(\omega_1, \omega_2)^{Re}] - Im[s_{\sin}(\omega_1, \omega_2)^{Re}] = 2A_1^+ A_2^+ \tag{3.13}$$

Which as required results in a two dimensional absorption lineshape, with sign discrimination, centred at the frequency $(+\Omega, -\Omega)$, due to the States procedure.

3.3 Phase Cycling

As discussed in Section 2.3.1 coherent states are created during the NMR experiment upon application of an rf pulse, that ultimately result in the observed NMR signal. In addition to the single quantum coherences discussed in Section 2.3.1 achieved upon

application of a 90° pulse, higher order coherences are achievable, such as double or triple quantum coherence, dependent upon the spin system. Pulse sequences in NMR utilise a series of different rf pulses and delays, in order to manipulate these coherences, to ultimately gain further insight into the spin system, where a wealth of information can be obtained. During a pulse sequence only certain coherences may be desired, dependent upon the particular interaction being considered. These coherence levels are best illustrated illustratively, as shown in Figure 3.2, corresponding to the case of the solution state COSY experiment. At the top of Figure 3.2 is the pulse sequence diagram, where pulses are indicated by solid blocks, the length of which depends upon the pulse used, e.g. 90° or 180° . Below the pulse sequence is the coherence transfer pathway diagram, which indicates the desired coherences for that particular pulse sequence. It is important to note that changes in coherences can only be obtained via application of an rf pulse, periods of free precession do not create change in coherence order.

The problem is that rf pulses are not particularly effective at selecting the coherence orders desired, resulting in a whole number of coherences being created, not just the pathways as indicated in the coherence pathway diagram in Figure 3.2. Therefore the technique of phase cycling is used, where upon subsequent acquisitions the phase associated with the rf pulses are varied, suppressing unwanted coherences.

Phase cycling follows a series of basic rules that enable the NMR spectroscopist to follow and create phase cycling schemes for even the most complex of pulse sequences, to achieve the desired coherence pathways. Firstly, the coherence pathway always starts at $p = 0$, coherence order 0. The required finishing point of a phase cycle is for single quantum coherence resulting in the signal observed, as shown in Section 2.3.1, $p = -1$. Therefore, the phases of the rf pulses need to be cycled to achieve the desired coherences between these two fixed points. The golden rules of phase cycling are:[100]

If the phase of a pulse or a group of pulses is shifted by ϕ then a coherence undergoing a change in coherence order Δp experiences a phase shift $-\phi\Delta p$, detected by the receiver. [100]

And the second golden rule of phase cycling is:

Step Number	ϕ_A	$-\phi_A \Delta p$	Receiver Phase
1	0	0	0
2	90	-90(270)	270
3	180	-180(180)	180
4	270	-270(90)	90

Table 3.1: Phase cycling table for the pulse sequence in Figure 3.2. The 4 step cycle, from Golden Rule 2, selects the desired coherence pathway, with the receiver phase determined using Golden Rule 1.

If a phase cycle uses steps of $360^\circ/N$ then, along with the desired pathway Δp , pathways $\Delta p \pm nN$, where $n = 1, 2, 3, \dots$, will also be selected. All other pathways are suppressed.[100]

These rules provide instructions to follow to construct the phase cycle, if we use the example from Figure 3.2, an initial coherence change from $p = 0$ to $p = 1$ upon application of the first pulse is required, $\Delta p = 1$. From the second golden rule if we select a 4 step phase cycle we obtain coherences $\Delta p = +1, +5, +9, -3, -7, -11$, thereby blocking the undesirable coherences $+2, +3, -1, -2$, but retaining the required $+1$ coherence. Although we detect other coherences in addition to the $p = +1$ path, such as $+5, +9$ etc., these will have negligible contribution and can safely be ignored due to inefficient excitation of these higher coherence orders. A phase cycle table can then be created-see Table 3.1, that shows the phase cycling scheme required for the pulse sequence in Figure 3.2, with both the phase of pulse A required and the corresponding receiver phase. This successfully results in signal only being detected that evolved as single quantum coherence during the period τ (between A and B pulses). For more advanced pulse sequences containing more pulses a total of $n - 1$ pulses need to be phase cycled, where n is the number of pulses in the pulse sequence.

3.4 Pulsed Experiments

3.4.1 Product Operators

The density operator analysis, as described in Section 2.2, is useful as it encodes all of the relevant information in order to describe the NMR experiment. However for the

analysis of more than a few coupled spins the density operator approach becomes less intuitive due to the increasingly expanding matrix calculations required. An alternative approach that can be adopted is to express the density matrix as a series of product operators. Upon following certain identities, the product operator analysis can help give information on the effect of rf pulses, helping to give a quantum mechanical approach but with an intuitive feel, enabling a much more detailed analysis of NMR pulse sequences. Despite its usefulness the product operator analysis does have its drawbacks, in that it is only applicable to describe systems evolving under weak J coupling, and it doesn't take into account relaxation effects. However for simple pulse sequences on spin $I = \frac{1}{2}$ nuclei it is extremely effective.

From Section 2.2 the three operators describing an isolated spin $I = \frac{1}{2}$ nucleus are:

$$\hat{I}_x, \hat{I}_y, \hat{I}_z \quad (3.14)$$

representing the magnetisation in each axis of the rotating frame. For the product operator analysis the hat will be omitted for brevity.

The effect of an x and y rf pulses on each of the operators is given by:

$$\begin{aligned} I_x &\xrightarrow{\beta_x} I_x \\ I_y &\xrightarrow{\beta_x} I_y \cos \beta + I_z \sin \beta \\ I_z &\xrightarrow{\beta_x} I_z \cos \beta - I_y \sin \beta \\ I_x &\xrightarrow{\beta_y} I_x \cos \beta - I_z \sin \beta \\ I_y &\xrightarrow{\beta_y} I_y \end{aligned} \quad (3.15)$$

$$I_z \xrightarrow{\beta_z} I_z \cos \beta + I_x \sin \beta \quad (3.16)$$

which shows that application of a pulse in a particular axis has no effect on the operator in that axis. By inserting values of the pulses, for instance 90° or 180° , the effects of the pulse on the operator are easily understood.

Upon a period of free evolution under the resonance offset, the operators behave

as:

$$\begin{aligned}
I_x &\xrightarrow{\Omega t} I_x \cos(\Omega t) + I_y \sin(\Omega t) \\
I_y &\xrightarrow{\Omega t} I_y \cos(\Omega t) - I_x \sin(\Omega t) \\
I_z &\xrightarrow{\Omega t} I_z
\end{aligned} \tag{3.17}$$

The above show what the effects of rf pulses and free evolution on a single isolated spin $I = \frac{1}{2}$ nucleus, however the power of product operators is in describing coupled spin systems. For a pair of spin $I = \frac{1}{2}$ J coupled nuclei the relevant product operators are now:

$$\begin{aligned}
&I_x, I_y, I_z, S_x, S_y, S_z, \\
&2I_x S_x, 2I_x S_y, 2I_x S_z, 2I_y S_x, \\
&2I_y S_y, 2I_y S_z, 2I_z S_x, 2I_z S_y, 2I_z S_z
\end{aligned} \tag{3.18}$$

where the factor 2 is purely for normalisation purposes. Evolution during free precession will now be under the effect of the J coupling, in addition to the resonance offset. In the product operator approach these can be dealt with sequentially, with the effect of the J evolution given by:

$$\begin{aligned}
I_x &\xrightarrow{\pi J_{IS} t} I_x \cos(\pi J_{IS} t) + 2I_y S_z \sin(\pi J_{IS} t) \\
2I_y S_z &\xrightarrow{\pi J_{IS} t} 2I_y S_z \cos(\pi J_{IS} t) - I_x \sin(\pi J_{IS} t) \\
I_y &\xrightarrow{\pi J_{IS} t} I_y \cos(\pi J_{IS} t) - 2I_x S_z \sin(\pi J_{IS} t) \\
2I_x S_z &\xrightarrow{\pi J_{IS} t} 2I_x S_z \cos(\pi J_{IS} t) + I_y \sin(\pi J_{IS} t)
\end{aligned} \tag{3.19}$$

where the factor of 2π has come from the fact the J coupling is considered in terms of rad s^{-1} rather than its usual Hz . For the anti-phase terms, such as $2I_x S_z$, the effect of a resonance offset is:

$$2I_x S_z \xrightarrow{\Omega_I t} 2I_x S_z \cos(\Omega_I t) + 2I_y S_z \sin(\Omega_I t) \tag{3.20}$$

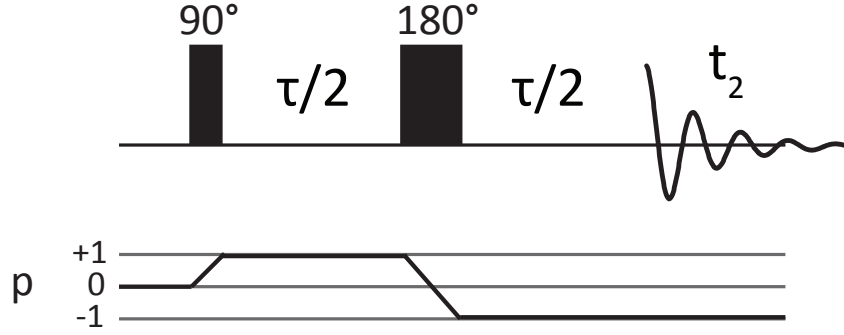


Figure 3.3: Pulse sequence for a two pulse spin echo experiment [25, 26]. The initial 90° pulse creates single quantum coherence that evolves during the delay $\tau/2$. The 180° pulse causes a refocusing of the magnetisation after the second $\tau/2$ delay period. The corresponding coherence transfer pathway is shown below the pulse sequence indicating the coherence changes associated with each step of the sequence.

and the effect of a pulse:

$$2I_x S_z \xrightarrow{(\beta_y)_I} 2I_x S_z \cos\beta - 2I_z S_z \sin\beta \quad (3.21)$$

where the subscript I denotes the pulse effecting the I spin, therefore the S term remains unchanged.

The product operator analysis is best understood by way of examples, its description for pulse sequences used within this thesis is given in the subsequent sections.

3.4.2 Spin Echo

First proposed in 1950 by Hahn [25] and later developed by Carr and Purcell [26], the spin echo has become a building block for many solid state NMR pulse sequences, with the pulse sequence shown in Figure 3.3. The main function of the spin echo in NMR spectroscopy is to refocus broadening effects from the Hamiltonians of undesired interactions. A simple magnetisation vector model can be easily used to describe the spin echo. Initially the spins are aligned with the B_0 field in the z -direction; this is then perturbed into the xy plane by the 90° pulse. The spins then precess freely for a time $\tau/2$ before the final 180° pulse flips them to their mirror image. During the final $\tau/2$ period the spins again are able to precess freely resulting in an echo forming. The refocusing echo originates from the fact that some spins will be subject to different local

magnetic fields, due to the interactions present. During the periods of free precession some spins will precess faster than others during the first period $\tau/2$; upon application of the 180° pulse the magnetisation is caused to flip, resulting in the faster precessing spins now being behind the slower spins. After the further $\tau/2$ period the spins catch up with one another, resulting in the refocusing effect.

The spin echo can be described quantum mechanically by the product operator analysis, as introduced in the last section. Considering the case of a pair of heteronuclear spin $I = \frac{1}{2}$ coupled nuclei:

$$I_z \xrightarrow{(90_x)_I} -I_y \quad (3.22)$$

The equilibrium magnetisation, I_z is perturbed into the $x - y$ plane, creating I_y . This is then followed by a period of free precession $\tau/2$ where evolution is due to both the resonance offset and the heteronuclear J coupling, which can be taken sequentially:

$$\begin{aligned} & \xrightarrow{\Omega_I \tau/2} -I_y \cos(\Omega_I \tau/2) + I_x \sin(\Omega_I \tau/2) \\ & \xrightarrow{\pi J_{IS} \tau/2} -I_y \cos(\Omega_I \tau/2) \cos(\pi J_{IS} \tau/2) + 2I_x S_z \cos(\Omega_I \tau/2) \sin(\pi J_{IS} \tau/2) \\ & \quad + I_x \sin(\Omega_I \tau/2) \cos(\pi J_{IS} \tau/2) + 2I_y S_z \sin(\Omega_I \tau/2) \sin(\pi J_{IS} \tau/2) \end{aligned} \quad (3.23)$$

Next the 180° pulse is applied:

$$\begin{aligned} & \xrightarrow{(180_y)_I} -I_y \cos(\Omega_I \tau/2) \cos(\pi J_{IS} \tau/2) - 2I_x S_z \cos(\Omega_I \tau/2) \sin(\pi J_{IS} \tau/2) \\ & \quad - I_x \sin(\Omega_I \tau/2) \cos(\pi J_{IS} \tau/2) + 2I_y S_z \sin(\Omega_I \tau/2) \sin(\pi J_{IS} \tau/2) \end{aligned} \quad (3.24)$$

before the final $\tau/2$ period of free precession:

$$\begin{aligned} & \xrightarrow{\Omega_I \tau/2} -I_y \cos(\pi J_{IS} \tau/2) - 2I_x S_z \sin(\pi J_{IS} \tau/2) \\ & \xrightarrow{\pi J_{IS} \tau/2} -I_y \end{aligned} \quad (3.25)$$

The identity $\cos^2 \theta + \sin^2 \theta = 1$ has been used for both of the above steps. Therefore after the second $\tau/2$ period $-I_y$ magnetisation is created, as was created after the initial 90° pulse, hence a refocusing of the magnetisation.

Typically in the solid state NMR experiment the observed linewidth, due to

the effects of magnetic inhomogeneities, doesn't solely correspond to T_2 as expected. This is due to varying magnetic fields experienced across the sample, such as from instrumental imperfections, resulting in a range of chemical shifts broadening the line. This means the observed NMR linewidth (T_2^*) is much broader than expected from transverse relaxation alone, $T_2^* \leq T_2$. However, from Equation 3.25 above for the case of the heteronuclear coupled spin pair, the effects of the resonance offset, and the heteronuclear J coupling, are refocused using the spin echo sequence. Due to this refocusing effect these inhomogeneities broadening the lineshape are clearly removed, resulting in a refocused line width that is smaller than the ordinary one pulse linewidth. Thus the coherence lifetime T_2' is much larger than the dephasing time of the FID T_2^* .

For a homonuclear coupled spin $\frac{1}{2}$ pair the product operator analysis gives:

$$I_z \xrightarrow{(90_x)_{IS}} -I_y \quad (3.26)$$

The 90° pulse can affect both I and S magnetisation, although the result above in Equation 3.26 is the same as for the heteronuclear case due to there being initially no magnetisation on the S spin. The period of free precession also results in the same result as for the heteronuclear case:

$$\begin{aligned} & \xrightarrow{\Omega_I \tau / 2} -I_y \cos(\Omega_I \tau / 2) + I_x \sin(\Omega_I \tau / 2) \\ & \xrightarrow{\pi J_{IS} \tau / 2} -I_y \cos(\Omega_I \tau / 2) \cos(\pi J_{IS} \tau / 2) + 2I_x S_z \cos(\Omega_I \tau / 2) \sin(\pi J_{IS} \tau / 2) \\ & \quad + I_x \sin(\Omega_I \tau / 2) \cos(\pi J_{IS} \tau / 2) + 2I_y S_z \sin(\Omega_I \tau / 2) \sin(\pi J_{IS} \tau / 2) \end{aligned} \quad (3.27)$$

The 180° pulse affects now both I and S magnetisation giving:

$$\begin{aligned} & \xrightarrow{(180_y)_{IS}} -I_y \cos(\Omega_I \tau / 2) \cos(\pi J_{IS} \tau / 2) + 2I_x S_z \cos(\Omega_I \tau / 2) \sin(\pi J_{IS} \tau / 2) \\ & \quad - I_x \sin(\Omega_I \tau / 2) \cos(\pi J_{IS} \tau / 2) - 2I_y S_z \sin(\Omega_I \tau / 2) \sin(\pi J_{IS} \tau / 2) \end{aligned} \quad (3.28)$$

and the final free precession during $\tau/2$ gives:

$$\begin{aligned} & \xrightarrow{\Omega_I \tau / 2} -I_y \cos(\pi J_{IS} \tau / 2) + 2I_x S_z \sin(\pi J_{IS} \tau / 2) \\ & \xrightarrow{\pi J_{IS} \tau / 2} -I_y \cos(\pi J_{IS} \tau) + 2I_x S_z \sin(\pi J_{IS} \tau) \end{aligned} \quad (3.29)$$

where the identities $\cos^2\theta - \sin^2\theta = \cos 2\theta$ and $2\sin\theta\cos\theta = \sin 2\theta$ have been used in the last step. The above procedure only accounts for the magnetisation on the I spin, however the S spin will behave exactly the same, giving the result for both spins as:

$$-(I_y + S_y)\cos(\pi J_{IS}\tau) + (2I_xS_z + 2I_zS_x)\sin(\pi J_{IS}\tau) \quad (3.30)$$

From Equation 3.30 it can be seen that the spin echo again refocuses the chemical shift, however this time unlike for the heteronuclear case, the J coupling is retained for the homonuclear spin system. The dependence on the homonuclear J coupling observed can be quite useful, and forms the building block of many advanced NMR experiments to exploit this homonuclear coupling. Upon carrying out multiple spin echo experiments with differing $\tau/2$ values the J modulation can be mapped out to extract a value for the J coupling, that may normally be masked by the large linewidths originating from the distributions of chemical shifts which themselves have been refocused by the spin echo. A thorough theoretical treatment of spin echo modulation by homonuclear J couplings under MAS is given in the article Duma *et al.*[112]

Another advantage of echo experiments is that the formation of the echo begins after the second $\tau/2$ period, meaning that the effects experienced from the ring down of the probe immediately after the pulse, do not distort the beginning of the signal acquisition. This has the advantage for resolving broad NMR lines that decay quite quickly, which may be distorted in the deadtime between the rf pulse and the beginning of the acquisition that is required in an ordinary one pulse experiment. For static NMR work, and work on broad quadrupole lines a quadrupole echo is commonly used.[113]

3.4.3 INADEQUATE and refocused INADEQUATE

A vast array of pulse sequences in NMR exploit the useful properties of spin echoes outlined in the previous section. One such experiment the INADEQUATE (Incredible natural abundance double quantum transfer), was developed in the early 1980s for use in solution NMR [36, 117, 118], with near identical versions implemented in the solid state by Lesage and co workers in the late 1990s.[114] The ordinary INADEQUATE pulse sequence was, however, quickly overtaken in the solid state by the refocused INADEQUATE,[115] where an additional spin echo was appended to the end of the

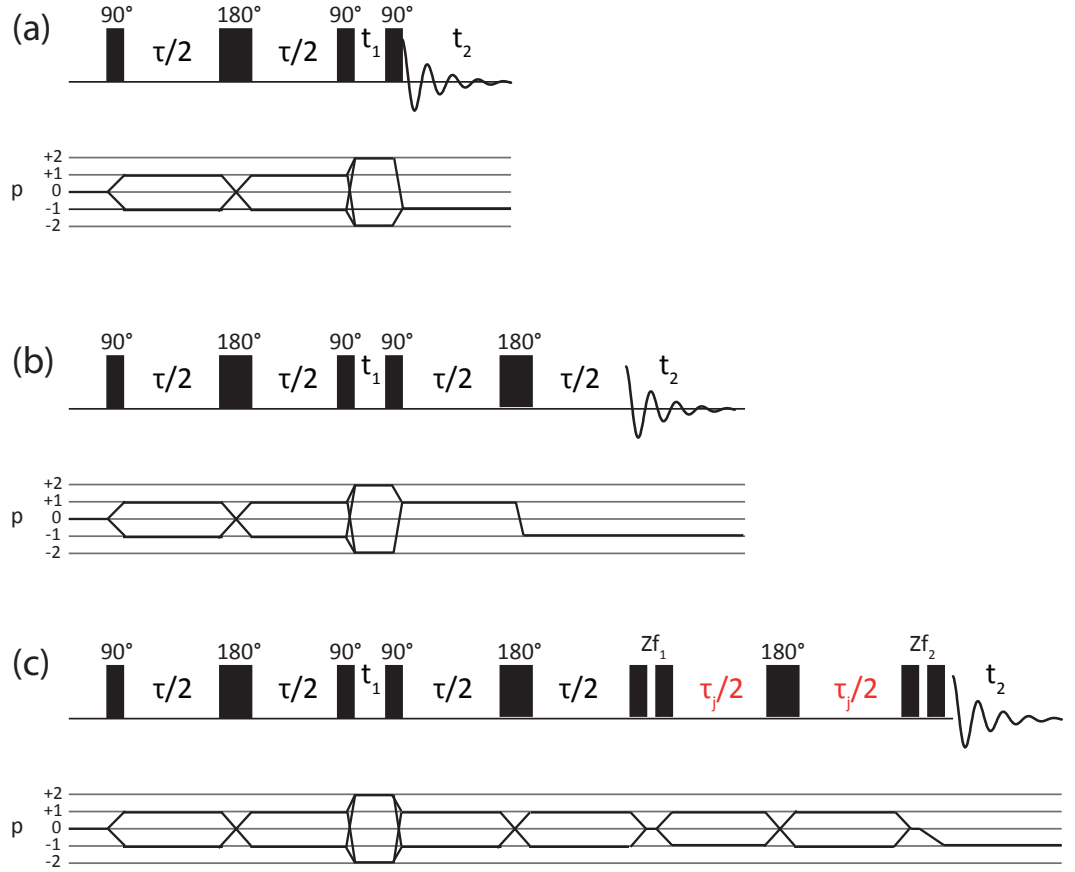


Figure 3.4: Pulse sequence diagrams and corresponding coherence transfer pathway diagrams of (a) INADEQUATE experiment which consists of an initial spin echo sequence with a further 90° pulse to create DQ coherence which evolves for the delay t_1 and is then converted to observable anti-phase signal by the final 90° pulse.[114] (b) refocused INADEQUATE experiment which contains a further spin echo appended on at the end of the INADEQUATE sequence to detect in-phase magnetisation.[115] (c) REINE experiment, which contains a further spin echo appended to the end of the refocused INADEQUATE sequence. The length of the final spin echo delay in the REINE experiment (τ_j) is incremented during a series of REINE experiments to observe a J modulation of the observed signal. Z -filters are shown instead of the 90° pulses, before the final spin echo period (Zf_1) and after the final spin echo period (Zf_2), to remove unwanted coherence orders that could result in lineshape distortions.[116]

INADEQUATE to provide in-phase magnetisation, rather than the anti-phase lineshapes produced in the INADEQUATE. The benefit of acquiring in-phase lineshapes lies in the fact that broader lines, typical in solid state NMR, are acquired without the effect of signal cancellation that can occur from anti-phase lineshapes.

Figure 3.4 shows the pulse sequence for both the INADEQUATE and refocused INADEQUATE experiments. Both experiments consist of an initial spin echo, which is used to remove evolution under offsets and hence chemical shielding inhomogeneities, and result in only evolution under the homonuclear J coupling. A 90° pulse then creates double quantum (DQ) coherence, which then evolves during the period t_1 , this is then converted to observable SQ coherence by the final 90° pulse where for the INADEQUATE experiment the signal is subsequently acquired as an anti-phase lineshape. The difference for the refocused INADEQUATE experiment comes from the fact that after the final 90° pulse, there is an additional $\tau - 180^\circ - \tau$ spin echo period, resulting in purely in-phase signal acquired. DQ coherence is only achievable for coupled spin systems, therefore signal from isolated uncoupled spins are suppressed by the double quantum filter, meaning that any signal observed will only originate from bonded nuclei. DQ coherence in itself isn't directly observable, however due to its evolution during t_1 and subsequent conversion to SQ coherence by the final 90° pulse, indirect observation is achieved.

Both the INADEQUATE and refocused INADEQUATE pulse sequences can be easily modified into 2D experiments upon incrementing the time period t_1 . Signals obtained in the 2D spectra occur in the F_1 (vertical) dimension, known as the double quantum (DQ) dimension, at the sum of the individual chemical shifts of the two coupled nuclei. These 2D maps can provide great insight into bonded networks, particularly when multiple connectivities are present.

The product operator analysis can provide an insightful explanation as to the working of the INADEQUATE and refocused INADEQUATE experiments. Considering a three spin $I = \frac{1}{2}$ homonuclear system, where I and S spins are coupled and R is an isolated spin of the same species, after the application of the first 90° pulse:

$$I_z + S_z + R_z \xrightarrow{(90_x)_{ISR}} -I_y - S_y - R_y \quad (3.31)$$

The spin echo period $\tau/2 - 180^\circ - \tau/2$ can be considered as an evolution due to the homonuclear J for a period of length τ , as the spin echo was shown to refocus the resonance offset, so it does not need to be considered:

$$\xrightarrow{\pi J_{IS}\tau} - (I_y + S_y)\cos(\pi J_{IS}\tau) + (2I_xS_z + 2I_zS_x)\sin(\pi J_{IS}\tau) - R_y. \quad (3.32)$$

The J evolution only affects the I and S terms, as the R spin is not coupled to the other spins. A further 90° pulse is then applied:

$$\xrightarrow{(90_x)_{ISR}} - (I_z + S_z)\cos(\pi J_{IS}\tau) - (2I_xS_y + 2I_yS_x)\sin(\pi J_{IS}\tau) - R_z. \quad (3.33)$$

Here the terms $(2I_xS_y + 2I_yS_x)$ correspond to DQ coherence which then evolve during the short period of t_1 , after which the final 90° pulse converts them back into SQ coherence:

$$\xrightarrow{(90_x)_{ISR}} (I_y + S_y)\cos(\pi J_{IS}\tau) - (2I_xS_z + 2I_zS_x)\sin(\pi J_{IS}\tau) + R_y \quad (3.34)$$

where the SQ coherence $(2I_xS_z + 2I_zS_x)$ results in an anti-phase signal obtained. This is the final step in the INADEQUATE pulse sequence, with R_y and $(I_y + S_y)$ contributions removed by phase cycling the first three pulses by $\phi = 90^\circ$ in a 4 step cycle.

For the refocused INADEQUATE experiment a further spin echo is appended to the end. Only considering the anti-phase terms in Equation 3.34 (as the other terms were removed by phase cycling):

$$\xrightarrow{\pi J_{IS}\tau} - (I_y + S_y)\sin^2(\pi J_{IS}\tau) - (2I_xS_z + 2I_zS_x)\sin(\pi J_{IS}\tau)\cos(\pi J_{IS}\tau). \quad (3.35)$$

Therefore, at the end of the refocused INADEQUATE experiment the first term in Equation 3.35 is the in-phase SQ coherence that is detected. The other term, the SQ anti-phase magnetisation is not observed as it induces no NMR signal. Although this anti-phase term can evolve into *sin* modulated in-phase magnetisation (anti-phase signal) through J modulations during t_2 , leading to lineshape distortions.

Real systems tend to be more complicated than the case described above of only two coupled spins. A more complicated three coupled spin product operator analysis

is given by Cadars *et al.* for the refocused INADEQUATE pulse sequence.[119]

The theoretical product operator treatment of the refocused INADEQUATE experiment shows that signals should only be observed originating from through bond correlations. Although this is true in solution NMR, there are certain cases in the solid state where signals can arise in the refocused INADEQUATE experiment that are not attributed to a through bond coupling, and in fact arise from residual higher order effects from anisotropic interactions, such as CSA and dipolar effects. Duma *et al.* discusses the effect of these residual interactions on the spin echo experiment.[112] Fayon *et al.* use experiment and theory to investigate unexpected additional peaks in the refocused INADEQUATE experiment, showing that for the case of identical chemical shifts, but differing CSA tensors, so called “ $n = 0$ rotational resonance”, where no coupling is present, signals can appear on or close to the $F_1 = 2F_2$ diagonal.[120] It is shown that these peaks occur if the MAS rates are much less than the size of the anisotropies, with their strength increasing with B_0 and decreasing with MAS rate.

3.4.4 Z-filters

Cadars *et al.* have shown that for a multiple coupled spin system that further lineshape distortions can arise in the refocused INADEQUATE experiment.[119] These undesirable distortions originate from ZQ and DQ coherences, created from anti-phase terms evolving into observable anti-phase NMR signal during the detection period, as mentioned previously. Cadars *et al.* have shown how for solids the implementation of a Z-filter at the end of the pulse sequence, that is a series of pulses separated by a short delay between them, combined with appropriate phase cycling, can be effective in removing most of these ZQ and DQ coherences, and consequently most of the lineshape distortions.[119] If the anti-phase term present at the end of the refocused INADEQUATE Equation 3.35 is considered, the product operator analysis of the Z-filter is:

$$2I_xS_z \xrightarrow{(90_x)IS} -2I_xS_y \quad (3.36)$$

If we use the expressions for the multiple quantum coherences:[121]

$$\begin{aligned}
2I_x S_x &= \frac{1}{2}(I^+ S^+ + I^+ S^- + I^- S^+ + I^- S^-) \\
2I_y S_y &= -\frac{1}{2}(I^+ S^+ - I^+ S^- - I^- S^+ + I^- S^-) \\
2I_x S_y &= \frac{1}{2i}(I^+ S^+ - I^+ S^- + I^- S^+ - I^- S^-) \\
2I_y S_x &= \frac{1}{2i}(I^+ S^+ + I^+ S^- - I^- S^+ - I^- S^-).
\end{aligned} \tag{3.37}$$

Equation 3.36 can be written as:

$$-2I_x S_y = \frac{1}{2i}(I^- S^- - I^+ S^+ + I^+ S^- - I^- S^+) \tag{3.38}$$

the phase cycling removes the DQ terms, leaving only the ZQ terms, giving:

$$\xrightarrow{\phi\text{-cycle}} \frac{1}{2i}(I^+ S^- - I^- S^+) = \frac{1}{2}(2I_y S_x - 2I_x S_y). \tag{3.39}$$

After the final 90 pulse:

$$\xrightarrow{(90-x)_{IS}} \frac{1}{2}(2I_x S_z - 2I_z S_x). \tag{3.40}$$

For the magnetisation that originated as in-phase the Z -filter has the effect of:

$$I_y \xrightarrow{(90_x)_{IS}} I_z \xrightarrow{(90-x)_{IS}} I_y \tag{3.41}$$

Therefore, in a successful Z -filter half of the terms (the DQ contribution) are removed, leaving only the ZQ coherences. To successfully remove the ZQ coherences a long enough Z -filter delay is required, through which these coherences dephase. Whereas the in-phase magnetisation that is converted to population states during the Z -filter experiences no dephasing, and thus is unaffected.

3.4.5 REINE

A modification of the conventional refocused INADEQUATE pulse sequence, first proposed by Cadars *et al.*, is the refocused INADEQUATE spin echo (REINE) pulse

sequence.[116] The REINE pulse sequence, shown in Figure 3.4, consists of the conventional refocused INADEQUATE with an additional spin echo appended upon the end, the idea being that the refocused INADEQUATE section provides a 2D map of the connectivities, with an additional J modulation introduced by the additional spin echo. Upon carrying out a series of 2D experiments and by incrementing the duration of the final spin echo period τ_j , values of the J couplings can be extracted from the intensity modulation of each of the peaks in the 2D spectra.

After the refocused INADEQUATE the product operator analysis results in Equation 3.35, upon application of the first Z -filter this becomes:

$$\xrightarrow{ZF_1} Z_1(2I_xS_z + 2I_zS_x)\cos(\pi J_{IS}\tau)\sin(\pi J_{IS}\tau) + (I_y + S_y)\sin^2(\pi J_{IS}\tau) \quad (3.42)$$

where Z_1 represents the efficiency of the Z -filter, with values $0 \leq Z_1 \leq 1$. $Z_1 = 0$ for a perfect Z -filter, and $Z_1 = 1$ for no Z -filter implemented. The evolution under the J coupling for the final REINE spin echo period is:

$$\begin{aligned} \xrightarrow{\pi J_{IS}\tau_j} Z_1[& (2I_xS_z + 2I_zS_x)\cos(\pi J_{IS}\tau)\sin(\pi J_{IS}\tau)\cos(\pi J_{IS}\tau_j) \\ & + (I_y + S_y)\sin(\pi J_{IS}\tau)\cos(\pi J_{IS}\tau)\sin(\pi J_{IS}\tau_j)] \\ & + (I_y + S_y)\sin^2(\pi J_{IS}\tau)\cos(\pi J_{IS}\tau_j) \\ & - (2I_xS_z + 2I_zS_x)\sin^2(\pi J_{IS}\tau)\sin(\pi J_{IS}\tau_j) \end{aligned} \quad (3.43)$$

Finally a further Z -filter is applied at the end of the pulse sequence:

$$\begin{aligned} \xrightarrow{ZF_2} Z_1Z_2(& 2I_xS_z + 2I_zS_x)\cos(\pi J_{IS}\tau)\sin(\pi J_{IS}\tau)\cos(\pi J_{IS}\tau_j) \\ & + Z_1(I_y + S_y)\sin(\pi J_{IS}\tau)\cos(\pi J_{IS}\tau)\sin(\pi J_{IS}\tau_j) \\ & + (I_y + S_y)\sin^2(\pi J_{IS}\tau)\cos(\pi J_{IS}\tau_j) \\ & - Z_2(2I_xS_z + 2I_zS_x)\sin^2(\pi J_{IS}\tau)\sin(\pi J_{IS}\tau_j) \end{aligned} \quad (3.44)$$

where again Z_2 represents the efficiency, this time of the second Z -filter. If two perfect Z -filters are implemented then the signal at the end of the REINE pulse sequence

should correspond to:

$$(I_y + S_y)\sin^2(\pi J_{IS}\tau)\cos(\pi J_{IS}\tau_j) \quad (3.45)$$

where an in-phase signal is acquired, modulated by the $\cos(\pi J_{IS}\tau_j)$ term. Comparing this result to that from the ordinary homonuclear spin echo, it can be seen that spin echo like behaviour is observed during the REINE experiment, however it is combined with the 2D separation of peaks as found in the refocused INADEQUATE experiment.

The REINE experiment has been applied to slightly disordered systems of ^{13}C in cellulose and ^{31}P in bis-phosphino amine sample by Cadars *et al.*[116] Guerry *et al.* showed its implementation on a disordered phosphate glass for the first time, enabling further insight to be extracted from these broad and usually featureless lineshapes.[122] It was shown that the advantage of the REINE experiment over the conventional spin echo on these glasses lies in the fact that the broad lines often are composed of many different connectivities, therefore upon measuring the J coupling using a spin echo the values obtained would be an averaged coupling value for each 1D peak, whereas in the REINE experiment, due to the separation of these usually overlapping peaks in the second (F_1) dimension, upon looking at each of these peaks separately, distinct values of the J couplings could be determined for each different connectivity. [122]

Guerry *et al.* showed a pixel by pixel fitting analysis, where a separate spin echo fit was carried out for each individual pixel across the REINE peaks, successfully providing a map of the J couplings across each of the peaks.[122] This enabled greater insight into the disorder within the glass network. Furthermore, unlike in the refocused INADEQUATE experiment, where correlation peaks may occur not arising from through bond correlations, Guerry *et al.* found no dependence or change in results obtained upon modelling the REINE data to take into account for a zero frequency term. Therefore all correlations should arise from through bond correlations, demonstrating the power of this technique.[122]

3.4.6 J -HMQC

A further NMR pulse sequence for investigation of correlations through J couplings is the J -HMQC experiment. Initially designed for solution state NMR by Bax *et al.*

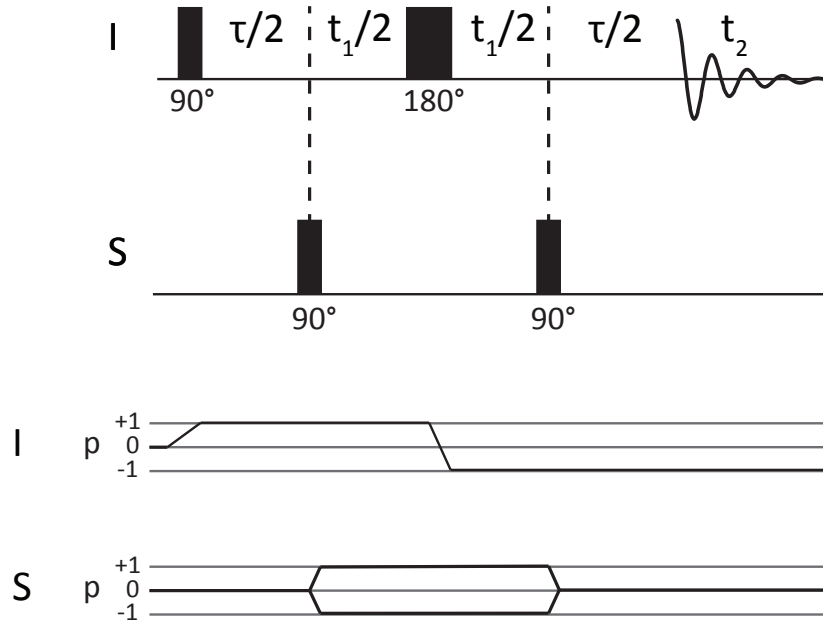


Figure 3.5: Pulse sequence diagram for a J -HMQC experiment.[124] The pulses applied to the two spin systems are shown one above the other. Detection occurs on the I spin, which consists of effectively a spin echo. Two 90° degree pulses on the S spin effectively flank the 180° pulse of the I spin echo, with the delay between these 90° pulses and the 180° pulse on the I spin incremented to create the second time dimension. Signals are only retained from heteronuclear J couplings, giving insight into the bonded network.

[123], its first implementation on solid state systems was carried out by Lesage *et al.* looking at the spin $I = \frac{1}{2}$ pair of ^{13}C and ^1H . [124] Unlike the refocused INADEQUATE experiment, rather than focusing on homonuclear couplings, the J -HMQC experiment exploits heteronuclear couplings, providing a 2D map of heteronuclear through bond connectivities. The pulse sequence is shown in Figure 3.5, consisting of two channels, one for spin I and one for spin S . Again the product operator analysis is useful for providing insight into the inner workings of the sequence. Considering the I spin, the sequence is effectively a spin echo, thus evolution under the resonance offset of spin I is refocused and can be safely neglected during this product operator approach. After the first $\tau/2$ delay the state of the system is due to $-I_y$ evolving under the heteronuclear coupling:

$$-I_y \cos(\pi J_{IS}\tau) + 2I_x S_z \sin(\pi J_{IS}\tau) \quad (3.46)$$

if the $\tau/2$ delay is selected so that $\tau = \frac{1}{2J_{IS}}$ then only the anti-phase term remains. Upon application of the 90° pulse on the S spin:

$$2I_xS_z \xrightarrow{(90_x)_S} -2I_xS_y. \quad (3.47)$$

Therefore, a mixture of heteronuclear multinuclear quantum coherences are created, which now can evolve during t_1 under the resonance offset of spin S :

$$\xrightarrow{\Omega_S t_1} -2I_xS_y \cos(\Omega_S t_1) + 2I_xS_x \sin(\Omega_S t_1) \quad (3.48)$$

The second 90° pulse on the S spin converts these multiple quantum coherences back into observable single quantum coherences:

$$\xrightarrow{(90_x)_S} -2I_xS_z \cos(\Omega_S t_1) + 2I_xS_x \sin(\Omega_S t_1), \quad (3.49)$$

where the second term still remains as multiple quantum coherence, and so remains unobservable and is ignored. The other term evolves during the final $\tau/2$ period under the J coupling from anti-phase to in-phase signal:

$$\xrightarrow{\pi J_{IS} \tau} -I_y \cos(\Omega_S t_1), \quad (3.50)$$

thus an in-phase doublet is obtained, centred on the offset of I . Phase cycling ensures that only the desired DQ coherences are present during t_1 , leading to signals from uncoupled nuclei to be suppressed.

In solids broad lines usually prevent the observation and resolution of the doublet splitting. However, in-phase signals are observed from the J -HMQC in the presence of a J coupling, giving clear indication on the connectivities present, even for broad solid lineshapes.

Although the analysis shown above was for a coupled heteronuclear spin $I = \frac{1}{2}$ pair, the J -HMQC experiment is also suitable for observing J correlations in systems involving quadrupole nuclei, with Massiot *et al.* looking at ^{27}Al - ^{31}P , and Iuga *et al.* even looking at the two quadrupole nuclei pair of ^{17}O and ^{27}Al . [125, 126] However, the limitation remains that the evolution time required to observe signal is inversely

proportional to the strength of the J coupling, and with couplings typically being very small, long evolution times are often necessary. Thus long enough coherence lifetimes (T_2') are ultimately required to ensure the signal survives.

3.4.7 MQMAS

As was discussed in Section 2.4.2 MAS is effective at removing first order effects due to anisotropic interactions, however for the quadrupole interaction due to its generally larger nature there is often need to consider second order contributions. The complex angular dependence of this second order contribution means that these anisotropic component are not fully removed under MAS alone. The multiple quantum experiment combined with magic angle spinning (MQMAS) was first proposed by Frydman and Harwood in 1995, showing that line narrowing of the central transition (CT) can be obtained under MAS by exploiting high coherence orders, correlating evolution under MQ coherences to that of SQ coherences, thus retaining isotropic information whilst refocusing the anisotropic contribution.[51] Equation 2.144 shows the frequency shift due to the second order quadrupole interaction under MAS between the transitions of m and $m - 1$. The angular dependant term in Equation 2.144 is known as the 4th order legendre polynomial and is the origin of the anisotropic broadening remaining under MAS. (Coefficients representing this term are given in for different spins (I) in Table A.1 located in the Appendix). Frydman and Harwood identified that the coefficients of the isotropic and anisotropic shifts differ between single and multiple quantum coherences. Therefore allowing SQ and MQ evolution to occur for a period equal to the ratio between multiple quantum and single quantum coherence, so called the MQMAS ratio, results in a refocusing of the anisotropic effects. For the case of 3Q coherence this ratio is given by:

$$k = \frac{C_4(I, 3/2)}{C_4(I, 1/2)} \quad (3.51)$$

where C_4 is the coefficient for the 4th order legendre polynomial.

Due to the popularity of the MQMAS technique there have been many studies, and hence many modifications to the pulse sequence from the one originally proposed by Frydman and Harwood. However, all MQMAS experiments follow the same basic

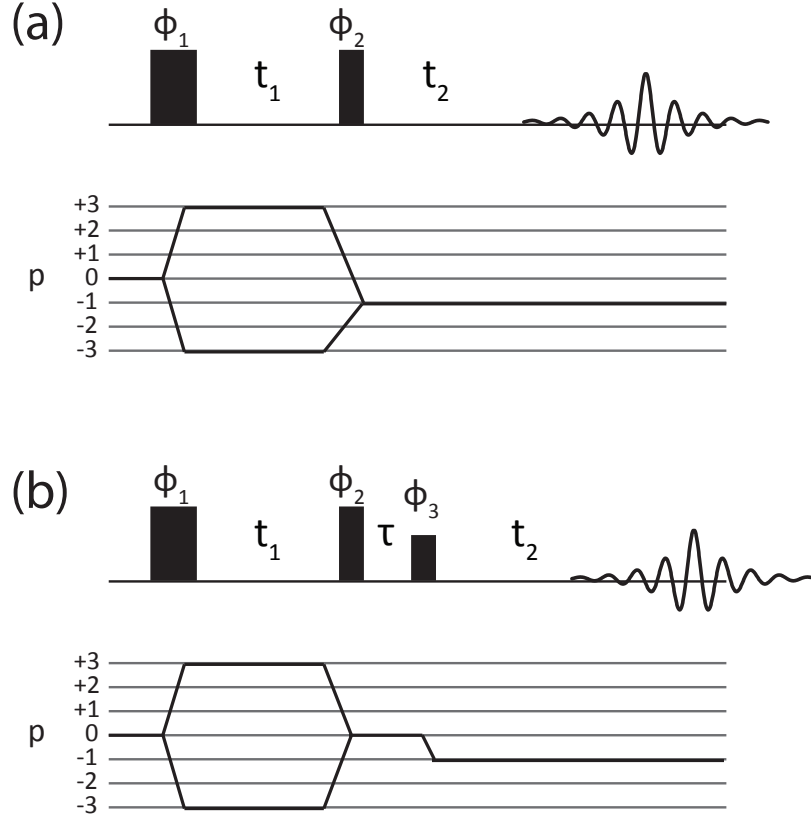


Figure 3.6: Pulse sequence diagram of amplitude modulated MQMAS experiments. (a) Two pulse MQMAS, consisting of ϕ_1 pulse creating 3Q coherence, which then evolves during t_1 period. ϕ_2 pulse then converts this 3Q coherence to SQ coherence, with an echo forming after t_2 , when the signal is then acquired. (b) Amplitude modulated Z-filtered MQMAS, where the difference is that the second pulse ϕ_2 , now converts the magnetisation to the $p = 0$ level for a period τ , before the final pulse ϕ_3 converts the signal to observable SQ coherence.

principles. Initially an rf pulse is applied to create the MQ coherences, which are then allowed to evolve during a period t_1 . The MQ coherences are then reconverted into observable SQ coherences by a further rf pulse, with the magnetisation then detected during the period t_2 . In principle, the multiple quantum coherences evolving during t_1 can be one of many, as selected by the user, for instance 3Q, 5Q 7Q, with the appropriate coherence order obtained by phase cycling. The inefficiency of rf pulses to excite only the desired coherence order, resulting in magnetisation being lost upon phase cycling away unwanted coherences, demonstrates one of the key problems in the MQMAS experiment; efficiency.[127, 128] Although it has been shown that some improvements in resolution may be obtained by looking at higher order coherences, the most commonly observed coherence order remains 3Q due to it being more efficient to

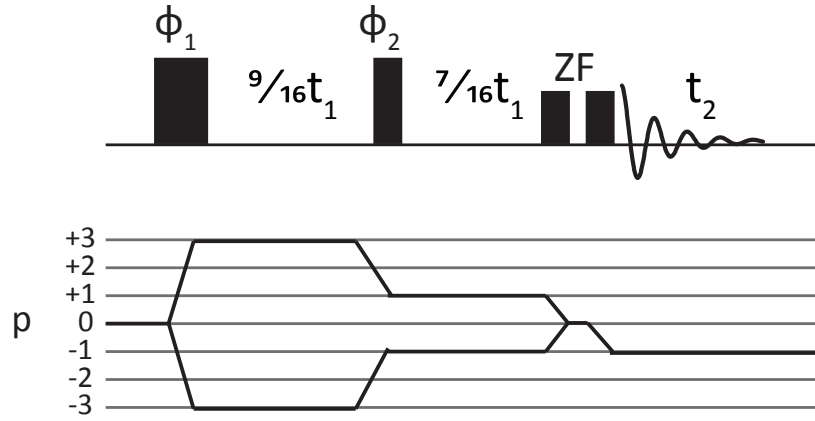


Figure 3.7: Amplitude modulated Split t_1 MQMAS pulse sequence and coherence pathway, for a $I = \frac{3}{2}$ nucleus, with Z -filter (ZF). The evolution period is split between SQ and 3Q evolution according to the MQMAS ratio.

generate, and therefore generally resulting in much better signal to noise.

Both amplitude and phase modulated MQMAS sequences have been shown in the literature, with the phase modulation coming from a single pathway, with a π refocusing pulse at the end of the sequence necessary to acquire a whole echo during t_2 , and after a Fourier transform a purely in-phase absorptive lineshape is observed.[129, 130] Amplitude modulated experiments allow the acquisition of both echo and anti echo pathways, as shown in Figure 3.6, thus combination of both pathways and Fourier transformation results in a largely absorptive lineshapes, with only slight dispersions arising from the not completely symmetric combination of the two pathways.[131] However, the effect of residual dispersive components were shown to be successfully removed by the implementation of a Z -filter by Amoureux *et al.*. During the Z -filters short delay τ , the magnetisation is stored along B_0 ($p = 0$), which is then converted into observable SQ magnetisation through the use of a final soft “selective” pulse.[132] The advantage of the Z -filter approach being that both echo and anti-echo pathways are symmetric, as can be seen from the coherence pathways in Figure 3.6, thus resulting in purely absorptive 2D spectra obtained.

MQMAS spectra display resonances with the inhomogeneous quadrupole broadening spread out along a ridge at a gradient corresponding to the MQMAS ratio, $-7/9$ for $I = 3/2$, and $19/12$ for $I = 5/2$ (for a 3QMAS experiment). Therefore, a shearing transformation is usually applied resulting in the anisotropic axis being parallel to F_2 and creating an isotropic F_1 dimension (F_{iso}). An alternative method, the “split t_1 ”,

removes this need for shearing by fully refocusing the anisotropic broadening during t_1 , by allowing SQ and TQ coherence to evolve during the t_1 period, see Figure 3.7. A review and comparison of the many MQMAS methods is given in the work by Brown and Wimperis.[133]

It is important to note that there are different conventions used when referencing the chemical shift axis of the F_1 dimension in the MQMAS experiment, after shearing. This is best discussed by Pike *et al.* with the two main methods outlined, with further discussions of the other axis conventions in the review by Milliot and Man.[128, 134] The main two conventions in use for scaling of the chemical shift are; the convention shown by Wimperis and co-workers,[135, 136] and the convention established by Amoureux and co-workers.[127]

In the Wimperis convention, the frequency difference between two points is divided by the Larmor frequency to obtain the chemical shift difference between the two points:

$$\delta(ppm) = \frac{\Delta\nu \times 10^6}{\nu_0}. \quad (3.52)$$

In the Amoureux convention this is then further scaled by the chemical shift scaling factor $x_{cs}(I, P)$ by:

$$\delta(ppm) = \frac{\Delta\nu \times 10^6}{x_{cs}(I, P)\nu_0}. \quad (3.53)$$

where $x_{cs}(I, P)$ is defined by:

$$x_{cs}(I, P) = \frac{k - p}{1 + k} \quad (3.54)$$

where p is the coherence order for the MQMAS and k is the MQMAS ratio given in Equation 3.51 (and Table A.1 in the Appendix A).

The difference in the two methods means that the chemical shift observed in the Amoureux convention is independent of the coherence order p . Therefore, carrying out a 5QMAS experiment or a 3QMAS experiment on the same sample, would result in the same chemical shift difference between two peaks, independent of the experimental method, due to the $x_{cs}(I, P)$ factor. Whereas in the Wimperis convention, the chemical shift will be different between two peaks for a 5QMAS or a 3QMAS experiment, for instance. Throughout this thesis the Amoureux convention will be implemented, with all MQMAS experiments being of $p = 3$ coherence order.

Care has to be taken with MQMAS experimental results due to the use of

multiple quantum coherences. As previously mentioned excitation of these coherences isn't quantitative, and can depend upon the strength of the C_Q for a particular site. However, the usefulness lies in the separation of resonances into a second dimension free from anisotropic quadrupole broadening, where it is possible to extract useful information on the number of sites and corresponding shifts. This information, which may not be possible to obtain via other methods, can be combined with ordinary MAS spectra and used to constrain fitting to obtain reasonably reliable NMR parameters.

Although useful the MQMAS experiment is not the only way to obtain line-shapes free from second order quadrupole broadening, however its convenience lies in the fact that it is accessible using conventional NMR equipment. Double Rotation (DOR) whereby a rotor is orientated at an angle within a second outer rotor, both of which spinning at specific angles to successfully satisfy the orientational dependence of the interaction, can also be used to removed anisotropy.[46–48] As can Dynamic Angle Spinning (DAS) whereby the sample is rotated sequentially at two different axis during different periods.[49, 50] However both of these methods require additional hardware and are much more experimentally challenging.

The satellite transition magic-angle spinning (STMAS) experiment is an alternative experimental method that doesn't require additional hardware, unlike DOR and DAS. Similar to the MQMAS experiment STMAS utilises refocusing of coherences, due to switching between coherences during the experiment. However, in the STMAS experiment rather than selecting multiple-quantum coherence, coherences associated with single-quantum satellite transitions are selected. This requires very accurate setting of the magic angle, which can result in long set up times, however spectra free from the broadening from the residual second order quadrupole interaction can be achieved upon its successful implementation.

3.5 Signal to Noise

A typical NMR experiment consists of repeatedly adding a series of free induction decays (FIDs), obtained upon carrying out the same experiment a number of times. The main reason for this approach is in order to obtain signal that is well distinguished from the random noise that may also be detected leading to poor quality spectra. The

signal to noise ratio is given by:

$$S/N \propto \sqrt{n}, \quad (3.55)$$

where n represents the number of distinct FIDs collected. Thereby, upon increasing the number of FIDs accumulated the noise increases, albeit at a smaller rate than the signal, resulting in a signal with sufficiently diminished noise after sufficient acquisitions.

3.6 Relaxation

During the NMR experiment the nuclear spin system will return to its equilibrium state, the process by which it does so is known as relaxation. There are two main important types of relaxation that play a role in the NMR experiment. Spin lattice, or sometimes called longitudinal relaxation (T_1), is the time it takes the magnetisation to return to its equilibrium position, in the case of the NMR experiment along the B_0 bulk magnetisation axis. The T_1 value, which can vary significantly from μs to hours or even days, needs to be taken into consideration by the spectroscopist, as it defines how often the NMR experiment can be repeated between acquiring successive FIDs, in order to ensure saturation does not occur.

The other important relaxation process is the spin-spin, or transverse (T_2) relaxation, which is the loss of the coherence of the magnetisation in the xy plane. This defines how long a period the NMR signal can be acquired for, as a loss of coherence means a loss of signal observed in the FID.

Many different interactions play a part in relaxation processes, although as a general rule the larger the interaction the more efficient the relaxation. Therefore, for a quadrupole broadened system the quadrupole interaction is usually the most dominant cause of relaxation. Relaxation can however give insightful information on the dynamics of the system under investigation, with a more thorough description given in the work of Slichter. [106]

3.7 Simulation Details

Throughout this thesis a number of software simulation packages have been used in order to extract meaningful information from the NMR lineshapes obtained. This

predominately involves extracting NMR interaction parameters, providing insight into the local environment of the nuclei under observation.

3.7.1 DMFit

DMFit is a software package developed by Massiot [152] for simulating solid state NMR lineshapes. Its capabilities includes simulating a wide range of NMR lineshapes, for instance taking into account quadrupole and CSA broadening, under both static and MAS conditions, in addition to simple ‘Gaussian/Lorentzian’ lineshapes.

The DMFit package has been used throughout this thesis for simulating lineshapes of $I = \frac{1}{2}$ nuclei under MAS, using the ‘Gaussian/Lorentzian’ function, whereby a ‘Gaussian/Lorentzian’ broadened lineshape is centred around an isotropic chemical shift. As these nuclei experience no quadrupole broadening effects and the anisotropic broadening is removed by MAS, this fitting method is suitable to extract details of chemical shifts, and the intensity that each lineshape contributes to the overall spectrum.

The program iteratively attempts to minimise differences between the experimental data and the simulation, using simple quadratic difference between the datasets. It provides reliable fitting parameters, however the user has to specify the exact number of lineshapes to simulate.

3.7.2 Quadfit

A significant proportion of this thesis has focused on looking at disordered systems, the NMR lineshapes of which, do not show well resolved distinct resonances. The observed lineshapes are broadened, comprising of an overlap of many resonances, due to a range of local environments such as different bond angles and bond distances. For the spin $I = \frac{1}{2}$ this is easily represented by broadening of the ‘Gaussian/Lorentzian’ fitting function in DMFit. However, for $I > \frac{1}{2}$ nuclei, due to the quadrupole broadening the lineshape will depend upon a larger set of parameters.

In the case of a quadrupole nuclei under MAS, it is desirable to extract the quadrupole parameters from the residual second order quadrupole broadening present within the NMR lineshape to obtain structural information. However, due to the disordered nature a distribution of these quadrupole parameters will be present. The

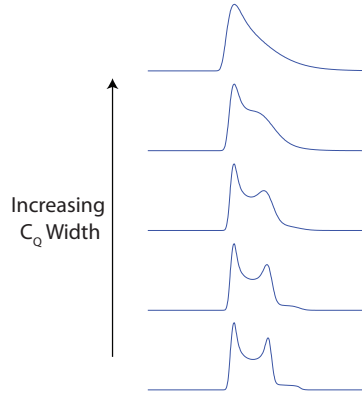


Figure 3.8: The effect on the Quadfit lineshape upon changing the C_Q width parameter for a second order quadrupole broadened lineshape under MAS. Upon increasing the C_Q width, indicative of an increase in disorder, the distinct second order lineshape is lost, resulting in a broadened tail. Lineshapes simulated at a Larmor frequency of 156 MHz for a spin $I = \frac{5}{2}$. Based on Figure 3 from [153]

Quadfit package is successful in handling these disorders.[153] This is achieved by fitting a resonance using multiple quadrupole lineshapes, all possessing slightly different NMR parameters. This is done using a Gaussian distribution of the lineshapes resulting in additional C_Q and η_Q width parameters, indicative of the distribution of quadrupole lineshapes, in addition to the C_Q and η_Q centre parameters, representing the average values.

Figure 3.8 shows how the C_Q width parameter affects the lineshape observed. When a small distribution is present, the C_Q width is low, and the line shows a typical second order quadrupole lineshape. Upon an increase in the distribution, the distinct features broaden out, resulting in a tail forming as evidenced towards the top of Fig 3.8. This is a typical lineshape observed for quadrupole lineshapes within a disordered structure, such as a glass.

There are inherent disadvantages in the Quadfit package in that perfect pulses and detection are assumed along with infinite spinning speeds. Nevertheless, by fitting data over multiple fields, and by constraining the field independent parameters, such as the quadrupole parameters, reliable values can be determined.

Throughout this thesis upon simulating the quadrupole lineshapes of the disordered systems the value of η_Q has been set to a nominal value, with the simulation focused on determining the C_Q parameter. In reality there will additionally be a range of η_Q values present, however owing to the large number of independent parameters it

was deemed that the C_Q parameter provided the greatest influence on the disordered lineshapes, and thus, more insight into the nuclear structure.

Chapter 4

Aluminium Doped Phosphate Bioactive Glasses

4.1 Introduction

Biodegradable materials or ‘biomaterials’ have generated a large research field in recent years with the ultimate goal of producing materials that can stimulate tissue or bone regrowth as they break down or demonstrate resorbable characteristics *in situ* as this healing process ensues. Commercially available Bioglass[®] is one such material, with the characteristic 45S5 composition, typically consisting of 45 mol% silica with Ca and a small amount of P. However the dissolution rate of this material can be long, up to years, and the long term reaction to silica is unknown.[72] Owing to chemical compositions more closely related to that of bone, Ca phosphate glasses show great potential for use as bone scaffolds rather than the traditionally used silica Bioglass[®]. [71, 137] Phosphate glasses have much higher dissolution rates due to the unstable nature of the phosphate network, and control of the dissolution rate can be maintained by varying the modifier oxide composition of these glasses. Many studies have been reported looking at the structure of bioactive glasses containing CaO, P₂O₅, and Na₂O, with neutron diffraction, and solid state NMR being the most widely used structural probes.[61, 73, 78, 79] The additional incorporation of oxides containing different cations has been investigated, such as TiO₂, Ga₂O₃, and Al₂O₃, in order to obtain greater control of the degradation rate of the glasses and also to fulfil specific roles such as drug delivery.[74, 76, 138] Specifically, the addition of Al to the glass net-

work has been shown to further increase the stability of the network leading to more favourable dissolution rates.[75]

Comprehensive reviews of the structure of simple phosphate glasses have been presented elsewhere, most notably by Brow and Hoppe.[63, 64] The generally accepted model consists of a network of phosphorus tetrahedra with three of the oxygens within the tetrahedra having the possibility of bonding covalently to other phosphorus tetrahedra, these are termed bridging oxygens (BO), with the fourth bonding by a double bond, with an enhanced π bond character, resulting in a terminal oxygen (TO). The tetrahedra are best described using the Q^n terminology, where n represents the number of bridging oxygens (BO) present within each tetrahedra. With the incorporation of modifier cations, such as Na^+ and Ca^{2+} , to the network, the bridging bonds are removed, resulting in a depolymerisation of the phosphate network thus producing non-bridging oxygens (NBO). The role that Al plays within the glass structure is a complicated one in that it is known to act as a network modifier removing BO. However, at certain concentrations, it is also known to play the role of a network intermediate, strengthening the network, leading to a decrease in glass dissolution rates.

Due to the disordered nature of glass structures, arising from the random incorporation of modifier cations into the network, solid state NMR has demonstrated itself to be a vital tool in the structural analysis of glassy materials, because of the ability of NMR to probe the local atomic environment, without the need for long-range periodic order. Advances in solid state NMR techniques have led to the development and implementation of numerous experiments for disordered materials, enabling a wealth of structural information to be determined. [139–146]

The use of two-dimensional (2D) correlation experiments that probe through bond connectivities within materials are one specific approach, notably the refocused INADEQUATE experiment.[114, 115, 119, 120, 147–149] Moreover, the development of the refocused INADEQUATE spin echo (REINE) experiment shows much promise for providing valuable structural information in disordered systems.[116] The REINE experiment combines the 2D separation of peaks due to different connectivities found in the refocused INADEQUATE experiment, with the additional modulation of the signal of each peak dependent upon the J couplings that is active during the final spin echo period. Guerry *et al.* recently applied the REINE experiment for the first time to

a glass, namely a cadmium containing phosphate glass, enabling correlations between J couplings and chemical shifts to be determined, resulting in better understanding of the phosphate chains present within the glass structure.[122]

In this chapter the application of a multinuclear ^{23}Na , ^{27}Al and ^{31}P solid state NMR investigation is presented, notably employing 2D ^{31}P REINE experiments, to a series of glasses with the nominal stoichiometry $x(\text{Al}_2\text{O}_3) (11-x)(\text{Na}_2\text{O}) 44.5(\text{CaO}) 44.5(\text{P}_2\text{O}_5)$ (with $x = 0, 3, 5, 8$). These glasses were recently the subject of an analysis by neutron diffraction and solid state ^{27}Al MAS NMR by Smith *et al.* where it was observed by neutron diffraction a change in Al species occurs with increasing Al_2O_3 content.[79] This was further confirmed by the ^{27}Al NMR showing a tendency for octahedral Al at low concentration and a subsequent change to tetrahedral Al at higher Al_2O_3 concentrations. The aim of this work is to provide further insight into these glass structures, in particular utilising complementary solid state NMR techniques to gain additional information of the environments of the other ions within the glass network.

4.2 Experimental Details

Phosphate glasses investigated are of the same composition as reported by Smith *et al.*, see Table 4.1, synthesized by identical methods.[79] All glasses were produced as glass rods and ground to a fine powder under an inert nitrogen atmosphere before packing into NMR rotors in the same atmosphere to ensure no uptake of water.

Single pulse ^{27}Al MAS NMR were performed at 14.1 T and 9.4 T, using Bruker Avance II-600 and Bruker DSX-400 spectrometers, which operated at the ^{27}Al Larmor frequencies of 156.18 MHz and 103.92 MHz, respectively. These measurements utilised Bruker 3.2 mm HX probes which enabled MAS frequencies of 20 kHz. Flip angle calibration was performed on a 1.1 M $\text{Al}(\text{NO}_3)_3$ solution from which a ‘non-selective’ (solution) $\pi/2$ pulse time of 19.8 μs was measured. This corresponds to a ‘selective’ (solid) pulse time of 6.6 μs for the $I = 5/2$ ^{27}Al nucleus. All measurements were undertaken with a $\pi/12$ tip angle (‘selective’) of 1.1 μs to ensure quantitative estimates of the complete Al speciation present. All ^{27}Al center of gravity (apparent) shifts were reported against the IUPAC recommended primary reference of $\text{Al}(\text{NO}_3)_3$ (in D_2O 1.1 M, δ 0.0 ppm) via a solid yttrium aluminium garnet (YAG) secondary reference in

	Mol % Al_2O_3	Mol % Na_2O	Mol % CaO	Mol % P_2O_5
0Al 11Na	0	11	44.5	44.5
3Al 8Na	3	8	44.5	44.5
5Al 6Na	5	6	44.5	44.5
8Al 3Na	8	3	44.5	44.5

Table 4.1: Compositions of glasses under investigation, with varying Al and Na content.

which the six coordinate resonance is established δ 0.7 ppm.[101, 150]

Single pulse ^{23}Na MAS NMR were performed at 14.1 T and 9.4 T using Bruker Avance II-600 and Bruker DSX-400 spectrometers, which operated at the ^{23}Na Larmor frequencies of 158.55 MHz and 105.49 MHz, respectively. These measurements utilised Bruker 3.2 mm HX probe which enabled MAS frequencies of 20 kHz at 9.4 T, and a Bruker 4.0 mm HX probe which enabled MAS frequencies of 12.5 kHz at 14.1 T. Flip angle calibration was performed on a NaCl solution from which a ‘non-selective’ (solution) $\pi/2$ pulse time of 6 μs was measured. This corresponds to a ‘selective’ (solid) pulse time of 3 μs for the $I = 3/2$ ^{23}Na nucleus. All measurements were undertaken with a $\pi/4$ tip angle (‘selective’) of 1.5 μs to ensure accurate estimates of the quadrupole parameters. All ^{23}Na center of gravity (apparent) shifts were reported against the IUPAC recommended primary reference of NaCl solution (in D_2O 0.1 M, δ 0.0 ppm) via a solid secondary NaCl reference of known isotropic chemical shift of δ 7.2 ppm.[150, 151] A common relaxation time of 5 s was deemed to be sufficient for all ^{23}Na and ^{27}Al measurements.

All ^{31}P experiments were carried out at 7.05 T, using a Varian/Chemagnetics Infinity Plus-300 spectrometer operating at a Larmor frequency of 121.48 MHz, and employed a Bruker 4 mm HX probe which enabled MAS frequencies of 12.5 kHz. A recycle delay of 15 s was used. These data were referenced to a secondary reference of ammonium dihydrogen phosphate ($\text{NH}_4\text{H}_2\text{PO}_4$, ADP) at δ 1.0 ppm, with respect to the primary IUPAC reference of 85 % H_3PO_4 .[101, 150] For the single pulse experiments, a tip angle of $\pi/4$ of 2.5 μs was implemented to achieve quantitative estimates of the P sites present. ^{31}P REINE experiments were carried out using the pulse sequence

as described by Guerry *et al.* (see Figure 3.4 in Chapter 3 for the pulse sequence diagram).[122] Using a 32 step phase cycle, a total of 256 transients were co-added for 22 t_1 increments, with the States procedure implemented to ensure sign discrimination in F_1 . [110] The spectral width was synchronised to the rotor spinning speed in both dimensions. Between 12 and 14 REINE experiments were carried out with varying $\tau_j/2$ values for each glass composition. With the build up $\tau/2$ delay of 6.8 ms kept fixed throughout. Processing of the REINE data was carried out using MATLAB.

Spectra fitting was performed using the DmFit software for ^{31}P one-pulse experiments, and the Quadfit software for ^{23}Na and ^{27}Al one-pulse experiments.[152, 153]

4.3 Results

4.3.1 ^{27}Al MAS NMR

Figure 4.1 shows ^{27}Al single pulse MAS-NMR spectra for each of the Al containing glasses, obtained at two different fields in order to obtain quantitative estimates of the quantity of each species present. Due to the incomplete removal of the second order quadrupole interaction by MAS, the line shapes are broadened showing asymmetrical resonances typical for Al in disordered environments. It can be seen that three resonances are clearly resolved assigned to 4, 5 and 6 coordinated Al, with chemical shifts becoming more negative with increasing coordination number.[60, 154] However, for the 8Al3Na glass, it is clear that there is an additional narrow resonance found in the 4-coordinate region that is attributed to crystallization occurring within the glass at this high Al composition.

The variation in Al speciation upon increasing Al content within the glass structure is also shown in Figure 4.1 with simulation parameters in Table 4.2. It can be seen that, upon initial incorporation of small amounts of Al into the structure, the Al is forming mostly an octahedral co-ordination, as widely reported in studies on other aluminophosphate glass series. [60, 75, 143, 154, 155] However, upon further increase of the Al content in the glass, it can be seen that the proportion of AlO_6 decreases at the expense of the formation of AlO_4 tetrahedral linkages. The density change can be seen to be following the same trend as previously determined by Manupriya *et al.* in that initial incorporation of Al into the glass leads to an increase in density, which

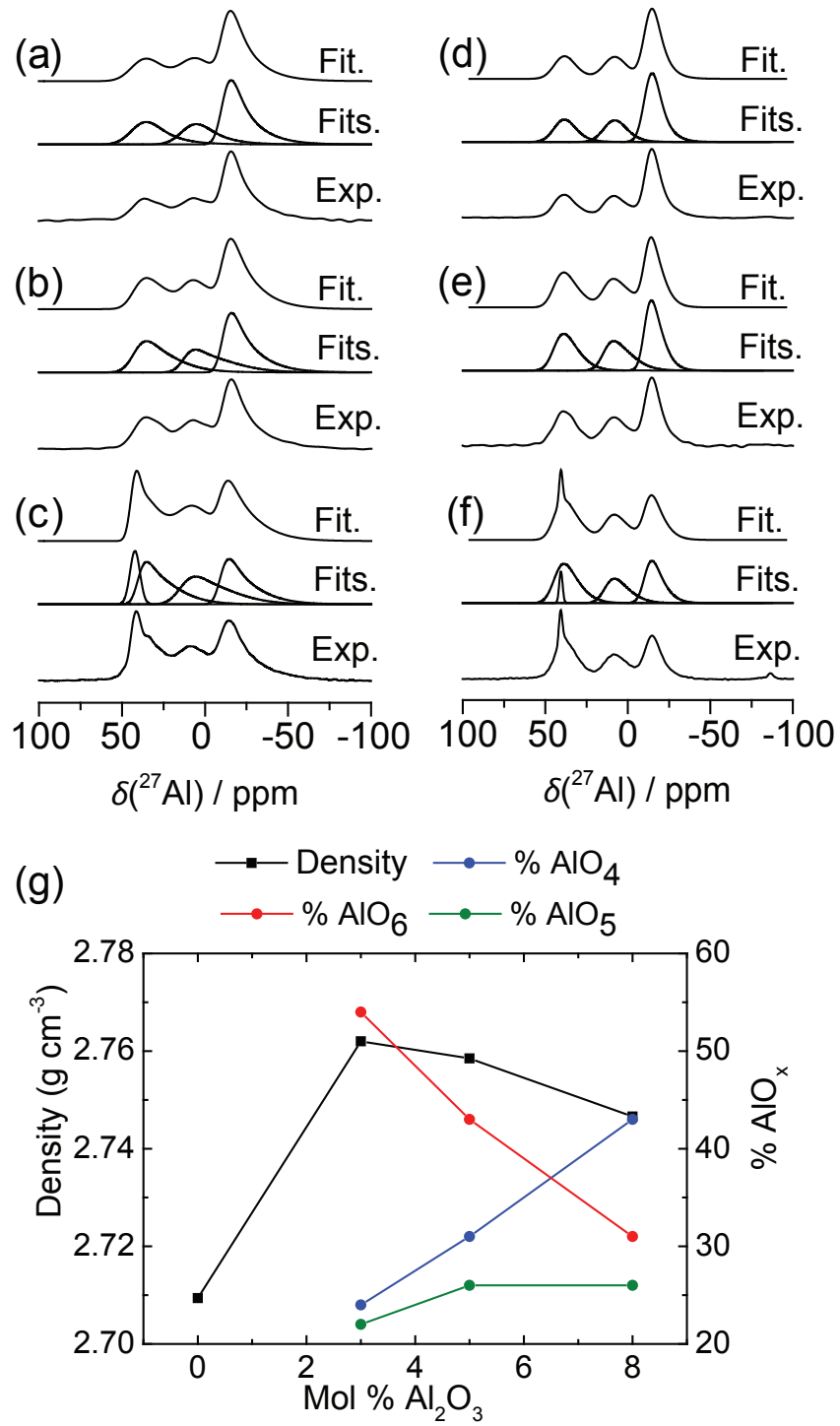


Figure 4.1: Top: ^{27}Al single pulse MAS-NMR spectra and simulated fits at 9.4 T (a)-(c), and 14.1 T (d)-(f), for glasses; 3Al8Na (a) and (d). 5Al6Na (b) and (e). 8Al3Na (c) and (f). Bottom: (g) The change in Al coordination and also the change in the density with increasing incorporation of Al_2O_3 content

Peak	$\delta(\text{ppm})$ (± 0.1)	C_Q Center (MHz) (± 0.5)	C_Q Width (MHz) (± 0.6)	η (± 0.05)	Int (%) (± 3)	Environment
8Al3Na						
1	41.5	0.7	0.1	0.1	9	Impurity
2	44.8	5.8	3.0	0.1	34	AlO ₄
3	17.3	6.4	3.0	0.1	26	AlO ₅
4	-8.2	5.3	3.3	0.1	31	AlO ₆
5Al6Na						
1	46.0	5.9	3.0	0.1	31	AlO ₄
2	17.3	6.8	3.0	0.1	26	AlO ₅
3	-9.2	5.1	3.3	0.1	43	AlO ₆
3Al8Na						
1	42.6	4.3	4.1	0.1	24	AlO ₄
2	12.2	4.3	4.1	0.1	24	AlO ₅
3	-10.5	4.5	4.1	0.1	54	AlO ₆

Table 4.2: ^{27}Al NMR parameters from simulation of single pulse NMR spectra. Parameters constrained from multiple field fitting, using Quadfit software package. [153]

would be expected due to Na_2O being less dense than Al_2O_3 . [75] However, as shown in Manupriya’s study there is a decrease in the density upon further Al incorporation, with the density following a similar trend to the amount of Al occupying octahedral sites; this phenomenon has also been discussed by Smith *et al.* [79]

4.3.2 ^{23}Na MAS NMR

The ^{23}Na MAS NMR data from these glasses exhibit broad and featureless lineshapes owing to a range of chemical shifts and quadrupole coupling constant (C_Q) values, resulting from the distribution of sites occupied by the Na cations (Figure 4.2). The ^{23}Na spectrum for the 8Al3Na glass, like the corresponding ^{27}Al data of the same sample, shows an additional unexpected narrow resonance due to the presence of a crystalline phase occurring for this composition. The simulation of the ^{23}Na single pulse spectra using the Quadfit software package enables details concerning the environments of the Na sites to be explicitly determined. [153] Figure 4.2 shows the change in the ^{23}Na chemical shift, mean quadrupolar coupling constant (C_Q) and quadrupolar coupling width (C_Q width that corresponds to the full-width at half-maximum height of the Gaussian distribution), for each glass composition extracted from these fits. It is observed that the C_Q width is particularly large in comparison to the mean C_Q value, with C_Q widths

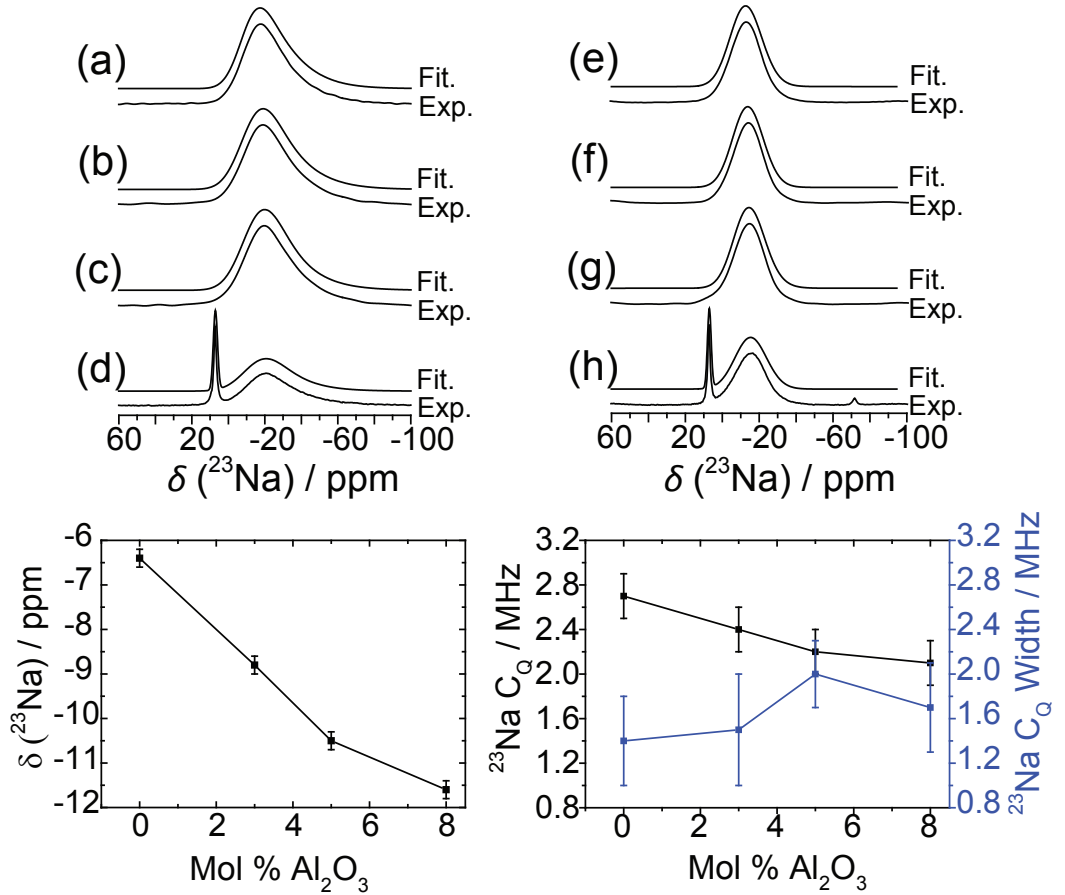


Figure 4.2: Top: ^{23}Na single pulse NMR spectra and simulated fits at 9.4 T (20 kHz MAS) (a)-(d), and 14.1 T (12.5 kHz MAS) (e)-(h), for glasses; 0Al11Na (a) and (e). 3Al18Na (b) and (f). 5Al6Na (c) and (g). 8Al3Na (d) and (h). Bottom: ^{23}Na change in chemical shift (left) and quadrupole parameters (right) with increasing incorporation of Al_2O_3 content. Fitting parameters are shown in the Appendix A.

ranging from 50 % up to 90 % of the total C_Q , thus emphasising the disorder of the environments occupied by the Na cations. As expected, the same trend is observed for the fits of the ^{27}Al spectra (see Table 4.2).

The presentation of data at the bottom of Figure 4.2, demonstrates that upon increasing incorporation of Al_2O_3 into the glass structure, a downfield shift of the ^{23}Na resonance to more negative ppm occurs with a concomitant decrease in the mean C_Q . This has been observed previously in other Na containing glass systems in the work by Brow *et al.*[59]

4.3.3 ^{31}P 1D MAS NMR

^{31}P MAS NMR spectroscopy has proved to be a powerful tool for glass characterization

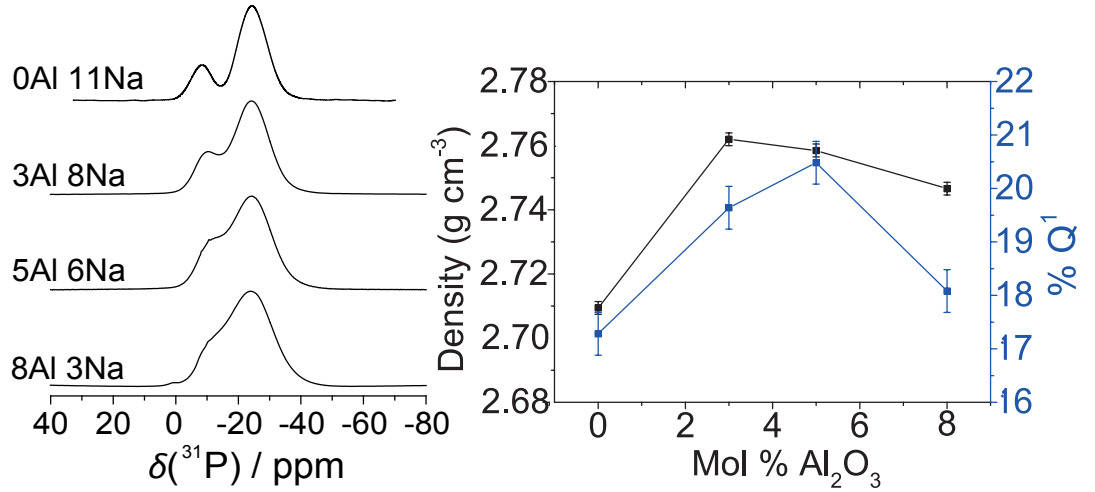


Figure 4.3: Left: ^{31}P one-pulse MAS NMR spectra for each glass composition at 7.05 T and 12.5 kHz MAS. Right: Change in the relative Q^1 species proportion and density with increasing incorporation of Al content within the glass. Fitting parameters are shown in the Appendix A.

owing to the ^{31}P isotropic chemical shift being strongly dependent on the nearest neighbour coordination, thus leading to a quantitative determination of the proportions of Q^n species present. Glasses with a phosphate composition of 45 mol % are typically expected to contain both Q^2 and Q^1 units, as evidenced by the ^{31}P spectra for each of the glasses in this series, see Figure 4.3.[64] For the 0Al11Na glass, it can be seen that the ^{31}P resonances are well resolved for both Q^1 and Q^2 sites; however, upon the incorporation of Al into the glass structure, it can be seen that the Q^1 resonance shifts to more negative ppm and broadens resulting in a significant overlap of these resonances. This phenomenon becomes more apparent as the Al content of the glass increases.

Figure 4.3 shows how the proportion of Q^1 species changes upon the increase in Al_2O_3 incorporation. It can be seen that this is following a similar trend to the density, and thus the proportion of AlO_6 , in that there is an initial increase in the amount of Q^1 with initial incorporation of Al. This is however, like the density, followed by a decrease for higher Al concentrations.

4.3.4 2D ^{31}P REINE MAS NMR

The REINE experiment previously presented by Cadars *et al.* and Guerry *et al.* is an extension of the commonly used refocused INADEQUATE experiment.[115, 116, 122] In the refocused INADEQUATE experiment, a double-quantum (DQ) filter selects

only spins with a J coupling to another spin. Therefore, a 2D map of connectivities results whereby a signal from two bonded nuclei appears, at the chemical shift of the nuclei being directly observed in the single-quantum (SQ) F_2 (horizontal) dimension, at a DQ frequency in the F_1 (vertical) dimension corresponding to the sum of the SQ chemical shifts of the two bonded nuclei. The modification applied in the REINE experiment entails the further addition of a spin echo appended to the end of the refocused INADEQUATE experiment. The length of this final spin echo can then be varied in a series of 2D experiments resulting in a modulation of each of the 2D peaks that is dependent on the J coupling between the two connected nuclei. By fitting this modulation, the J coupling(s) can then be extracted for the summed intensity of each 2D peak or for individual pixels within each 2D peak.

^{31}P REINE measurements have been undertaken on each of the glasses in this series. Maximum signal intensity is observed for each of the REINE peaks for all glasses for the shortest employed final spin echo evolution duration of 0.8 ms. These 2D ^{31}P REINE spectra are shown for each of the glasses in Figure 4.4, with connectivities between structural moieties corresponding to Q^1 - Q^1 , Q^1 - Q^2 , Q^2 - Q^1 and Q^2 - Q^2 clearly present in the data for the 0Al11Na glass presented in Figure 4.4. However, as observed in the one-pulse spectra, a broadening and overlap of resonances is occurring with increasing Al content, resulting in uncertainty in the determination of distinct positions for each of the 2D REINE peaks; e.g., deciding where the Q^1 - Q^1 resonance ends and the Q^1 - Q^2 resonance begins becomes increasingly difficult for the glasses with higher Al_2O_3 content.

The modulation of the signal in the REINE experiment due to the final spin echo period ($\tau_j/2 - \pi - \tau_j/2$) is that of a damped cosine function, whose form varies depending on the number of phosphate units, that the nucleus corresponding to the SQ resonance is coupled to. For the peak occurring in the F_2 dimension at the chemical shift of the Q^1 species, the function

$$I(\tau_j) = I_0 \cos(\pi J \tau_j) e^{-\tau_j/T_2'} \quad (4.1)$$

is used because of the dependence on only one J coupling, since the Q^1 unit is coupled to only one other phosphate unit. T_2' is the spin echo dephasing time.[115] For the peak

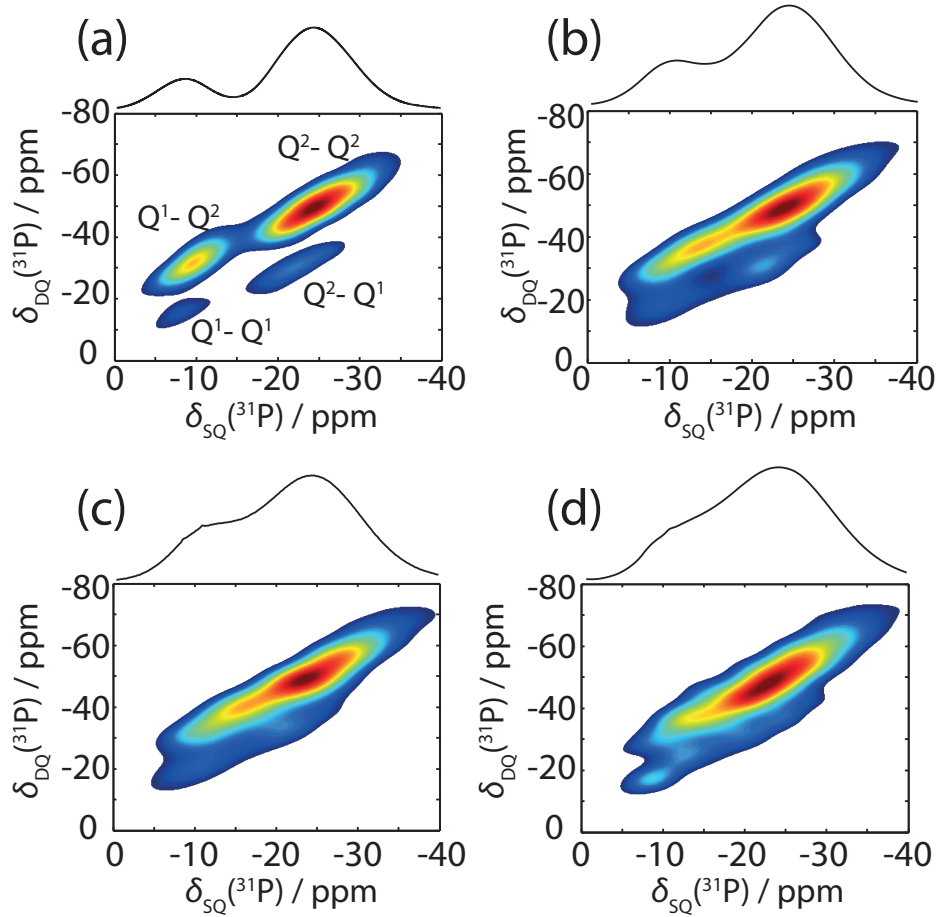


Figure 4.4: ^{31}P REINE spectra (7.05 T with 12.5 kHz MAS) at $\tau_j = 0.8$ ms for each glass composition, (a) 0Al11Na, (b) 3Al8Na, (c) 5Al6Na, (d) 8Al3Na, showing the maximum signal intensity for each REINE peak.

in the F_2 dimension at the chemical shift of the Q^2 species, the fitting function can either be:

$$I(\tau_j) = I_0 \cos(\pi J_1 \tau_j) \cos(\pi J_2 \tau_j) e^{-\tau_j/T_2'} \quad (4.2)$$

which is appropriate where the J coupling between the two bonded P units is different. Alternatively:

$$I(\tau_j) = I_0 \cos^2(\pi J \tau_j) e^{-\tau_j/T_2'} \quad (4.3)$$

becomes a more appropriate function where the two J couplings are identical or almost identical (In such cases, fitting using Equation 4.2 becomes unstable due to the interchange of the two J coupling values upon fitting).

Time-domain spin echo curves due to the modulation of the summed intensity

of the Q^1 - Q^1 and Q^1 - Q^2 REINE peaks are shown in Figure 4.5. The peaks show well defined zero crossings enabling a good fit to be obtained to Equation 4.1, aiding in accurate determination of the mean J couplings. The advantage of the REINE experiment over the ordinary spin echo experiment is the ability to distinguish between the ${}^2J_{Q^1Q^1}$ and ${}^2J_{Q^1Q^2}$ couplings that cannot be achieved using a conventional spin echo experiment. By contrast, the REINE experiment enables separate values to be extracted, due to the 2D resolution in a refocused INADEQUATE spectrum of distinct Q^1 - Q^2 and Q^1 - Q^1 peaks that appear at different DQ frequencies. From Equation 4.1, it can be seen that the first zero crossing occurs at $\tau_j/2 = J/4$. In Figure 4.5, the position of this zero crossing for the 0Al11Na glass is shown as a vertical dashed line for both the Q^1 - Q^2 and Q^1 - Q^1 peaks. Firstly, it is important to notice that the zero crossing for the Q^1 - Q^1 peak occurs at a significantly later time than that of the Q^1 - Q^2 peak. This indicates a larger J coupling arising for the Q^1 - Q^2 peak (${}^2J_{Q^1Q^2}$) than for the Q^1 - Q^1 peak (${}^2J_{Q^1Q^1}$). This can be seen from the bottom of Figure 4.5 (and the Table A.4 in the Appendix A), where the fitted J coupling of 11.9 ± 0.7 Hz for ${}^2J_{Q^1Q^1}$ is smaller than that for ${}^2J_{Q^1Q^2}$ of 16.8 ± 0.3 Hz. Upon following the dotted lines down, with an increase in the Al content in the glass, it can be seen that the zero crossing moves to a longer $\tau_j/2$ time. Specifically, considering the plots at the bottom of Figure 4.5, where the change in J coupling for both peaks are presented as a function of increasing Al_2O_3 content in the glass: a marked decrease is observed in both ${}^2J_{Q^1Q^2}$ from 16.8 ± 0.3 Hz to 13.1 ± 0.6 Hz, and ${}^2J_{Q^1Q^1}$ from 11.9 ± 0.7 Hz to 10.6 ± 0.7 Hz.

Another very useful feature of the REINE experiment is the ability to map out distributions of J couplings throughout each of the 2D REINE peaks for a disordered glass.[122] This is of particular interest due to the disordered nature of the P environments within the glass structure, due to the range of bond angles, bond distances, and next nearest neighbour coordinations that are present. Figure 4.6 (a)-(d) shows the ${}^{31}\text{P}$ REINE signal of the Q^1 - Q^2 peak at $\tau_j/2 = 18$ ms, normalized with respect to the corresponding maximum signal intensity at $\tau_j/2 = 0.8$ ms. It can be seen from these spectral regions that different parts of the peaks are clearly showing varying modulations. In particular, owing to this evolution time being close to the zero crossing for the 5Al6Na and 8Al3Na glasses, regions exhibiting notably both positive and negative modulation are present within the peak. This marked difference in spin echo modula-

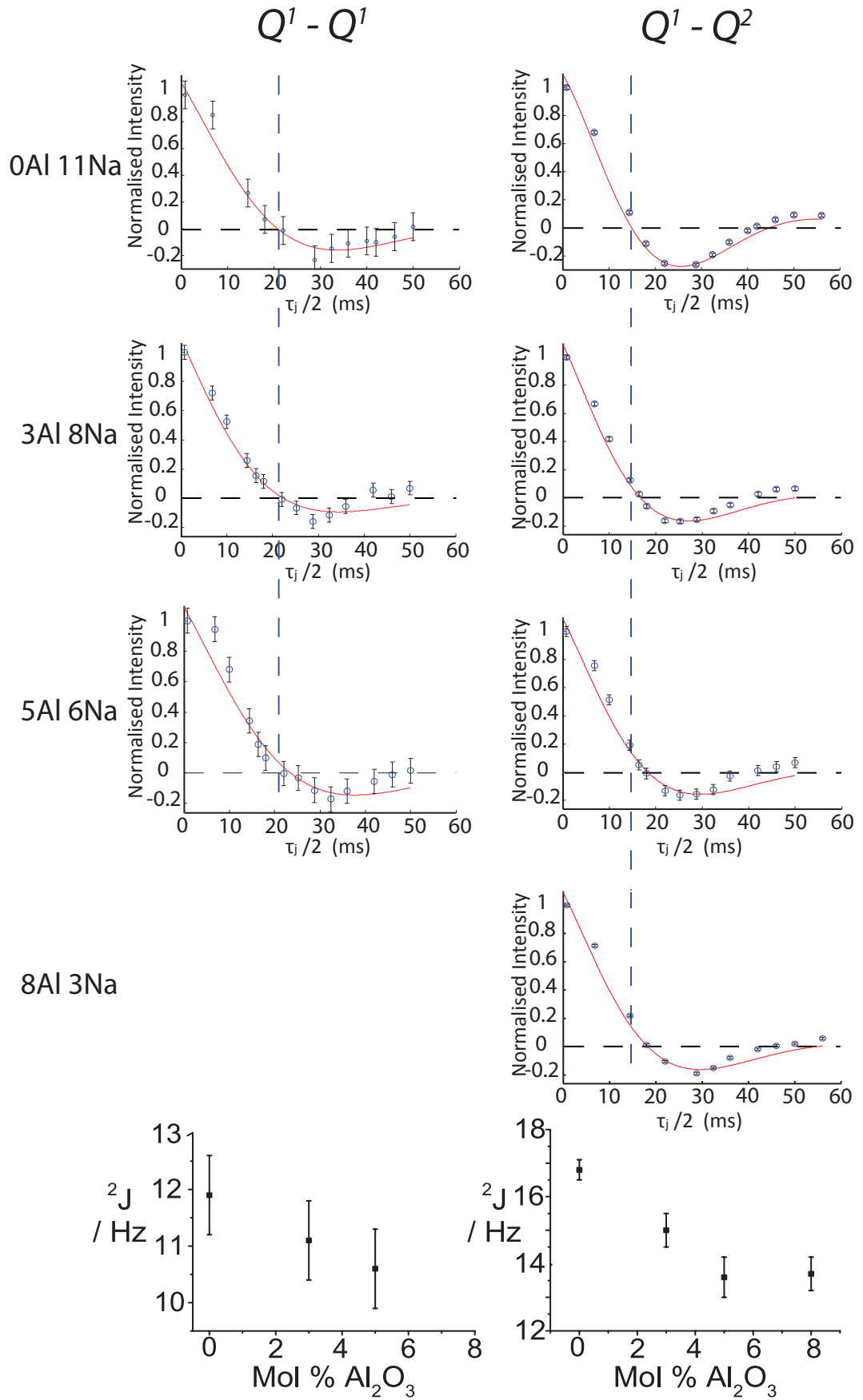


Figure 4.5: Time-domain spin echo curves obtained from the summed intensity for the Q^1-Q^1 (left) and Q^1-Q^2 (right) ^{31}P REINE peaks for each glass composition. Solid lines are fits to Equation 4.1, (fit parameters and correlation coefficients are shown in Table A.4 in the Appendix A). Bottom graphs show the change in the J coupling with increasing Al_2O_3 content for the Q^1-Q^1 (left) and Q^1-Q^2 (right) peaks, showing an overall decrease in the J couplings with increasing Al_2O_3 content.

tion is indicative of a difference in the J coupling across the peak, as is shown in Figure 4.6 (e)-(h), where a pixel by pixel fitting has been carried out for each of these regions, with regions that cross zero earlier displaying larger J couplings, as expected for the damped cosine modulation. The J coupling variations across each of the Q^1 - Q^2 peaks are significant, with a change from 17.8 ± 0.4 Hz to 16.2 ± 0.3 Hz for the 0Al11Na glass, and an even more significant change for the 8Al3Na glass of 17.4 ± 0.3 Hz to 10.5 ± 0.7 Hz.

From Figure 4.6, it can be seen that the variation in the J coupling for the Al containing glasses, (f)-(h), is in the direction of the F_2 (horizontal) dimension, corresponding to a correlation of the J coupling value with the chemical shift of the P unit being directly observed, as found previously from spin echo experiments.[148] However the converse is found for the glass with no Al content, Figure 4.6(e), in that a F_1 (vertical) variation is now present, corresponding to the J coupling being correlated with the chemical shift of the coupled nucleus. This F_1 (vertical) variation was also found in the REINE analysis of the 0.575CdO-0.425P₂O₅ glass by Guerry *et al.*[122]

4.4 Discussion

From the NMR results it is clear that the incorporation of Al into this Ca phosphate glass series is having a marked effect on the structure. Arguably the most important change is that of the Al coordination. The reason for the change from octahedral to tetrahedral Al coordination has been previously discussed by Brow *et al.*, where AlO₄ is forming in order to maintain charge balance within the network, due to AlO₄ units having more electrons to donate than the AlO₆ units, for glasses with a higher $|O|/|P|$ ratio.[60] As previously stated, AlO₅ units are also present within the glass, however with a proportion that is somewhat lower than that of the other two species, this proportion of AlO₅ units is not changing significantly throughout the series.

A change in the glass structure is also indicated by the ²³Na NMR spectra, with a decrease of the C_Q and a shift to more negative ppm being observed, upon increasing Al content. This is indicative of the Na sites becoming more shielded and more symmetrical as more Al enters the glass structure. A shift to more negative ppm is also found in the ³¹P NMR spectra for the Q^1 resonance along with a subsequent

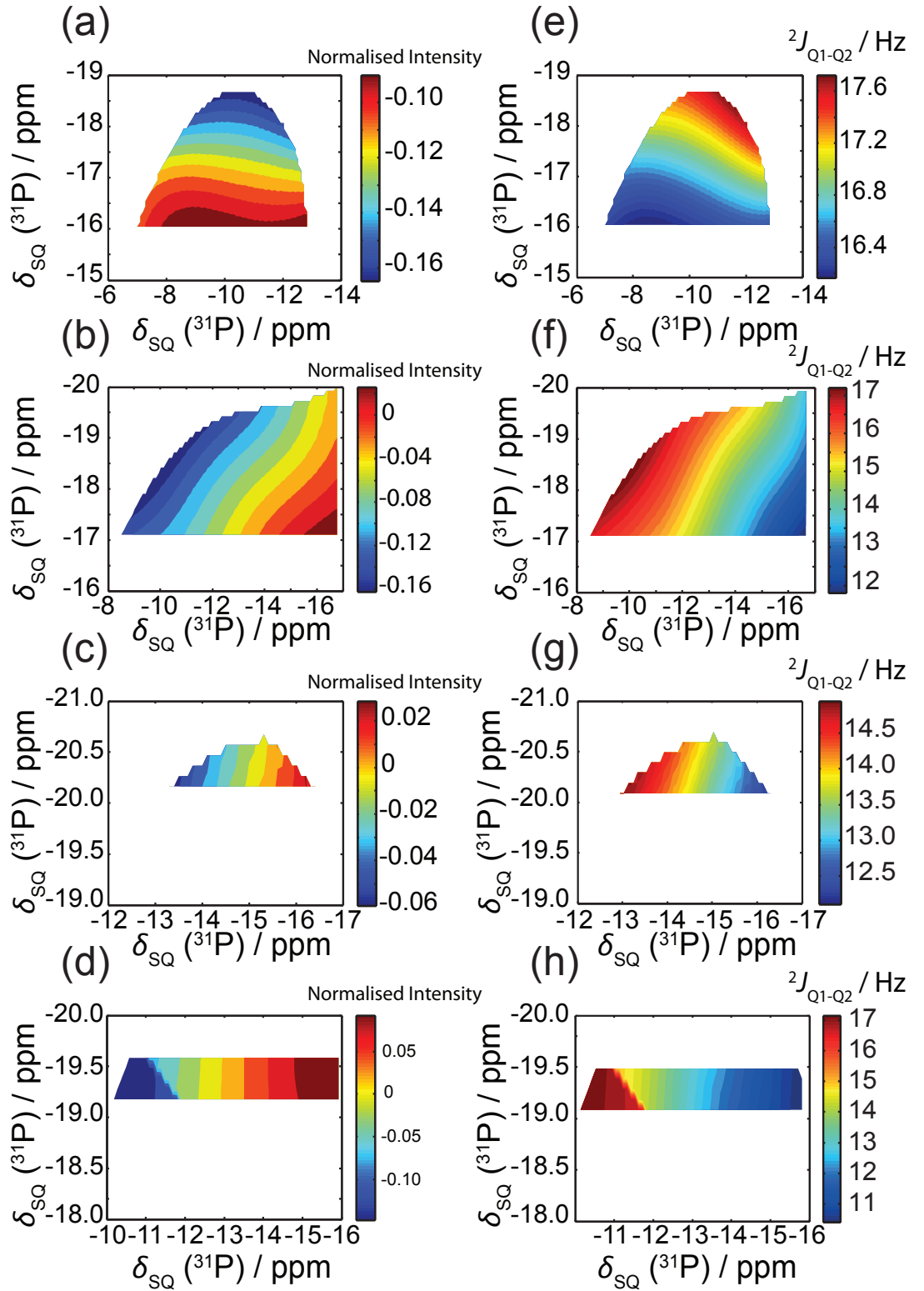


Figure 4.6: ^{31}P Q^1 - Q^2 REINE peak (7.05 T with 12.5 kHz MAS) (a)-(d) intensity at $\tau_j/2 = 18$ ms normalised to regions for which the intensity at $\tau_j/2 = 0.8$ ms exceeds 66% of the maximum signal intensity. (e)-(h) Pixel by Pixel spin echo fitting of the same area showing distribution of J couplings. (a) and (e) 0Al11Na glass. (b) and (f) 3Al8Na glass. (c) and (g) 5Al6Na glass. (d) and (h) 8Al3Na glass.

broadening. This can be envisaged to be due to an increase in the relative proportion of AlO_4 units at higher Al content, probably due to the formation of Al-O-P tetrahedral linkages, thus leading to the shift of the Q^1 peak to more negative ppm, because an Al as a next nearest neighbour causes a more shielded P environment, as compared to if the next nearest neighbour was a modifier Na or Ca cation. This gives rise to an apparent broadening of the P Q^1 resonance due to there being a greater number of possible P sites, owing to Al now taking part in the network bonding, in addition to the Na and Ca ions that are the only cations present in the 0Al11Na glass. This has been shown previously by ^{27}Al - ^{31}P CP MAS studies on Al phosphate glasses.[143, 155]

This initial increase in the amount of Q^1 upon the incorporation of Al into the network indicates that the AlO_6 present within these glasses is most likely removing P-O-P linkages, thus resulting in a large number of Q^1 units due to the large number of bonds available for the AlO_6 moiety. However, it should also be noted that the relative proportion of Q^1 units for the glass with the highest Al content, where most of the Al is in tetrahedral coordination, is of a similar scale to the glass containing only Na, and no Al. This implies that the AlO_4 units are removing P-O-P linkages in favour of forming P-O-Al tetrahedral clusters, however due to the enhanced covalent nature this does not completely reduce the connectivity of the network.

As previously mentioned the dependence of the REINE signal modulation of the peaks occurring at the Q^2 frequency in the F_2 dimension can follow two different functions, (Equation 4.2 and 4.3), depending on the connectivity of the P network. For the Q^2 - Q^2 peak, the summed intensity spin echo fits are shown in Figure 4.7 for each of the glasses studied (fitting parameters are shown in Table A.5 in the Appendix A). The glass with no Al in the structure (Figure 4.7(a)), and the glass with the least Al in the structure (3Al8Na) (Figure 4.7(b)), show REINE modulations that only give reliable fits to the \cos^2 fitting function, Equation 4.3. This implies that the J couplings of the two bonded units are approximately identical in size, owing to long chains or rings being predominant within the phosphate Q^2 network. However as previously noted, the J coupling for these glasses are slightly larger than those found for the glasses with higher Al content. Coupled with the fact that there is a clear proportion of Q^1 - Q^2 units present within the glasses (evidenced by the presence of Q^1 - Q^2 and Q^2 - Q^1 peaks), it is safe to conclude that long chains rather than rings make up the largest contribution to

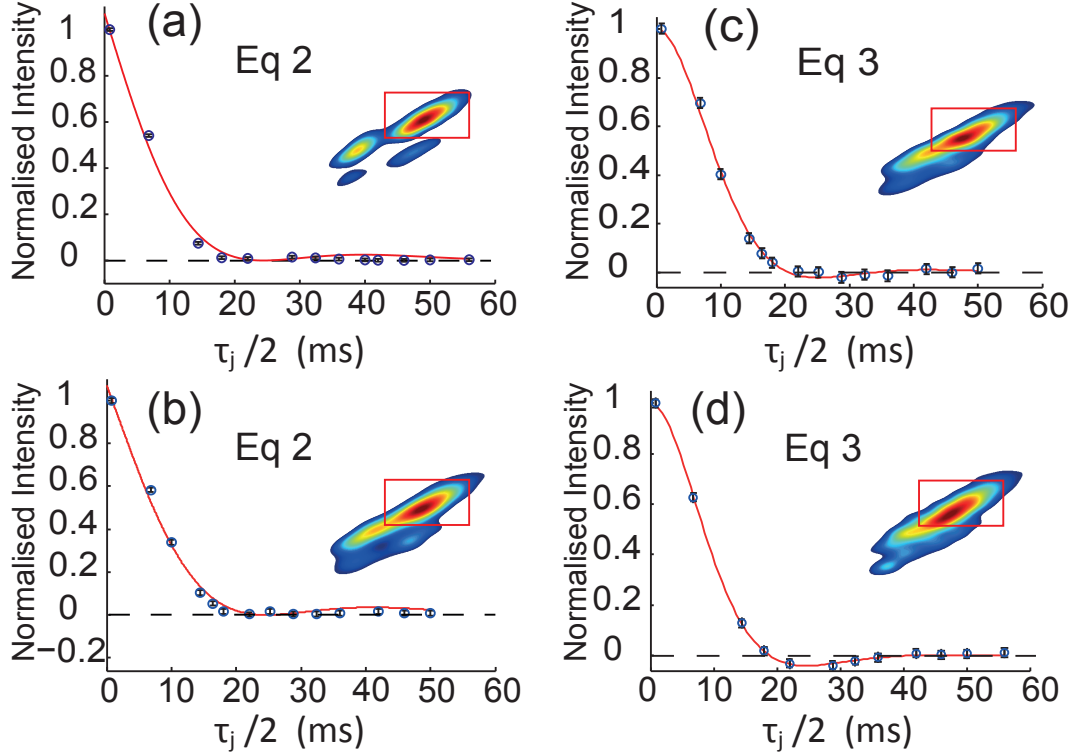


Figure 4.7: Time domain spin echo curves obtained from the summed intensity of the ^{31}P Q^2 - Q^2 REINE peaks (7.05 T with 12.5 kHz MAS) for each glass composition. Fit carried out using Equation 4.2, for (a) 0Al11Na glass and (b) 3Al8Na glass. Fit carried out using Equation 4.3, for (a) 5Al6Na glass and (b) 8Al3Na glass. Parameters and correlation coefficients shown in Table A.5 in the Appendix A.

the network. For the glasses with the higher Al concentrations (5Al6Na and 8Al3Na), the fitting function that gave the most accurate fits was that of $\cos(\pi J_1 \tau_j) \cos(\pi J_2 \tau_j)$, Equation 4.3, where the two J couplings are significantly different. This implies that tetraphosphate chains (Q^1 - Q^2 - Q^2 - Q^1) are now predominant within the glass structure, as opposed to the longer chains found for the other two glasses. This apparent decrease in chain length only implies that P-O-P bonds are being removed. However, it does not account for the formation of P-O-Al bonds, so as to form Al- Q^1 - Q^2 - Q^2 - Q^1 tetrahedral linkages, which could explain this observation.

From previous studies, $^2J_{\text{Si-O-Si}}$, $^2J_{\text{B-O-B}}$ and $^2J_{\text{P-O-P}}$ DFT calculations, have all shown a clear decrease in the J coupling with decreasing bond angle and, consequently, bond distance.[156–159] Therefore, upon incorporation of Al_2O_3 into the glass structure, it is safe to assume that the decrease in J coupling is indicating a decrease in the P-O-P bond angle and P-P distance, signifying that the P network is becoming more condensed and less linear. This assertion is in agreement with the results

from the ^{23}Na MAS NMR data in that, upon increasing the Al_2O_3 content within the glasses, the Na environment is becoming more shielded, probably due to this decrease in linearity of the P network, with the Na becoming trapped inside the phosphate network. Another point to note is that the Al is taking up more AlO_4 coordination with higher Al incorporation in the glasses, thus the Al tetrahedral linkages are probably forming between the P tetrahedra resulting in strong P-O-Al cross linkages, and thus a more condensed network. These conclusions are in agreement with the work by Manupriya *et al.* who found that the bioactivity of glasses with $>5\text{mol}\%$ Al_2O_3 is greatly reduced, probably emanating from the increased strength of the Al-O-P linkages and a more condensed network at higher Al incorporation, resulting in the much longer dissolution times.[75]

4.5 Summary and Conclusion

Overall, it has been shown that addition of Al into Ca phosphate glass formulations in favour of Na can drastically change the glass structure. With small amounts of Al incorporated the changes are relatively minor, with the AlO_6 that is formed playing the role of a network modifier, in a similar fashion to the Na cation. However, further incorporation of Al into the network results in the formation of strong tetrahedral AlO_4 linkages, thus producing a more condensed and cross-linked glass structure. Although the aim of Al incorporation into these materials is to improve the glass stability, it appears that the incorporation of too much Al can have an adverse effect on its bioactive properties, as shown by Manupriya *et al.* who found that above 5 mol% Al_2O_3 the bioactivity of the glass is affected.[75] This is indicating that the ideal glass composition may be somewhere in the intermediate regime, where the Al is stabilising the network to a certain degree with some strong tetrahedral linkages, however the presence of AlO_6 is still a sizeable contribution to the structure making the glass easier to decompose. Due to their potential use as biomaterials, determining the structure of Ca phosphate glasses is an important goal, with NMR being the ideal tool for the materials scientist. Whilst much structural information can be obtained from a simple single pulse MAS experiment, it has been shown that the REINE experiment offers great promise in providing further insight into the bonding arrangements of the PO_4 network.

Chapter 5

Gallium Doped Phosphate Bioactive Glasses

5.1 Introduction

Over the last 50 to 60 years antibiotics have been vital in improving public health, through tackling bacteria related diseases. [160] However, overuse of antibiotics is leading to an added problem, with an increased likelihood for resistant bacteria strains to multiply, thus rendering some antibiotics useless in their fight against disease. Even though this threat is imminent the amount of new antibiotics in their final stages of development remains small, and few novel methods for tackling bacteria are forthcoming. [161] One potential method of alternative treatment could nevertheless rely on exploiting the antibacterial properties that certain cations have been found to possess. Studies have shown that Cu, Ag, and Ga ions are all effective in reducing the presence of bacteria, utilising a completely original method to that of antibiotic drugs.[76, 162–170] Beneficial effects of Ga^{3+} are already recognised, with Ga^{3+} already used in the treatment of certain medical conditions. For instance, Ga^{3+} can prevent bone resorption thus could help to treat osteoporosis, and Ga^{3+} has already been approved by the US agency Food and Drug Administration (FDA) for the care of Hypercalcaemia associated with bone tumour metastases.[168, 171] Studies have shown Ga^{3+} to inhibit the growth of bacteria *Rhodococcus equi*,[166] *Pseudomonas aeruginosa*, [76, 167] and *M. tuberculosis*[163] to name but a few, which has been attributed to the Ga^{3+} disrupting the Fe^{3+} metabolism in these micro-organisms. Fe^{3+} is an essential part of bacteria

metabolism, and the similar ionic radii of Ga^{3+} to Fe^{3+} enables Ga^{3+} to prevent the metabolism by a ‘Trojan Horse’ type mechanism, owing to the fact the Ga^{3+} does not undergo redox reactions, unlike Fe^{3+} which is critical for bacterial growth.[163, 167, 171]

The most promising method of delivery of antibacterial ions remains in the form of incorporating the cation into a host material that can be implanted into the body, thus releasing the ions over time. Most appealing among these delivery devices remains the use of bioactive glass type materials, owing to their ability to incorporate a wide range of cations, and the subsequent ability to tailor the degradation rate as required, steadily releasing the antibacterial cation in-situ over a suitable time period.[172] A few studies have been carried out on Ga doped phosphate bioactive glasses, owing to the similar composition of calcium phosphate materials to that of bone, and their ability to form a bioactive interface.[76, 168] The usually fast dissolution rates of phosphate based bioactive glasses, can actually be controlled and strengthened by the incorporation of Ga into the network, thus aiding with the controlled delivery of the antibacterial Ga^{3+} ions.[76, 168, 173]

As important as understanding their bioactivity a knowledge of the structure of bioactive glasses is vital in order to appreciate how best to tailor them to suit specific needs. Numerous studies using various structural characterisation techniques have been carried out, with solid state NMR showing great promise, owing to the lack of long range order in these disordered systems, which is perfectly handled by the atomic specificity of NMR.[73, 78, 79, 138, 169, 173, 174] Most studies have concentrated on the spin $1/2$ ^{31}P nuclei, which gives information on the Q^n species present, or the quadrupole ^{23}Na nuclei which can give some insight on the local Na environment. Ga has two NMR active isotopes ^{71}Ga and ^{69}Ga , both are spin $I = 3/2$ so experience broadening due to the quadrupole interaction. Both isotopes have different quadrupole moments, with both being significantly large, however ^{71}Ga is the smaller of the two and despite its less abundant nature (39.6 % compared to 60.4 % for ^{69}Ga) it is more appealing to NMR spectroscopists. Despite its difficulties, ^{71}Ga NMR is becoming more widely used, with the increase in magnetic field strengths available helping to reduce the significant second order quadrupole broadening, with studies on crystalline Ga phosphates, such as GaPO_3 , [175] Ga doped TCP, [176] and other GaPOs, [177] showing resonances can be resolved enabling distinction between different Ga coordination environments. ^{71}Ga

NMR has also been utilised on numerous glass type materials, including amorphous Ga fluorides,[178, 179] Ga chalcogenide glasses,[180] and caesium gallate glasses.[181] However there have been few ^{71}Ga NMR studies on phosphate glasses, with Valappil *et al.* using ^{71}Ga to show Ga is present in Ga phosphate glasses as GaO_6 , however the quality of the data is poor, owing to low signal-to-noise and insufficient MAS rates, making it impossible to draw any firm conclusions from the data.[76, 168] Belkhir *et al.* present the best data to date, with three different Ga coordination environments resolved in a Na phosphate glass series.[182] Although again the MAS rates employed were far from adequate to completely separate the presence of spinning side bands from the central transition resonances, consequently limiting the usefulness of the results obtained.[182]

Another quadrupole nucleus that has shown potential to become a powerful structural probe is that of ^{17}O , owing to its vital importance in inorganic oxides. Although the low natural abundance of ^{17}O (0.037 %) means labelling schemes usually have to be undertaken in order to increase the number of NMR active spins in the system to a measurable level.[183–185] However its moderate magnetic moment (-1.132 J T^{-1}) and small quadrupole moment (-25.56 mbarns), along with large chemical shift range, can make ^{17}O an informative nucleus of choice.[186] There have been numerous studies of ^{17}O NMR of glass materials with distinction between bridging (BO) and non-bridging oxygens (NBO) in silicates.[183, 187–192] Though often requiring 2D multiple quantum magic angle spinning (MQMAS) experiments, due to the lines being broadened by the second order quadrupole interaction, which is not averaged to zero by conventional MAS, making their identification from 1D NMR unsuccessful. Zeyer *et al.* first managed to resolve BO and NBO from phosphate based glasses using ^{17}O NMR, with the two sites showing clear differences in quadrupolar coupling parameters, 4.7 MHz for NBO, and 7.7 MHz for BO.[183] Assignments were initially made by Zeyer *et al.* by comparison of the intensities to expected compositions.[183] This was further supported by Zeyer using the empirical correlation between C_Q and the average percentage of ionic character, as first devolved by Schramm and Oldfield, showing the more covalent P-O-P bond in the BO to have a larger C_Q than the more ionic P-O-Na bonds in the NBO.[193] More recently these assignments have been confirmed through the use of first principles calculations, with Vasconcelos *et al.* linking ^{17}O assignments

Table 5.1: Compositions of glasses under investigation, with varying Ga and Na content.

	Mol % Ga_2O_3	Mol % Na_2O	Mol % CaO	Mol % P_2O_5
P45Ga1	1	24	30	45
P45Ga3	3	22	30	45
P45Ga5	5	20	30	45
P45Ga10	10	15	30	45
P45Ga15	15	10	30	45
P50Ga0	0	20	30	50
P50Ga1	1	19	30	50
P50Ga3	3	17	30	50
P50Ga5	5	15	30	50
P50Ga10	10	10	30	50
P50Ga15	15	5	30	50
P55Ga1	1	14	30	55
P55Ga3	3	12	30	55
P55Ga5	5	10	30	55
P55Ga10	10	5	30	55

with DFT calculations on crystalline Na phosphates, and Forler *et al.* taking a similar approach for phosphate glass.[185, 190]

In this study we look at a quaternary gallo-phosphate based bioactive glass series using multinuclear solid state NMR methods, including exploiting the recent increase in availability of high magnetic fields and fast MAS rates, to aid in the challenging NMR of ^{17}O and ^{71}Ga quadrupolar nuclei. The more information we have on the structure of these biologically important materials the better their bioactivity can hopefully be understood.

5.2 Experimental Details

Melt-quenched glass samples were prepared using $\text{NH}_4\text{H}_2\text{PO}_4$ (Sigma-Aldrich, 99.5%), Na_2CO_3 (Sigma-Aldrich, 99.5+%), Ga_2O_3 (Alfa Aesar, 99.99%) and CaO . (^{17}O labelled CaO was used for the labelled samples, obtained from Franck Fayon at Université d'Orleans,) After mixing thoroughly the precursors were placed in a 90 % Pt-10 % Rh crucible and placed into a furnace preheated to 300°C for 30 minutes. The furnace temperature was then rapidly increased to 600°C and held for 30 minutes, the temperature was then increased to 1100°C and held at this temperature for 60 minutes. The

samples were then quenched by placing the bottom of the crucible into an ice water mix being careful not to get water in the sample. For the ^{17}O samples during the heating process an argon flow was passed through the furnace to reduce the probability of ^{17}O exchange with the O in the air. The compositions of the three glass series are shown in Table 5.1.

Single pulse ^{31}P MAS NMR experiments were performed at 2.35 T using a Chemagnetics Infinity spectrometer operating at the ^{31}P Larmor frequency of 40.48 MHz. These measurements utilised a 2.5 mm Bruker HX probe using MAS frequencies of 20 kHz. An excitation pulse length of 2 μs corresponding to a nutation frequency of $\pi/4$ was employed with a delay between subsequent pulses of 15 s, to ensure quantitative estimations of the P sites present is achieved. Chemical shift referencing and pulse calibrations were performed on a crystalline secondary solid reference sample of BPO_4 (δ_{iso} -29.5 ppm), with all ^{31}P chemical shifts being directly referenced to the IUPAC primary reference of 85% H_3PO_4 (δ_{iso} 0 ppm).[91, 150]

The ^{31}P refocused INADEQUATE Spin Echo (REINE) experiments were performed on the P45 glass series at 7.05 T using a Varian/Chemagnetics InfinityPlus spectrometer operating at the ^{31}P Larmor frequency of 121.48 MHz.[116, 122] These experiments used a Bruker 4 mm HX probe with MAS frequencies of 12.5 kHz. A total of 256 transients were co-added for 22 t_1 increments, with the pulse delay between transients set to 15 s to achieve maximum signal in a reasonable experimental time period. $\pi/2$ and π pulse lengths of 4 μs and 8 μs respectively were utilised with $\tau/2$ delays set to 6.8 ms. Spectral widths were synchronised with the MAS speed at 12.5 kHz in both the F_1 and F_2 dimensions. Between 12 and 14 different REINE experiments were carried out for each sample with varying $\tau_j/2$ times, ranging from 0.8 ms to 48 ms. REINE spectra were processed using MATLAB. Spectra were referenced via a secondary solid ammonium dihydrogen phosphate ($\text{NH}_4\text{H}_2\text{PO}_4$) at δ_{iso} 1.0 ppm, with respect to 85 % H_3PO_4 .[91, 150]

Single pulse ^{23}Na MAS NMR experiments were performed at 14.1 T and 9.4 T using Bruker Avance II-600 and Bruker DSX-400 spectrometers which operated at the ^{23}Na Larmor frequencies of 158.55 MHz and 105.49 MHz, respectively. These measurements utilised a Bruker 4 mm HX probe which enabled MAS frequencies of 15 kHz. Flip angle calibration was performed on a NaCl solution from which a ‘non-

selective' (solution) $\pi/2$ pulse time of 6 μs was measured, which corresponded to a 'selective' (solid) pulse time of 3 μs for the $I = 3/2$ ^{23}Na nucleus. All measurements were undertaken with a $\pi/4$ tip angle ('selective') of 1.5 μs to ensure accurate estimates of the quadrupole parameters. All ^{23}Na center of gravity (apparent) shifts were reported against the IUPAC recommended primary reference of NaCl solution (in D_2O 0.1 M, δ 0.0 ppm), via a secondary solid NaCl reference at a known shift of δ 7.2 ppm.[150, 151] A common relaxation time of 5 s was deemed to be sufficient for all ^{23}Na measurements.

Single pulse ^{71}Ga MAS NMR experiments were performed at 14.1 T using a Bruker Avance II-600 spectrometer operating at the ^{71}Ga Larmor frequency 182.79 MHz. These measurements utilised a Bruker 2.5 mm HX probe functioning at a MAS frequency of 31.25 kHz. Single pulse ^{71}Ga MAS NMR experiments were also performed at 20.0 T, using a Bruker Avance III-850 spectrometer operating at the ^{71}Ga Larmor frequency of 259.32 MHz. Experiments at 20.0 T were carried out using a Bruker 1.3 mm HXY probe using 60 kHz MAS frequency. Flip angle calibration was performed on a 1.1 M $(\text{GaNO}_3)_3$ solution from which a 'non-selective' (solution) $\pi/2$ pulse time of 12 μs was measured. This corresponds to a 'selective' (solid) pulse time of 6 μs for the $I = 3/2$ ^{71}Ga nucleus. All measurements were undertaken with a $\pi/12$ tip angle ('selective') of 1 μs to ensure quantitative estimates of the different ^{71}Ga species present. A common recycle delay of 1 s was utilised between subsequent transients to ensure sufficient relaxation. All ^{71}Ga center of gravity (apparent) shifts were reported against the IUPAC recommended primary reference of $\text{Ga}(\text{NO}_3)_3$ (in D_2O 1.1 M, δ 0.0 ppm) [150]

A ^{31}P ^{71}Ga J -HMQC experiment was performed on the P45Ga15 glass at 20.0 T using a Bruker 1.3 mm HXY probe in triple resonance mode at a MAS frequency of 60 kHz. The pulse sequence of the J -HMQC experiment is shown in Figure 3.5 (Chapter 3, owing to the quicker relaxation of the ^{71}Ga nucleus than ^{31}P nucleus, detection was carried out on the ^{71}Ga channel, enabling a much smaller pulse delay of 1 s to be used.[125] 8000 transients were coadded for 28 t_1 slices, with a $\tau/2$ delay of 3.33 ms. A $\pi/2$ pulse of 7 μs was implemented on the ^{31}P channel, and a 3.5 μs $\pi/2$ pulse and 7 μs π pulse on the ^{71}Ga channel.

^{17}O spin echo MAS NMR experiments were carried out at 11.75 T and 14.1 T using Bruker Avance III-500 and Avance II-600 spectrometers, operating at a Larmor

frequency of 67.80 MHz and 81.26 MHz, respectively. These measurements utilised a Bruker 4 mm HX probe which enabled MAS frequencies of 15 kHz. Pulse flip angle calibration was performed on H₂O, from which a ‘non-selective’ (solution) $\pi/2$ pulse time of 9 μ s was measured. This corresponds to a ‘selective’ (solid) pulse time of 3 μ s for the $I = 5/2$ ¹⁷O nucleus. Spin echo experiments used a $\pi/2 - \pi$ pulse scheme with a 3 μ s and 6 μ s pulse lengths corresponding to a ‘selective’ (solid) $\pi/2$ and π pulses, respectively, with a τ delay of 6.67 μ s rotor synchronized to the MAS frequency. All ¹⁷O center of gravity (apparent) shifts were reported against the IUPAC recommended primary reference of H₂O (δ 0 ppm).[150] A common relaxation time of 2 s was found to be sufficient for all ¹⁷O measurements.

¹⁷O MQMAS experiments were performed using the amplitude modulated Z -filter pulse scheme.[132] At 14.1 T 1260 transients were co-added for each of the 128 t_1 slices. Pulse times of the initial excitation ‘hard’ pulse to produce triple quantum coherence, and the conversion ‘hard’ pulse, were 6 μ s and 2 μ s respectively (approximately 100 kHz rf), with the ‘soft’ Z -filter pulses 18 μ s (approximately 13 kHz rf). At 11.75 T 2016 transients were required to obtain sufficient signal to noise, meaning only 64 t_1 slices were able to be obtained in a reasonable experimental time scale. Higher rf fields were achievable at 11.75 T, with pulse times of the initial excitation ‘hard’ pulse to produce triple quantum coherence, and the conversion ‘hard’ pulse, were 3.75 μ s, and 1.25 μ s respectively (corresponding to over 150 kHz rf), with the ‘soft’ Z -filter pulses of 20 μ s (approximately 12.5 kHz rf). Shearing was carried out during processing and the F_1 axis was referenced using the Amoureux convention, as discussed in Section 3.4.7.

5.3 Results

5.3.1 1D ³¹P Single Pulse MAS NMR

³¹P single pulse MAS NMR data are shown for each glass series in Figure 5.1 (a)-(c). According to the binary model it is expected that two P sites will be present for any particular glass which can be predicted by the nominal P content within the glass network.[64] Although the glasses under investigation here are quaternary systems the same general rules are thought to apply. From Brow’s review on phosphate glass

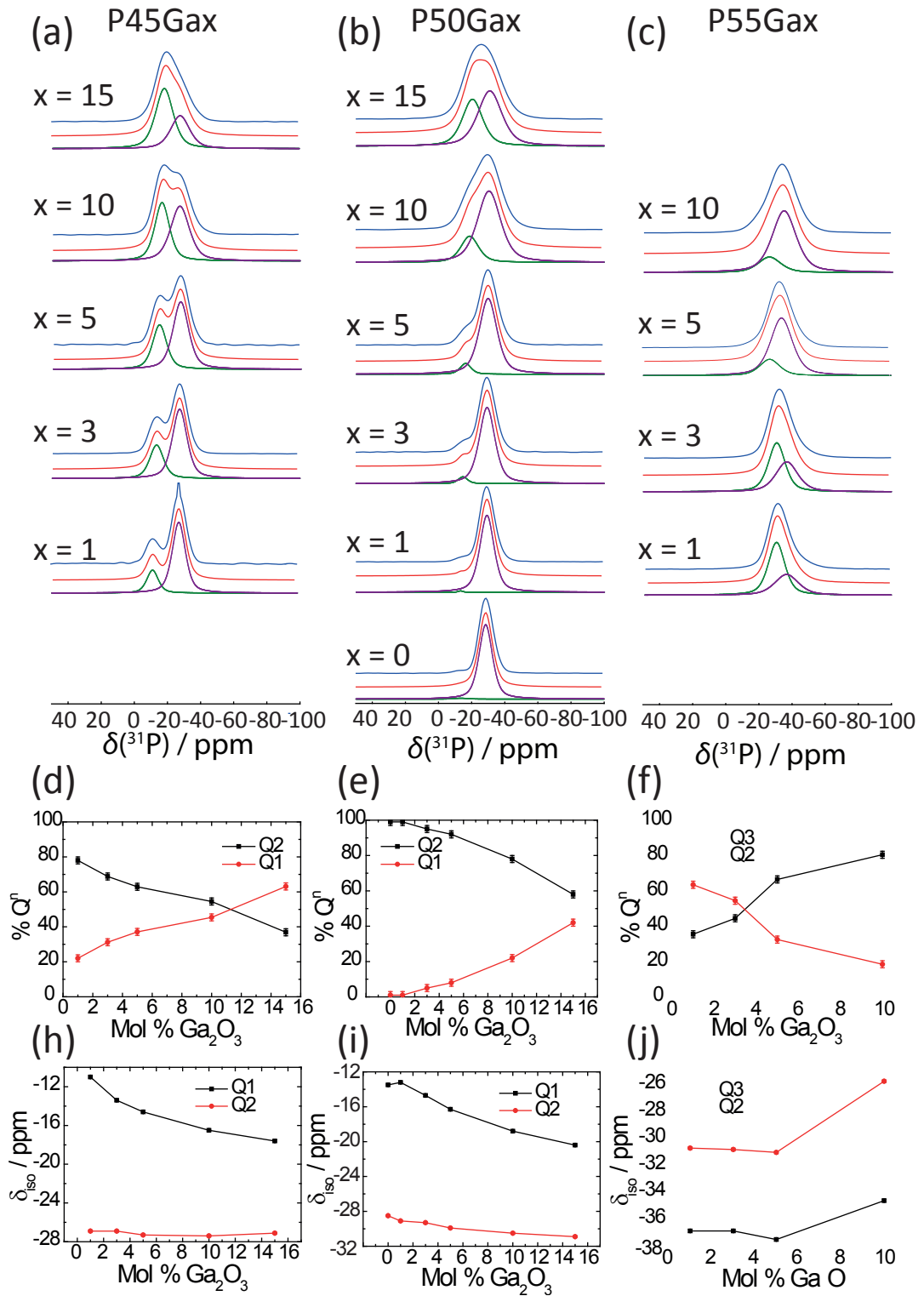


Figure 5.1: (a)-(b) 2.35 T ^{31}P single pulse MAS NMR data and spectral simulations for three Ga-containing phosphate glass series. The MAS frequency was 20 kHz throughout, and the ^{31}P Larmor frequency was 40.48 MHz. (d)-(f) Change in % Q species upon Ga_2O_3 incorporation from the ^{31}P single pulse MAS NMR simulated fits. (h)-(j) Change in δ_{iso} upon Ga_2O_3 incorporation from the ^{31}P single pulse MAS NMR simulated fits.

	$\delta_{iso}(\text{ppm})$ $\pm 0.1 \text{ ppm}$	Int (%) $\pm 2\%$	Environment
P45Ga1			
1	-11.0	22	Q^1
2	-26.9	78	Q^2
P45Ga3			
1	-13.4	32	Q^1
2	-26.9	78	Q^2
P45Ga5			
1	-14.6	37	Q^1
2	-27.3	63	Q^2
P45Ga10			
1	-16.5	46	Q^1
2	-27.4	54	Q^2
P45Ga15			
1	-17.6	63	Q^1
2	-27.1	37	Q^2
P50Ga0			
1	-13.5	1	Q^1
2	-28.5	99	Q^2
P50Ga1			
1	-13.1	1	Q^1
2	-29.1	99	Q^2
P50Ga3			
1	-14.7	5	Q^1
2	-29.3	95	Q^2
P50Ga5			
1	-16.3	8	Q^1
2	-29.9	92	Q^2
P50Ga10			
1	-18.8	22	Q^1
2	-30.5	78	Q^2
P50Ga15			
1	-20.4	42	Q^1
2	-30.9	58	Q^2
P55Ga1			
1	-30.7	64	Q^2
2	-36.9	36	Q^3
P55Ga3			
1	-30.8	55	Q^2
2	-36.9	45	Q^3
P55Ga5			
1	-31.0	33	Q^2
2	-37.5	67	Q^3
P55Ga10			
1	-25.7	19	Q^2
2	-34.6	81	Q^3

Table 5.2: Fitting parameters from ^{31}P NMR of Ga glass samples carried out at 2.35 T. Simulations carried out using DmFit software package.[152]

systems, polyphosphate glasses with $P_2O_5 \leq 50$ are expected to contain Q^1 and Q^2 species, while ultraphosphate glasses with $P_2O_5 \geq 50$ are expected to be dominated by Q^2 and Q^3 species. Therefore, from the series studied here it can be predicted that the P45 series should contain both Q^1 and Q^2 units, the P55 series Q^3 and Q^2 units, and since the P50 series sits on the compositional boundary Q^2 units would be expected to dominate. From Figure 5.1 it can be observed that the P45 glass series shows the most well resolved indication of two distinct P environments, particularly at low Ga concentration, with the two detected ^{31}P resonances at δ_{iso} -11.0 to -17.6 ppm and δ_{iso} -26.9 to -27.4 ppm assigned to Q^1 and Q^2 P environments, respectively. This behaviour observed from this Ga containing phosphate glass system is consistent with Brow's model. As the Ga content is increased in this series the resonances broaden and become less resolved (as observed for the Al glass series in Chapter 4), however the presence of Q^1 and Q^2 P environments remains indisputable. For the P50 glass series two ^{31}P resonances are again observed; as predicted the majority of P content assumes Q^2 coordination due to the series lying on the boundary between ultra and poly phosphate glass, however a small amount of Q^1 units are still present. From Figure 5.1 it can be seen that the P55 series as expected contains both Q^2 and Q^3 sites, which appear to be quite broadened and poorly resolved even at low Ga concentration in comparison to the Q^1 and Q^2 resonances observed from the P45 and P50 series.

Table 5.2 and Figure 5.1 (d)-(j) report the variation in the simulation parameters elucidated from the ^{31}P MAS NMR data in Figure 5.1 (a)-(c); this enables the direct quantification of the individual Q^n species and their changing trends induced by Ga incorporation. For the P45 glass series it is apparent that upon Ga incorporation the number of Q^2 units (which is initially the most significant contribution) decreases as the number of Q^1 units increases, with Q^1 becoming the largest contribution in the $x = 15$ glass. This suggests the Ga is depolymerising the P-O-P bonds in the Q^2 phosphate units. This is a very similar observation to that reported in Chapter 4 for the Al containing phosphate glass series, and is not surprising since both Al and Ga are trivalent cations of similar ionic radii. For the P50 glass series the Ga free glass (i.e. $x = 0$, or P50Ga0) exhibits that virtually all of the P is in a Q^2 coordination environment. Upon initial Ga incorporation (i.e. $x = 1$, or P50Ga1), there is no detectable change in the Q^2 content, however further Ga incorporation causes the

amount of Q^2 to significantly decrease, with the $x = 15$ glass showing the largest Q^1 content of this series. This demonstrates that Ga incorporation plays a similar role in both the P50 and P45 series. For the P55 series, which contains a significant amount of Q^3 species, it is observed that for low Ga concentrations the majority (64 %) of the P is in a Q^2 environment. However, Ga incorporation into this network demonstrates that an opposing trend to that of the other P50 and P45 glass series ensues. In this case Ga incorporation induces a condensation or polymerisation of the network, thus resulting in a decrease in Q^2 and a subsequent increase in Q^3 speciation.

From Table 5.2 and Figure 5.1 (h)-(j) the variation of the ^{31}P shift values for each series upon Ga_2O_3 incorporation can be observed. From Figure 5.1 (h) it can be seen that upon Ga incorporation for the P45 series the Q^1 unit shifts to more -ve ppm from -11 to -17.6 ppm. Whilst the Q^1 units shift in a similar direction, this shift is much smaller (about 0.4 ppm), which probably is within error values. Similarly for the P50 glass series as shown in Figure 5.1 (i) shifts in both the Q^1 resonance to more -ve ppm upon Ga incorporation, along with a much more noticeable shift in the Q^2 resonance of ~ 2 ppm to more -ve ppm. The shift of the ^{31}P resonances to more -ve ppm indicates an increase in shielding of the P sites upon Ga incorporation, therefore even though the amount of Q^1 units are increasing upon Ga incorporation, these Q^1 sites are more shielded, most likely due to Ga ion surrounding the P units cross linking phosphate chains. Figure 5.1 (j) displays the trends for the P55 glass series, with the first three data points indicating a similar trend of shift to more -ve ppm as displayed in the other two series, although here changes are less significant as there is now no Q^1 units present. However for the final glass in this series P55Ga10 there is a significant shift in the opposite sense to more +ve ppm for both Q species, indicating a de-shielding of the ^{31}P site.

5.3.2 2D ^{31}P REINE MAS NMR

Further information can be obtained on P connectivities using the ^{31}P refocused INADEQUATE spin echo (REINE) experiment as shown by Guerry *et al.* on a cadmium phosphate glass, and in Chapter 4 on a series of Al doped phosphate glasses.[122] REINE experiments have here been carried out on the P45 glass series since they possess the largest proportion of Q^1 units, which are the most informative as they de-

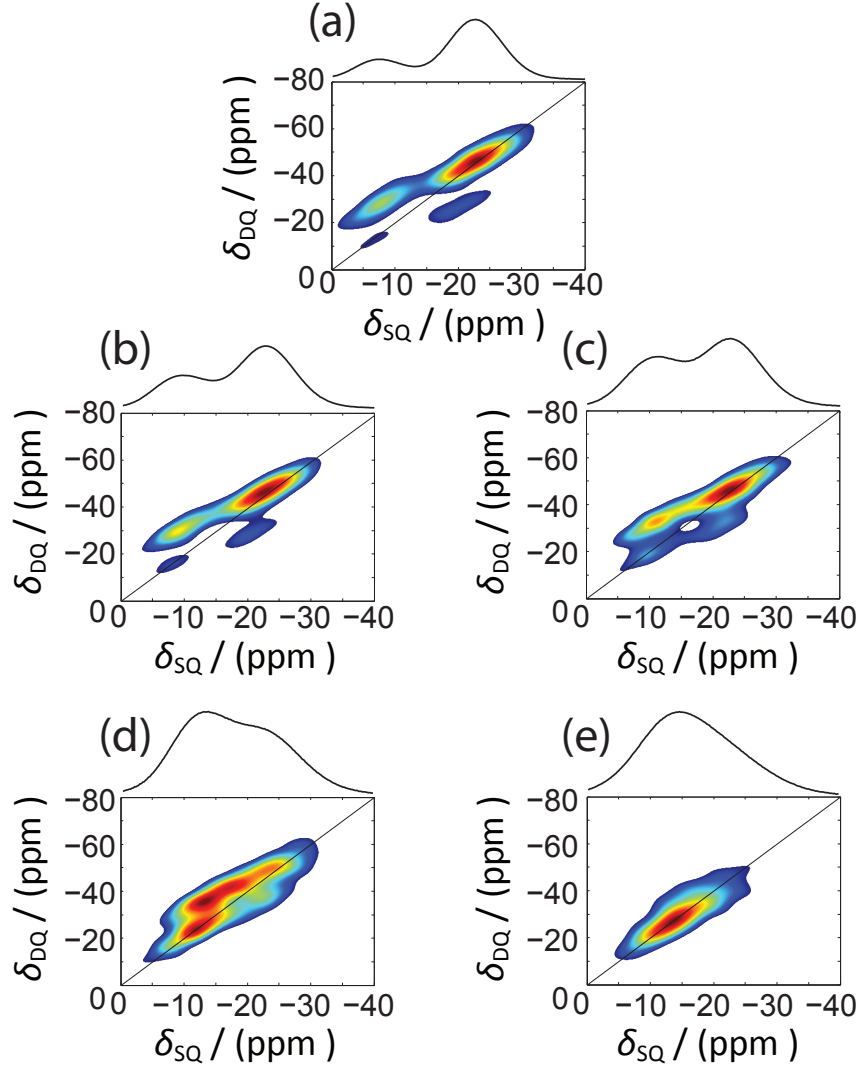


Figure 5.2: ^{31}P REINE spectra (7.05 T with 12.5 kHz MAS) at $\tau_j = 0.8$ ms for each glass composition, (a) P45Ga1, (b) P45Ga3, (c) P45Ga5, (d) P45Ga10, (e) P45Ga15 showing the maximum signal intensity for each REINE peak.

scribe only one P-O-P bond. The existence of only one P-O-P bond in the Q^1 unit means the REINE analysis is reliant upon one J coupling value only, whereas higher coordinations such as Q^2 and Q^3 (as found for the P50 and P55 series) depend upon multiple P-O-P linkages and multiple J couplings, thus rendering the analysis ambiguous and difficult to be carried out with any real accuracy. Figure 5.2 shows REINE data for each of the P45 glasses with the final spin echo period $\tau_j/2$ set as small as possible (0.8 ms), thus resulting in the maximum signal intensity, similar to what would be observed in a regular refocused INADEQUATE experiment.[114, 115] For low Ga contents the spectra show four distinct peaks corresponding to connectivities of Q^1 - Q^1 , Q^1 - Q^2 , Q^2 - Q^1 and Q^2 - Q^2 , as would be expected in a disordered glassy material. As

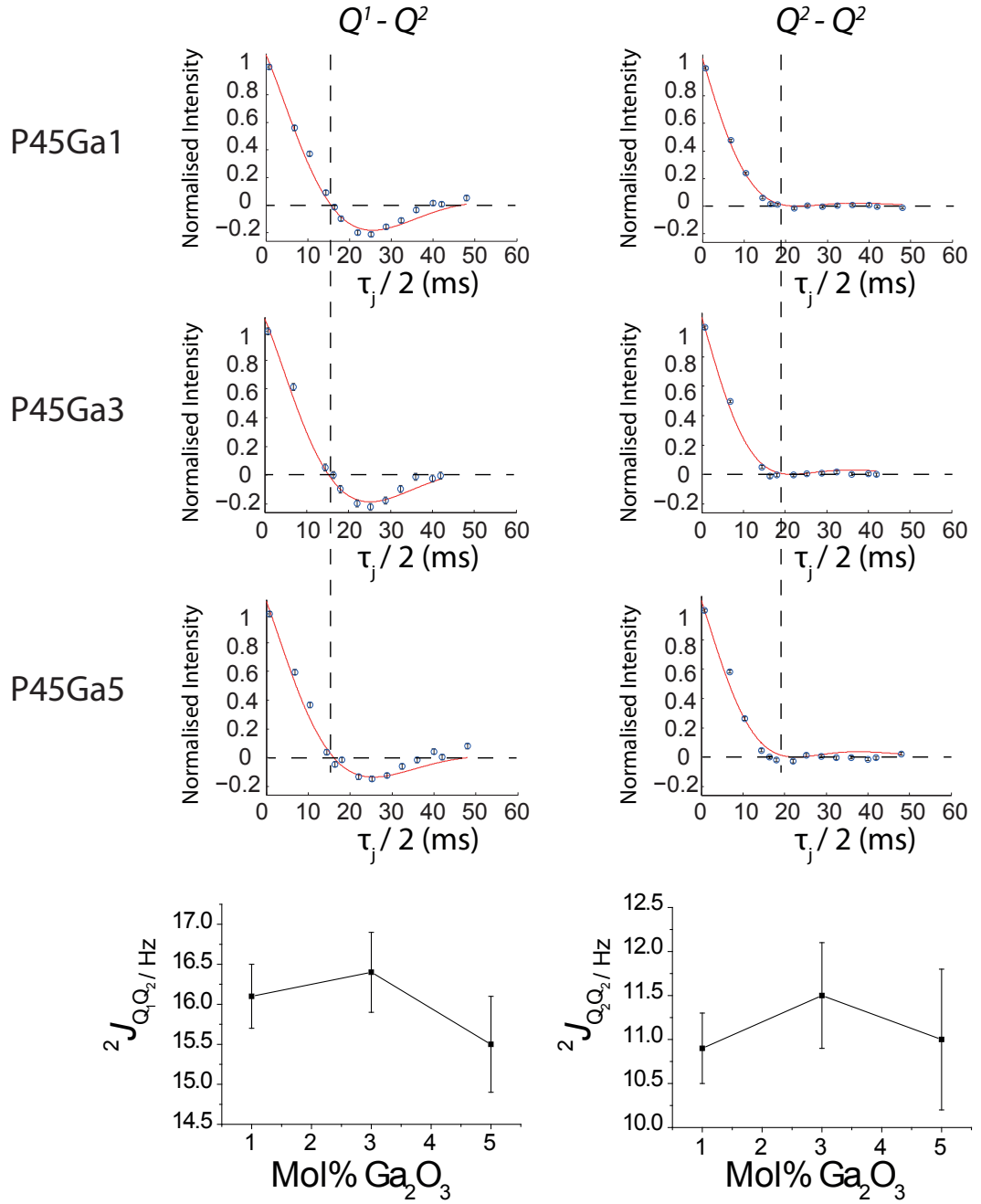


Figure 5.3: Time-domain spin echo curves obtained from the summed intensity for the Q^1-Q^2 (left) and Q^2-Q^2 (right) ^{31}P REINE peaks for each glass composition. Solid lines are fits to Equation 4.1 for Q^1-Q^2 , and Equation 4.3 for Q^2-Q^2 (fit parameters and correlation coefficients are shown in Table A.6 in the Appendix A). Bottom graphs show the change in the J coupling with increasing Ga_2O_3 content for the Q^1-Q^2 (left) and Q^2-Q^2 (right) peaks, showing no evident change in the J couplings with increasing Ga_2O_3 content.

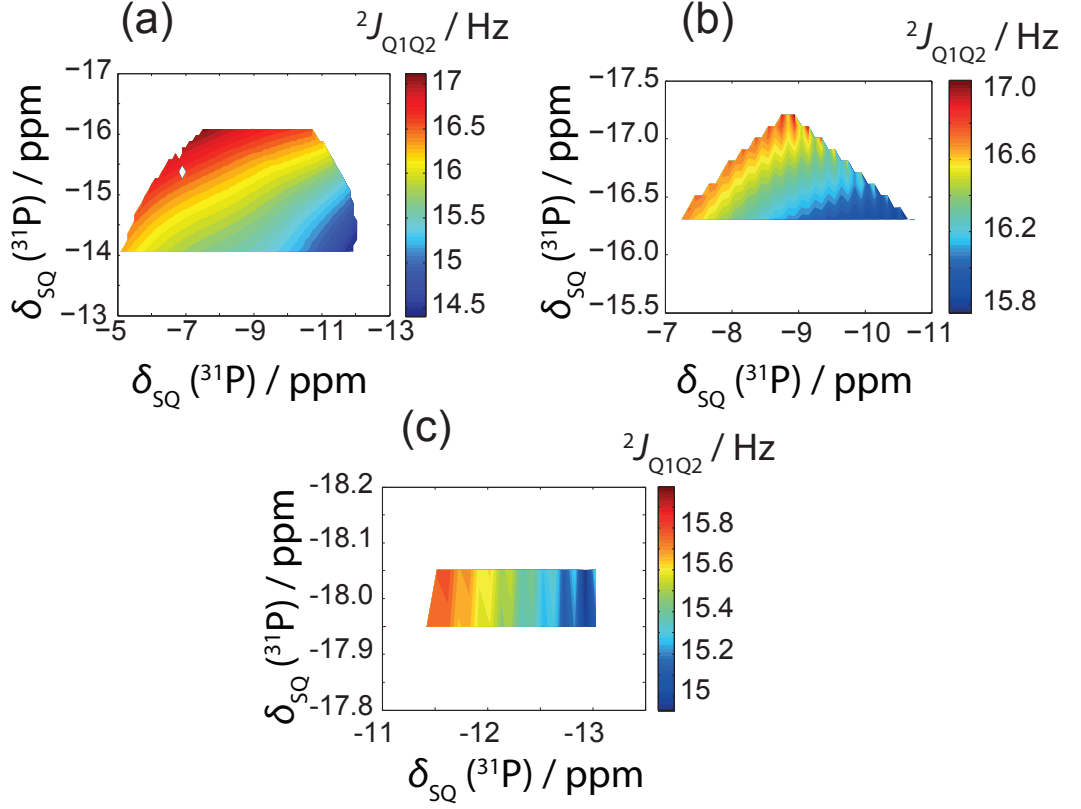


Figure 5.4: ^{31}P Q^1 - Q^2 REINE peak (7.05 T with 12.5 kHz MAS). Pixel by Pixel spin echo fitting showing distribution of J couplings. (a) P45Ga1 (b) P45Ga3 (c) P45Ga5 glasses.

the Ga content is increased the four resonances are no longer well resolved, with the $x = 15$ glass showing only a single broadened resonance, as also evidenced by the single pulse ^{31}P MAS NMR data in Figure 5.1 depicting increase linewidths and reducing resolution of the sites. This makes determining distinct regions corresponding to Q^1 and Q^2 coordinations less accurate at higher Ga levels. The most effective method to further study the REINE analysis is to sum the intensity across a whole resonance, and then map out how this changes with increasing the final $\tau_j/2$ evolution period. This behaviour should be modulated according to Equations 4.1, 4.2 and 4.3 shown in Chapter 4, and subsequently dependent upon the J coupling between the two bonded P sites. This is shown in Figure 5.3 for the Q^1 - Q^2 peak with corresponding fits using Equation 4.1. However as observed, successful fits from the REINE analysis were only obtainable for the $x = 1, 3$, and 5 glasses, with the corresponding data obtained from the $x = 10$ and 15 glasses unable to be simulated with appropriate fitting functions. Clearly the Ga is having an effect on the glass network which is preventing the REINE

analysis. This is most likely due to disorder broadening, due to the fact that for these glasses with highest Ga content the lineshapes are becoming very broad resulting in an overlap of many sites, this prevents the REINE analysis as the regions are no longer dependent upon one (in the case of Q^1) or two (in the case of Q^2) J couplings, and is in fact a complex mixture of many sites, and thus many J values. This prevents the usual modelling of the J modulation to that of the Equations 4.1 4.2 and 4.3.

Figure 5.3 also shows the summed intensity REINE spin echo curves for the Q^2 - Q^2 peaks which was carried out using Equation 4.3, the \cos^2 function. The use of Equation 4.3 can give information on the short range chain length within the glass, owing to the fact that this indicates that the J coupling between the Q^2 unit under observation is the same between both of its bonded nuclei, thus indicating long chains are predominant, as both of its nearest neighbour nuclei will also be Q^2 units. The J couplings measured from the Q^1 - Q^2 and Q^2 - Q^2 peaks are shown in Figure 5.3, showing how the J couplings from the summed intensity peaks change as we incorporate Ga into the glass network. It can be clearly seen that there is little to no variation in the J coupling in both the Q^1 - Q^2 and Q^2 - Q^2 peaks, as opposed to what was observed in Chapter 4 for the Al containing glass, whereby there was a decrease in J coupling as Al entered the glass network even for small incorporation. Therefore it can be assumed that the Ga is having little effect on the local P-O-P bond angles and bond lengths, which have recently been found to show correlations on the size of J couplings observed, unlike that observed for Al.[156–159]

Another useful analysis that can be carried out on the data obtained from REINE experiments involves fitting each individual pixel of a resonance with one of the appropriate fitting functions, see Equations 4.1,4.2 and 4.3 Chapter 4, in order to map out how the J couplings change across the resonance linewidth. This is shown for the Q^1 - Q^2 resonance in Figure 5.4 which clearly demonstrates that a large variation in the J couplings is observed, which varies from about 17 Hz to 14.5 Hz, evidently reflecting a change in the P environments. Different trends have been previously reported on whether the J coupling appears to change in the horizontal (F_2) dimension or the vertical (F_1) dimension, from these type of pixel fitting maps (see Chapter 4).[122] From Figure 5.4 it can be noted that for the P45Ga5 glass the variation is clearly in the horizontal (F_2) dimension indicating that the J coupling is strongly correlated

Peak	$\delta(\text{ppm})$ (± 0.5)	C_Q Center (MHz) (± 0.8)	C_Q Width (MHz) (± 0.3)	η (± 0.05)
P45Ga1	-4.8	2.6	1.7	0.1
P45Ga3	-5.5	2.6	1.7	0.1
P45Ga5	-6.6	2.5	1.7	0.1
P45Ga10	-8.7	2.3	1.7	0.1
P45Ga15	-11.5	2.1	1.7	0.1
P50Ga0	-5.2	2.6	1.9	0.1
P50Ga1	-7.1	2.6	1.9	0.1
P50Ga3	-8.9	2.6	1.9	0.1
P50Ga5	-8.0	2.6	1.9	0.1
P50Ga10	-9.7	2.5	1.9	0.1
P50Ga15	-11.9	2.4	1.9	0.1
P55Ga1	-7.8	2.5	1.9	0.1
P55Ga3	-9.2	2.5	1.9	0.1
P55Ga5	-10.0	2.4	1.9	0.1
P55Ga10	-11.1	2.4	1.9	0.1

Table 5.3: ^{23}Na NMR parameters from simulation of single pulse NMR spectra. Parameters constrained from multiple field fitting, using Quadfit software package. [153]

to the chemical shift of the Q^1 unit being directly observed, with a more negative ppm resulting in a smaller J coupling. This horizontal variation is also observed to occur consistently for both of the P45Ga3 and P45Ga1 glasses, however now with an additional dependence on the chemical shift in the vertical (F_1) dimension, showing that the ^{31}P J couplings in these systems are influenced by a more complicated interplay of the chemical shift of the directly observed nucleus and its coupled partner. These finding shows that the J coupling is not simply correlated to the chemical shift of the P site under investigation, as previously shown by Fayon *et al.* on Pb phosphate glasses, and for the Al phosphate glasses in Chapter 4, nor is it supporting the correlation with the observed nuclei's coupled partner as shown by Guerry *et al.* [122, 148]

5.3.3 ^{23}Na Single Pulse MAS NMR

The acquired ^{23}Na MAS NMR data and corresponding spectral simulations for all three glass series are shown in Figure 5.5, with fitting parameters shown in Table 5.3. Each observed lineshape is typical of Na in disordered glass environments which give rise to distributions of isotropic chemical shifts and quadrupolar coupling constants. It

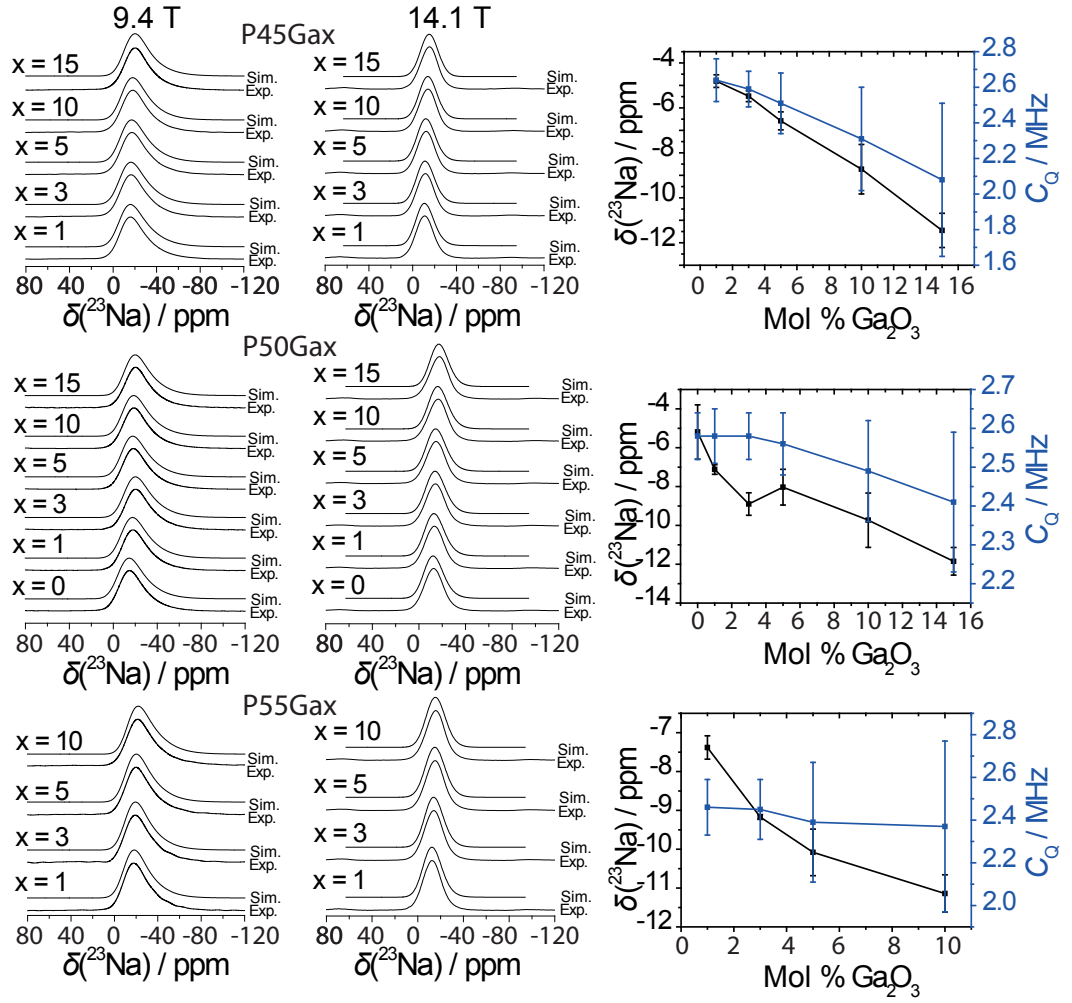


Figure 5.5: Left: ^{23}Na single pulse NMR spectra and simulated fits at 9.4 T (12.5 kHz MAS) and 14.1 T (12.5 kHz MAS). Right: ^{23}Na change in chemical shift (black) and C_Q Center (blue) with increasing incorporation of Ga_2O_3 content.

can be observed that for all glass series the quadrupole coupling constant (C_Q centre) decreases as the Ga content increases. Figure 5.5 also indicates that changes in the average isotropic chemical shift of the Na resonances can be accurately detected. These data thus show that for all series incorporating increasing amount of Ga into the network a corresponding shift to more negative ppm is observed, indicating that the Na environment is becoming more shielded. These trends mirror that found from the ^{23}Na results for the Al phosphate glasses in Chapter 4, indicating the Na sites are becoming more shielded and more symmetrical in their environment, perhaps becoming incorporated into a more cross linked and condensed network.

5.3.4 ^{71}Ga Single Pulse MAS NMR

In the field of solid state NMR, the ^{71}Ga nucleus still remains an uncommon nucleus of study primarily due to the large quadrupolar broadening experienced by this spin $3/2$ nucleus. However, with the increase in available high magnetic field strengths, and development of MAS NMR probes capable of achieving MAS rates fast enough to sufficiently average the second order quadrupole interaction, the ^{71}Ga nucleus is thus becoming more increasingly accessible by MAS NMR techniques.[76, 168, 175–180, 182, 194] The ^{71}Ga measurements exhibited in Figure 5.6 were initially carried out at 14.1 T using the fastest available MAS frequency of 31.25 kHz; the results for each glass series shown in Figure 5.6 show three resolvable resonances observable under these experimental conditions. Although this was the fastest MAS frequency achievable on this system, it is not quite fast enough to ensure that the first series of spinning side bands do not influence the spectrum; i.e. the sideband of the left resonance would lie outside of the resonance on the right hand side, and vice versa. Fortunately, however no substantial spinning side band structure was observed, thus enabling the unambiguous determination of three distinct resonances. Similar measurements were then performed at the higher field of 20.0 T, using a faster MAS rate of 60 kHz which is achievable on this high field system. Here this MAS speed is fast enough to ensure that any spinning sidebands would lie outside of the resonance defining the central transition spectrum, though again no spinning sideband structure is observed. The multifield data is useful in that it enables each spectrum to be simulated and constrains parameters over two magnetic fields which are well separated ultimately yielding reliable information on the isotropic chemical shifts and quadrupole parameters which are field independent. These simulations are shown along with the spectra and the corresponding parameters in Figure 5.6 and Table 5.4. The agreement achieved between the results at these two magnetic fields clearly shows that although the MAS frequency employed at 14.1 T is slightly lower than would ideally be desired, it is not affecting the results obtained owing to the fact that the C_Q values characterising these Ga positions are small and no spinning sidebands structure is present. An unambiguous assignment of the three ^{71}Ga resonances, can be performed. showing Ga to be 4-fold coordinated to O (GaO_4), 5-fold coordinated to O (GaO_5), and 6-fold coordinated to O (GaO_6), with increasing shift to more negative ppm, see Figure 5.6. This assignment was made upon looking

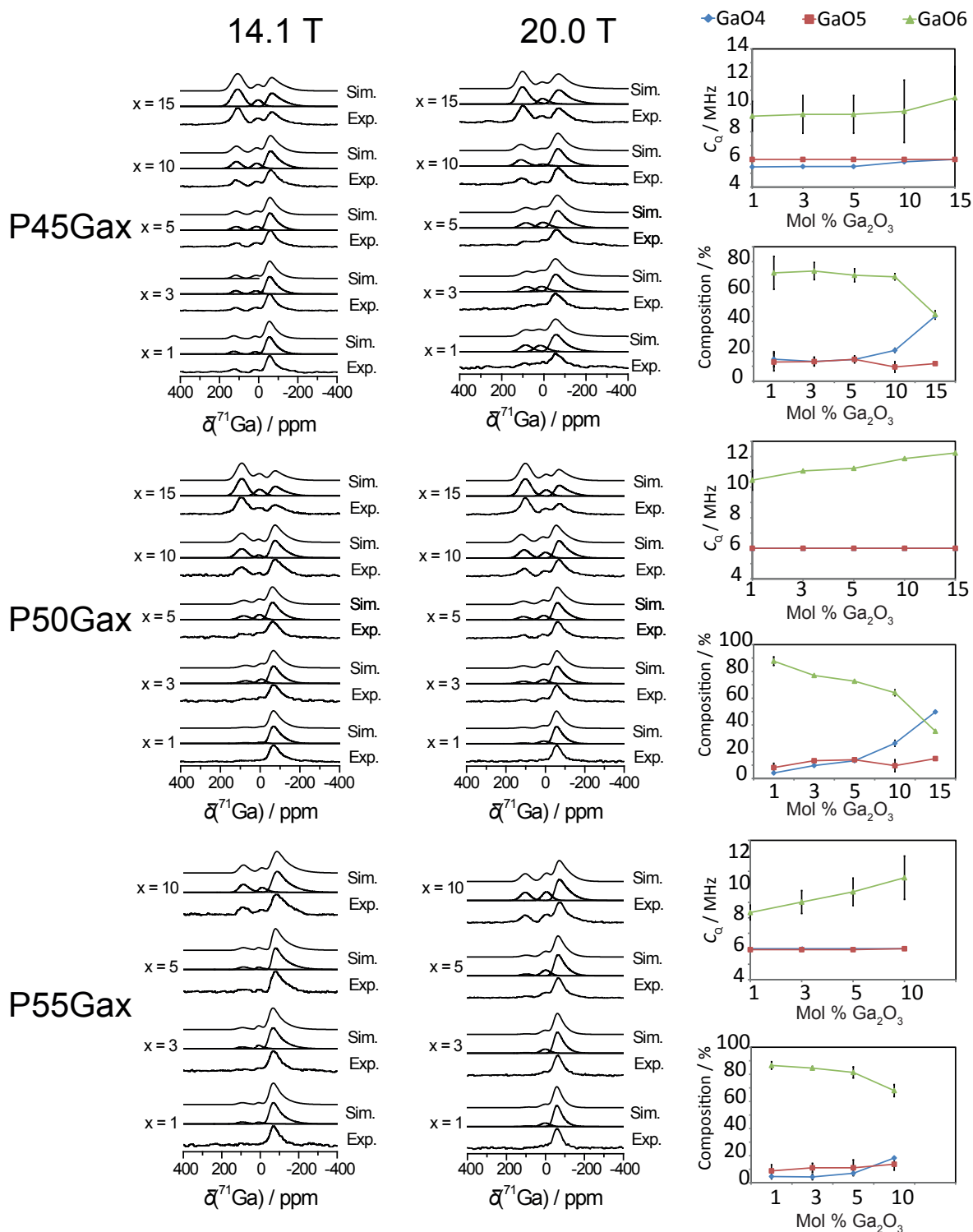


Figure 5.6: ^{71}Ga single pulse MAS-NMR carried out at 14.1 T and 20.0 T using 31.25 kHz and 60 kHz MAS respectively, along with simulated fits using Quadfit software package.[153] Change in C_Q center and intensity of each Ga species shown with incorporation of Ga into the network.

Peak	$\delta(\text{ppm})$	C_Q Center (MHz)	C_Q Width (MHz)	η (± 0.05)	Int (%)	Environment
P45Ga1						
1	121.2	5.5	4.8	0.1	15	GaO ₄
2	33.8	4.7	4.4	0.1	13	GaO ₅
3	-30.1	9.1	1.1	0.1	72	GaO ₆
P45Ga3						
1	113.8	5.5	4.8	0.1	13	GaO ₄
2	28.9	6.0	4.8	0.1	13	GaO ₅
3	-30.1	9.3	6.8	0.1	74	GaO ₆
P45Ga5						
1	114.8	5.5	4.8	0.1	15	GaO ₄
2	24.1	6.0	4.8	0.1	15	GaO ₅
3	-35.2	9.3	6.8	0.1	70	GaO ₆
P45Ga10						
1	127.1	5.8	4.8	0.1	21	GaO ₄
2	23.4	6.0	4.8	0.1	10	GaO ₅
3	-37.2	9.5	6.8	0.1	69	GaO ₆
P45Ga15						
1	121.7	6.0	4.8	0.1	44	GaO ₄
2	19.9	6.0	4.8	0.1	12	GaO ₅
3	-37.7	10.5	7.1	0.1	44	GaO ₆
P50Ga0						
1	106.2	6.0	4.8	0.1	4	GaO ₄
2	13.2	6.0	4.8	0.1	8	GaO ₅
3	-37.5	10.5	7.0	0.1	88	GaO ₆
P50Ga3						
1	105.5	6.0	4.8	0.1	10	GaO ₄
2	13.2	7.6	4.8	0.1	13	GaO ₅
3	-36.1	11.1	7.0	0.1	77	GaO ₆
P50Ga5						
1	110.4	6.0	4.8	0.1	13	GaO ₄
2	18.0	6.0	4.8	0.1	14	GaO ₅
3	-34.0	11.2	7.0	0.1	73	GaO ₆
P50Ga10						
1	113.2	6.0	4.8	0.1	26	GaO ₄
2	14.6	6.0	4.8	0.1	10	GaO ₅
3	-41.7	11.9	7.0	0.1	64	GaO ₆
P50Ga15						
1	110.4	6.0	4.8	0.1	50	GaO ₄
2	11.8	6.0	4.8	0.1	15	GaO ₅
3	-41.7	12.2	7.0	0.1	35	GaO ₆
P55Ga1						
1	105.8	6.0	4.8	0.1	5	GaO ₄
2	17.9	5.9	4.8	0.1	9	GaO ₅
3	-42.1	8.3	6.7	0.1	86	GaO ₆
P55Ga3						
1	112.1	6.0	4.8	0.1	4	GaO ₄
2	17.9	5.9	4.8	0.1	11	GaO ₅
3	-40.1	9.0	6.7	0.1	85	GaO ₆
P55Ga5						
1	109.1	6.0	4.8	0.1	7	GaO ₄
2	16.55	5.9	4.8	0.1	11	GaO ₅
3	-47.0	9.7	6.7	0.1	82	GaO ₆
P55Ga10						
1	111.9	6.0	4.8	0.1	18	GaO ₄
2	7.6	6.0	4.8	0.1	14	GaO ₅
3	-47.7	10.6	6.7	0.1	68	GaO ₆

Table 5.4: ^{71}Ga NMR parameters from simulation of single pulse NMR spectra. Parameters constrained from multiple field fitting, using Quadfit software package. [153]

at the few papers in the literature on ^{71}Ga NMR of phosphate materials, with Amri *et al.* and Belkebir *et al.* showing for Ga phosphate materials that the tetrahedral GaO_4 lies in the region 110 to 130 ppm, GaO_5 in the region of 0 to 30 ppm, and octahedral GaO_6 -30 to -70 ppm.[177, 182] The intensities of each species can be seen in Figures 5.6, however it is immediately clear that the initial low level incorporation of Ga into the glass network results in octahedral coordination of this species, whereby increasing Ga incorporation results in an increase in tetrahedral Ga at the expense of octahedral. The proportion of five-coordinated GaO_5 is fairly consistent throughout all these glass systems at about the 10 % level. This behaviour is similar to that observed in the ^{27}Al MAS NMR studies carried out in Chapter 4 on Al phosphate glasses, thus demonstrating the fact that Ga is likely having a very similar role within the phosphate glass network to Al.

There are few trends observed for the C_Q centre parameters within each system, except that the C_Q centre values characterising the six coordinated Ga sites increases for each series as the Ga content increases. This increase becomes more substantial as the phosphate content increases, with the P45 series showing a change of ~ 1 MHz, the P50 series of ~ 2 MHz and the P55 series of ~ 2.5 MHz (even though the highest Ga content for the latter series is only 10 mol%). This is indicating the GaO_6 is occupying a less shielded environment upon its higher incorporation, most likely involved in a less pronounced role within the glass network, perhaps linking end chain units.

5.3.5 $\{^{31}\text{P}\}$ - ^{71}Ga J -HMQC

A $\{^{31}\text{P}\}$ - ^{71}Ga J -HMQC experiment was carried out on the P45Ga15 glass; this glass was selected as the best candidate for this experiment as it contains the highest Ga content of that series. This measurement was undertaken at 20.0 T with the spectrum shown in Figure 5.7. This experiment presents numerous challenges owing to low signal to noise arising from numerous factors, thus requiring very long acquisition times. This included the fact that the volume of the sample was small due to the necessity for fast MAS, and other difficulties were induced by the large linewidths of both the ^{31}P (and also more significantly) the ^{71}Ga resonances. Despite these limitations the J -HMQC experiment shown in Figure 5.7 clearly shows signal indicating the presence of Ga-O-P bonds within the glass network, as would be expected. Correlations are observed

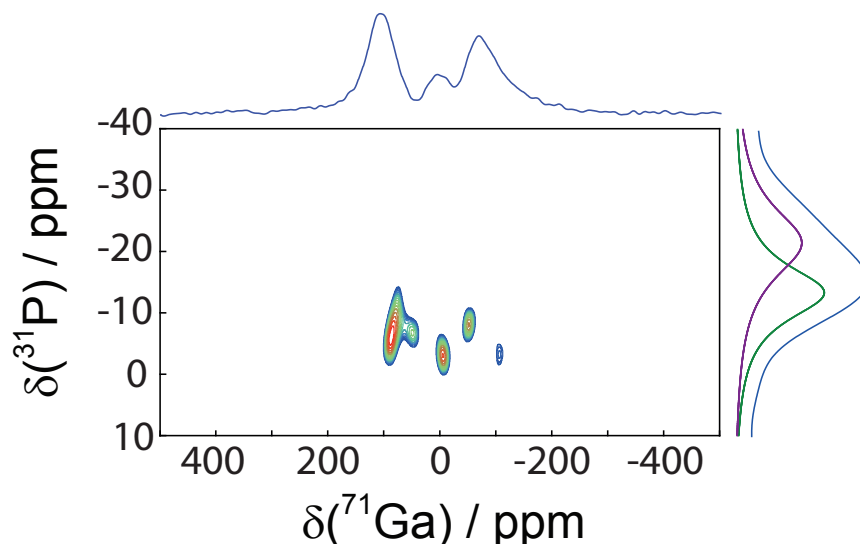


Figure 5.7: $\{^{31}\text{P}\}\text{-}^{71}\text{Ga}$ J -HMQC of P45Ga15 glass carried out at 20.0 T using 60 kHz MAS. 8000 transients were coadded for 28 t_1 slices, with a $\tau/2$ delay of 3.33 ms.

between each of the three Ga sites and the P Q^1 unit, as is indicated by the MAS projections displayed on each of the corresponding axis. The lack of correlation with the Q^2 site indicates that the Ga has more tendency to enter the glass network bonding to the Q^1 sites, as may be expected due to the less P-O-P BO sites. A noticeable difference in intensity between each of the correlations is observed, with the four coordinated GaO_4 site showing the most intense correlation, and the six coordinated GaO_6 the least. This could be attributed to the $\tau/2$ delay used in this experiment favouring the tetrahedral GaO_4 resonance, due to the $\tau/2$ delay being dependant on the J coupling, which probably differs between sites. However, this change in intensity of the sites most likely will arise from the fact that the J coupling is largely dependent upon the covalence of the bond, the covalence of the GaO_4 bonds will be greater, owing to its tendency to take up more of a network former role than that of the GaO_6 resonance, which acts more like a network modifier. Attempts to repeat the experiment at a lower field (14.1 T) were unsuccessful, even upon utilising a larger sample volume. This is most likely due to the fact that at lower field the lines become broader due to the increase in the second order quadrupole interaction, consequently making the experiment more difficult to perform.

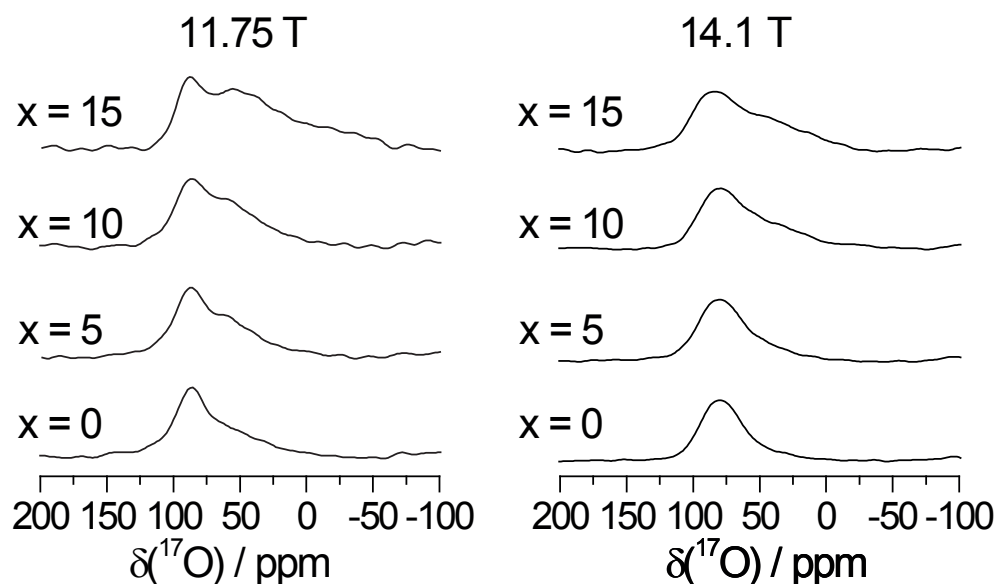


Figure 5.8: ^{17}O Spin Echo NMR of P50Gax ^{17}O labelled samples, carried out at 11.75 T and 14.1 T using 12.5 kHz MAS.

5.3.6 ^{17}O Spin Echo MAS NMR and 3QMAS

In order to combat the low natural abundance of the ^{17}O nucleus, successful ^{17}O enrichment was achieved for a select few of the glass samples from the P50 series. The ^{17}O spin echo experiment was performed at 11.75 and 14.1 T as shown in Figure 5.8, with the data exhibiting reasonably broad resonances, emanating from the disordered glass structure and the different O species characterising the network. Two distinct types of O species will undoubtedly be present corresponding to bridging (BO) O involved in P-O-P bonding, and non-bridging (NBO) oxygen corresponding to $\text{P-O}^-\text{M}^+$ oxygen bonding (where M corresponds to a metal cation). Looking at Figure 5.8, the 1D ^{17}O MAS NMR data clearly indicates the presence of multiple sites present, however their resolution is limited by the quadrupole broadening of the resonances. This can be investigated further upon utilising the MQMAS experiment, enabling distinct resonances to be resolved via extension into a second dimension free from the quadrupole broadening. ^{17}O MQMAS results, carried out at two fields, are shown in Figure 5.9. Upon looking at all of the ^{17}O MQMAS data the two anticipated resonances can be identified, with the intense resonance at around $\delta_{F1} = 90$ to 120 ppm assigned to the NBO site, with the BO resonance seen to be present at around $\delta_{F1} = 170$ to 180 ppm with a much lower intensity. [183, 185] The overlap of the chemical shift in the horizontal (F_2)

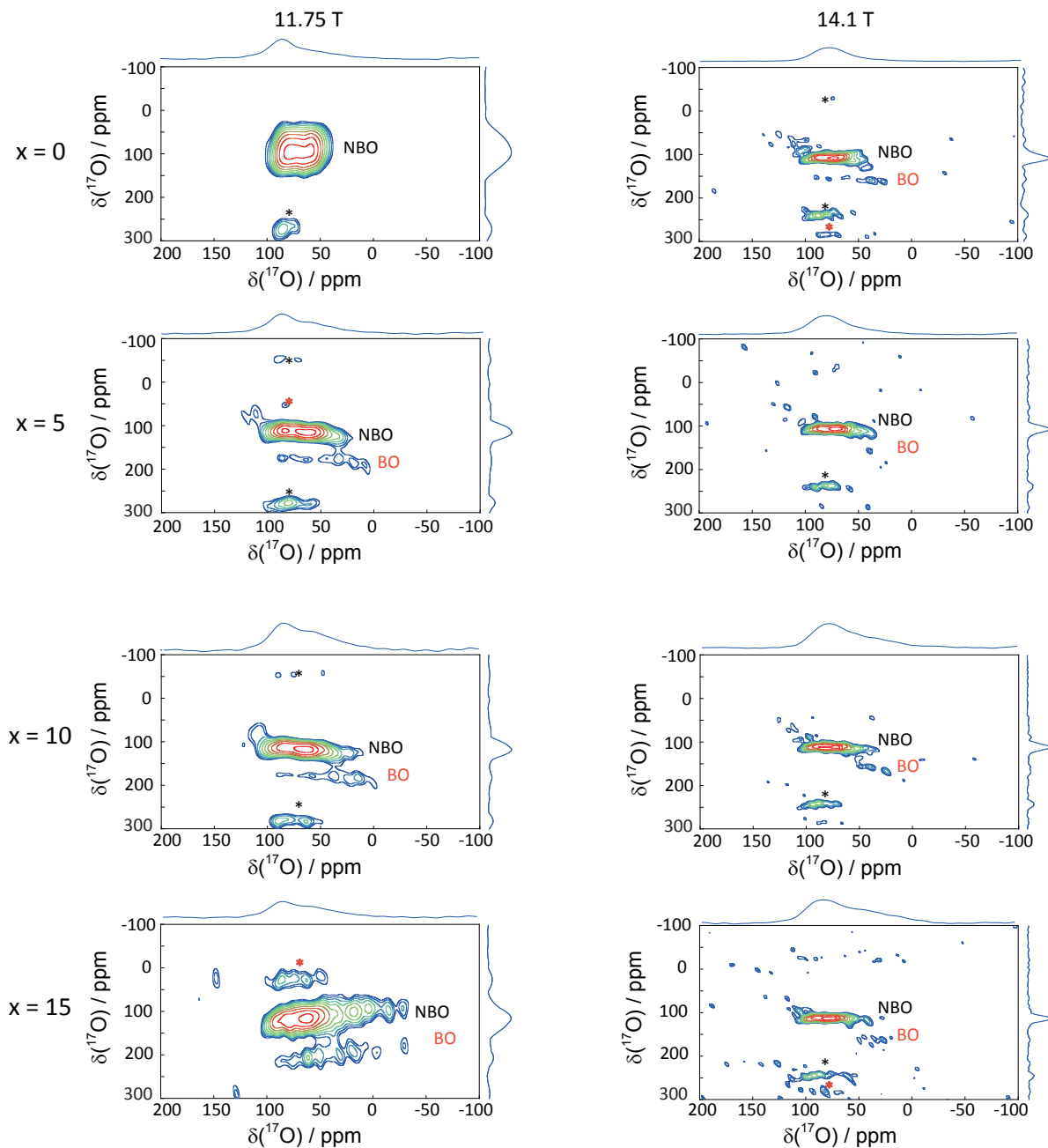


Figure 5.9: ^{17}O 3QMAS NMR of P50Gax ^{17}O labelled samples, carried out at 11.75 T and 14.1 T using 12.5 kHz MAS. NBO and BO resonances clearly indicated, with corresponding spinning sidebands denoted by *

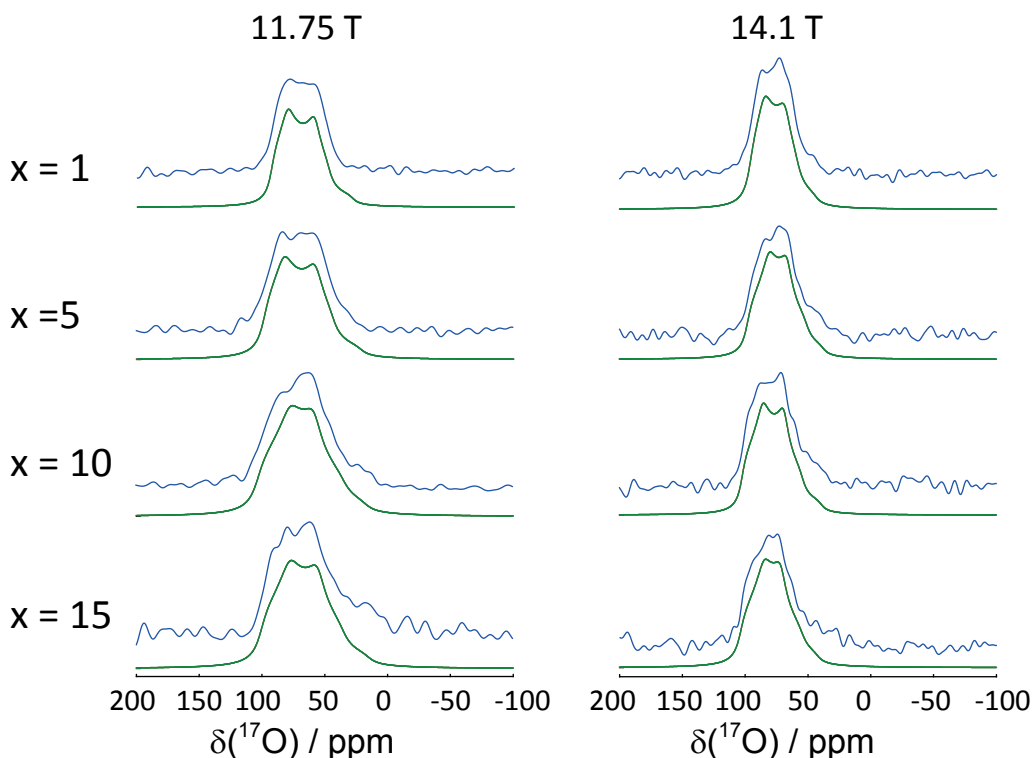


Figure 5.10: Slices of NBO resonance from ^{17}O 3QMAS of P50G_x glasses. Simulations carried out using DmFit software package. [152]

dimension of these two resonances, clearly identifiable from these MQMAS spectra, enforces the difficulty in their observation from the 1D spectra, and the usefulness of the 2D method in resolving multiple sites broadened by the quadrupole interaction.

Further information can be obtained from the MQMAS results upon extracting slices along the ^{17}O F_2 MAS dimension, which if done at the shift corresponding to the NBO, a spectra free from the BO contribution can be obtained, thus enabling fitting of the lineshape to determine the quadrupole and other NMR parameters of this NBO site. Extracted slices and corresponding simulations are shown in Figure 5.10 for all glass samples at both fields, with simulated parameters shown in Table 5.5. Unlike in the echo experiments, it can be seen that the NBO lineshapes themselves are not broad and featureless, but actually show a distorted second ordered quadrupole lineshape, indicating that even though there is overall disorder in the glass structure, the ^{17}O NBO show relatively little chemical shift dispersion.

Although the slices from the MQMAS show relatively small chemical shift dispersion from the quadrupole nature of their lineshapes, due to disorder inherent in

	$\delta(\text{ppm})$ 11.75 T	$\delta(\text{ppm})$ 14.1 T	C_Q Center (MHz)	η	Environment
P50Ga0	97.4	99.0	4.7 ± 0.2	0.35 ± 0.02	NBO
P50Ga5	103.5	100.2	5.0 ± 0.1	0.43 ± 0.09	NBO
P50Ga10	106.0	105.1	5.2 ± 0.1	0.50 ± 0.05	NBO
P50Ga15	104.1	105.4	5.1 ± 0.1	0.50 ± 0.04	NBO

Table 5.5: ^{17}O NMR parameters from simulation of slices from 3QMAS NMR spectra.

the glass structure some chemical shift dispersion will undoubtedly be present. This is clearly evidenced by the F_1 projections in the MQMAS being broad indicating a wide range local O environments. It can be observed that upon incorporation of Ga into the glass network the chemical shift dispersion of the NBO sites is increasing, particularly noticeable when observing the broadening of the NBO for the 11.75 T data, comparing the $x = 5$ and $x = 15$ glass results. This increase in chemical shift dispersion comes about due to O becoming involved in a greater number of coordinations due to the new Ga sites that are being occupied and created with its incorporation.

Using the NMR parameters extracted from fitting the MQMAS data, information about the glass structure can be inferred. Previous studies have shown that the C_Q parameter of ^{17}O is strongly correlated to the covalence of the bond present, as seen from the clearly differing C_Q values for both the BO and NBO sites.[186, 193] However, Vasconcelos *et al.* went further to show that the C_Q parameter is sensitive to the O coordination present, whereas η_q is sensitive to the angular geometry of the P- ^{17}O bond, and δ_{cs} is reliant on the much longer range order.[185] C_Q values determined here for the NBO are in the range (4.7 ± 0.2) and (5.2 ± 0.1) MHz which is similar to other reported values on crystalline and glassy phosphates, with Zeyer *et al.* finding 4.7 MHz, and Vasconcelos *et al.* in a NaPO_3 glass 4.3 to 4.5 MHz.[183, 185] For the results found in these glass systems the C_Q values for the NBO sites do not change significantly. However, the η_q value changes from (0.35 ± 0.02) to (0.50 ± 0.04) , thus indicating that even though the C_Q and bond covalence isn't varying significantly, there is an effect on the P-O bond as we incorporate Ga into the network indicated by the change in η_q . δ_{cs} also changes as Ga is incorporated into the glass structure, with a decrease of around 7 ppm, indicating an alteration in the long range order of the glass,

as might be expected with Ga subsequently being incorporated, and its tendency as seen from ^{71}Ga NMR, to take up varying coordinations dependent upon the content of Ga therein.

Unfortunately, due to the low signal to noise of the BO site and the fact that probably not all of the lineshape is being excited, extracting lineshape slices from this peak is not possible. Even upon using the extracted data from the MQMAS for the NBO slice to constrain parameters and then adding in a further peak to represent the BO site, the number of independent parameters were too many to constrain to achieve reliable fits for the spin echo data at two fields. However, the C_Q of the BO can be predicted to fall within the region of 7 to 8 MHz from the apparent linewidth of the resonance, which is typical of values determined from other studies on these type of materials.[183, 185]

5.4 Discussion and Conclusions

As shown in the numerous previous studies on phosphate glass systems using NMR, the spin $I = 1/2$ ^{31}P nucleus still remains a powerful tool in the characterisation of structure, specifically in determining the Q species present. The fact that the P50 and P45 series both show an increase in Q^1 and decrease in Q^2 as Ga enters the network, indicates that Ga is entering the glass network and removing P-O-P bonds within these Q^2 units, thus creating P-O-Ga linkages. This is further confirmed by the $\{^{31}\text{P}\}$ - ^{71}Ga J -HMQC experiment showing the Ga being predominately coordinated to the Q^1 unit in the P45Ga15 glass. This also accounts for the broadening and overlap of the two resonances, due to the increase in P local environments upon Ga incorporation. For the P55 series it is observed that there appears to be a ‘polymerisation’ of the glass network caused by Ga incorporation, in that the amount of Q^3 units increases significantly. However, this can be again thought of as the Ga associating with the Q^2 units, which are initially dominant, however this time rather than removing P-O-P bonds the Ga is instead removing the NBO. This leads to an apparent increase in Q^3 units, however in fact probably corresponds to Q^2 units, with two P-O-P bonds and one P-O-Ga bond. This is further supported by the fact that the chemical shift of these resonances is moving to more positive ppm, which is similar to the P45 P50 series. This

is also supported by the ^{71}Ga NMR in that it is shown that Ga enters the network in a variety of coordinations, ultimately tending to a four fold GaO_4 coordination upon higher incorporation. Similar trends are found from ^{27}Al and ^{31}P NMR studies on Al phosphate glasses in Chapter 4, thus suggesting Ga has a similar structural role in the glass network to that of Al, as may be anticipated due to Ga sitting just below Al in the same group in the periodic table. Further proof of this conclusion could be made upon carrying out additional $\{^{31}\text{P}\}$ - ^{71}Ga J -HMQC experiments on the P55 glass series, in order to confirm where the Ga is coordinated within the phosphate network for this series.

Although similarities between the role of Ga and Al in the glass networks are observed, the REINE analysis suggests that there must be some difference between the two nuclei. For instance the REINE analysis was only successful for glasses with low Ga contents (under 5 mol% Ga_2O_3), whereas for the ^{27}Al glass the REINE experiment was found to work even for glasses with 8 mol% Al_2O_3 . In addition, unlike as found for the Al containing glasses, there is no significant change in the J couplings observed from the REINE results in the Ga series, which indicates small change on the local P-O-P bond angles and bond lengths. Therefore unlike Al, Ga is having less effect on the actual geometry of the P tetrahedra upon its initial incorporation in this P45 series. This is contradicted in the P50 series by the fact that there is an observed change in the value of η_Q from the ^{17}O measurements, indicating changes in P-O bonds upon Ga incorporation. However any comparisons may be unfair, in that the REINE analysis has been carried out on the P45 series, whereas the ^{17}O measurements are on the P50 series. Therefore, further investigation of ^{17}O measurements on the P45 series would provide further insight, to determine if the η_Q , which is related to the P-O bond angle, shows invariance in the P45 series, as found from the REINE analysis of this series and the role of Ga within the P network may in fact be very different for both series, despite similar trends in its coordination.[185]

Other trends observed in the ^{17}O NMR parameters are however consistent with the other multinuclear NMR results. Firstly the ^{17}O chemical shift observed is found to change upon Ga incorporation, thus proving the change in the long range order of the glass. This is also evident from ^{71}Ga NMR, by the changing Ga incorporation, from GaO_6 at low concentrations, to increasingly condensed network linked by GaO_4

cross links for higher Ga contents. The change in chemical shift of the ^{23}Na resonances also shows this change in long range order, as the ^{23}Na site becomes more shielded as the Ga content increases. However the lack of a change in the ^{17}O C_Q , for the NBO, is implying that the short range order around the ^{17}O nucleus is fairly consistent throughout the Ga incorporation. Slices taken from the ^{17}O MQMAS of the NBO site clearly show a second order quadrupole lineshape, with only slight distortions to it. This has been found in other phosphate glasses, indicating that the distribution of NMR parameters for these NBO sites are not too large, in that the lineshape shows only a slight distortion from the typical second order line observed.[185]

MQMAS can be notoriously difficult due to the lack of efficiency of exciting and reconverting multiple quantum coherences, which explains the lack of signal observed for the BO for all the ^{17}O results. This could perhaps be further improved by carrying out an STMAS experiment instead; however the difficulty inherent in this experimental approach lies in the accurate setting of the magic angle, making it less practical for multiple samples.[195–199] More important information perhaps would come from carrying out DFT calculations on simple glass models, in order to predict the NMR parameters of each of the sites. This approach has been carried out in many previous studies on phosphate materials however, so the assignments made in this study are thought to be very reliable.[185, 190] A greater understanding of the structure of these glass systems would be gained from ^{17}O labelling of the other samples in the other series, however owing to the cost of producing and buying ^{17}O label, this was not viable for each series in this study, and the middle ground series of P50 had to be settled upon.

Phosphate glasses are not the only version of bioactive glasses, with silicon bioactive glass already a well-developed branch of biomaterials. Further NMR studies on silicate type bioactive glasses, with similar compositions to the phosphate glasses studied here, are now in progress, to look at the Ga incorporation into these materials. The recent advances in NMR as utilised here in this study, such as high B_0 fields and fast MAS, will enable further information to be extracted, exploiting these new tools available to look at the usually inaccessible ^{17}O and ^{71}Ga nuclei.

Previous studies have included investigations into the biological activity of similar types of glasses, however no biological studies have been carried out on glasses with these exact compositions.[76, 168] Therefore, the most suitable bioactive glass in

these series is unknown. However it is known that Ga^{3+} ions are a useful addition to the glass, due to the antibacterial properties of Ga, so the glass that would be ideally suited for applications would steadily release these Ga^{3+} ions over time. Although the common problem with phosphate bioactive glasses remains that they have very quick dissolution rates, the benefits of the incorporation of Ga could be twofold; in that as well as a Ga release mechanism, the Ga ions actually help stabilise the phosphate network. This is confirmed by ^{71}Ga NMR, with the increase in the GaO_4 network former within the glass, stabilising the network. Therefore, the ideal composition cannot be stated without further studies into their actual bioactive properties and degradation rates, however from studies on similar Al phosphate glasses, a glass with intermediate Ga content is most likely to be the most suited.[75] Though these glasses would of course need to be tailored for the specific needs of the application required.

Chapter 6

A Multinuclear NMR Study of the Tri-cluster and Defect Sites in Mullite and Boron Doped Mullite Systems

6.1 Introduction

Mullites are interesting aluminosilicate materials with uses in both traditional and advanced ceramics. The mullite structure is the only aluminosilicate formed at ambient pressure and can be found to occur in a few places in nature, such as where magma meets Al_2O_3 rich sediments on the Isle of Mull in Scotland, and in volcanic rocks in the Eifel Mountains in Germany.[81] However, the majority of mullite materials are produced synthetically, enabling the formation of families of materials with the nominal stoichiometric form:

$$\text{Al}_2[\text{Al}_{2+2x}\text{Si}_{2-2x}]\text{O}_{10-x} \quad 0.2 < x < 0.9. \quad (6.1)$$

The most common series of mullite ceramics encountered are when $x = 0.25$ [$3\text{Al}_2\text{O}_3 : 2\text{SiO}_2$], and $x = 0.4$ [$2\text{Al}_2\text{O}_3 : \text{SiO}_2$], so called 3:2 and 2:1 mullite series respectively.

The structure of mullite is closely related to the crystalline aluminosilicate sillimanite, Al_2SiO_5 . In a similar manner to the sillimanite structure, the mullite motif

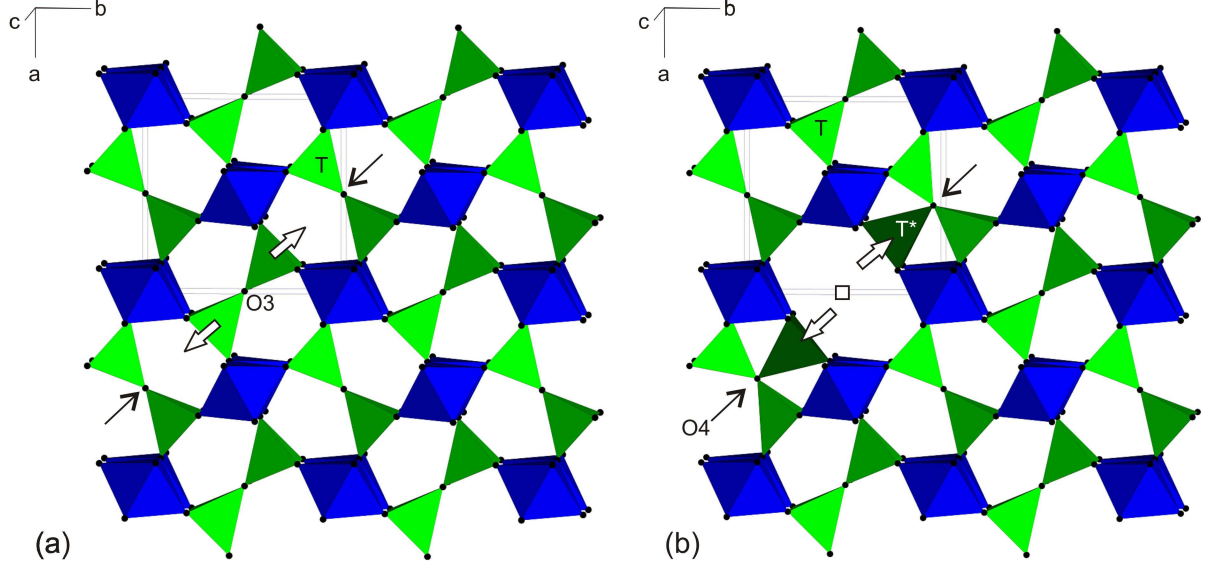


Figure 6.1: Crystal structure of mullite derived from the crystalline sillimanite according to the substitution mechanism: $O^{2-} + 2Si^{4+} = 2Al^{3+} + \square$. White and black arrows indicate the migration direction of the T to AlT^* position and the displacement of $O3$, respectively, resulting in a new oxygen site $O4$. (a) In sillimanite octahedral chains (blue) are linked by tetrahedral groups (green). (b) In mullite octahedral chains are linked by tetrahedral groups or by tri-cluster of tetrahedra. Oxygen vacancies are indicated by squares.[81, 200]

consists of chains of aluminium octahedra (AlO_6) running down the crystallographic c -axis, with Al and Si tetrahedra (TO_4) cross linking these octahedral chains. The mullite system is characterised by a fundamental difference since there exists an excess of Al with respect to Si, with some of the corner shared O linking the tetrahedral SiO_4 sites being removed due to charge compensation:



consequently leaving behind an oxygen vacancy (\square). The removal of this oxygen results in an orientational rearrangement where one tetrahedra ‘flips back’ to facilitate the formation of a 3 coordinated O environment. This ultimately results in the formation of a new site, the so called tri-cluster (AlT^*) site. The structure of mullite is shown in Figure 6.1 along with the associated vacancy formation mechanism.

Although the general structure of mullite is thought to be well established there still remain some disputes relating to its structure, which is why the material has been the focus of numerous studies using a wide variety of spectroscopic

methods.[80, 81, 201, 202]. Owing to the underlying disorder in mullite due to this substitution mechanism, solid state NMR has remained one of the key structural tools, enabling further insight into the structure of mullite to be determined.[92–95, 203]. Early publications using solid state NMR to investigate mullite materials focused on ^{29}Si and ^{27}Al single pulse MAS experiments. The structure is believed to consist of three Al positions, a 6 coordinated AlO_6 moiety, a 4 coordinated AlO_4 moiety and the proposed AlT^* species, with the identification of the AlO_4 and AlO_6 sites presenting a trivial problem using ^{27}Al MAS NMR. In contrast, the presence of the tri-cluster AlT^* site has proven more difficult to characterise with Merwin *et al.* reporting marginal evidence of this ^{27}Al resonance using single pulse MAS NMR techniques, and later Kunath-Fandrei *et al.* used satellite transition (SATRAS) NMR methods in order to infer its presence.[92, 203] To date the only direct observation of this elusive AlT^* site remains the work by Bodart *et al.* on a 2:1 mullite system displaying its presence via ^{27}Al 3QMAS NMR.[97] Previous ^{29}Si MAS NMR studies have shown that the mullite structure possesses numerous Si sites, with an array of distinct ^{29}Si resonances being reported.[92–94, 96] The common consensus is that the most intense ^{29}Si resonance at ~ -86 ppm is attributed to a sillimanite-type environment,[92–94, 96] with the accompanying resonances present being attributed to changes in the next-nearest-neighbour environment of each SiO_4 tetrahedra, determined by calculations as shown by Ban and Okada.[93]

A fundamental question surrounding the mullite structure pertains to the specific structure of the tri-cluster; i.e. whether Si actually takes part in the tri-cluster formation, or whether this species only accommodates participation by the AlO_4 cations. Ban and Okada attributed two resonances in their ^{29}Si spectrum to a (Si, Al, Al^*) type cluster which previously was deemed unlikely to occur.[93] However, a year later Kunath-Fandrei *et al.* claimed no Si is involved in tri-clusters, due to the proportion of T^* (atom next to the oxygen vacancy) and T' (the atom linked to the T^*) resonances measured by ^{27}Al MAS NMR, implying that Si involvement in tri-clusters is not possible.[203] Other studies have argued for and against the presence of Si within the tri-cluster, with no real consensus being reached.[95, 201, 204] Another fundamental aspect of the mullite structure that remains unresolved relates to the ordering of the AlO_4 and SiO_4 tetrahedra. The sillimanite structure possesses alternating AlO_4 and

SiO₄ species, however owing to the O vacancies present in mullite the same cannot be true. Angel *et al.* showed that the mullite structure has a well-defined ordering scheme, and Schmücker *et al.* showed by ²⁹Si NMR and simulations, that the Al/Si distribution of tetrahedra is not strictly random but there is little tendency to de-mix.[96, 201] This aspect remains a subject of much debate.

Due to the mullite structure being able to accommodate a wide variety of different dopant cations, attention is not solely limited to pure aluminosilicate mullites.[205] B doped mullites, bridge the gap between pure aluminosilicate mullite and that of aluminoborates and have been the subject of many studies in recent years.[86, 206, 207] Pure Al borates, such as Al₁₈B₄O₃₃ and Al_{6-x}B_xO₉, have a wide range of uses including reinforcement for uses in metal matrix composites owing to their high strength,[208] refractory linings due to high resistance to B rich glass melts, and components in nuclear reactors because of their neutron absorbing capabilities.[80, 85, 86, 90, 205, 209, 210] In comparison, aluminosilicate mullites have excellent mechanical and thermal properties, such as low thermal expansion coefficients, low thermal conductivity, and excellent creep resistance. Hence, the combination of these two materials means B doped mullite has great potential for uses in a very wide range of material science and engineering applications.

Structural studies on B incorporation into mullite structures have shown that there are significant changes upon the lattice parameters, thus clearly evidencing the incorporation of B into the mullite framework.[86, 89, 206] Griesser *et al.* showed that B is in a BO₃ coordination,[86] and subsequent studies by Lühns *et al.* further showed that this incorporation occurs as BO₃ units substituting for the tetrahedral units, cross-linking the octahedral chains perpendicular to the *c*-axis.[206] This occurs via the substitution mechanism;



and these studies were supported by Rietveld refinements with difference Fourier calculations and gridsearch analysis of neutron diffraction data, along with ¹¹B MAS NMR.[207] This substitution scheme is illustrated in Figure 6.2.

Owing to the recent experimental advances in solid state MAS NMR instrumen-

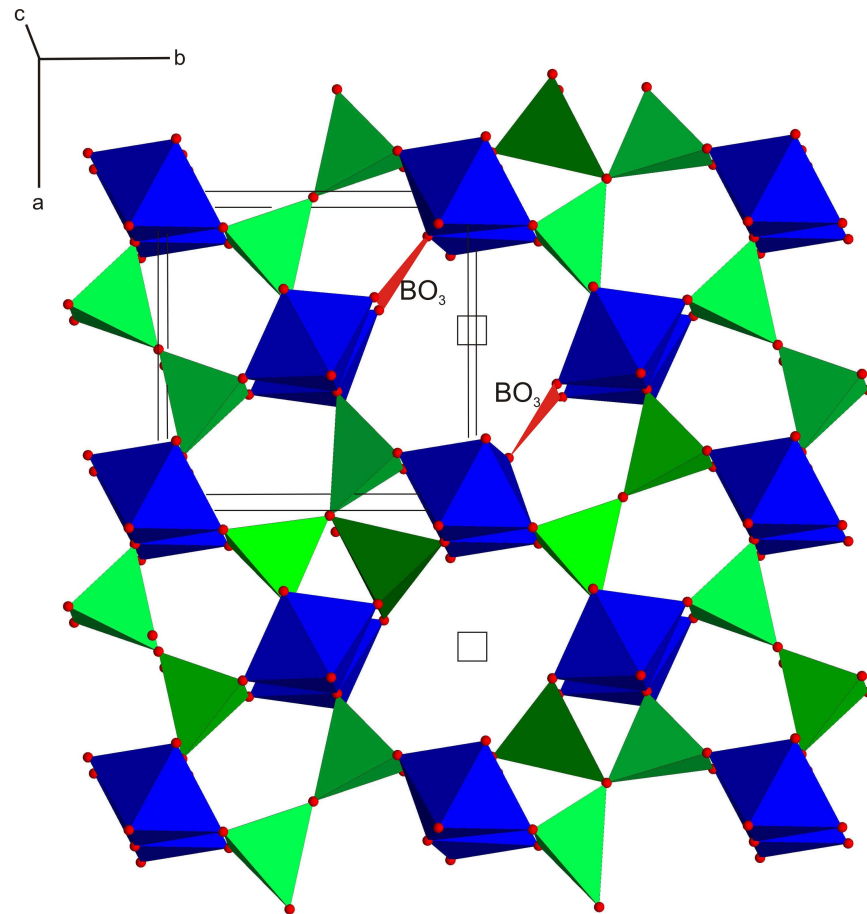


Figure 6.2: Crystal structure of B doped mullite showing the Si B substitution mechanism. Only one site of B incorporation and one tri-cluster site is shown for clarity. Figure taken from the work carried out in [206].

tation and techniques a thorough multinuclear solid state NMR investigation into the structure of mullite is provided. This study uses an array of different NMR experimental methodologies to help further prove and clarify details of the mullite structure, and B incorporation therein.

6.2 Experimental Details

Samples starting from the 3:2 mullite composition ($\text{Al}_{4.5}\text{Si}_{1.5}\text{O}_{9.75}$) with increasing B contents (1, 4, 6 mol% B_2O_3) along with labelled samples were synthesised as indicated in Lühns *et al.* see Table 6.1.[206] An additional sample of pure 2:1 mullite was obtained as single crystal form which was then crushed before carrying out NMR measurements. Pure crystalline sillimanite of gem quality was also used. Purity of the samples was checked by XRD before NMR studies were conducted.

All ^{27}Al single pulse MAS NMR measurements were performed at 9.4 T using a Bruker Avance-400 spectrometer, 11.75 T using a Bruker Avance III-500 spectrometer and 14.1 T using a Bruker Avance II-600 spectrometer, at Larmor frequencies of 103.92 MHz, 130.31 MHz, and 156.18 MHz, respectively. All ^{27}Al MAS NMR experiments utilised a Bruker 3.2 mm HX probe which enabled MAS frequencies of 15 kHz. The multifield data was used to constrain quantitative estimates of the proportion of each Al site present, and also to constrain the quadrupole NMR parameters upon simulation of the data. Flip angle calibration was performed on a 1.1 M $\text{Al}(\text{NO}_3)_3$ solution from which a ‘non-selective’ (solution) $\pi/2$ pulse time of 19.8 μs was measured. This corresponds to a ‘selective’ (solid) pulse time of 6.6 μs for the $I = 5/2$ ^{27}Al nucleus. All measurements were undertaken with a $\pi/12$ tip angle (‘selective’) pulse of 1.1 μs to ensure quantitative estimates of the different ^{27}Al species present, along with a delay between subsequent pulses of 5 s. All ^{27}Al centre of gravity (apparent) shifts were reported against the IUPAC recommended primary reference of $\text{Al}(\text{NO}_3)_3$ (in D_2O 1.1 M, δ 0.0 ppm), via a solid yttrium aluminium garnet (YAG) secondary in which the six coordinate resonance is a known shift of δ 0.7 ppm.[101, 150]

^{27}Al 3QMAS experiments were performed at 9.4 T and 14.1 T, using the three pulse amplitude modulated Z -filtered sequence.[132] Triple quantum excitation and reconversion pulses of 4.2 μs 1.4 μs (9.4 T), 2.25 μs 0.75 μs (14.1 T) respectively, were

Reference Name	Mol % Al_2O_3	Mol % SiO_2	Mol % B_2O_3
3:2 mullite (^{29}Si Labelled)	60	40	0
1 % B doped 3:2 mullite	61	38	1
4 % B doped 3:2 mullite	62	34	4
6 % B doped 3:2 mullite	64	30	6
6 % B doped 3:2 mullite (^{29}Si Labelled)	64	30	6
2:1 mullite	66.5	33.5	0
Sillimanite	50	50	0

Table 6.1: Compositions of samples under investigation in this study. Composition shown is the initial composition of the gel before synthesis.

implemented while the soft $\pi/2$ Z -filter pulse was set to 26 μs (9.4 T) and 22 μs (14.1 T). A maximum of 720 transients were co-added for between 128 and 256 t_1 increments.

All ^{11}B solid state MAS NMR measurements were performed at a B_0 field of 14.1 T using a Bruker Avance II-600 spectrometer, at a ^{11}B Larmor frequency of 192.30 MHz. These measurements utilised a Bruker 4 mm HX MAS probe at MAS frequencies of 12 kHz. A recycle delay of 6 s was common to all experiments. The acquired ^{11}B MAS NMR data were referenced to the IUPAC primary standard $\text{BF}_3\cdot\text{Et}_2\text{O}$ at δ 0 ppm, via a secondary solid reference of NaBH_4 at δ -42.06 ppm.[150, 211] Pulse time calibrations were performed on NaBH_4 and a ‘non-selective (solution) $\pi/2$ pulse time of 6 μs was obtained which corresponded to a ‘selective (solid) pulse time of 3 μs ; all single pulse experiments used a pulse time of 1 μs corresponding to a tip angle of $\pi/6$. An additional experiment with an empty MAS NMR rotor was performed in order to subtract the background signal arising from the boron nitride stator material in the probe.

^{11}B 3QMAS data was obtained on the sample containing the highest B content, using the amplitude modulated Z -filter experiment (p1 - t_1 (3Q evolution) - p2 - τ - p3 - t_2 (acquire)).[132] The optimized pulse lengths of the triple quantum excitation (p1) and reconversion (p2) pulses were p1 = 3.6 μs and p2 = 1 μs , respectively, implemented with an rf power of 125 kHz, while the soft $\pi/2$ Z -filter (p3) pulse was set to 22 μs which was delivered with an rf power of 11 kHz. 1536 transients were co-added for 28 t_1 slices, with the Z -filter τ period set to 20 μs .

Owing to the fact ^{29}Si has a nuclear spin of $I = 1/2$ and thus experiences no quadrupole broadening, experiments were carried out at the lower B_0 field of 7.05 T using a Varian/Chemagnetics InfinityPlus spectrometer, at the ^{29}Si Larmor frequency of 59.62 MHz. However, due to its low natural abundance (4.7 %) experiments were

performed using a Bruker 7 mm HX probe with 5 kHz MAS, to enable maximum sample volume. A 3 μ s pulse corresponding to a flip angle of $\pi/4$ was used. Owing to the long T_1 's of the ^{29}Si nucleus in these systems it was not possible to leave the ^{29}Si natural abundance samples long enough to enable quantitative estimates of the different sites present. However, a pulse delay of 120 s with about 800 scans was used to enable maximum silicon signal, whilst still trying to achieve as much quantification as possible in a realistic experimental time scale (experimental time 26 hours). Chemical shifts were referenced to the IUPAC primary standard TMS (δ 0 ppm) via a secondary solid reference of Kaolinite (δ -92 ppm), which was also used for flip angle calibration.[150, 212]

Labelled ^{29}Si samples, of an undoped and one doped mullite, were synthesised using SiO_2 with 100 % ^{29}Si content, in order to be able to quantify the sites present ensuring no saturation occurs. This was again carried out at 7.05 T using a Varian/Chemagnetics InfinityPlus spectrometer, at the ^{29}Si Larmor frequency of 59.62 MHz. A 3 μ s pulse corresponding to a flip angle of $\pi/4$, and 1800 s delay between subsequent pulses, with only 32 transients required to be co-added in order to gain sufficient signal to noise (experimental time 16 hours).

In order to further gain information on the connectivity of the mullite structure a 1D ^{29}Si refocused INADEQUATE was carried out, which would not have been possible without the ^{29}Si labelling of the samples.[114, 115] The 1D refocused INADEQUATE experiment was carried out at 14.1 T using a Bruker Avance II-600 spectrometer, on both the undoped and 6 % B doped 3:2 mullite, using a Bruker HX 4 mm probe at 12.5 kHz MAS. A delay between subsequent transients of 30 s was deemed to be sufficient, owing to the lack of quantification of the DQ excitation and conversion of this type of experiment. An optimum $\tau/2$ delay of 1 ms was used providing maximum signal intensity.

$\{^{29}\text{Si}\}$ - ^{27}Al J -HMQC experiments, using the sequence by Massiot *et al.*, was carried out on the ^{29}Si labelled mullite samples at 11.75 T using a Bruker Avance III-500 spectrometer, at Larmor frequencies of 99.35 MHz and 130.31 MHz for the ^{29}Si and ^{27}Al nuclei, respectively. A MAS frequency of 20 kHz was used, with a Bruker 3.2 mm HXY probe.[125] The rf field strengths were kept low for ^{27}Al to ensure selective excitation of the central transition (40 kHz for both ^{27}Al and ^{29}Si). Detection

was carried out on the ^{27}Al channel owing to the shorter T_1 of the quadrupolar ^{27}Al nucleus, with a delay between subsequent transients of 5 s. A total of 64 transients were co-added for each of the 256 t_1 slices with a $\tau/2$ delay of 8 ms.

NMR parameters are obtained from simulating the ^{27}Al data using the quadfit software package, and for ^{11}B and ^{29}Si using DMFit software package.[152, 153]

6.3 Results

6.3.1 ^{27}Al MAS NMR

Figure 6.3 shows the ^{27}Al MAS NMR data acquired at three different B_0 fields using single pulse methods for each of the 3:2 mullite systems. Multiple field data enables more quantitative estimates of the NMR parameters and relative intensities of each site, along with small tip angles trying to achieve uniform excitation independent of the quadrupolar effect of each site. It can be seen from the raw data that there are clearly a number of sites present, however the exact number is difficult to ascertain due to the broad ^{27}Al linewidths. As mentioned in previous chapters the broadening of these resonances originates from two main phenomena; (a) the positional disorder in the mullite structure induces a chemical shift dispersion and a distribution of ^{27}Al quadrupole parameters (*i.e.*, distributions in δ_{iso} , C_Q , and η), and (b) the second order quadrupolar broadening is not completely averaged to zero by conventional MAS techniques alone. The tailing of each ^{27}Al resonance to higher field (or more negative ppm) is highly characteristic of the disorder phenomenon influencing these data.[92, 203] This data can be directly compared to the ^{27}Al single pulse MAS NMR data of crystalline sillimanite shown in Figure 6.4, which shows resonances in the same spectral region as that of the mullite samples, however crystalline sillimanite exhibits very distinct second order broadened quadrupole lineshapes, emanating from the discrete tetrahedral (AlO_4) and octahedral (AlO_6) Al positions in the unit cell. This broadening of the 1D ^{27}Al MAS NMR data casts some ambiguity over the analysis in the mullite samples of the number of resonances actually present, as it is not immediately determined with certainty, as has been demonstrated in other ^{27}Al MAS NMR studies of mullites.[92, 94] Hence, some recourse to more advanced 2D MAS NMR techniques is required.

Figure 6.5 shows 3QMAS data acquired at 9.4 and 14.1 T from the 3:2 mullite

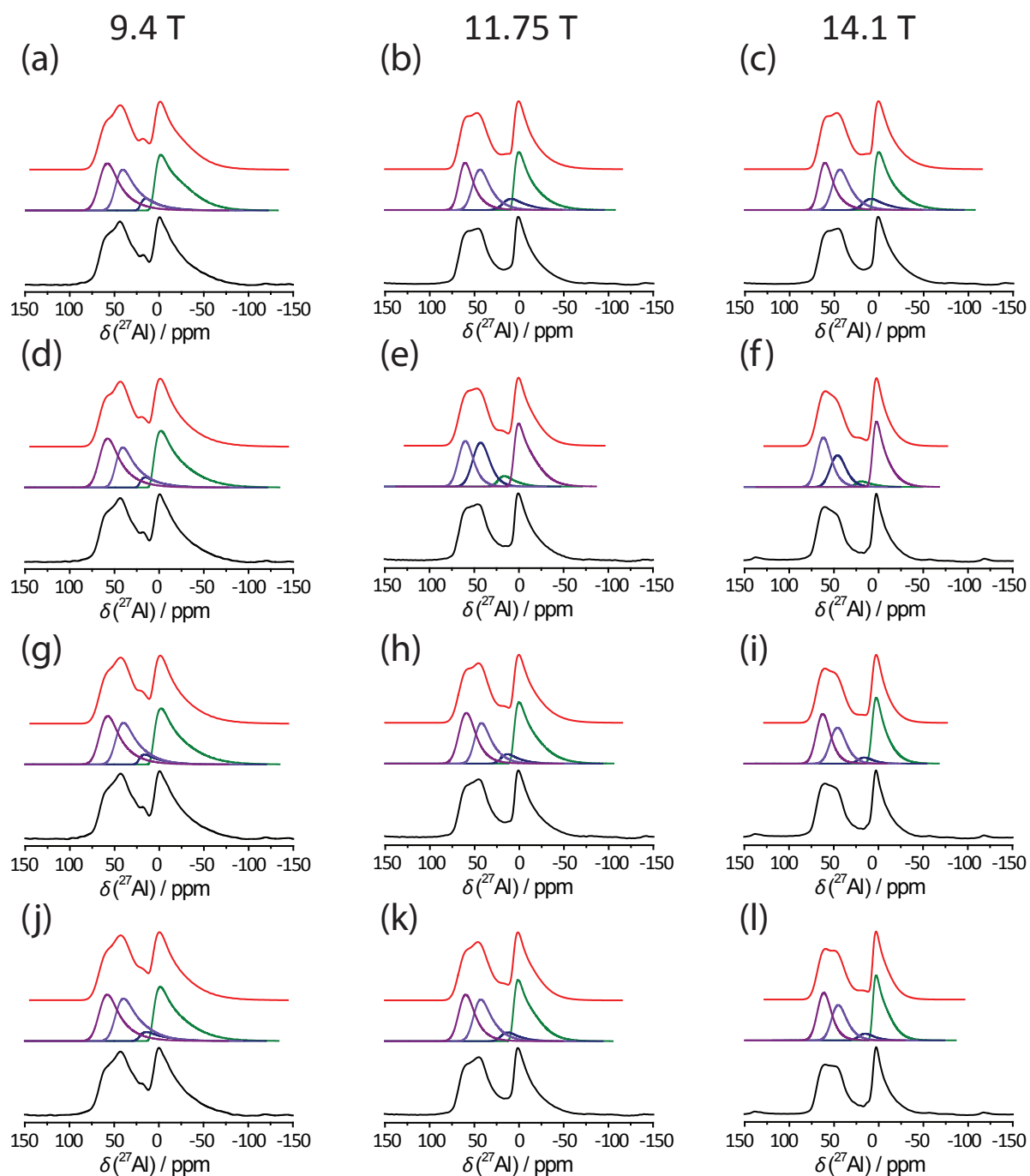


Figure 6.3: Multifield single pulse ^{27}Al MAS NMR spectra along with simulated fits of 3:2 mullite samples, using 15 kHz MAS. (a)-(c) undoped 3:2 mullite, (d)-(f) 1% B doped mullite, (g)-(i) 4% B doped mullite, (j)-(l) 6% B doped mullite.

Peak	$\delta(\text{ppm})$	C_Q Centre (MHz)	C_Q Width (MHz)	η (± 0.05)	Int (%) (± 1)	
Sillimanite						
1	3.8 \pm 1.0	8.9 \pm 0.1	-	0.4	47	AlO ₆
2	63.8 \pm 0.4	7.0 \pm 0.1	-	0.4	53	AlO ₄
3:2 Mullite (²⁹Si Labelled)						
1	9.3 \pm 2.2	7.25 \pm 0.1	4.71 \pm 1.1	0.1	39	AlO ₆
2	22.8 \pm 2.8	7.0 \pm 1.3	4.5 \pm 0.1	0.1	7	AlO ₅
3	52.1 \pm 1.2	5.9 \pm 0.1	4.4 \pm 0.1	0.1	25	AlT*
4	67.1 \pm 0.3	5.2 \pm 0.1	4.7 \pm 0.1	0.1	29	AlO ₄
1% B doped 3:2 Mullite						
1	9.4 \pm 0.5	7.7 \pm 1.1	4.71 \pm 0.1	0.1	40	AlO ₆
2	25.4 \pm 2.3	7.0 \pm 1.2	5.0 \pm 0.9	0.1	5	AlO ₅
3	50.9 \pm 1.4	5.7 \pm 0.1	4.3 \pm 0.1	0.1	25	AlT*
4	66.1 \pm 1.0	5.3 \pm 0.1	4.7 \pm 0.1	0.1	30	AlO ₄
4% B doped 3:2 Mullite						
1	9.5 \pm 0.4	7.3 \pm 0.4	4.7 \pm 0.1	0.1	40	AlO ₆
2	23.1 \pm 1.3	6.2 \pm 0.3	4.5 \pm 0.1	0.1	5	AlO ₅
3	51.1 \pm 1.3	5.8 \pm 0.1	4.3 \pm 0.1	0.1	25	AlT*
4	66.8 \pm 0.8	5.2 \pm 0.1	4.7 \pm 0.1	0.1	30	AlO ₄
6% B doped 3:2 Mullite						
1	10.1 \pm 0.4	7.4 \pm 0.4	4.2 \pm 0.2	0.1	38	AlO ₆
2	22.8 \pm 1.7	6.5 \pm 0.1	4.5 \pm 0.1	0.1	5	AlO ₅
3	51.9 \pm 0.8	6.3 \pm 0.2	4.5 \pm 0.1	0.1	27	AlT*
4	66.6 \pm 0.3	5.2 \pm 0.1	4.7 \pm 0.1	0.1	30	AlO ₄
2:1 Mullite						
1	8.2 \pm 0.6	7.2 \pm 0.1	5.4 \pm 0.1	0.1	46	AlO ₆
2	53.1 \pm 0.6	6.4 \pm 0.1	4.3 \pm 0.1	0.1	29	AlT*
3	66.6 \pm 0.1	5.2 \pm 0.1	4.7 \pm 0.1	0.1	25	AlO ₄

Table 6.2: ²⁷Al MAS NMR parameters from simulation of single pulse NMR spectra. Parameters constrained from multiple field fitting, using Quadfit software package.[153]

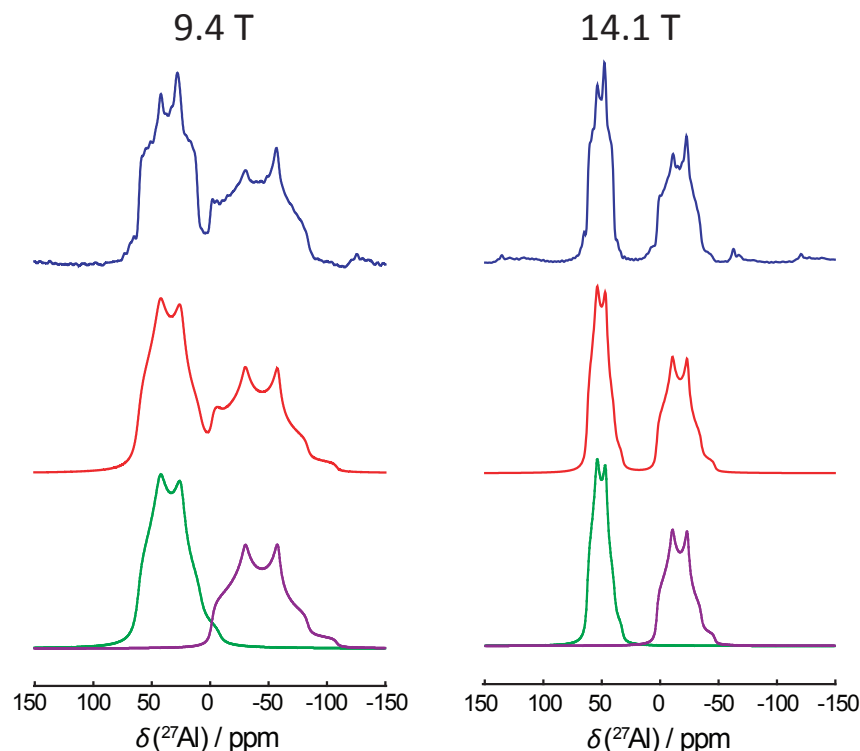


Figure 6.4: Multifield single pulse ^{27}Al MAS NMR spectra along with simulated fits of sillimanite, using 15 kHz MAS.

system and each of the B-doped 3:2 mullite systems. These data clearly demonstrate the existence of three Al positions within each of the mullite systems. The assignment of the two dominant resonances to the AlO_4 and AlO_6 sites is trivial from comparison of the sillimanite ^{27}Al MAS NMR data.[92, 95, 97] However, the 3QMAS clearly shows the presence of another resonance near the tetrahedral AlO_4 resonance, and this is assigned to the Al participating in the tri-cluster species (AlT^*). The presence of this resonance has been postulated to be present in this location; however, these 3QMAS NMR results provide the first unequivocal evidence of its actual existence for a 3:2 mullite, with a similar resonance observed in a 2:1 mullite system by Bodart *et al.*[92, 97, 203] Using the average chemical shifts of these resonances from the 3QMAS data it was then possible to go back to the quantitative single pulse data in order to simulate the 1D ^{27}Al MAS NMR lineshapes accurately. The corresponding simulation parameters elucidated from the analysis are shown in Table 6.2. The presence of a small AlO_5 impurity ($\sim 5\%$) was also required to permit accurate simulation of the ^{27}Al MAS NMR resonances, as has been shown by McManus *et al.* for amorphous aluminosilicates with approximately mullite composition.[213] This is clearly evidenced from the 9.4 T ^{27}Al single pulse

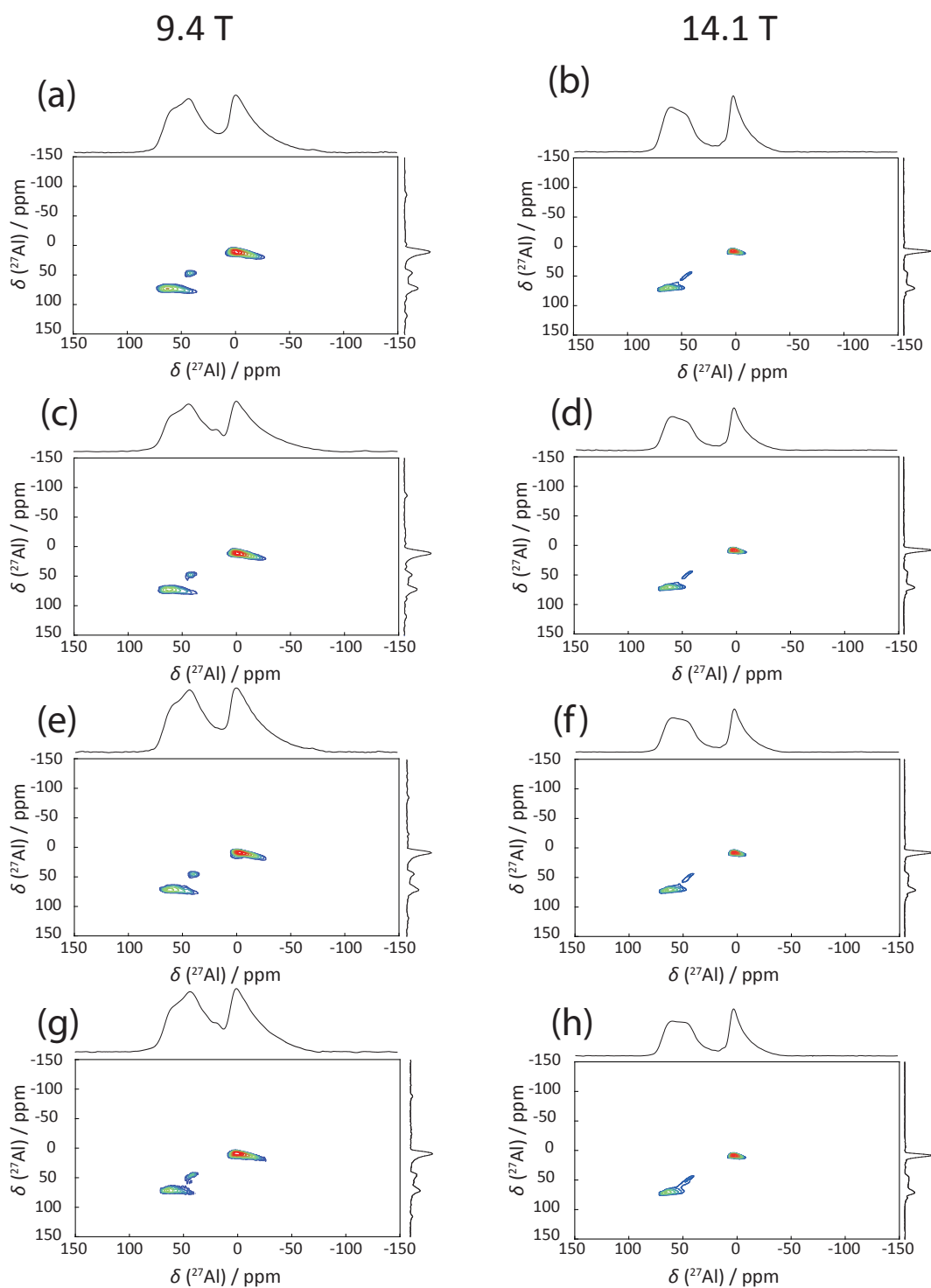


Figure 6.5: Multifield 3QMAS ^{27}Al spectra of 3:2 mullite samples, using 15 kHz MAS. (a)-(b) undoped 3:2 mullite, (c)-(d) 1% B doped mullite, (e)-(f) 4% B doped mullite, (g)-(h) 6% B doped mullite.

MAS NMR data, with its lack of observation from the MQMAS data attributed to the difficulty in exciting triple quantum coherence of distorted resonances with large C_Q values and the low contribution of this site to the overall structure.[214] Owing to its small contribution it is not considered integral to the mullite structure.

The assignment of the Al position contributing to the tri-cluster species AlT^* can be further tested by studying a related 2:1 mullite system, as shown previously by Bodard *et al.*[97] Corresponding 1D ^{27}Al MAS NMR and 2D ^{27}Al 3QMAS data measured from a 2:1 mullite sample is shown in Figure 6.6 where some changes from the 3:2 mullite data can be detected. Upon increasing Al content in the nominal stoichiometry of the mullite composition scheme as described in Equation 6.2, results in x increasing from 0.25 (for the 3:2 mullite) to 0.4 (for the 2:1 mullite) to ensure charge compensation. This results in more O vacancies, and hence more AlT^* tri-cluster species being formed. This is corroborated by the 2:1 mullite exhibiting a greater measured tri-cluster presence (29 %) in comparison to the 3:2 mullite (25 %), which is accompanied by a concomitant decrease in the AlO_4 content by a similar amount (as would be expected).

Upon inspection of the NMR parameters summarised in Table 6.2 which have been elucidated from the ^{27}Al MAS NMR data presented in Figure 6.3 no significant changes or trends are observed from B incorporation into the 3:2 mullite framework. Lühns *et al.* used neutron diffraction techniques to determine split positions for two O atoms in the AlO_6 octahedron induced by B atoms entering into a corner sharing arrangement with the AlO_6 species.[207] From the ^{27}Al MAS NMR data of Figures 6.3 and 6.5 this distortion cannot be detected as inherent linewidths do not permit a degree of sensitivity able to describe the minor distortion and rotation of the AlO_6 octahedra caused by this interaction.

6.3.2 ^{11}B MAS NMR

The ^{11}B MAS NMR technique is a vital tool in order to further understand the consequences of doping B into the 3:2 mullite framework. Figure 6.7 depicts the single pulse ^{11}B MAS NMR data from the 1, 4 and 6 % B doped systems characterised by a well defined second order quadrupole broadened resonance and isotropic chemical shifts typical of a BO_3 coordination. Simulations of the ^{11}B MAS NMR data are presented

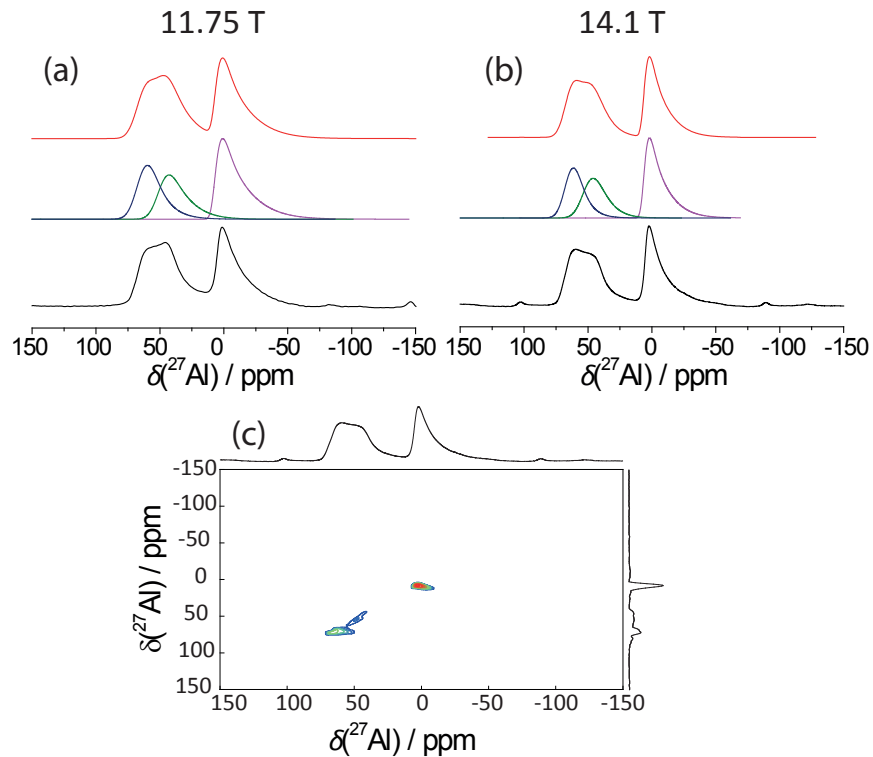


Figure 6.6: Multifield ^{27}Al MAS NMR spectra of 2:1 mullite. (a) and (b) Single pulse with corresponding simulated fits at 11.75 T and 14.1 T, respectively. (c) 3QMAS at 14.1 T, all using 15 kHz MAS.

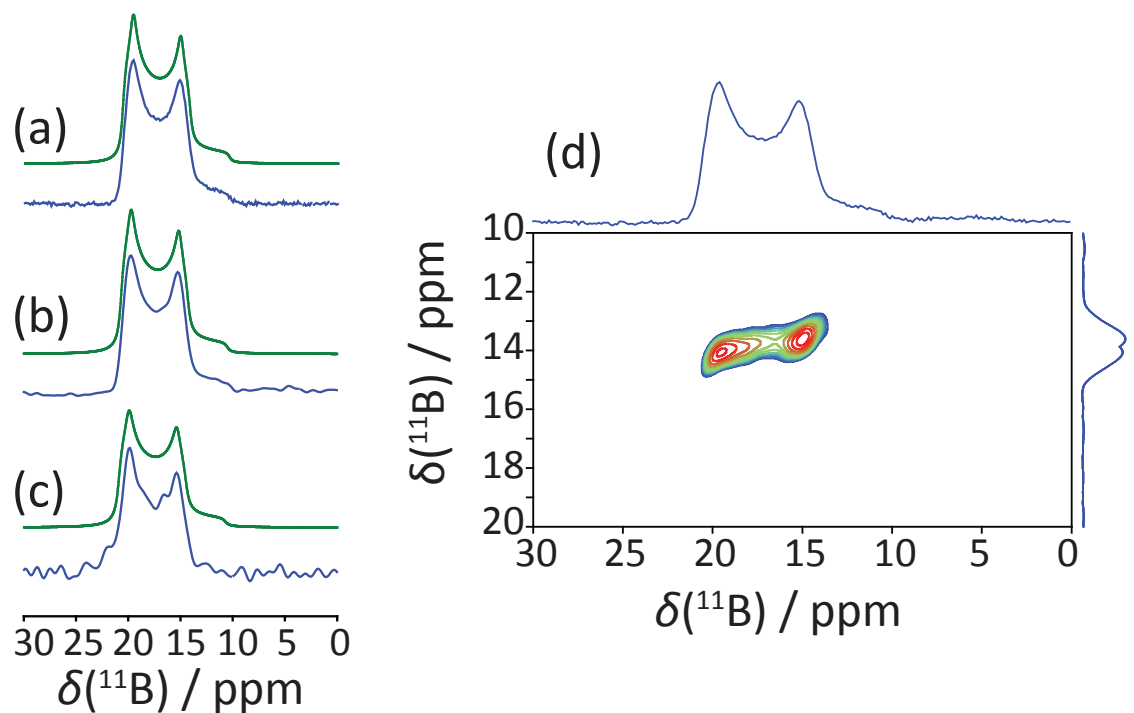


Figure 6.7: ^{11}B MAS NMR spectra at 14.1 T using 12 kHz MAS. Single pulse (a) 1% B doped mullite, (b) 4% B doped mullite, (c) 6% B doped mullite. (d) 3QMAS of 6% B doped mullite.

	δ_{iso} (ppm)	C_Q (MHz)	η	Environment
1 % B doped 3:2 mullite	22.1 \pm 0.5	2.6 \pm 0.1	0.15 \pm 0.01	BO ₃
4 % B doped 3:2 mullite	21.9 \pm 0.5	2.6 \pm 0.1	0.15 \pm 0.01	BO ₃
6 % B doped 3:2 Mullite	21.8 \pm 0.5	2.6 \pm 0.1	0.16 \pm 0.01	BO ₃

Table 6.3: ^{11}B MAS NMR parameters obtained from simulating single pulse ^{11}B MAS NMR data, using the DMFit software package. [152]

in Figure 6.7 along with the corresponding simulation parameters in Table 6.3. Unlike for the ^{27}Al MAS NMR data where the apparent disorder in the Al positions necessitates the simulation using a distribution of quadrupole parameters (the C_Q width parameter), the ^{11}B MAS NMR simulations were simulated using one distinct second order quadrupole broadened lineshape, thus displaying the more local order occupied by the B species. Nevertheless a ^{11}B 3QMAS experiment was performed on the 6 % B doped system, displayed in Figure 6.7. Despite the presence of a distinct second order quadrupole broadened lineshape for the ^{11}B MAS NMR data, the 3QMAS data displays a slight disorder in the B environment evidenced by the contour in the 3QMAS being slightly offset from parallel with respect to the F_2 axis, as one may expect from one distinct ordered B environment. Therefore, this ^{11}B 3QMAS data indicates that a slight distribution of B bond angles and subsequently bond lengths are occupied within the B doped mullite framework.

6.3.3 ^{29}Si MAS NMR

Figure 6.8 shows the single pulse ^{29}Si MAS NMR data for the undoped and the 1, 4 and 6 % B doped 3:2 mullite systems. The undoped and 6 % systems are ^{29}Si labelled and only these samples provide a realistic opportunity to measure quantitative data since the ^{29}Si T_1 's are in excess of 1800 s. These data show that 8 distinct ^{29}Si resonances can be identified (see Table 6.4), which is greater than the 3-5 resonances reported in previous studies.[92, 93, 95, 96] The assignment of some of the Si resonances has been previously attempted and reported in the literature,[92, 93, 95, 96], however the ^{29}Si labelling of some samples can assist in deducing more reliable assignments. The most

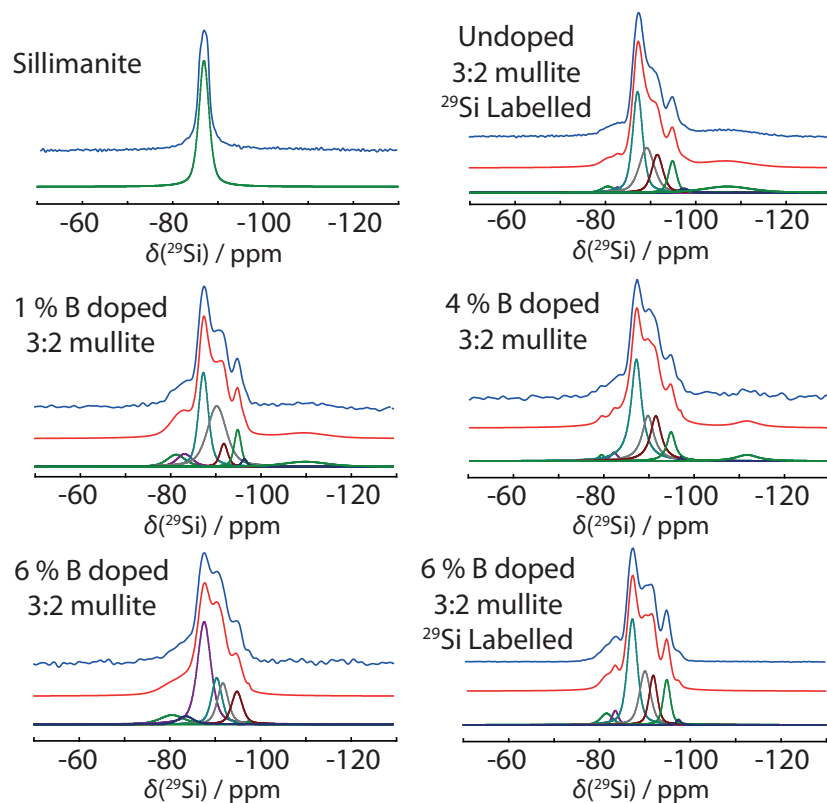


Figure 6.8: ^{29}Si single pulse MAS NMR spectra of sillimanite along with 3:2 mullites. Simulated fits are shown below the experimental data. Experiments were carried out at 7.05 T using 5 kHz MAS.

logical and convenient place to start when assigning these data is to look at the ^{29}Si spectrum of sillimanite, which is characterised by a single resonance at ~ -87 ppm. This resonance represents a Si site with three neighbouring AlO_4 tetrahedra. This structural position is denoted AAA, where A represents an aluminium neighbour. From this we can then infer that the resonance at the same chemical shift in the mullite data is due to the same local arrangement (see Table 6.4). It is then logical to assume that the next three sites moving upfield to more negative ppm is due to the increasing substitution of Si in place of neighbouring AlO_4 tetrahedra thus inducing increased electronegativity to yield the series AAA, SAA, SSA, SSS, (see Table 6.4) [96] It can also be observed that some of the ^{29}Si spectra in Figure 6.8 show a broad resonance in the -107 to -111 ppm region, that can be attributed to unreacted silica that isn't involved in the mullite structure.[215]

The resonances observed downfield at more positive chemical shifts ~ -80 and -82 ppm have only been observed previously by Jaymes *et al.* and Ban and Okada, and were assigned to the rare and unexpected Si sites involved in tri-cluster formation; these

		$\delta(\text{ppm})$ $\pm 0.5 \text{ ppm}$	Int (%) $\pm 1\%$	Environment
Sillimanite	1	-86.9	100	AAA
Undoped	1	-80.6	3 (3)	AAAA
3:2 mullite	2	-82.7	1 (1)	SAAA
²⁹Si Labelled	3	-87.1	35 (40)	AAA
	4	-89.2	24 (27)	SAA
	5	-91.5	15 (17)	SSA
	6	-94.9	9 (10)	SSS
	7	-97.4	2 (2)	SS□
	8	-107.0	11	Silica
1 % B doped	1	-81.2	7	AAAA
3:2 mullite	2	-83.1	6	SAAA
	3	-87.3	29	AAA
	4	-90.2	36	SAA
	5	-91.8	6	SSA
	6	-94.9	8	SSS
	7	-96.3	1	SS□
	8	-109.9	7	Silica
4 % B doped	1	-79.5	2	AAAA
3:2 mullite	2	-82.3	2	SAAA
	3	-87.2	41	AAA
	4	-89.8	21	SAA
	5	-91.5	19	SSA
	6	-94.9	9	SSS
	7	-97.0	1	SS□
	8	-111.7	5	Silica
6 % B doped	1	-80.5	7	AAAA
3:2 mullite	2	-83.5	4	SAAA
	3	-87.6	45	AAA
	4	-90.4	16	SAA
	5	-91.7	15	SSA
	6	-94.8	12	SSS
	7	-97.5	1	SS□
6 % B doped	1	-81.6	5	AAAA
3:2 mullite	2	-83.5	3	SAAA
²⁹Si Labelled	3	-87.3	40	AAA
	4	-90.0	23	SAA
	5	-91.9	15	SSA
	6	-94.8	13	SSS
	7	-97.4	1	SS□

Table 6.4: Simulation parameters derived from the ²⁹Si MAS NMR data from the 3:2 mullite systems carried out at 7.05 T. Simulations were performed using the DMFit software package.[152] Numbers in parentheses indicate when silica is not considered, enabling direct comparison between ²⁹Si labelled systems.

are denoted AAAA and SAAA and their presence is clear from the ^{29}Si MAS NMR data in Figure 6.8.[93, 94] It can be observed that the relative number of Si atoms occupying these positions is only small, which could explain the lack of any observation of Si involvement within tri-cluster formation in many other studies.[92, 96] There is a slight increase in the sites when B is incorporated, however this change is probably within experimental error ranges.

The last outstanding assignment involves the very small resonance at -97 ppm. Previous predictions by Ban and Okada assigned a resonance at -92 to -92.5 ppm to represent a Si position that is predominately surrounded by other Si sites.[93] Their work also noted a silicon site next to an oxygen vacancy exhibits a more upfield or more negative chemical shift. Although the shift observed in this work is much more negative than those quoted by Ban and Okada, they do not account for a Si position surrounded by all Si tetrahedra which are subsequently near O vacancies denoted $\text{SS}\square$, this could account for the more negative shift observed in this work. While this assignment is speculative and lacks further corroboration, it represents a small contribution at the $\sim 1\text{-}2\%$ level (see the quantitative data from the undoped and 6 % B doped mullite systems Table 6.4) to the overall 3:2 mullite framework.

As previously mentioned above strict quantitative comparisons can only be made between the two ^{29}Si labelled systems (i.e. undoped and 6 % B doped mullites). As expected the Si positions participating in the SSA, SAA, and SSS moieties become more prevalent as the composition digresses from the crystalline parent sillimanite structure with increasing B incorporation. This reflects increasing disorder in the mullite structure, however this increasing disorder is not observed from the corresponding ^{27}Al MAS NMR studies as these effects are lost in the disorder broadened linewidths representing the AlO_6 and AlO_4 moieties. These differences between the level of disorder reflected by the ^{27}Al MAS NMR and ^{29}Si MAS NMR studies are more accentuated in the corresponding results for the 2:1 mullite system. The minor perturbations observed in the ^{27}Al MAS NMR data (see Figure 6.6) are accompanied by extremely large changes in the corresponding ^{29}Si MAS NMR data of Figure 6.9. The increasing Al content in the 2:1 system causes a more comprehensive departure from the speciation characterising the sillimanite structure (i.e. AAA units) to a system which is now completely dominated by SSA, SAA and SSS units.

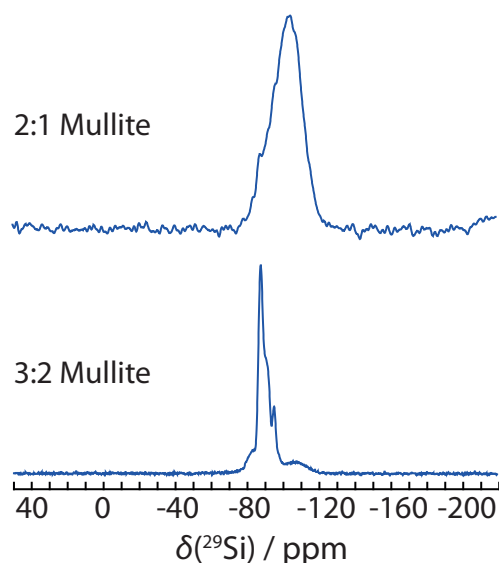


Figure 6.9: Comparison of ^{29}Si single pulse MAS NMR spectra of 2:1 mullite (top) and 3:2 mullite (bottom), at 7.05 T using 5 kHz MAS.

The nature of the tri-cluster species itself can be inferred from the high quality NMR data presented, with both the ^{27}Al MAS NMR and ^{29}Si MAS NMR data as previously mentioned indicating its presence with the involvement of Al and Si, respectively. There appears to be evidence for the existence of multiple tri-cluster environments being formed although they are not equally probable. The most dominant tri-cluster statistically reflected by the ^{27}Al MAS NMR data is the AlT^* moiety comprised of three AlO_4 tetrahedra; this is observed in the simulated data displayed in Table 6.2, which indicates ~ 25 to 27% AlT^* being present. However, the ^{29}Si MAS NMR data shown in Figure 6.8 and Table 6.4 also indicates that Si is directly involved in the tri-cluster formation, although they are not as statistically prevalent (i.e. they appear only at the ~ 2 to 5% level). From the assignments and simulations of the ^{29}Si MAS NMR data in Figure 6.8 and Table 6.4 it can be observed that tri-clusters composed of two Al one Si (AAAA) are more favoured than the scenario of one Al two Si (SAAA). As evidenced by the intensities of these ^{29}Si resonances particularly from the ^{29}Si labelled samples where quantitative measurements have been undertaken.

6.3.4 ^{29}Si refocused INADEQUATE

In order to further corroborate the suggested ^{29}Si assignments discussed in the previous section, which directly impinge upon the proposed structures comprising the tri-cluster

species, some recourse is made to more advanced NMR techniques to substantiate these data. This is especially important here for the 3:2 mullite system as these ^{29}Si MAS NMR studies reveal a multitude of resolved and partially resolved resonances. For the structural characterisation of these systems the use of correlation experiments is necessary to help assist and confirm the proposed assignments that are important for the analysis. The refocused INADEQUATE experiment produces signals only from bonded homonuclear spins, so in theory this approach should be able to delineate which resonances represent these Si positions that participate in Si-O-Si linkages within the mullite framework, providing the J couplings are large enough and T_2 relaxation times not too short.[114, 115] Figure 6.10 shows the 1D ^{29}Si refocused INADEQUATE spectrum of the undoped and 6 % B doped 3:2 mullite, showing the presence of three resonances at -91, -94 and -97 ppm representing the SSA, SSS and $\text{SS}\square$ moieties, respectively. The presence of the first two resonances is expected from the assignments above, with both the SSA and SSS moieties inferring multiple Si-O-Si linkages. In addition the presence of the -97 ppm resonance further supports its assignment from ^{29}Si MAS NMR as $\text{SS}\square$, suggesting again multiple Si-O-Si linkages. Furthermore, the low intensity of this resonance implying its low statistical occurrence corroborates the assignment of a Si tetrahedra near a vacancy, which is further supported by its greater intensity in the refocused INADEQUATE in Figure 6.10 of the 6 % B doped system; i.e. where greater O vacancy concentration is expected.

Perhaps one surprise from looking at the Si assignments is the absence of a signal in the refocused INADEQUATE spectrum from the resonance at $\sim -89/-90$ ppm, assigned to be SAA environment, as it would be expected that one Si-O-Si bond might be present. The lack of this resonance is most likely attributed to the magnitude of the corresponding J coupling being too weak to result in an observable double quantum signal. The nature of the one Si-O-Si tetrahedral bond within the SAA unit probably contains a Si-O-Si bond cross linking the octahedral chains (as opposed to silicon linkages along the c -axis) having a small corresponding J coupling. Further Si incorporation leads to the formation of SSA and SSS units having additional Si-O-Si linkages along the c -axis, the J couplings of which are much larger, and thus explain the signal observed from the refocused INADEQUATE experiment. Further work to corroborate this involving DFT calculations would help in the assignment of

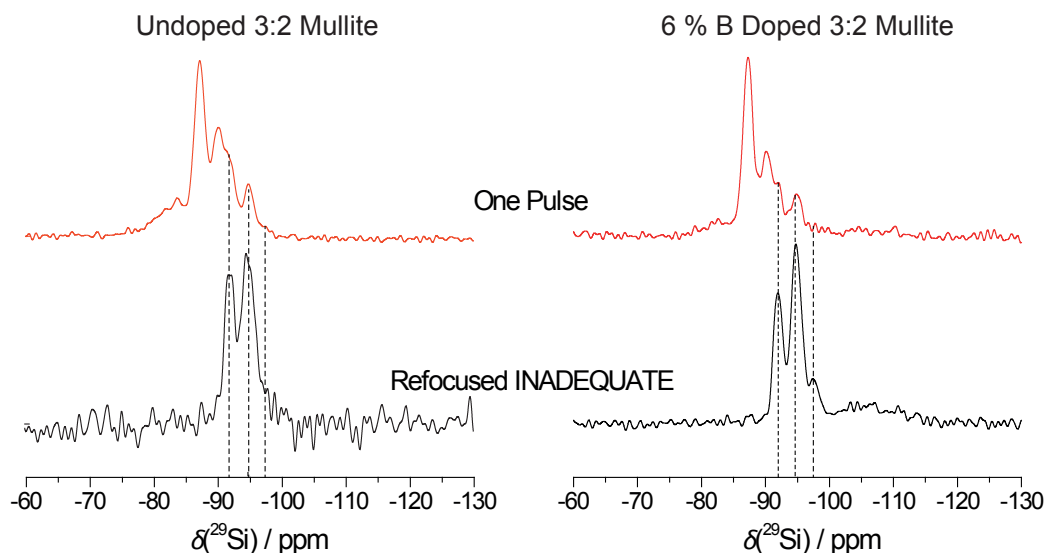


Figure 6.10: 1D ^{29}Si refocused INADEQUATE of 3:2 undoped (left) and 6 % B doped mullite (right) along with their respective ^{29}Si single pulse MAS NMR data, carried out at 14.1 T using 12.5 kHz MAS and $\tau/2 = 1$ ms. The observation of resonances in the refocused INADEQUATE experiment indicates Si-O-Si linkages present.

the Si resonances made, along with corresponding predictions of J couplings for each individual Si environment, thus further supporting this reasoning.

6.3.5 $\{^{29}\text{Si}\}$ - ^{27}Al J -HMQC

In addition to Si-O-Si linkages, it's clear that Al-O-Si linkages are fundamental to the mullite structure. In contrast to the refocused INADEQUATE experiment, which elucidates signals through homonuclear J couplings between like nuclei, the heteronuclear J -HMQC experiment should identify correlations when Si-O-Al linkages are present. Figure 6.11 shows the $\{^{29}\text{Si}\}$ - ^{27}Al J -HMQC data for both the undoped and 6 % B doped 3:2 mullites. The most striking observation is the presence of correlations between the SiO_4 tetrahedra and the AlO_4 tetrahedra as predicted by the structure. However, there is a clear absence of any correlation to the octahedral AlO_6 moieties, even though there exists an unambiguous structural link between the AlO_6 and SiO_4 moieties in the mullite structure. This $\{^{29}\text{Si}\}$ - ^{27}Al J -HMQC experiment was attempted with many different $\tau/2$ delays to reflect some sampling of a spread of heteronuclear J coupling values, but the same result was obtained. As previously mentioned when discussing the refocused INADEQUATE results, the lack of a correlation is most likely indicative of a small J coupling of a magnitude insufficient to induce a double quantum

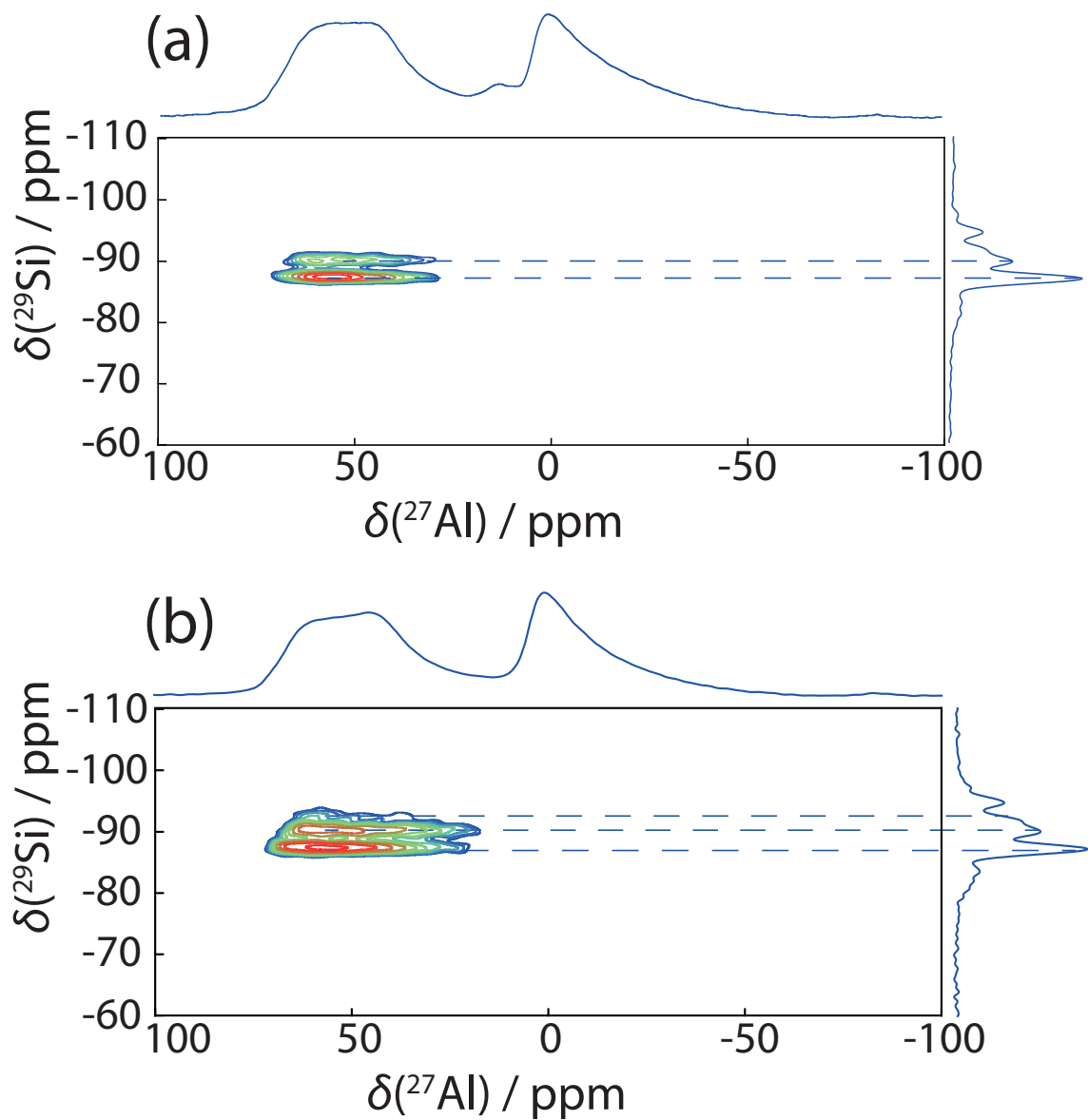


Figure 6.11: $\{^{29}\text{Si}\}$ - ^{27}Al J -HMQC of (a) 3:2 undoped and (b) 6 % B doped mullites carried out at 11.75 T using 20 kHz MAS. 64 transients are co-added for 256 t_1 slices, with a $\tau/2$ delay of 8 ms. Single pulse MAS NMR projections are used to aid in characterisation of sites present.

signal. Therefore, the lack of a correlation between the AlO_6 octahedra and the SiO_4 tetrahedral moieties is not totally unsurprising, due to the less covalent nature of the AlO_6 bonding than that of the tetrahedral AlO_4 and hence a smaller J coupling for this site. The absence of this expected AlO_6 SiO_4 correlation from the J -HMQC data helps indirectly justify the assignment of the SAA ^{29}Si resonance and its lack of observation from the refocused INADEQUATE experiment, as again a correlation is not observed that is undoubtedly present within the mullite structure. Thus, from these correlation experiments caution must be taken when making assignments, in that the lack of observation of a correlation does not always rule out the presence of a connectivity, as clearly demonstrated here.

An important feature of the $\{^{29}\text{Si}\}$ - ^{27}Al J -HMQC data shown in Figure 6.11 can be observed by a direct comparison of the results obtained from the undoped and 6 % B doped mullite systems. These data show that for the undoped 3:2 mullite sample there exists two correlations linking the AlO_4 tetrahedra with SiO_4 tetrahedra, and these SiO_4 environments correspond to SAA and AAA moieties; both of these relationships are easily rationalised. In the 6 % B doped sample these same two correlations are present, however with an additional correlation with SSA also observed. This correlation is also easily rationalised (and anticipated), however it is only observed in the 6 % B doped structure and not from the undoped mullite structure. Therefore, only in the 6 % B doped sample are all of the correlations that would be anticipated from the AAA, SAA, SSA assignments actually observed. The observation of the SSA moiety for the 6 % B doped sample cannot be explained by an increase in the intensity of this site when compared to that of the undoped sample, as from the ^{29}Si simulation parameters shown in Table 6.4, the SSA resonance represents (within error ranges) the same contribution in both mullite species. Thus B doping must be directly influencing the structure within the vicinity of the SSA site itself. These structural changes are evidentially resulting in changes to the J couplings thus bringing the couplings into a magnitude regime that is able to be detected by the J -HMQC experiment. This is evidentially providing a fingerprint as to the location of the B incorporation within the mullite framework, showing it to preferentially locate within the near vicinity of the SSA moiety.

6.4 Discussion and Conclusion

Tri-cluster species have been observed by MQMAS NMR in other structures, most notably in using ^{17}O MAS NMR,[126, 216] in addition to ^{27}Al 3QMAS measurements on a 2:1 mullite by Bodart *et al.*[97]. The ^{27}Al 3QMAS NMR experiments performed on both undoped and B doped 3:2 mullite structures in this study have unequivocally provided further confirmation as to the existence, and provided insight into the nature, of these Al tri-cluster environments. Occurrence of Si within the tri-cluster species has additionally been identified from the high quality ^{29}Si MAS NMR obtained, the existence of which has been a subject for debate for some time. The ^{29}Si resonances observed at ~ -80 to -81 and -82 to -83 ppm have been subsequently assigned to AAAA and SAAA, respectively, associated with the Si involvement within tri-clusters, the low occupancy of which illustrating the lack of prior observations of these Si tri-cluster sites. Thus, the nature of the tri-cluster species has been determined to be predominately comprised of three AlO_4 moieties, with the presence of tri-clusters comprised of one SiO_4 two AlO_4 and then two SiO_4 one AlO_4 becoming statistically less prevalent within the mullite framework, with their presence indicated from the ^{29}Si and ^{27}Al MAS NMR data.

Determining ordering of the Si and Al tetrahedra within the mullite structure is best observed by comparing the data obtained to that of sillimanite, with its regular ordering of tetrahedra, A S A S A. From the ^{29}Si MAS NMR it is clear that Si occupies a vast number of environments within the mullite framework in comparison to sillimanite’s well ordered one distinct environment. In addition, ^{27}Al MAS NMR shows that for sillimanite the two second order quadrupolar broadened lineshapes are representing two well-ordered Al speciations. However, in the mullite structure it can be observed that the ^{27}Al MAS NMR resonances are broad with tails characteristic of a distribution of environments displaying a range of quadrupole parameters, as evidenced by the C_Q widths, which are not insignificant when compared to the overall C_Q value. The ^{27}Al 3QMAS data also indicates a significant chemical shift dispersion present, with the resonances in the F_1 (vertical) axis slightly offset from being parallel to the F_2 axis, thus representing a range of Al sites with varying bond angles, bond lengths, and nearest neighbours. Therefore, it can be concluded that there is a lack of

any complete ordering on the short scale within the mullite structure, and any ordering present will ultimately lead to a large unit cell.

Incorporation of B into the mullite structure is well evidenced, due to the observed changes in the lattice parameters, as shown in Lührs *et al.* and Griesser *et al.*[86, 206] These studies also inferred the presence of B in BO_3 coordination using FTIR spectroscopic techniques, with the ^{11}B MAS NMR data within this study supporting these findings. Lührs *et al.* have suggested the incorporation of B being due to a substitution with Si according to Equation 6.3, with the B cross linking the octahedral Al chains. This is further corroborated by the ^{11}B MAS NMR data, in particular due to the low η_Q value of 0.15 suggesting a near-three fold axis of rotation, as expected for a slightly distorted trigonal planar BO_3 environment. Although the resonances observed are due to one B environment which has a distinct second order quadrupole lineshape, there is a slight disorder evidenced in the contours of the 3QMAS, due to it being not perfectly horizontal. This is implying that even though the B is occupying one environment within the mullite structure, there is most likely a range of bond angles and bond lengths associated with this site, as would be expected due to the vacancies present.

From the $\{^{29}\text{Si}\}$ - ^{27}Al J -HMQC correlation experiment the incorporation of B into the 3:2 mullite structure can be attributed to be occurring in close proximity to the SSA moiety. Evidence of this is given from the presence of a correlation between the SSA Si moiety and the AlO_4 moiety within the 6 % B doped mullite, unlike in the case of the undoped mullite, thus the B incorporation is clearly changing the local SSA environment. A $\{^{29}\text{Si}\}$ - ^{11}B J -HMQC correlation experiment, similar to the $\{^{29}\text{Si}\}$ - ^{27}Al J -HMQC correlation experiment, was attempted on the ^{29}Si labelled sample, to provide further insight regarding the B incorporation within the Si network, however this was unsuccessful with no signal observed. The difficulty in this experiment emanates from the low B content within these systems, however further complications may arise from J coupling values being too small to achieve double quantum correlation signals, as was observed for the AlO_6 and SiO_4 correlations.

Solid state NMR has been shown to be a key tool in the structural characterisation of mullite type materials, here helping to tackle the key unanswered questions regarding these complex structures. Attempts to provide further clarity to these data

involving the implementation of DFT calculations using the CASTEP code are in their early stages. This should support the assignments made for the ^{29}Si resonances within this study, along with providing further conclusive evidence to that nature of the tri-cluster species. The main difficulties with this approach remains in constructing a super cell of the mullite structure, which due to its disordered nature will have to be very large to accurately predict reliable NMR results. In addition, ^{17}O NMR would also provide further insight into the nature of the tri-cluster species, with this quadrupolar nucleus being a diagnostic tool in structural characterisation. However, the major limitation here is not with the NMR itself, and is in fact with the method of enriching the sample with ^{17}O , due to its very low natural abundance.

Chapter 7

Summary

7.1 Phosphate Bioactive Glasses

A significant proportion of this thesis has focused on using solid state MAS NMR methods to investigate the structure of phosphate based glasses for potential uses as biomaterials. Due to their disordered nature, NMR has been the natural choice for many studies in the development of these technologically promising materials. It has long been known that the bioactivity of these systems is strongly correlated to their atomic structure, thus making structural knowledge paramount in being able to tailor bioactivity for their specific functions.

The advantages of phosphate based bioactive glasses over their silica counterparts, lies mainly in the similarity in their composition to that of hydroxyapatite found in bone, in addition to their much quicker breakdown rates *in situ*. However, the increase in dissolution rates can sometimes provide a limitation, being too quick for the desired function. Therefore, attempts have been focused on strengthening the phosphate network to provide much more favourable dissolution times. The work by Manupriya *et al.*, showing Al to favourably decrease the glass dissolution rates, has been further investigated using solid state MAS NMR techniques in Chapter 4.[75] The strengthening of the glass network by the incorporation of Al ions has been supported by the ^{27}Al solid state one pulse MAS NMR showing the change in Al from initially octahedral to the more network former tetrahedral coordination, strengthening the phosphate network. The strengthening of the network is also supported by the ^{23}Na solid state one pulse MAS NMR data showing the Na ions becoming more shielded, as

the network becomes more condensed upon Al incorporation.

In Chapter 5 Ga doped phosphate based glasses were investigated using solid state MAS NMR techniques, with the intention that Ga may have a similar structural role to that of Al within the glass network, but with the additional benefit of the antibacterial properties of Ga^{3+} cations. ^{71}Ga solid state one pulse MAS NMR helped support this assumption, with Ga, like Al, entering the glass network in octahedral coordination subsequently taking up a tetrahedral coordination upon its higher incorporation. Although no studies on bioactivity or dissolution rates of these exact glass compositions are found in the literature, it can be expected that the results may mirror that of the Al glasses, however further research in this area would prove insightful.

Successful ^{17}O isotopic labelling was completed enabling ^{17}O solid state MAS NMR to be exploited on one series of the Ga doped glasses. This provided greater insight into the structure of the network, allowing the distinction between NBO and BO resonances. However, the observation of the latter resonance was not straightforward, with difficulty in observing the BO resonance from MQMAS due to the resonance being very broad, indicating the care that is needed when using ^{17}O NMR to determine the number of resonances and NMR parameters.

The implementation of the ^{31}P 2D REINE experiment, the first time this has been demonstrated on a coherent suite of samples, has provided a much deeper insight into the disordered nature of the phosphate network. The decrease of the J coupling upon the incorporation of Al, has provided further evidence to support the condensing of the Al doped phosphate glass network in Chapter 4. In addition, the distribution of J couplings permitted by the pixel by pixel fitting method provides a much greater insight into the distribution of phosphate sites present within the glass. For the Ga doped glass however, the REINE results indicated very little change in the average J coupling throughout the incorporation of Ga, demonstrating that the effect of the two cations within the glass structure is evidently not strictly identical.

Overall the results obtained from the REINE experiment provided insightful information on the J couplings within the phosphate network permitting far more detail than would be obtained from the implementation of the conventional spin echo experiment alone. Despite the drawbacks of the REINE technique, including the long experimental time required which may limit its wide accessibility, the results in this

thesis clearly evidence its suitability as a tool for probing disorder particularly in phosphate materials.

7.2 Mullites

The results presented in Chapter 6 show one of the most comprehensive studies using a multinuclear solid state MAS NMR approach in investigating the mullite structure to date. Recent advances in the field of solid state NMR, both in hardware, permitting much faster MAS rates and higher magnetic fields helping to provide higher resolution spectra, along with the development of more complex pulse sequences such as the MQMAS and correlation experiments, have enabled further insight into the structure, which was not obtainable prior to these advances.

Many of the unanswered questions in the complex mullite structure have been successfully addressed with this NMR approach. Firstly the presence of the tri-cluster species, central to the mullite structure has long been proposed, with all structural studies pertaining to its central role.[80, 83, 84] Bodart *et al.* have provided the best evidence to date of the Al tri-cluster species from ^{27}Al 3QMAS data on a 2:1 mullite system.[97] The ^{27}Al 3QMAS results shown in Chapter 6, corroborate this assignment resulting in a clear and unambiguous observation of the Al tri-cluster site for the 3:2 mullite systems investigated in this study.

^{29}Si solid state MAS NMR on mullite materials has been widely reported in the literature, however the capability of using 100 % ^{29}Si labelled samples in this study has enabled high resolution quantitative results to be obtained. The assignments of the many ^{29}Si resonances have been conducted with the additional aid of correlation experiments, in order to confirm connectivities within the aluminosilicate network. Furthermore, the data has provided explicit evidence for the composition of the tri-cluster site, with a tri-cluster comprised of three AlO_4 moieties being the most prevalent, with the presence of tri-clusters comprised of two AlO_4 one SiO_4 , and one AlO_4 two SiO_4 moieties becoming statistically less prevalent. A lack of ordering in the Al Si tetrahedral network has been shown, due to the broad nature and chemical shift dispersion of the ^{27}Al resonances, thus suggesting a wide range of sites occupied by Al, due to a range of nearest neighbours, bond angles and bond lengths. This results in the appar-

ent ‘disorder’ in the mullite structure, pertaining to a very large unit cell. Attempts are currently being made to construct an accurate unit cell, by collaborators at the University of Bremen using x-ray and neutron diffraction data, along with the NMR data presented here. Upon creation of the cell, DFT CASTEP calculations will then be attempted, if the size of the unit cell permits this. This approach will provide unequivocal confirmation of the assignments of the ^{29}Si solid state MAS NMR data presented here, along with supporting the composition of the tri-cluster proposed.

In addition to providing valuable insight into the ‘conventional’ 3:2 mullite structure, the effect of B doping to a 3:2 mullite system has been determined using ^{11}B MAS NMR. The results of Lühns *et al.* have been corroborated, with B confirmed to occupy a BO_3 coordination, with a second order quadrupole lineshape observed, indicating one occupied site.[207] Although a slight dispersion in the F_1 dimension of the ^{11}B 3QMAS experiment indicates a slight range of bond lengths, and or bond angles. The nature of the incorporation of B into the 3:2 mullite structure previously determined to be cross linking the octahedral Al chains has been confirmed,[207] with the $\{^{29}\text{Si}\}$ - ^{27}Al J -HMQC correlation experiment indirectly providing a much deeper insight into this occupation of B, in that it is clearly in the near vicinity of the SAA Si moiety. This is evidenced by the observation of the SSA resonance from the J -HMQC correlation experiment for the 6 % B doped system, with a lack of this signal in the undoped 3:2 mullite, thus indicating changes to the local SSA environment dependant upon B.

Overall the NMR data presented in Chapter 6 has provided valuable insight into the complex structure of 3:2 mullite systems, with the advances in the field of solid state NMR demonstrating its effectiveness, hopefully stimulating more research in this area in the near future. Further research is being planned, with attempts to ^{17}O isotopically label 3:2 mullite systems, with the hope that this informative nucleus can provide further insight into the mullite structure. This should open up a whole new range of experiments that could be conducted, including both correlation experiments and MQMAS, to further investigate the tri-cluster moiety in particular.

Bibliography

- [1] E. Rutherford. The scattering of alpha and beta particles by matter and the structure of the atom. *Phil.Mag.*, 21:669–688, 1911.
- [2] J. Chadwick. Possible existence of a neutron. *Nature*, 129:312, February 1932.
- [3] I. I. Rabi, J. R. Zacharias, S. Millman, and P. Kusch. A new method of measuring nuclear magnetic moment. *Physical Review*, 53(4):318–318, 1938.
- [4] C. J. Gorter and L. J. F. Broer. Negative result of an attempt to observe nuclear magnetic resonance in solids. *Physica*, 9(6):591–596, 1942.
- [5] E. M. Purcell, H. C. Torrey, and R. V. Pound. Resonance absorption by nuclear magnetic moments in a solid. *Physical Review*, 69(1-2):37–38, 1946.
- [6] F. Bloch, W. W. Hansen, and M. Packard. The nuclear induction experiment. *Physical Review*, 70(7-8):474–485, 1946.
- [7] F. Bloch, W. W. Hansen, and M. Packard. Nuclear induction. *Physical Review*, 69(3-4):127–127, 1946.
- [8] W. G. Proctor and F. C. Yu. The dependence of a nuclear magnetic resonance frequency upon chemical compound. *Physical Review*, 77(5):717–717, 1950.
- [9] W. C. Dickinson. Dependence of the nuclear resonance position on chemical compound. *Physical Review*, 77(5):736–737, 1950.
- [10] W. D. Knight. Nuclear magnetic resonance shift in metals. *Physical Review*, 76(8):1259–1260, 1949.
- [11] N. F. Ramsey. Magnetic shielding of nuclei in molecules. *Physical Review*, 78(6):699–703, 1950.
- [12] G. E. Pake. Nuclear resonance absorption in hydrated crystals: Fine structure of the proton line. *The Journal of Chemical Physics*, 16(4):327–336, 1948.
- [13] J. T. Arnold, S. S. Dharmatti, and M. E. Packard. Chemical effects on nuclear induction signals from organic compounds. *The Journal of Chemical Physics*, 19(4):507–507, 1951.
- [14] E. L. Hahn. An accurate nuclear magnetic resonance method for measuring spin-lattice relaxation times. *Physical Review*, 76(1):145–146, 1949.
- [15] H. C. Torrey. Transient nutations in nuclear magnetic resonance. *Physical Review*, 76(8):1059–1068, 1949.
- [16] M. P. Klein and G. W. Barton. Enhancement of signal to noise ratio by continuous averaging: Application to magnetic resonance. *Review of Scientific Instruments*, 34(7):754–759, 1963.

- [17] R. R. Ernst and W. A. Anderson. Application of fourier transform spectroscopy to magnetic resonance. *Review of Scientific Instruments*, 37(1):93–102, 1966.
- [18] F. A. Nelson and H. E. Weaver. Nuclear magnetic resonance spectroscopy in superconducting magnetic fields. *Science*, 146(3641):223–232, 1964.
- [19] H. S. Gutowsky, D. W. McCall, and C. P. Slichter. Coupling among nuclear magnetic dipoles in molecules. *Physical Review*, 84(3):589–590, 1951.
- [20] E. L. Hahn and D. E. Maxwell. Spin echo measurements of nuclear spin coupling in molecules. *Physical Review*, 88(5):1070–1084, 1952.
- [21] E. R. Andrew, A. Bradbury, and R. G. Eades. Nuclear magnetic resonance spectra from a crystal rotated at high speed. *Nature*, 182(4650):1659–1659, 1958.
- [22] E. R. Andrew, A. Bradbury, and R. G. Eades. Removal of dipolar broadening of nuclear magnetic resonance spectra of solids by specimen rotation. *Nature*, 183(4678):1802–1803, 1959.
- [23] I. J. Lowe. Free induction decays of rotating solids. *Physical Review Letters*, 2(7):285–287, 1959.
- [24] E. L. Hahn. *Hahn, Erwin L.: Pulsed NMR A Personal History*. John Wiley & Sons, Ltd, 2007.
- [25] E. L. Hahn. Spin echoes. *Physical Review*, 80(4):580, 1950.
- [26] H. Y. Carr and E. M. Purcell. Effects of diffusion on free precession in nuclear magnetic resonance experiments. *Physical Review*, 94(3):630, 1954.
- [27] S. R. Hartmann and E. L. Hahn. Nuclear double resonance in the rotating frame. *Physical Review*, 128(5):2042–2053, 1962.
- [28] L. R. Sarles and R. M. Cotts. Double nuclear magnetic resonance and the dipole interaction in solids. *Physical Review*, 111(3):853–859, 1958.
- [29] A. Pines, M. G. Gibby, and J. S. Waugh. Proton enhanced nuclear induction spectroscopy. a method for high resolution NMR of dilute spins in solids. *The Journal of Chemical Physics*, 56(4):1776–1777, 1972.
- [30] E. O. Stejskal, Jacob Schaefer, and R. A. McKay. High-resolution, slow-spinning magic-angle carbon-13 NMR. *Journal of Magnetic Resonance*, 25(3):569–573, 1977.
- [31] W. P. Aue, E. Bartholdi, and R. R. Ernst. Two dimensional spectroscopy. application to nuclear magnetic resonance. *The Journal of Chemical Physics*, 64(5):2229–2246, 1976.
- [32] A. A. Maudsley, L. Moller, and R. R. Ernst. Cross-correlation of spin-decoupled NMR spectra by heteronuclear two-dimensional spectroscopy. *Journal of Magnetic Resonance*, 28(3):463–469, 1977.
- [33] G. Bodenhausen and R. Freeman. Correlation of proton and C-13 NMR-spectra by heteronuclear 2-dimensional spectroscopy. *Journal of Magnetic Resonance*, 28(3):471–476, 1977.

- [34] G. A. Morris and R. Freeman. Enhancement of nuclear magnetic resonance signals by polarization transfer. *Journal of the American Chemical Society*, 101(3):760–762, 1979.
- [35] B. C. Gerstein, R. G. Pembleton, R. C. Wilson, and L. M. Ryan. High resolution NMR in randomly oriented solids with homonuclear dipolar broadening: Combined multiple pulse NMR and magic angle spinning. *The Journal of Chemical Physics*, 66(1):361–362, 1977.
- [36] A. Bax, R. Freeman, and S. P. Kempell. Natural abundance carbon-13-carbon-13 coupling observed via double-quantum coherence. *Journal of the American Chemical Society*, 102(14):4849–4851, 1980.
- [37] P. C. Lauterbur. Image formation by induced local interactions: Examples employing nuclear magnetic resonance. *Nature*, 242(5394):190–191, 1973.
- [38] A. N. Garroway, P. K. Grannell, and P. Mansfield. Image formation in NMR by a selective irradiative process. *Journal of Physics C: Solid State Physics*, 7(24):457, 1974.
- [39] A. W. Overhauser. Polarization of nuclei in metals. *Physical Review*, 92(2):411–415, 1953.
- [40] T. R. Carver and C. P. Slichter. Polarization of nuclear spins in metals. *Physical Review*, 92(1):212–213, 1953.
- [41] K. H. Hausser and D. Stehlik. *Dynamic Nuclear Polarization in Liquids*, volume Volume 3, pages 79–139. Academic Press, 1968.
- [42] L. R. Becerra, G. J. Gerfen, R. J. Temkin, D. J. Singel, and R. G. Griffin. Dynamic nuclear-polarisation with a cyclotron-resonance maser at 5-T. *Physical Review Letters*, 71(21):3561–3564, 1993.
- [43] G. J. Gerfen, L. R. Becerra, D. A. Hall, R. G. Griffin, R. J. Temkin, and D. J. Singel. High frequency (140 GHz) dynamic nuclear polarization: Polarization transfer to a solute in frozen aqueous solution. *The Journal of Chemical Physics*, 102(24):9494–9497, 1995.
- [44] J. H. Ardenkar-Larsen, B. Fridlund, A. Gram, G. Hansson, M. H. Hansson, L. and Lerche, R. Servin, M. Thaning, and K. Golman. Increase in signal-to-noise ratio of >10,000 times in liquid-state NMR. *Proceedings of the National Academy of Sciences*, 100(18):10158–10163, 2003.
- [45] R. Eckman, L. Muller, and A. Pines. Deuterium double-quantum NMR with magic angle spinning. *Chemical Physics Letters*, 74(2):376–378, 1980.
- [46] A. Llor and J. Virlet. Towards high-resolution NMR of more nuclei in solids - sample spinning with time-dependent spinner axis angle. *Chemical Physics Letters*, 152(2-3):248–253, 1988.
- [47] A. Samoson, E. Lippmaa, and A. Pines. High-resolution solid-state NMR averaging of 2nd-order effects by means of a double-rotor. *Molecular Physics*, 65(4):1013–1018, 1988.
- [48] R. Dupree. *Double Rotation (DOR) NMR: from NMR of Quadrupolar Nuclei in Solid Materials*. John Wiley & Sons, Ltd, 2007.

- [49] K. T. Mueller, B. Q. Sun, G. C. Chingas, J. W. Zwanziger, T. Terao, and A. Pines. Dynamic-angle spinning of quadrupolar nuclei. *Journal of Magnetic Resonance (1969)*, 86(3):470–487, 1990.
- [50] M. A. Eastman, P. J. Grandinetti, Y. K. Lee, and A. Pines. Double-tuned hopping-coil probe for dynamic-angle-spinning NMR. *Journal of Magnetic Resonance*, 98(2):333–341, 1992.
- [51] L. Frydman and J. S. Harwood. Isotropic spectra of half-integer quadrupolar spins from bidimensional magic-angle-spinning NMR. *Journal of the American Chemical Society*, 117(19):5367–5368, 1995.
- [52] C. M. Rienstra, L. Tucker-Kellogg, C. P. Jaroniec, M. Hohwy, B. Reif, M. T. McMahon, B. Tidor, T. Lozano-Perez, and R. G. Griffin. De novo determination of peptide structure with solid-state magic-angle spinning NMR spectroscopy. *Proceedings of the National Academy of Sciences*, 99(16):10260–10265, 2002.
- [53] F. Castellani, A. van Rossum, B. Diehl, M. Schubert, K. Rehbein, and H. Oschkinat. Structure of a protein determined by solid-state magic-angle-spinning NMR spectroscopy. *Nature*, 420(6911):98–102, 2002.
- [54] A. H. Silver and P. J. Bray. Nuclear magnetic resonance absorption in glass. I. Nuclear quadrupole effects in boron oxide, soda boric oxide, and borosilicate glasses. *The Journal of Chemical Physics*, 29(5):984–990, 1958.
- [55] A. R. Grimmer, P. Starke, W. Wiek, and M. Magi. High-resolution solid-state Si-29 NMR von silica-gels. *Zeitschrift Fur Chemie*, 22(2):44–44, 1982.
- [56] E. Lippmaa, A. Samoson, M. Magi, R. Teeaar, J. Schraml, and J. Gotz. High-resolution Si-29 NMR study of the structure and devitrification of lead-silicate glasses. *Journal of Non-Crystalline Solids*, 50(2):215–218, 1982.
- [57] W. Schiller, D. Muller, and G. Scheler. Al-27 NMR-studies on the aluminoborosilicate glass-alumina reaction during sintering. *Zeitschrift Fur Chemie*, 22(2):44–45, 1982.
- [58] S. Schramm and E. Oldfield. High-resolution solid-state NMR-studies of quadrupolar nuclei - quadrupole-induced shifts in variable-angle sample-spinning of a borosilicate glass. *Journal of the Chemical Society-Chemical Communications*, (17):980–981, 1982.
- [59] R. K. Brow, R. J. Kirkpatrick, and G. L. Turner. The short-range structure of sodium-phosphate glasses. 1. MAS NMR-studies. *Journal of Non-Crystalline Solids*, 116(1):39–45, 1990.
- [60] R. K. Brow, R. J. Kirkpatrick, and G. L. Turner. Nature of alumina in phosphate-glass .2. structure of sodium aluminophosphate glass. *Journal of the American Ceramic Society*, 76(4):919–928, 1993.
- [61] H. Eckert. Structural characterization of noncrystalline solids and glasses using solid-state NMR. *Progress in Nuclear Magnetic Resonance Spectroscopy*, 24:159–293, 1992.
- [62] R. J. Kirkpatrick and R. K. Brow. Nuclear magnetic resonance investigation of the structures of phosphate and phosphate-containing glasses: a review. *Solid State Nuclear Magnetic Resonance*, 5(1):9–21, 1995.

- [63] U. Hoppe. A structural model for phosphate glasses. *Journal of Non-Crystalline Solids*, 195(1-2):138–147, 1996.
- [64] R. K. Brow. Review: the structure of simple phosphate glasses. *Journal of Non-Crystalline Solids*, 263(1-4):1–28, 2000.
- [65] L. L. Hench, A. E. Clark, and H. F. Schaake. Effects of microstructure on the radiation stability of amorphous semiconductors. *Journal of Non-Crystalline Solids*, 810(0):837–843, 1972.
- [66] L.L Hench. The story of Bioglass. *Journal of Materials Science: Materials in Medicine*, 17(11):967–978, 2006.
- [67] M. Jarcho. Calcium phosphate ceramics as hard tissue prosthetics. *Clinical Orthopaedics and Related Research*, 157:259–278, 1981.
- [68] E. S. Tadjoedin, G. L. De Lange, D. M. Lyaruu, L. Kuiper, and E. H. Burger. High concentrations of bioactive glass material (biogran) vs. autogenous bone for sinus floor elevation. *Clinical Oral Implants Research*, 13(4):428–436, 2002.
- [69] T. Gilchrist, D.M. Healy, and C. Drake. Controlled silver-releasing polymers and their potential for urinary tract infection control. *Biomaterials*, 12(1):76 – 78, 1991.
- [70] E. A. Abou Neel, I. Ahmed, J. Pratten, S. N. Nazhat, and J. C. Knowles. Characterisation of antibacterial copper releasing degradable phosphate glass fibres. *Biomaterials*, 26(15):2247–2254, 2005.
- [71] E. A. Abou Neel, D. M. Pickup, S. P. Valappil, R. J. Newport, and J. C. Knowles. Bioactive functional materials: a perspective on phosphate-based glasses. *Journal of Materials Chemistry*, 19(6):690–701, 2009.
- [72] V. Salih, K. Franks, M. James, G. W. Hastings, J. C. Knowles, and I. Olsen. Development of soluble glasses for biomedical use Part II: The biological response of human osteoblast cell lines to phosphate-based soluble glasses. *Journal of Materials Science-Materials in Medicine*, 11(10):615–620, 2000.
- [73] I. Ahmed, M. Lewis, I. Olsen, and J. C. Knowles. Phosphate glasses for tissue engineering: Part 1. processing and characterisation of a ternary-based $P(2)O(5)-CaO-Na(2)O$ glass system. *Biomaterials*, 25(3):491–499, 2004.
- [74] A. A. El-Kheshen, F. A. Khaliifa, E. A. Saad, and R. L. Elwan. Effect of Al_2O_3 addition on bioactivity, thermal and mechanical properties of some bioactive glasses. *Ceramics International*, 34(7):1667–1673, 2008.
- [75] Manupriya, K. S. Thind, K. Singh, G. Sharma, and V. Rajendran. Influence of addition of $Al(2)O(3)$ on physical, structural, acoustical and in-vitro bioactive properties of phosphate glasses. *Physica Status Solidi a-Applications and Materials Science*, 206(7):1447–1455, 2009.
- [76] S. P. Valappil, D. Ready, E. A. Abou Neel, D. M. Pickup, L. A. O’Dell, W. Chrzanowski, J. Pratten, R. J. Newport, M. E. Smith, M. Wilson, and J. C. Knowles. Controlled delivery of antimicrobial gallium ions from phosphate-based glasses. *Acta Biomaterialia*, 5(4):1198–1210, 2009.

- [77] N. J. Lakhkar, J-H. Park, N. J. Mordan, V. Salih, I. B. Wall, H-W. Kim, S. P. King, J. V. Hanna, R. A. Martin, O. Addison, J. F.W. Mosselmans, and J. C. Knowles. Titanium phosphate glass microspheres for bone tissue engineering. *Acta Biomaterialia*, 8(11):4181 – 4190, 2012.
- [78] D. M. Pickup, I. Ahmed, P. Guerry, J. C. Knowles, M. E. Smith, and R. J. Newport. The structure of phosphate glass biomaterials from neutron diffraction and P-31 nuclear magnetic resonance data. *Journal of Physics-Condensed Matter*, 19(41), 2007.
- [79] J. M. Smith, S. P. King, E. R. Barney, J. V. Hanna, R. J. Newport, and D. M. Pickup. Structural study of $\text{Al}_2\text{O}_3\text{-Na}_2\text{O-CaO-P}_2\text{O}_5$ bioactive glasses as a function of aluminium content. *Journal of Chemical Physics*, 138(3), 2013.
- [80] Hartmut. Schneider and Sridhar Komarneni. *Mullite*. Wiley-VCH ; Chichester : John Wiley [distributor], Weinheim, 2005.
- [81] H. Schneider, J. Schreuer, and B. Hildmann. Structure and properties of mullite - a review. *Journal of the European Ceramic Society*, 28(2):329–344, 2008.
- [82] N. L. Bowen and J. W. Greig. The system: $\text{Al}_2\text{O}_3\text{-SiO}_2$. *Journal of the American Ceramic Society*, 7(4):238–254, 1924.
- [83] H Saalfeld and W Guse. Structure refinement of 3:2 mullite($3\text{Al}_2\text{O}_3\cdot 2\text{SiO}_2$). *Neus Jahrbuch Fur Mineralogie-Monatshefte*, (4):145–150, 1981.
- [84] R. J. Angel and C. T. Prewitt. Crystal structure of mullite; a re-examination of the average structure. *American Mineralogist*, 71(11-12):1476–1482, 1986.
- [85] H. Wada, K. Sakane, T. Kitamura, M. Sunai, and N. Sasaki. Thermal-expansion of aluminum borate. *Journal of Materials Science Letters*, 12(22):1735–1737, 1993.
- [86] K. J. Griesser, A. Beran, D. Voll, and H. Schneider. Boron incorporation into mullite. *Mineralogy and Petrology*, 92(3-4):309–320, 2008.
- [87] A Dietzel and H Scholze. Untersuchungen im system $\text{B}_2\text{O}_3\text{-Al}_2\text{O}_3\text{-SiO}_2$. *Glastechn Ber* 28, pages 47–51, 1955.
- [88] G. Werding and W. Schreyer. Alkali-free tourmaline in the system $\text{MgO-Al}_2\text{O}_3\text{-B}_2\text{O}_3\text{-SiO}_2\text{-H}_2\text{O}$. *Geochimica et Cosmochimica Acta*, 48(6):1331 – 1344, 1984.
- [89] G. Zhang, Z. Fu, Y. Wang, H. Wang, J. Wang, W. and Zhang, S. W. Lee, and K. Niihara. Boron-doped mullite derived from single-phase gels. *Journal of the European Ceramic Society*, 30(12):2435–2441, 2010.
- [90] M. Fisch, T. Armbruster, D. Rentsch, E. Libowitzky, and T. Pettke. Crystal-chemistry of mullite-type aluminoborates $\text{Al}_{18}\text{B}_4\text{O}_{33}$ and Al_5BO_9 : A stoichiometry puzzle. *Journal of Solid State Chemistry*, 184(1):70–80, 2011.
- [91] G. L. Turner, K. A. Smith, R. J. Kirkpatrick, and E. Oldfield. Structure and cation effects on P-31 NMR chemical-shifts and chemical-shift anisotropies of ortho-phosphates. *Journal of Magnetic Resonance*, 70(3):408–415, 1986.
- [92] L. H. Merwin, A. Sebal, H. Rager, and H. Schneider. Si-29 and Al-27 MAS NMR-spectroscopy of mullite. *Physics and Chemistry of Minerals*, 18(1):47–52, 1991.

- [93] T. Ban and K. Okada. Analysis of local cation arrangement in mullite using Si-29 magic-angle-spinning nuclear-magnetic-resonance spectra. *Journal of the American Ceramic Society*, 76(10):2491–2496, 1993.
- [94] I. Jaymes, A. Douy, D. Massiot, and J. P. Coutures. Characterization of mono- and diphasic mullite precursor powders prepared by aqueous routes. Al-27 and Si-29 MAS-NMR spectroscopy investigations. *Journal of Materials Science*, 31(17):4581–4589, 1996.
- [95] I. Jaymes, A. Douy, D. Massiot, and J. P. Coutures. Evolution of the Si environment in mullite solid solution by Si-29 MAS-NMR spectroscopy. *Journal of Non-Crystalline Solids*, 204(2):125–134, 1996.
- [96] M Schmucker, H Schneider, KJD MacKenzie, ME Smith, and DL Carroll. AlO₄/SiO₄ distribution in tetrahedral double chains of mullite. *Journal of the American Ceramic Society*, 88(10):2935–2937, 2005.
- [97] P.R. Bodart, J. Parmentier, R.K. Harris, and D.P. Thompson. Aluminium environments in mullite and an amorphous sol-gel precursor examined by ²⁷Al triple-quantum MAS NMR. *Journal of Physics and Chemistry of Solids*, 60(2):223 – 228, 1999.
- [98] Melinda J. Duer. *Introduction to solid-state NMR spectroscopy*. Blackwell, Oxford, 2004.
- [99] Malcolm H. Levitt. *Spin dynamics : basics of nuclear magnetic resonance*. Wiley ; Chichester : John Wiley [distributor], Hoboken, N.J., 2nd ed. edition, 2008.
- [100] P. J. Hore, J. A. Jones, and Stephen Wimperis. *NMR : the toolkit*. Oxford University Press, Oxford, 2000.
- [101] K.J.D. MacKenzie and M.E. Smith. *Multinuclear Solid State NMR of Inorganic Materials*. Pergamon Materials Series. Pergamon Press, Oxford, 2002.
- [102] David C. Apperley, Robin K. Harris, and Paul Hodgkinson. *Solid-state NMR : basic principles & practice*. Momentum, New York, 2012.
- [103] Morris Edgar Rose. *Elementary theory of angular momentum*. John Wiley & Sons, New York, 1957.
- [104] S. Chandra Shekar and Alexej Jerschow. *Tensors in NMR: from NMR of Quadrupolar Nuclei in Solid Materials*. John Wiley & Sons, Ltd, 2007.
- [105] Roderick E. Wasylishen. *Indirect Nuclear Spin-Spin Coupling Tensors*. John Wiley & Sons, Ltd, 2007.
- [106] Charles P. Slichter. *Principles of magnetic resonance*. Berlin : Springer-Verlag, 1990 (1992 [printing]), 3rd enl. and updated ed. edition. C.P. Slichter. Previous ed.: 1978. Reprinted with corrections.
- [107] A. Abragam. *Principles of nuclear magnetism*. Oxford : Clarendon Press, 1983(1986). International series of monographs on physics.
- [108] Sharon E. Ashbrook and Stephen Wimperis. *Quadrupolar Coupling: An Introduction and Crystallographic Aspects: From NMR of Quadrupolar Nuclei in Solid Materials*. John Wiley & Sons, Ltd, 2007.

- [109] Pascal P. Man. *Quadrupolar Interactions:: From NMR of Quadrupolar Nuclei in Solid Materials*. John Wiley & Sons, Ltd, 2007.
- [110] D. J. States, R. A. Haberkorn, and D. J. Ruben. A two-dimensional nuclear overhauser experiment with pure absorption phase in four quadrants. *Journal of Magnetic Resonance (1969)*, 48(2):286–292, 1982.
- [111] D. Marion and K. Wuthrich. Application of phase sensitive two-dimensional correlated spectroscopy (COSY) for measurements of ^1H - ^1H spin-spin coupling constants in proteins. *Biochemical and Biophysical Research Communications*, 113(3):967–974, 1983.
- [112] L. Duma, W. C. Lai, M. Carravetta, L. Emsley, S. P. Brown, and M. H. Levitt. Principles of spin-echo modulation by J-couplings in magic-angle-spinning solid-state NMR. *Chemphyschem*, 5(6):815–833, 2004.
- [113] A. C. Kunwar, G. L. Turner, and E. Oldfield. Solid-state spin-echo fourier-transform NMR of K-39 and Zn-67 salts at high-field. *Journal of Magnetic Resonance*, 69(1):124–127, 1986.
- [114] A. Lesage, C. Auger, S. Caldarelli, and L. Emsley. Determination of through-bond carbon-carbon connectivities in solid-state NMR using the INADEQUATE experiment. *Journal of the American Chemical Society*, 119(33):7867–7868, 1997.
- [115] A. Lesage, M. Bardet, and L. Emsley. Through-bond carbon-carbon connectivities in disordered solids by NMR. *Journal of the American Chemical Society*, 121(47):10987–10993, 1999.
- [116] S. Cadars, A. Lesage, M. Trierweiler, L. Heux, and L. Emsley. NMR measurements of scalar-coupling distributions in disordered solids. *Physical Chemistry Chemical Physics*, 9(1):92–103, 2007.
- [117] A. Bax, R. Freeman, T. A. Frenkiel, and M. H. Levitt. Assignment of C-13 NMR-spectra via double-quantum coherence. *Journal of Magnetic Resonance*, 43(3):478–483, 1981.
- [118] A. Bax, R. Freeman, and T. A. Frenkiel. An NMR technique for tracing out the carbon skeleton of an organic-molecule. *Journal of the American Chemical Society*, 103(8):2102–2104, 1981.
- [119] S. Cadars, J. Sein, L. Duma, A. Lesage, T. N. Pham, J. H. Baltisberger, S. P. Brown, and L. Emsley. The refocused INADEQUATE MAS NMR experiment in multiple spin-systems: Interpreting observed correlation peaks and optimising lineshapes. *Journal of Magnetic Resonance*, 188(1):24–34, 2007.
- [120] F. Fayon, D. Massiot, M. H. Levitt, J. J. Titman, D. H. Gregory, L. Duma, L. Emsley, and S. P. Brown. Through-space contributions to two-dimensional double-quantum J correlation NMR spectra of magic-angle-spinning solids. *Journal of Chemical Physics*, 122(19):194313, 2005.
- [121] O. W. Sorensen, G. W. Eich, M. H. Levitt, G. Bodenhausen, and R. R. Ernst. Product operator-formalism for the description of NMR pulse experiments. *Progress in Nuclear Magnetic Resonance Spectroscopy*, 16:163–192, 1983.
- [122] P. Guerry, M. E. Smith, and S. P. Brown. P-31 MAS refocused INADEQUATE Spin-Echo (REINE) NMR spectroscopy: Revealing J coupling and chemical shift

two-dimensional correlations in disordered solids. *Journal of the American Chemical Society*, 131(33):11861–11874, 2009.

- [123] A. Bax, R. H. Griffey, and B. L. Hawkins. Correlation of proton and N-15 chemical-shifts by multiple quantum NMR. *Journal of Magnetic Resonance*, 55(2):301–315, 1983.
- [124] A. Lesage, D. Sakellariou, S. Steuernagel, and L. Emsley. Carbon-proton chemical shift correlation in solid-state NMR by through-bond multiple-quantum spectroscopy. *Journal of the American Chemical Society*, 120(50):13194–13201, 1998.
- [125] D. Massiot, F. Fayon, B. Alonso, J. Trebosc, and J. P. Amoureux. Chemical bonding differences evidenced from J-coupling in solid state NMR experiments involving quadrupolar nuclei. *Journal of Magnetic Resonance*, 164(1):160–164, 2003.
- [126] D. Iuga, C. Morais, Z. H. Gan, D. R. Neuville, L. Cormier, and D. Massiot. NMR heteronuclear correlation between quadrupolar nuclei in solids. *Journal of the American Chemical Society*, 127(33):11540–11541, 2005.
- [127] J. P. Amoureux and C. Fernandez. Triple, quintuple and higher order multiple quantum MAS NMR of quadrupolar nuclei. *Solid State Nuclear Magnetic Resonance*, 10(4):211–223, 1998.
- [128] K. J. Pike, R. P. Malde, S. E. Ashbrook, J. McManus, and S. Wimperis. Multiple-quantum MAS NMR of quadrupolar nuclei. do five-, seven- and nine-quantum experiments yield higher resolution than the three-quantum experiment? *Solid State Nuclear Magnetic Resonance*, 16(3):203–215, 2000.
- [129] D. Massiot, B. Touzo, D. Trumeau, J. P. Coutures, J. Virlet, P. Florian, and P. J. Grandinetti. Two-dimensional magic-angle spinning isotropic reconstruction sequences for quadrupolar nuclei. *Solid State Nuclear Magnetic Resonance*, 6(1):73–83, 1996.
- [130] S. P. Brown, S. J. Heyes, and S. Wimperis. Two-dimensional MAS multiple-quantum NMR of quadrupolar nuclei. removal of inhomogeneous second-order broadening. *Journal of Magnetic Resonance, Series A*, 119(2):280 – 284, 1996.
- [131] C. Fernandez and J. P. Amoureux. Triple-quantum MAS-NMR of quadrupolar nuclei. *Solid State Nuclear Magnetic Resonance*, 5(4):315–321, 1996.
- [132] J. P. Amoureux, C. Fernandez, and S. Steuernagel. Z filtering in MQMAS NMR. *Journal of Magnetic Resonance Series A*, 123(1):116–118, 1996.
- [133] S. P. Brown and S. Wimperis. Two-dimensional multiple-quantum MAS NMR of quadrupolar nuclei: A comparison of methods. *Journal of Magnetic Resonance*, 128(1):42–61, 1997.
- [134] Y Millot and P.P Man. Procedures for labeling the high-resolution axis of two-dimensional MQ-MAS NMR spectra of half-integer quadrupole spins. *Solid State Nuclear Magnetic Resonance*, 21(1-2):21–43, 2002.
- [135] S.P Brown, S.E Ashbrook, and S. Wimperis. Al-27 multiple-quantum magic angle spinning NMR study of the thermal transformation between the microporous aluminum methylphosphonates AlMePO-beta and AlMePO-alpha. *Journal of Physical Chemistry B*, 103(5):812–817, 1999.

- [136] S.E. Ashbrook, A.J. Berry, and S. Wimperis. Three- and five-quantum O-17 MAS NMR of forsterite Mg_2SiO_4 . *American Mineralogist*, 84(7-8):1191–1194, 1999.
- [137] J. C. Knowles. Phosphate based glasses for biomedical applications. *Journal of Materials Chemistry*, 13(10):2395–2401, 2003.
- [138] A. Kiani, J. V. Hanna, S. P. King, G. J. Rees, M. E. Smith, N. Roohpour, V. Salih, and J. C. Knowles. Structural characterization and physical properties of P_2O_5 - CaO - Na_2O - TiO_2 glasses by fourier transform infrared, raman and solid-state magic angle spinning nuclear magnetic resonance spectroscopies. *Acta Biomaterialia*, 8(1):333–40, 2012.
- [139] K. K. Olsen, J. W. Zwanziger, P. Hartmann, and C. Jager. Short and intermediate range order in glass: nuclear magnetic resonance probes of site connectivities and distances. *Journal of Non-Crystalline Solids*, 222:199–205, 1997.
- [140] P. Zhang, P. J. Grandinetti, and J. F. Stebbins. Anionic species determination in CaSiO_3 glass using two-dimensional Si-29 NMR. *Journal of Physical Chemistry B*, 101(20):4004–4008, 1997.
- [141] J. C. C. Chan and H. Eckert. Dipolar coupling information in multispin systems: Application of a compensated REDOR NMR approach to inorganic phosphates. *Journal of Magnetic Resonance*, 147(2):170–178, 2000.
- [142] D. P. Lang, T. M. Alam, and D. N. Bencoe. Solid-state $(31)\text{P}/\text{Al}$ -27/ Al -27 and P -31/ Na -23 TRAPDOR NMR investigations of the phosphorus environments in sodium aluminophosphate glasses. *Chemistry of Materials*, 13(2):420–428, 2001.
- [143] L. van Wullen, G. Tricot, and S. Wegner. An advanced NMR protocol for the structural characterization of aluminophosphate glasses. *Solid State Nuclear Magnetic Resonance*, 32(2):44–52, 2007.
- [144] I. Hung, A. Wong, A. P. Howes, T. Anupold, A. Samoson, M. E. Smith, D. Holland, S. P. Brown, and R. Dupree. Separation of isotropic chemical and second-order quadrupolar shifts by multiple-quantum double rotation NMR. *Journal of Magnetic Resonance*, 197(2):229–236, 2009.
- [145] I. Hung, A. P. Howes, B. G. Parkinson, T. Anupold, A. Samoson, S. P. Brown, P. F. Harrison, D. Holland, and R. Dupree. Determination of the bond-angle distribution in vitreous B_2O_3 by B-11 double rotation (DOR) NMR spectroscopy. *Journal of Solid State Chemistry*, 182(9):2402–2408, 2009.
- [146] A. P. Howes, N. M. Vedishcheva, A. Samoson, J. V. Hanna, M. E. Smith, D. Holland, and R. Dupree. Boron environments in Pyrex (R) glass-a high resolution, double-rotation NMR and thermodynamic modelling study. *Physical Chemistry Chemical Physics*, 13(25):11919–11928, 2011.
- [147] F. Fayon, G. Le Saout, L. Emsley, and D. Massiot. Through-bond phosphorus-phosphorus connectivities in crystalline and disordered phosphates by solid-state NMR. *Chemical Communications*, (16):1702–1703, 2002.
- [148] F. Fayon, I. J. King, R. K. Harris, J. S. O. Evans, and D. Massiot. Application of the through-bond correlation NMR experiment to the characterization of crystalline and disordered phosphates. *Comptes Rendus Chimie*, 7(3-4):351–361, 2004.

- [149] L. A. O'Dell, P. Guerry, A. Wong, E. A. Abou Neel, T. N. Pham, J. C. Knowles, S. P. Brown, and M. E. Smith. Quantification of crystalline phases and measurement of phosphate chain lengths in a mixed phase sample by P-31 refocused INADEQUATE MAS NMR. *Chemical Physics Letters*, 455(4-6):178–183, 2008.
- [150] RK Harris, ED Becker, SMC De Menezes, R Goodfellow, and P Granger. NMR nomenclature. nuclear spin properties and conventions for chemical shifts - (IUPAC recommendations 2001). *Pure and Applied Chemistry*, 73(11):1795–1818, 2001.
- [151] S.F. Dec, G.E. Maciel, and J.J. Fitzgerald. Solid-state Na-23 and Al27 MAS NMR-study of the dehydration of Na2O.Al2O3.3H2O. *Journal of the American Chemical Society*, 112(25):9069–9077, 1990.
- [152] D. Massiot, F. Fayon, M. Capron, I. King, S. Le Calve, B. Alonso, J. O. Durand, B. Bujoli, Z. H. Gan, and G. Hoatson. Modelling one- and two-dimensional solid-state NMR spectra. *Magnetic Resonance in Chemistry*, 40(1):70–76, 2002.
- [153] T. F. Kemp and M. E. Smith. Quadfit-a new cross-platform computer program for simulation of NMR line shapes from solids with distributions of interaction parameters. *Solid State Nuclear Magnetic Resonance*, 35(4):243–252, 2009.
- [154] R. K. Brow, R. J. Kirkpatrick, and G. L. Turner. Local-structure of xAl2O3.(1-x)NaPO3 Glasses - An NMR and XPS study. *Journal of the American Ceramic Society*, 73(8):2293–2300, 1990.
- [155] J. M. Egan, R. M. Wenslow, and K. T. Mueller. Mapping aluminum/phosphorus connectivities in aluminophosphate glasses. *Journal of Non-Crystalline Solids*, 261(1-3):115–126, 2000.
- [156] N. S. Barrow, J. R. Yates, S. A. Feller, D. Holland, S. E. Ashbrook, P. Hodgkinson, and S. P. Brown. Towards homonuclear J solid-state NMR correlation experiments for half-integer quadrupolar nuclei: experimental and simulated 11B MAS spin-echo dephasing and calculated 2J(BB) coupling constants for lithium diborate. *Phys Chem Chem Phys*, 13(13):5778–89, 2011.
- [157] S. Cadars, D. H. Brouwer, and B. F. Chmelka. Probing local structures of siliceous zeolite frameworks by solid-state NMR and first-principles calculations of (29)Si-O-(29)Si scalar couplings. *Physical Chemistry Chemical Physics*, 11(48):11660–11660, 2009.
- [158] P. Florian, F. Fayon, and D. Massiot. (2)J Si-O-Si scalar spin-spin coupling in the solid state: Crystalline and glassy wollastonite CaSiO(3). *Journal of Physical Chemistry C*, 113(6):2562–2572, 2009.
- [159] S. E. Lister, A. Soleilhavoup, R. L. Withers, P. Hodgkinson, and J. S. O. Evans. Structures and phase transitions in (MoO(2))(2)P(2)O(7). *Inorganic Chemistry*, 49(5):2290–2301, 2010.
- [160] R. Wise. Antimicrobial resistance: priorities for action. *Journal of Antimicrobial Chemotherapy*, 49(4):585–586, 2002.
- [161] S. R. Norrby, C. E. Nord, and R. Finch. Lack of development of new antimicrobial drugs: a potential serious threat to public health. *Lancet Infectious Diseases*, 5(2):115–119, 2005.

- [162] R. J. C. McLean, A. A. Hussain, M. Sayer, P. J. Vincent, D. J. Hughes, and T. J. N. Smith. Antibacterial activity of multilayer silver copper surface-films on catheter material. *Canadian Journal of Microbiology*, 39(9):895–899, 1993.
- [163] O. Olakanmi, B. E. Britigan, and L. S. Schlesinger. Gallium disrupts iron metabolism of mycobacteria residing within human macrophages. *Infection and Immunity*, 68(10):5619–5627, 2000.
- [164] A. M. Mulligan, M. Wilson, and J. C. Knowles. The effect of increasing copper content in phosphate-based glasses on biofilms of *Streptococcus sanguis*. *Biomaterials*, 24(10):1797–1807, 2003.
- [165] A. M. Mulligan, M. Wilson, and J. C. Knowles. Effect of increasing silver content in phosphate-based glasses on biofilms of *Streptococcus sanguis*. *Journal of Biomedical Materials Research Part A*, 67A(2):401–412, 2003.
- [166] J. R. Harrington, R. J. Martens, N. D. Cohen, and L. R. Bernstein. Antimicrobial activity of gallium against virulent *rhodococcus equi* in vitro and in vivo. *Journal of Veterinary Pharmacology and Therapeutics*, 29(2):121–127, 2006.
- [167] Y. Kaneko, M. Thoendel, O. Olakanmi, B. E. Britigan, and P. K. Singh. The transition metal gallium disrupts *pseudomonas aeruginosa* iron metabolism and has antimicrobial and antibiofilm activity. *Journal of Clinical Investigation*, 117(4):877–888, 2007.
- [168] S. P. Valappil, D. Ready, E. A. Abou Neel, D. M. Pickup, W. Chrzanowski, L. A. O’Dell, R. J. Newport, M. E. Smith, M. Wilson, and J. C. Knowles. Antimicrobial gallium-doped phosphate-based glasses. *Advanced Functional Materials*, 18(5):732–741, 2008.
- [169] D. M. Pickup, S. P. Valappil, R. M. Moss, H. L. Twyman, P. Guerry, M. E. Smith, M. Wilson, J. C. Knowles, and R. J. Newport. Preparation, structural characterisation and antibacterial properties of ga-doped sol-gel phosphate-based glass. *Journal of Materials Science*, 44(7):1858–1867, 2009.
- [170] G. Lusvardi, G. Malavasi, L. Menabue, and S. Shrutti. Gallium-containing phosphosilicate glasses: Functionalization and in-vitro bioactivity. *Materials Science & Engineering C-Materials for Biological Applications*, 33(6):3190–3196, 2013.
- [171] L. R. Bernstein. Mechanisms of therapeutic activity for gallium. *Pharmacological Reviews*, 50(4):665–682, 1998.
- [172] A. Hoppe, N. S. Guldal, and A. R. Boccaccini. A review of the biological response to ionic dissolution products from bioactive glasses and glass-ceramics. *Biomaterials*, 32(11):2757–2774, 2011.
- [173] D. M. Pickup, R. M. Moss, D. Qiu, R. J. Newport, S. P. Valappil, J. C. Knowles, and M. E. Smith. Structural characterization by X-ray methods of novel antimicrobial gallium-doped phosphate-based glasses. *Journal of Chemical Physics*, 130(6), 2009.
- [174] I. Abrahams, K. Franks, G. E. Hawkes, G. Philippou, J. Knowles, P. Bodart, and T. Nunes. Na-23, Al-27 and P-31 NMR and X-ray powder diffraction study of Na/Ca/Al phosphate glasses and ceramics. *Journal of Materials Chemistry*, 7(8):1573–1580, 1997.

- [175] V. Montouillout, C. M. Morais, A. Douy, F. Fayon, and D. Massiot. Toward a better description of gallo-phosphate materials in solid-state NMR: 1D and 2D correlation studies. *Magnetic Resonance in Chemistry*, 44(8):770–775, 2006.
- [176] C. Mellier, F. Fayon, V. Schnitzler, P. Deniard, M. Allix, S. Quillard, D. Massiot, J. M. Boulter, B. Bujoli, and P. Janvier. Characterization and properties of novel gallium-doped calcium phosphate ceramics. *Inorganic Chemistry*, 50(17):8252–8260, 2011.
- [177] M. Amri, S. E. Ashbrook, D. M. Dawson, J. M. Griffin, R. I. Walton, and S. Wimperis. A multinuclear solid-state NMR study of templated and calcined chabazite-type GaPO-34. *Journal of Physical Chemistry C*, 116(28):15048–15057, 2012.
- [178] B. Bureau, G. Silly, J. Y. Buzare, C. Legein, and D. Massiot. From crystalline to glassy gallium fluoride materials: an NMR study of Ga-69 and Ga-71 quadrupolar nuclei. *Solid State Nuclear Magnetic Resonance*, 14(3-4):181–190, 1999.
- [179] B. Bureau, G. Silly, J. Y. Buzare, B. Boulard, and C. Legein. Nuclear magnetic resonance quadrupolar parameters and short range order in disordered ionic fluorides. *Journal of Physics-Condensed Matter*, 12(26):5775–5788, 2000.
- [180] Y. Ledemi, B. Bureau, G. Le Caer, L. Calvez, C. Roiland, G. Tricot, P. Florian, V. Nazabal, and D. Massiot. ^{71}Ga NMR in chalcogenide and chalcogen-halide glasses. *Journal of Non-Crystalline Solids*, 383(0):216–221, 2014.
- [181] J. H. Zhong and P. J. Bray. Determination of gallium coordination in cesium gallate glasses by high-resolution pulsed NMR. *Journal of Non-Crystalline Solids*, 94(1):122–132, 1987.
- [182] A. Belkebir, J. Rocha, A. P. Esculcas, P. Berthet, S. Poisson, B. Gilbert, Z. Gabelica, G. Llabres, F. Wijzen, and A. Rulmont. Structural characterization of glassy phases in the system $\text{Na}_2\text{O}-\text{Ga}_2\text{O}_3-\text{P}_2\text{O}_5$ by MAS-NMR, EXAFS and vibrational spectroscopy. i. cations coordination. *Spectrochimica Acta Part a-Molecular and Biomolecular Spectroscopy*, 56(3):423–434, 2000.
- [183] M. Zeyer, L. Montagne, V. Kostoj, G. Palavit, D. Prochnow, and C. Jaeger. O-17 nuclear magnetic resonance study of $\text{Na}_2\text{O}-\text{P}_2\text{O}_5$ glasses. *Journal of Non-Crystalline Solids*, 311(3):223–232, 2002.
- [184] A. Flambard, L. Montagne, and L. Delevoye. A new O-17-isotopic enrichment method for the NMR characterisation of phosphate compounds. *Chemical Communications*, (32):3426–3428, 2006.
- [185] F. Vasconcelos, S. Cristol, J. F. Paul, G. Tricot, J. P. Amoureux, L. Montagne, F. Mauri, and L. Delevoye. O-17 solid-state NMR and first-principles calculations of sodium trimetaphosphate ($\text{Na}_3\text{P}_3\text{O}_9$), tripolyphosphate ($\text{Na}_5\text{P}_3\text{O}_{10}$), and pyrophosphate ($\text{Na}_4\text{P}_2\text{O}_7$). *Inorganic Chemistry*, 47(16):7327–7337, 2008.
- [186] S. E. Ashbrook and M. E. Smith. Solid state O-17 NMR - an introduction to the background principles and applications to inorganic materials. *Chemical Society Reviews*, 35(8):718–735, 2006.
- [187] J. F. Stebbins and Z. Xu. NMR evidence for excess non-bridging oxygen in an aluminosilicate glass. *Nature*, 390(6655):60–62, 1997.

- [188] J. F. Stebbins, E. V. Dubinsky, K. Kanehashi, and K. E. Kelsey. Temperature effects on non-bridging oxygen and aluminum coordination number in calcium aluminosilicate glasses and melts. *Geochimica Et Cosmochimica Acta*, 72(3):910–925, 2008.
- [189] L. Peng and J. F. Stebbins. High resolution ^{17}O MAS and triple-quantum MAS NMR studies of gallosilicate glasses. *Journal of Non-Crystalline Solids*, 354(27):3120–3128, 2008.
- [190] N. Forler, F. Vasconcelos, S. Cristol, J. F. Paul, L. Montagne, T. Charpentier, F. Mauri, and L. Delevoye. New insights into oxygen environments generated during phosphate glass alteration: a combined O-17 MAS and MQMAS NMR and first principles calculations study. *Physical Chemistry Chemical Physics*, 12(31):9054–9063, 2010.
- [191] R. A. Martin, H. L. Twyman, G. J. Rees, E. R. Barney, R. M. Moss, J. M. Smith, R. G. Hill, G. Cibin, T. Charpentier, M. E. Smith, J. V. Hanna, and R. J. Newport. An examination of the calcium and strontium site distribution in bioactive glasses through isomorphous neutron diffraction, X-ray diffraction, EXAFS and multinuclear solid state NMR. *Journal of Materials Chemistry*, 22(41):22212–22223, 2012.
- [192] F. Munoz, L. Delevoye, L. Montagne, and T. Charpentier. New insights into the structure of oxynitride NaPON phosphate glasses by ^{17}O -NMR. *Journal of Non-Crystalline Solids*, 363:134–139, 2013.
- [193] S. Schramm and E. Oldfield. High-resolution O-17 NMR of solids. *Journal of the American Chemical Society*, 106(9):2502–2506, 1984.
- [194] G. Le Caer, B. Bureau, and D. Massiot. An extension of the Czeh model for the distributions of electric field gradients in disordered solids and an application to NMR spectra of Ga-71 in chalcogenide glasses. *Journal of Physics-Condensed Matter*, 22(6), 2010.
- [195] Z. H. Gan. Isotropic NMR spectra of half-integer quadrupolar nuclei using satellite transitions and magic-angle spinning. *Journal of the American Chemical Society*, 122(13):3242–3243, 2000.
- [196] S. E. Ashbrook, A. J. Berry, W. O. Hibberson, S. Steuernagel, and S. Wimperis. High-resolution O-17 NMR spectroscopy of wadsleyite ($\beta\text{-Mg}_2\text{SiO}_4$). *Journal of the American Chemical Society*, 125(39):11824–11825, 2003.
- [197] S. E. Ashbrook and S. Wimperis. High-resolution NMR of quadrupolar nuclei in solids: the satellite-transition magic angle spinning (STMAS) experiment. *Progress in Nuclear Magnetic Resonance Spectroscopy*, 45(1-2):53–108, 2004.
- [198] S. E. Ashbrook, A. J. Berry, D. J. Frost, A. Gregorovic, C. J. Pickard, J. E. Readman, and S. Wimperis. O-17 and Si-29 NMR parameters of MgSiO_3 phases from high-resolution solid-state NMR spectroscopy and first-principles calculations. *Journal of the American Chemical Society*, 129(43):13213–13224, 2007.
- [199] Zhehong Gan. *Satellite Transition NMR Spectroscopy of Half-Integer Quadrupolar Nuclei under Magic-Angle Spinning*. John Wiley & Sons, Ltd, 2007.
- [200] Hanna Luehrs. *The Influence of Boron on the Crystal Structure and Properties of Mullite*. PhD thesis, Universitat Bremen, 2013.

- [201] R. J. Angel, R. K. McMullan, and C. T. Prewitt. Substructure and superstructure of mullite by neutron-diffraction. *American Mineralogist*, 76(3-4):332–342, 1991.
- [202] R. X. Fischer, H. Schneider, and D. Voll. Formation of aluminum rich 9:1 mullite and its transformation to low alumina mullite upon heating. *Journal of the European Ceramic Society*, 16(2):109–113, 1996.
- [203] G. Kunathfandrei, P. Rehak, S. Steuernagel, H. Schneider, and C. Jager. Quantitative structural-analysis of mullite by Al-27 nuclear-magnetic-resonance satellite transition spectroscopy. *Solid State Nuclear Magnetic Resonance*, 3(5):241–248, 1994.
- [204] T. Epicier, M. A. Okeefe, and G. Thomas. Atomic imaging of 3-2 mullite. *Acta Crystallographica Section A*, 46:948–962, 1990.
- [205] R. X. Fischer and H. Schneider. Crystal chemistry of borates and borosilicates with mullite-type structures: a review. *European Journal of Mineralogy*, 20(5):917–933, 2008.
- [206] H. Luehrs, R. X. Fischer, and H. Schneider. Boron mullite: Formation and basic characterization. *Materials Research Bulletin*, 47(12):4031–4042, 2012.
- [207] Hanna Luehrs, H., Anatoliy Senyshyn, P. King Scott, V. Hanna John, Hartmut Schneider, and X. Fischer Reinhard. Neutron diffraction and ¹¹B solid state NMR studies of the crystal structure of B-doped mullite, 2013.
- [208] J. Wang, G. L. Ning, X. F. Yang, Z. H. Gan, H. Y. Liu, and Y. Lin. Large-scale synthesis of Al₄B₂O₉/Al₁₈B₄O₃₃ whiskers via a novel method. *Materials Letters*, 62(8-9):1208–1211, 2008.
- [209] M. Garsche, E. Tillmanns, H. Almen, H. Schneider, and V. Kupcik. Incorporation of chromium into aluminum borate 9Al₂O₃.2B₂O₃ (A₉B₂). *European Journal of Mineralogy*, 3(5):793–808, 1991.
- [210] H. Wada, K. Sakane, T. Kitamura, Y. Kayahara, A. Kawahara, and N. Sasaki. Thermal-conductivity of aluminum borate. *Nippon Seramikkusu Kyokai Gakujutsu Ronbunshi-Journal of the Ceramic Society of Japan*, 102(8):695–701, 1994.
- [211] S. Hayashi and K. Hayamizu. Shift references in high-resolution solid-state NMR. *Bulletin of the Chemical Society of Japan*, 62(7):2429–2430, 1989.
- [212] P. F. Barron, R. L. Frost, J. O. Skjemstad, and A. J. Koppi. Detection of 2 silicon environments in kaolins by solid-state Si-29 NMR. *Nature*, 302(5903):49–50, 1983.
- [213] J. McManus, S.E. Ashbrook, K.J.D MacKenzie, and S Wimperis. ²⁷Al multiple-quantum MAS and ²⁷Al(1H) CPMAS NMR study of amorphous aluminosilicates. *Journal of Non-Crystalline Solids*, 282(23):278 – 290, 2001.
- [214] S. H. Wang, Z. Xu, J. H. Baltisberger, L. M. Bull, J. F. Stebbins, and A. Pines. Multiple-quantum magic-angle spinning and dynamic-angle spinning NMR spectroscopy of quadrupolar nuclei. *Solid State Nuclear Magnetic Resonance*, 8(1):1–16, 1997.
- [215] B. L. Sherriff and H. D. Grundy. Calculations of Si-29 MAS NMR chemical-shift from silicate mineral structure. *Nature*, 332(6167):819–822, 1988.

- [216] J. F. Stebbins, J. V. Oglesby, and S. Kroeker. Oxygen triclusters in crystalline CaAl_4O_7 (grossite) and in calcium aluminosilicate glasses: O-17 NMR. *American Mineralogist*, 86(10):1307–1311, 2001.

Appendix A

Appendix

A.1 Reduced Wigner rotation matrix elements $d_{kl}^j(\beta)$

$$\begin{aligned}
d_{00}^0(\beta) &= 1 \\
d_{00}^1(\beta) &= \cos\beta \\
d_{01}^1(\beta) &= d_{-10}^1(\beta) = -d_{0-1}^1(\beta) = -d_{10}^1(\beta) = \frac{1}{\sqrt{2}}\sin\beta \\
d_{1-1}^1(\beta) &= d_{-11}^1(\beta) = \sin^2\left(\frac{\beta}{2}\right) = \frac{1}{2}(1 - \cos\beta) \\
d_{11}^1(\beta) &= d_{-1-1}^1(\beta) = \cos^2\left(\frac{\beta}{2}\right) = \frac{1}{2}(1 + \cos\beta) \\
d_{00}^2(\beta) &= \frac{1}{2}(3\cos^2\beta - 1) \\
d_{10}^2(\beta) &= d_{0-1}^2(\beta) = -d_{01}^2(\beta) = -d_{-10}^2(\beta) = -\sqrt{\frac{3}{2}}\sin\beta\cos\beta \\
d_{1-1}^2(\beta) &= d_{-11}^2(\beta) = \frac{1}{2}(2\cos\beta + 1)(1 - \cos\beta) \\
d_{11}^2(\beta) &= d_{-1-1}^2(\beta) = \frac{1}{2}(2\cos\beta - 1)(1 + \cos\beta) \\
d_{20}^2(\beta) &= d_{02}^2(\beta) = d_{-20}^2(\beta) = d_{0-2}^2(\beta) = \sqrt{\frac{3}{8}}\sin^2\beta \\
d_{21}^2(\beta) &= -d_{12}^2(\beta) = -d_{-2-1}^2(\beta) = -d_{-1-2}^2(\beta) = -\frac{1}{2}\sin\beta(\cos\beta + 1) \\
d_{2-1}^2(\beta) &= d_{1-2}^2(\beta) = -d_{-21}^2(\beta) = -d_{-12}^2(\beta) = \frac{1}{2}\sin\beta(\cos\beta - 1) \\
d_{22}^2(\beta) &= d_{-2-2}^2(\beta) = \cos^4\left(\frac{\beta}{2}\right) \\
d_{2-2}^2(\beta) &= d_{-22}^2(\beta) = \sin^4\left(\frac{\beta}{2}\right)
\end{aligned} \tag{A.1}$$

A.2 Coefficients for the Second Order Quadrupole Interaction along with MQMAS ratio

Spin (I)	Transition (m)	C_0 (rank 0)	C_2 (rank 2)	C_4 (rank 4)	k
3/2	1/2	3	24	54	N/A
3/2	3/2	-9	0	-42	-7/9
5/2	1/2	8	64	144	N/A
5/2	3/2	6	120	228	19/12
5/2	5/2	-50	-40	-300	-25/12

Table A.1: Coefficients for the Second Order Quadrupole Interaction for spin 3/2 and 5/2 nuclei. The MQMAS ratio k relates to the rank 4 term. The table is taken from Frydman and Harwood J. Am. Chem. Soc., Vol. 117, No. 19, 1995, in their ground breaking paper on MQMAS.

A.3 ^{23}Na MAS NMR parameters from simulation of Al doped bioactive glasses single pulse NMR spectra.

Peak	$\delta(\text{ppm})$ (± 0.5)	C_Q Center (MHz) (± 0.3)	C_Q Width (MHz) (± 0.5)	η (± 0.05)
0Al11Na	-6.4	2.7	1.5	0.1
3Al8Na	-8.8	2.4	1.6	0.1
5Al6Na	-10.5	2.2	2.0	0.1
8Al3Na	-11.6	2.1	1.7	0.1

Table A.2: ^{23}Na MAS NMR parameters from simulation of single pulse MAS NMR spectra. Parameters constrained from multiple field fitting, using Quadfit software package. [153]

A.4 Simulation parameters from ^{31}P MAS NMR data of Al phosphate glasses.

	$\delta(\text{ppm})$ $\pm 0.1 \text{ ppm}$	Int (%) $\pm 0.5\%$	Environment
0Al11Na			
1	-8.0	17	Q^1
2	-24.5	83	Q^2
3Al8Na			
1	-10.1	19.5	Q^1
2	-24.2	80	Q^2
5Al6Na			
1	-11.5	20	Q^1
2	-24.3	80	Q^2
8Al3Na			
1	-12.3	18	Q^1
2	-24.3	82	Q^2

Table A.3: Fitting parameters from ^{31}P NMR of Al glass samples carried out at 7.05 T. Simulations carried out using DmFit software package.[152]

A.5 Fitting Results from Time-Domain spin echo fits of ^{31}P REINE curves for $Q^1 - Q^1$ and $Q^1 - Q^2$ peaks of Al phosphate glasses

	Peak	ϵ^2	Fitted Parameters ($^2J_{QQ}$ in Hz, T'_2 in ms)	Correlation Coefficient
0Al11Na	$Q^1 - Q^1$	36.3×10^{-3}	$^2J_{Q^1Q^1} = 11.9 \pm 0.7$ $T'_2 = 38.8 \pm 3.7$	$T'_2 - ^2J_{Q^1Q^1}$: -0.0323
	$Q^1 - Q^2$	18.0×10^{-3}	$^2J_{Q^1Q^2} = 16.8 \pm 0.3$ $T'_2 = 40.1 \pm 2.0$	$T'_2 - ^2J_{Q^1Q^2}$: -0.0046
3Al8Na	$Q^1 - Q^1$	34.1×10^{-3}	$^2J_{Q^1Q^1} = 11.1 \pm 0.7$ $T'_2 = 31.8 \pm 3.1$	$T'_2 - ^2J_{Q^1Q^1}$: 0.2425
	$Q^1 - Q^2$	25.4×10^{-3}	$^2J_{Q^1Q^2} = 15.0 \pm 0.5$ $T'_2 = 31.9 \pm 2.1$	$T'_2 - ^2J_{Q^1Q^2}$: 0.0060
5Al6Na	$Q^1 - Q^1$	57.6×10^{-3}	$^2J_{Q^1Q^1} = 10.6 \pm 0.7$ $T'_2 = 42.0 \pm 5.0$	$T'_2 - ^2J_{Q^1Q^1}$: 0.1027
	$Q^1 - Q^2$	44.0×10^{-3}	$^2J_{Q^1Q^2} = 13.6 \pm 0.6$ $T'_2 = 34.0 \pm 3.0$	$T'_2 - ^2J_{Q^1Q^2}$: 0.0521
8Al3Na	$Q^1 - Q^2$	15.8×10^{-3}	$^2J_{Q^1Q^2} = 13.1 \pm 0.6$ $T'_2 = 31.0 \pm 2.2$	$T'_2 - ^2J_{Q^1Q^2}$: 0.0534

Table A.4: Fitting Results from Time-Domain spin echo fits of ^{31}P REINE curves for $Q^1 - Q^1$ and $Q^1 - Q^2$ peaks (7.05 T with 12.5 kHz MAS)

A.6 Fitting Results from Time-Domain spin echo fits of ^{31}P REINE curves for $Q^2 - Q^2$ peaks of Al phosphate glasses

	Peak	ϵ^2	Fitted Parameters ($^2J_{QQ}$ in Hz, T'_2 in ms)	Correlation Coefficient
0Al11Na	$Q^2 - Q^2$	5.2×10^{-3}	$^2J_{Q^2Q^2} = 10.2 \pm 0.5$ $T'_2 = 23.5 \pm 1.5$	$T'_2 - ^2J_{Q^2Q^2}$: 0.4632
3Al8Na	$Q^2 - Q^2$	5.3×10^{-3}	$^2J_{Q^2Q^2} = 10.1 \pm 0.4$ $T'_2 = 26.5 \pm 1.6$	$T'_2 - ^2J_{Q^2Q^2}$: 0.5907
5Al6Na	$Q^2 - Q^2$	2.3×10^{-3}	$^2J_{Q^1Q^2} = 12.1 \pm 0.5$ $^2J_{Q^2Q^2} = 7.5 \pm 0.7$ $T'_2 = 15.8 \pm 1.0$	$T'_2 - ^2J_{Q^1Q^2}$: 0.6678 $T'_2 - ^2J_{Q^2Q^2}$: 0.4618 $^2J_{Q^1Q^2} - ^2J_{Q^2Q^2}$: -0.038
8Al3Na	$Q^2 - Q^2$	27×10^{-3}	$^2J_{Q^1Q^2} = 13.2 \pm 0.1$ $^2J_{Q^2Q^2} = 6.0 \pm 0.3$ $T'_2 = 14.8 \pm 0.3$	$T'_2 - ^2J_{Q^1Q^2}$: 0.7247 $T'_2 - ^2J_{Q^2Q^2}$: 0.5560 $^2J_{Q^1Q^2} - ^2J_{Q^2Q^2}$: 0.2949

Table A.5: Fitting Results from Time-Domain spin echo fits of ^{31}P REINE curves for $Q^2 - Q^2$ peaks (7.05 T with 12.5 kHz MAS).

A.7 Fitting Results from Time-Domain spin echo fits of ^{31}P REINE curves for $Q^1 - Q^2$ and $Q^2 - Q^2$ peaks of Ga phosphate glasses

	Peak	ϵ^2	Fitted Parameters ($^2J_{QQ}$ in Hz, T'_2 in ms)	Correlation Coefficient
P45Ga1	$Q^1 - Q^2$	16.7×10^{-3}	$^2J_{Q^1Q^2} = 16.1 \pm 0.1$ $T'_2 = 31.5 \pm 1.7$	$T'_2 - ^2J_{Q^1Q^2}$: -0.0031
	$Q^2 - Q^2$	3.3×10^{-3}	$^2J_{Q^2Q^2} = 10.9 \pm 0.4$ $T'_2 = 21.3 \pm 1.0$	$T'_2 - ^2J_{Q^2Q^2}$: 0.6589
P45Ga3	$Q^1 - Q^2$	13.1×10^{-3}	$^2J_{Q^1Q^2} = 16.4 \pm 0.5$ $T'_2 = 31.4 \pm 1.8$	$T'_2 - ^2J_{Q^1Q^2}$: -0.1081
	$Q^2 - Q^2$	6.6×10^{-3}	$^2J_{Q^2Q^2} = 11.5 \pm 0.6$ $T'_2 = 22.1 \pm 1.6$	$T'_2 - ^2J_{Q^2Q^2}$: 0.4001
P45Ga5	$Q^1 - Q^2$	26.2×10^{-3}	$^2J_{Q^1Q^2} = 15.5 \pm 0.6$ $T'_2 = 27.6 \pm 2.0$	$T'_2 - ^2J_{Q^1Q^2}$: 0.0454
	$Q^2 - Q^2$	18.0×10^{-3}	$^2J_{Q^2Q^2} = 11.0 \pm 0.8$ $T'_2 = 24.5 \pm 2.5$	$T'_2 - ^2J_{Q^2Q^2}$: 0.5077

Table A.6: Fitting Results from Time-Domain spin echo fits of ^{31}P REINE curves for $Q^1 - Q^2$ and $Q^2 - Q^2$ peaks (7.05 T with 12.5 kHz MAS)